Fusing Synthetic Biology with Nanotechnology: Integrating Proteins into Carbon Nanotube Field-Effect Transistors

Rebecca Elizabeth Alice Gwyther

School of Biosciences

Cardiff University

A thesis submitted to Cardiff University for the degree of
Doctor of Philosophy

April 2023

Acknowledgements

List of Publications

Gwyther, R., Lee, C.S., Côte, S., Ramakrishnan, K., Palma, M., Jones, D., 2023. Optimising CNT-FET Biosensor Design: Predictive Modelling of Biomolecular Electrostatic Gating and its Application to Beta-Lactamase Detection. *Pending publication*.

Lee, C.S., **Gwyther, R.**, Freeley, M., Jones, D., Palma, M., 2022. Fabrication and Functionalisation of Nanocarbon-based Field-Effect Transistor Biosensors. *ChemBioChem*, 23, e202200282.

Cervantes-Salguero, K., Freeley, M., **Gwyther, R.**, Jones, D., Chávez, J., Palma, M., 2022. Single Molecule DNA Origami Nanoarrays with Controlled Protein Orientation. *Biophysics Rev. 3,* 031401.

Gwyther, R., Nekrasov, N., Emelianov, A., Nasibulin, A., Ramakrishnan, K., Bobrinetskiy, I. and Jones, D., 2022. Differential Bio-Optoelectronic Gating of Semiconducting Carbon Nanotubes by Varying the Covalent Attachment Residue of a Green Fluorescent Protein. *Advanced Functional Materials*, 32(22), p.2112374.

Xu, X., Bowen, B., **Gwyther, R.**, Freeley, M., Grigorenko, B., Nemukhin, A., Eklöf-Österberg, J., Moth-Poulsen, K., Jones, D. and Palma, M., 2021. Tuning Electrostatic Gating of Semiconducting Carbon Nanotubes by Controlling Protein Orientation in Biosensing Devices. *Angewandte Chemie*, 133(37), pp.20346-20351.

Freeley, M., **Gwyther, R.**, Jones, D. and Palma, M., 2021. DNA-Directed Assembly of Carbon Nanotube–Protein Hybrids. *Biomolecules*, 11(7), p.955.

Gwyther, R., Jones, D. and Worthy, H., 2019. Better together: building protein oligomers naturally and by design. *Biochemical Society Transactions*, 47(6), pp.1773-1780.

Thomas, S., Jamieson, W., **Gwyther, R.**, Bowen, B., Beachey, A., Worthy, H., Macdonald, J., Elliott, M., Castell, O. and Jones, D., 2020. Site-Specific Protein Photochemical Covalent Attachment to Carbon Nanotube Side Walls and Its Electronic Impact on Single Molecule Function. *Bioconjugate Chemistry*, 31(3), pp.584-594.

Abstract

Proteins are nature's own nanomachines. Crafted through years of evolution, they are optimised to perform a range of cellular functions. To translate this into a useful nanotechnological application, proteins can be integrated into fundamental electronic devices known as carbon nanotube field-effect transistors (NT-FETs). I do this by engineering in non-natural amino acid p-azido-L-phenylalanine (AzF), which can be activated by UV light to covalently bind the carbon nanotube channel of an NT-FET. This creates an intimate environment for signal transduction, whereby an external biochemical signal (e.g., a chemical reaction, or incoming charge density from a protein-protein interaction) is transduced into an electrical signal. Potential applications for this will be dependent on the protein interfaced, but this thesis will consider two key themes: biosensing and optoelectronic gating.

Chapter 3 builds on previous research by the Jones and Palma collaboration to develop a biosensor for antibiotic resistance (ABR). I do this by covalently integrating BLIP-II (Beta-Lactamase Inhibitory Protein II) to an NT-FET, transducing binding events with ABR biomarkers, the class A β-lactamases. NT-FETs were functionalised with defined BLIP-II^AzF variants to sample different orientations of analytes TEM-1 and KPC-2 β-lactamase. The distinct electrical signals generated correlated to the unique electrostatic surface being sampled, providing evidence for electrostatic gating.

Chapter 4 builds on the experimental results from Chapter 3 to consider whether the BLIP-II^AzF—NT-FET interface can be effectively modelled to predict AzF mutation site success in mediating proximal analyte sensing. Using molecular dynamics, data on AzF side chain rotamer propensity was extracted, and *in silico* modelling was performed to assess the possible binding orientations of BLIP-II^AzF variants at the NT-FET interface. Distance and electrostatic potential of incoming β-lactamases were measured and showed correlation to the electrostatic gating observed in Chapter 3.

Chapter 5 was devised in collaboration with the Bobrinetskiy lab, as I looked to exploit nature's own light-responsive elements by covalently integrating sfGFP (superfolder Green Fluorescent Protein) into an NT-FET platform. By defining sfGFP orientation through two distinct AzF anchor sites, light was shown to induce optoelectronic memory and optoelectronic gating. Further novelty was discovered as water regenerated the optoelectronic gating response after six months of protein dehydration.

Table of Contents

List of Units

Unit	Definition	Measure for
A	Amps	Current
A W^{-1}	Amps per watt (of incident radiant power)	Photoresponse
Å	Angstrom	Distance
Å^2	Angstrom^2	B-factor
AU	Arbitrary unit	Relative quantity
AU µM^{-1}	Arbitrary unit per µM^{-1}	Relative quantity
aM	Attomolar	Concentration
cm	Centimetre	Distance
°C	Degrees centigrade	Temperature
fs	Femtosecond	Time
g	Grams	Mass
Hz	Hertz	Frequency
$k_B T e_c^{-1}$	Energy (product of Boltzmann constant and temperature) per unit charge	Electrostatic potential
K	Kelvin	Temperature
L	Litre	Volume
µA	Microamps	Current
µL	Microlitre	Volume
µm	Micrometre	Distance

μM	Micromolar	Concentration
mL	Millilitre	Volume
mM	Millimolar	Concentration
mW	Milliwatt	Current
mW cm^{-2}	Milliwatt per centimetre^2	Power
M	Molar	Concentration
M^{-1}cm^{-1}	Per molar per centimetre	Molar absorption coefficient
nA	Nanoamps	Current
nm	Nanometer	Distance
nM	Nanomolar	Concentration
N m^{-1}	Newton-metre	Torque
nN	Nanonewtons	Force
ns	Nanosecond	Time
%	Percent	Quantity
pM	Picomolar	Concentration
ps	Picosecond	Time
rpm	Revolutions per minute	Rotational frequency
s	Second	Time
S	Siemens	Resistance
V	Volt	Voltage

1. Introduction

Work in this chapter contributed to two published, peer-reviewed review papers where I am 1st, or joint 1st, author. With permission from the publisher, text and figures have been taken and adapted for my thesis.

Lee, C.S., **Gwyther, R.**, Freeley, M., Jones, D., Palma, M., 2022. Fabrication and Functionalisation of Nanocarbon-based Field-Effect Transistor Biosensors. *ChemBioChem*, 23, e202200282.

Gwyther, R., Jones, D. and Worthy, H., 2019. Better together: building protein oligomers naturally and by design. *Biochemical Society Transactions*, 47(6), pp.1773-1780.

1.1 Introduction to field of research

Pushing the boundaries of interdisciplinary research, this thesis covers the fields of synthetic biology, biochemistry, nanotechnology and physics. Ilook to integrate nature's own nanomachines, proteins, into a fundamental electronic device, the field-effect transistor (FET).

FETs are characterised by their ability to impart an electric field on the semiconducting channel that connect its source and drain electrode. This external 'gate voltage' ultimately controls the flow of current between the source and drain and has significant application throughout the digital world. Carbon nanotube field-effect transistors (NT-FETs) represent a subset of FET that has gained significant momentum. Diversifying from traditional FETs, carbon nanotubes (CNTs) replace the traditional channel material of silicon to provide superior electronic and physical characteristics. Engineers and physicists recognise this as an opportunity to improve FET scaling and speed (Avouris 2007), while biochemists identify CNTs as a compatible interface for biological molecules and chemical groups, alike (Yao et al. 2021).

The concept of integrating proteins with CNTs in this setup is to establish an intimate communication platform to transduce an extraneous signal (e.g., a chemical reaction, or incoming charge density) into an electrical one (Kaisti 2017; Yao et al. 2021). Through a synergistic protein—CNT interface, signal transduction can have the same effect as a gating voltage, with conductance increasing or decreasing in response to the extraneous signal. Potential applications for this depend on the protein integrated, but this thesis will consider two key themes:

biosensing and optoelectronic gating. For biosensing, I integrate a receptor protein to the widespread markers of antimicrobial resistance: β-lactamase, to transduce protein binding events. For optoelectronic gating, I integrate the light-responsive superfolder green fluorescent protein to transduce light absorption at defined wavelengths. The generation of these bionanohybrid devices represents a step forward for sustainable electronics and advanced functional design, where highly evolved proteins are integrated into a sensitive electrical platform to function in useful way.

1.2 Carbon nanotube field-effect transistors (NT-FETs)

1.2.1 Background to NT-FETs

Field-effect transistors (FETs) are embedded in modern day electronics. First proposed in 1926 (Lilienfeld 1926), the transistor was conceptualised around a three terminal device with a source, drain and gate electrode. A semiconducting channel connecting the source and drain electrode was shown to have its conductance modulated by application of an external gate voltage, allowing conductance to be switched 'on' and 'off' (Kahng 1960; Horowitz 1998). This translates as the well-known binary states '1' and '0' used by logic circuits, and underlies their mass usage in the digital world (Service 2009).

In the years since their discovery, FETs have been diversified through experimentation with different channel materials, types of gate and gate-channel insulation (Pachauri and Ingebrandt 2016; Lee et al. 2022). The advent of carbon-nanotube FETs (NT-FET) in 1998 stimulated great interest, as the traditional silicon channel was replaced by one dimensional semiconducting carbon nanotubes (CNTs) (Martel et al. 1998; Tans et al. 1998). CNTs offered supreme electrical performance, with high charge mobility and effective coupling between the gate voltage and channel conductance (Dürkop et al. 2004; Avouris 2007). These properties excited physicists and engineers alike, with the scaling down of FETs a continual challenge for high-density and ultrafast logic circuits (Service 2009; Obite et al. 2018). The electrical platform and physical structure of CNTs then captured the attention of biochemists who recognised it could be adapted for protein integration through CNT functionalisation (Liu and Guo 2012; Lee et al. 2022). These unique properties have allowed NT-FET application to spread from logic

circuits and computing to biosensing and bionanohybrid devices, and will be covered in great detail throughout the introduction.

1.2.2 General structure and operating principle

NT-FETs are comprised of three key components: the channel, the electrodes (source, drain and gate), and the base substrate. Materials for these can vary between transistors, so the examples below will be specific to NT-FETs fabricated in this thesis. The channel is comprised of semiconducting single-walled carbon nanotubes (SWCNTs) which connect the gold metal contacts of the source and drain electrode (Figure 1.1). The base substrate is the main body of the NT-FET and is comprised of heavily doped silicon. In Figure 1.1, the substrate is shown to dual function as the bottom gate electrode when a voltage is applied. An insulative dielectric layer then exists between the channel and substrate, to prevent excess charge leaking from the gate (Service 2009).
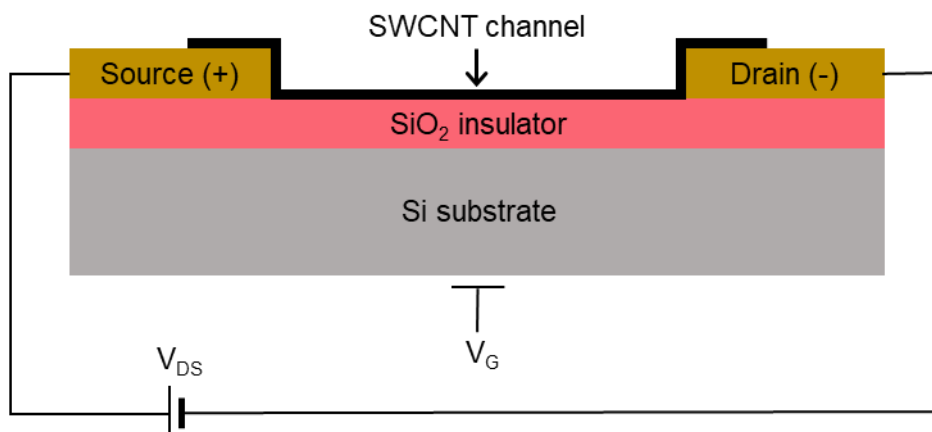
Figure 1.1 – Schematic of typical NT-FET. The NT-FET has three terminals: source, drain and gate. In this example, the silicon substrate takes on the role of the bottom gate, imparting an electric field on the SWCNT channel to modulate the current passing through. An insulative layer of SiO_2 separates the gate from the semiconducting channel.

The general operating principle of an NT-FET is as follows. A bias voltage is applied between the source and drain electrode (V_{DS}) so charge carriers can flow in the semiconductor channel, forming the source-drain current (I_{DS}). Schottky energy barriers may have to be crossed as current passes between the two metal-

semiconductor junctions, depending on the type of metal contact used (Obite et al. 2018). Charge carriers in the semiconductor channel then have their flow regulated by a perpendicular electric field imparted by the gate electrode. The voltage applied to the gate (V_G) can be positive or negative and will directly affect conductance by increasing or decreasing charge carrier population, depending on the doping behaviour of the semiconductor (Pachauri and Ingebrandt 2016). The NT-FETs fabricated in this thesis used p-type semiconducting SWCNTs, which operate with positively charged holes as the majority charge carrier. N-type semiconducting SWCNTs, by contrast, use electrons as their majority charge carrier. When a positive gate voltage is applied to a p-type semiconductor, holes are repelled from the region under the gate, reducing conductance (Figure 1.2). When a negative gate voltage is applied to a p-type semiconductor, holes accumulate near the gating region, increasing conductance (Lee et al. 2009). The reverse gating effects then apply in n-type semiconductors (Avouris 2007). It is important to note that gate voltages will eventually reach a threshold (V_T) that switches the NT-FET from its 'on' high current state to its 'off' low current state, as charge carriers become immobile. In my p-type NT-FETs, the on > off threshold will be a positive V_T, and off > on threshold will be a negative V_T. Gate voltage sweeps collecting data on this are known as transfer characteristics.
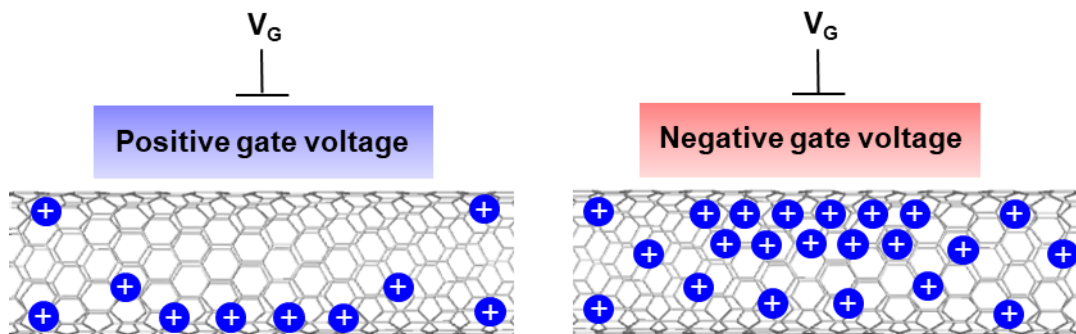
Figure 1.2 – Effect of gating voltage on p-type NT-FET. Applying a positive gate voltage repels holes from the region under the gate, while a negative gate voltage attracts them.

As an important note on charge mobility, the unipolar (e.g., p-type or n-type) flow of charge associated with NT-FET switching is controlled by aspects of transistor design (Figure 1.3 (A)). SWCNTs are naturally ambipolar, allowing simultaneous injection of positively charged holes and negatively charged electrons into the

valence and conductance band, respectively. The Schottky energy barrier between the metal source / drain electrodes and SWCNT channel has a considerable role to play, as it dictates how easy it is for charge to cross from one material to the other. To consider the height of the Schottky barrier, we look at the work function of the contact metal (Zorn and Zaumseil 2021). The gold electrodes used in my fabricated NT-FETs have a high work function (Hölzl and Schulte 1979), resulting in the metal's highest energy level (Fermi level) lying close to the semiconductor valence band (Figure 1.3 (B)). This results in a small Schottky energy barrier for holes to overcome to cross into the semiconductor channel and presents as a small increase in resistance at the interface. By comparison, electrons wanting to move from the metal to conduction band have a far greater energy barrier to cross, which helps contribute to a unipolar flow of holes in this p-type device (Avouris 2007; Obite et al. 2018). P-type behaviour is then further instilled by the environment, where unintentional p-doping occurs from an adsorbed oxygen / water layer (Aguirre et al. 2009). Mechanisms to better control unipolar flow include double gating to increase the thickness of the Schottky barrier, and chemical doping in the contact regions to permit electron doping or accepting, but neither of these were employed in my NT-FET design (Avouris 2007; Chae and Lee 2014).
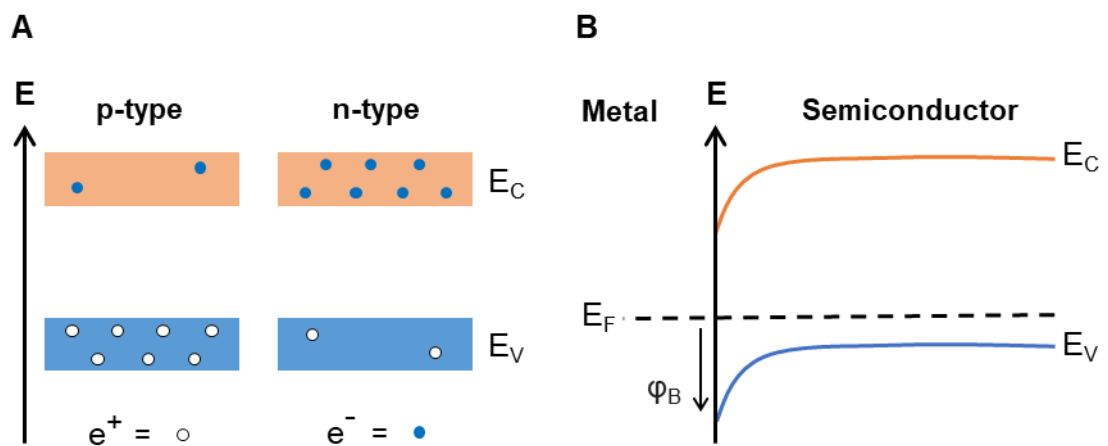
Figure 1.3 – Conduction and valence energy bands. (A) Schematic diagram of p-type and n-type semiconductors. Holes (e^+) in the valence (E_V) band are the majority charge carrier in p-type, while electrons (e^-) in the conduction (E_C) band are the majority charge carrier in n-type. (B) Energy band diagram of metal with high work function. The metal Fermi level (E_F) is close to the valence band of the

semiconductor, so holes cross the small Schottky energy barrier (φ_B) to carry charge between the two.

1.2.3 Semiconductor channel: SWCNTs

The choice of material comprising the semiconductor channel has a significant impact on electrical characteristics. FETs in the traditional metal-oxide semiconductor setup use silicon and silicon dioxide as the channel and dielectric materials, respectively, but these have reached their effective electrical limit in the continued miniaturisation of transistors (Moore 1965; Service 2009). An effort to diversify the channel materials has led to the use of organic polymers and silicon nanowire, but the most promising material – and earmarked to replace silicon – are CNTs (Horowitz 1998; Tans et al. 1998; Avouris 2007; Bishop et al. 2020; Lee et al. 2022).

CNTs are formed from sheets of sp^2 hybridised graphene one atom thick, rolled into seamless hollow tubes. One complete graphene roll forms a single-walled CNT, while several nanotubes nested inside one another form a multi-walled CNT (Avouris 2007). SWCNTs were chosen to be my NT-FET channel material, as they possess remarkable physical and electrical properties. SWCNTs have a diameter of approximately 1-2 nm (Avouris 2007), but maintain an aspect ratio of up to 132,000,000:1 (Wang et al. 2009), which is testament to their exceptional mechanical strength and stiffness. Their extensive surface area enhances compatibility for integration with biological molecules, as proteins can attach around the majority of SWCNT circumference, and not just the apex. SWCNTs also possess unique electrical properties which vary inherently with the vector of the honeycomb lattice and tube curvature. Classified by their chiral index, and requiring stringent purification, SWCNTs can fall into three categories: zig zag, chiral and armchair (Figure 1.4; Ramnani et al. 2016). Armchair SWCNTs always possess metallic properties, having no band gap between the valence and conductance bands. Chiral and zig zag SWCNTs can be either metallic or semiconducting, with certain diameters and helicities inducing the large semiconducting band gap (Dresselhaus et al. 2004). The band gap separates the valence and conduction bands, where the majority of charge is transported for p-type and n-type SWCNTs, respectively.
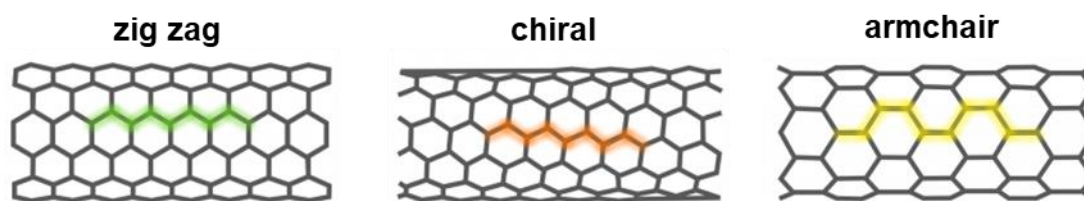
Figure 1.4 – Carbon nanotube network geometry. The nanotube longitudinal axis depends on the chiral angle (θ). Zig zag nanotubes correspond to θ = 0°, chiral nanotubes correspond to 0 < θ < 30°, and armchair nanotubes correspond to θ = 30°.

Once fabricated in the NT-FET setup, distinct electrical properties have been observed for semiconducting SWCNTs. These include (i) ballistic conductance, where charge flows without losing energy, (ii) effective coupling between the gate voltage and channel, for supreme conductance switching, and (iii) no scattering of charge from 'dangling' bonds (Avouris 2007). These properties supersede those of conventional channel materials, and have established SWCNTs as the channel material of choice in future FET design (Obite et al. 2018).

1.2.4 Gate electrode

The gate electrode regulates the current flowing between the source and drain electrodes by imparting a perpendicular electric field on the channel. Four different types exist: bottom, top, extended, and liquid (Figure 1.5), and the choice is dependent on the experimental purpose. The bottom gate is used most frequently for biosensing, as it allows a general exploration of electrical characteristics, such as threshold voltage shifts, on/off ratio changes and conductance changes. Top and extended gates are often used for studying charged analyte gating effects when there is a risk of damaging the channel material, and a liquid gate will be used to focus on a narrow gate voltage range (Lee et al. 2022).
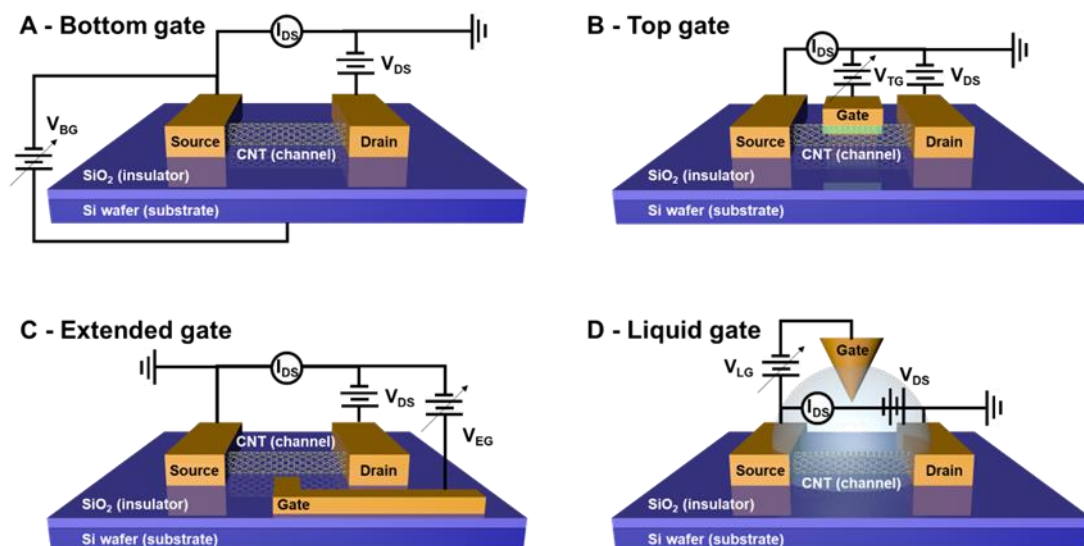
Figure 1.5 – Types of gate electrode. The bottom gate is most commonly used in NT-FETs with biosensing application, but top, extended and liquid gates also exist as alternative gating strategies. Figure copied with permission from Lee et al. (2022).

1.3 Operational mechanisms of NT-FETs

1.3.1 Conductance doping by proteins

NT-FETs are a prime signal transduction platform. The one-dimensional layer of carbon atoms is directly exposed to the environment, allowing small changes at the interface to translate as detectable electrical signals (Tran and Mulchandani 2016). On approach to the SWCNT surface, or through direct functionalisation, proteins use their inherent mass, size and electrostatic surface charge to induce a change in conductance through four key mechanisms. Firstly, direct charge transfer can occur between the protein and SWCNT. This interaction may donate electrons (n-doping), or accept electrons (p-doping), with the change in conductance dependent on p-type or n-type nature of the NT-FET (Bradley et al. 2004; Ghasemi and Salimi 2023). Proteins with inherent charge transfer pathways are more likely to utilise this mechanism, e.g., superfolder green fluorescent protein (sfGFP), where light absorption is coupled to electron donation (Bogdanov et al. 2009). The second mechanism, charge scattering, can occur as a side-effect of SWCNT functionalisation. Geometric deformations to the pristine sp^2 network can reduce conductance in both p-type and n-type NT-FETs (Star et al. 2003; Ee et al. 2007). Electrostatic gating from proximal charged proteins is the third mechanism and

8

operates similarly to a gate voltage. In a p-type NT-FET, proximal positive charge will repel holes and reduce conductance, while a proximal negative charge will attract holes and increase conductance (Artyukhin et al. 2006). The fourth mechanism is modification to the Schottky barriers at the interface of the carbon nanotube and metal contact. Protein adsorption here, regardless of charge, reduces the work function of the metal, correlating to an increase in Schottky barrier height and a decrease in conductance in p-type NT-FETs (Chen et al. 2004). Of these four mechanisms, Heller et al. (2008) identified electrostatic gating and Schottky barrier modifications to be primarily responsible for signal transduction in biosensing NT-FETs, paving the way for label-free sensing (Samuel and Rao 2022).

1.3.2 Output characteristics

To gather electrical data on NT-FETs and measure if any conductance doping has occurred, several different approaches can be taken. Firstly, current voltage characteristics (I/V) can be collected from the source and drain electrodes. NT-FETs should exhibit ohmic behaviour (current increasing linearly with voltage) if there is low contact resistance between the metal electrode and SWCNT channel. I/Vs can be compared before and after protein integration or sensing, where a change in conductance or resistance will present as a change in gradient – indicating physical or chemical changes to the surface of the SWCNT (Tlili et al. 2011). A second analysis technique is real-time sensing. Commonly used in biosensing assays, a constant voltage will be applied to the source electrode while current is measured in real-time from the drain electrode. Application of a gate voltage is optional and will depend on the type of assay. For example, the threshold voltage is often applied in analyte sensing assays to increase sensitivity, with a larger relative change in current induced by conductance doping. In a p-type NT-FET, a real-time increase in current can occur from negative electrostatic gating, whilst a decrease in current can occur from positive electrostatic gating or Schottky barrier modifications (Chen et al. 2004; Xu et al. 2021).

Transfer characteristics are a final form of output from NT-FETs, recording current from the drain electrode with a constant source voltage, and sweeping gate voltage. Collecting this data before and after protein integration or sensing can result in distinct electrical changes. In a p-type NT-FET, positive electrostatic charge in close proximity to SWCNTs equates to a negative gating voltage, shifting the transfer curve leftwards (Figure 1.6 (A)). Subsequently, negative electrostatic charge will

shift the transfer curve rightwards, towards more positive gate voltages. This horizontal shift along the V_G axis is also anticipated to occur from direct charge transfer, with n-doping shifting the curve leftwards and p-doping rightwards (Heller et al. 2008). Schottky barrier modifications then induce a change of slope in the transfer curve. Depicted in Figure 1.6 (B) as an ambipolar device, the curve changes asymmetrically for the p- and n-branches as a direct consequence of protein adsorption at the metal-SWCNT junction. An increase in Schottky barrier height for p-type NT-FETs (and the p-branch of the ambipolar device) pushes the Fermi level further from the valence band, resulting in an increased energy barrier for holes to cross and a loss of conductance. The opposite effect is then observed in n-type NT-FETs (and the n-branch of the ambipolar device), with the increase in Schottky barrier aligning the Fermi level closer to the conduction band. This results in a smaller energy barrier for electrons to cross, and thus an increase in conductance (Heller et al. 2008; Tran and Mulchandani 2016).
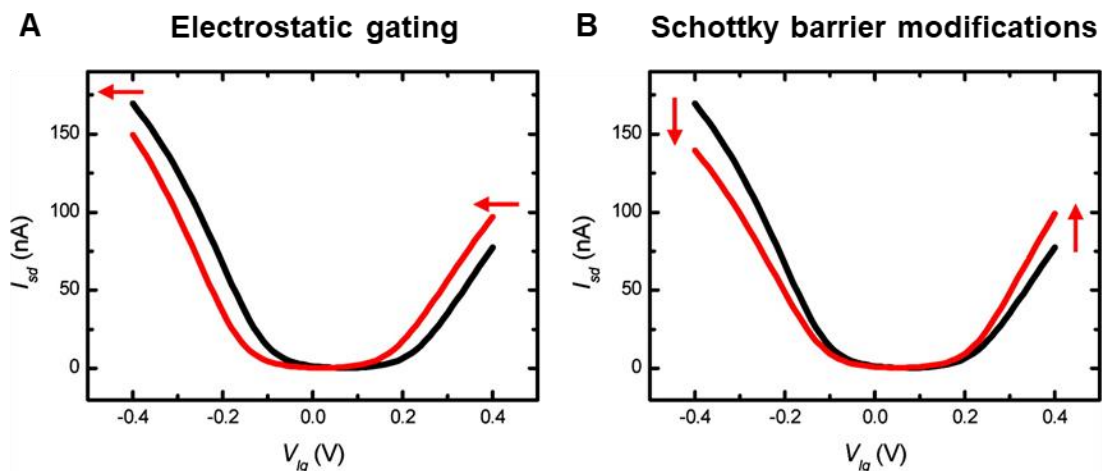
Figure 1.6 – Transfer characteristics in ambipolar NT-FET. Before analyte addition (black) and after (red). (A) Electrostatic gating results in horizontal shifts along the V_G axis, whilst modifications to the Schottky barrier (B) results in an asymmetrical change in slope. Figure adapted from Heller et al. (2008).

1.3.3 Debye screening effect

As one of the key mechanisms identified in conductance doping, electrostatic gating has an opposing parameter that is critical to its effect and function. The Debye screening effect is a phenomenon which occurs in ionic solutions to counter electrostatic potential (Stern et al. 2007). Through electrostatic interactions, solvated

counterions will surround charged biomolecules, and with increasing distance, electrostatic potential will decay towards zero (Israelachvili 1991). The point at which charge is fully neutralised is given by the Debye length (λ_D). Equation 1.1 shows the calculation of the Debye length in aqueous phase at room temperature; where l_B is the Bjerrum length (0.7 nm), and ρ_i and z_i are the density and valence of ionic species, respectively (Israelachvili 1991).

Equation 1.1

$$\lambda_D = \frac{1}{\sqrt{4\pi l_B \sum_i \rho_i z_i^2}}$$

Considering ρ_i and z_i, the salt concentration of a buffer has a significant role to play in NT-FET sensitivity. The Debye length for phosphate buffered saline (PBS), a common buffer used to mimic physiological conditions, is calculated at 0.7 nm. This highlights the limitations of NT-FETs in label-free sensing of biological samples, with common receptor proteins, e.g., antibodies, spanning 10-15 nm in height, and analytes needing to come within one Debye length to exert a gating effect (Rudikoff and Potter 1976; Teillaud et al. 1983).

To design biosensing NT-FETs that can operate within the Debye length, the protein—NT-FET interface must be systematically optimised through the analyte sensing mechanism, choice of receptor protein, and NT-FET functionalisation strategy. The latter two will be discussed in detail in sections 1.4 and 1.5, while the first will be considered here. The analyte sensing mechanism fundamentally depends on a shift in the charged environment within the Debye length of the SWCNT. Three different types of analyte can be considered: small charged biomolecules, small uncharged biomolecules, and large macromolecules, e.g., proteins. When small charged biomolecules bind NT-FETs, a change in conductance can be caused by the electrostatic gating effect. If the small biomolecule is uncharged, gating needs to induced by changes to the charged receptor. For example, binding of an uncharged analyte to a DNA aptamer can induce a conformational change that shifts the phosphate-sugar backbone, in turn changing the negative charge density within the Debye length (Figure 1.7 (A); Zheng et al. 2016a). Gating can also be induced by charged products, if the uncharged analytes comprise as substrates for NT-FETs functionalised with

enzymes (Figure 1.7 (B); Lee et al. 2022). The situation is more complex for macromolecules such as proteins. Proteins have a 3D structure with an electrostatic surface profile that varies inherently with the charged amino acids that comprise it. The gating effect will thus depend on the nature of the electrostatic surface that comes with the Debye length, establishing the potential for proteins to be identified by unique electrostatic signatures (Figure 1.7 (C)).
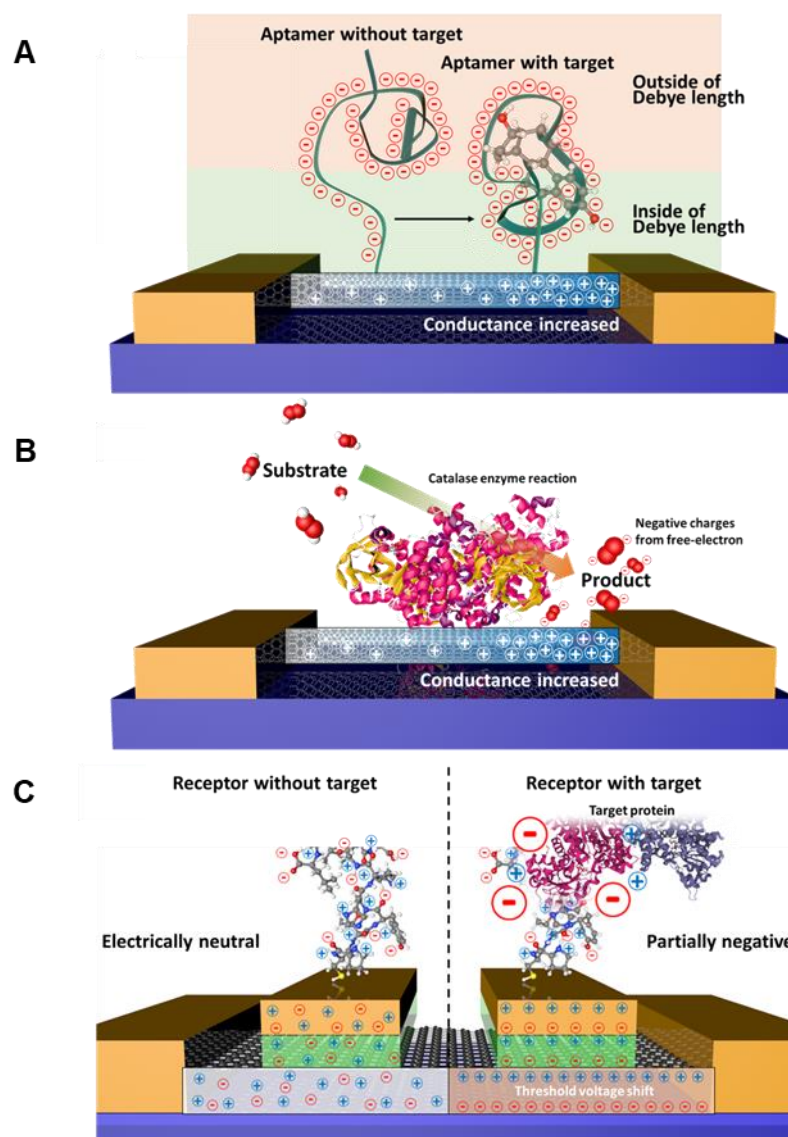
Figure 1.7 – Analyte sensing mechanisms. Signals can be generated by: (A) conformational changes of the charged receptors, (B) charged molecules produced from an enzymatic reaction and (C) changes in local charge from analyte binding. Figure copied with permission from Lee et al. (2022).

1.4 Integrating biomolecules into NT-FETs and their applications

The integration of biomolecules into NT-FETs can be considered from two perspectives: SWCNT functionalisation, or biomolecule functionalisation. Functionalisation in this instance describes the introduction of specific chemical reactivity to covalently or non-covalently link two typically unreactive species (SWCNTs and biomolecules). The methodologies available to both strategies are discussed in detail below, with examples noted for devices involved in biosensing and optoelectronic transduction. A final focus is then placed on the functionalisation strategy used in this thesis, regarding key aspects around genetic reprogramming, mechanistic pathways and conformational rotamers.

1.4.1 Functionalisation of SWCNTs for biomolecule attachment

Once an NT-FET has been fabricated, SWCNTs can undergo functionalisation to introduce biochemically compatible handles and linker groups. This can be done via covalent or non-covalent approaches (Figure 1.8) and allows the selective and controllable interfacing with biomolecules.
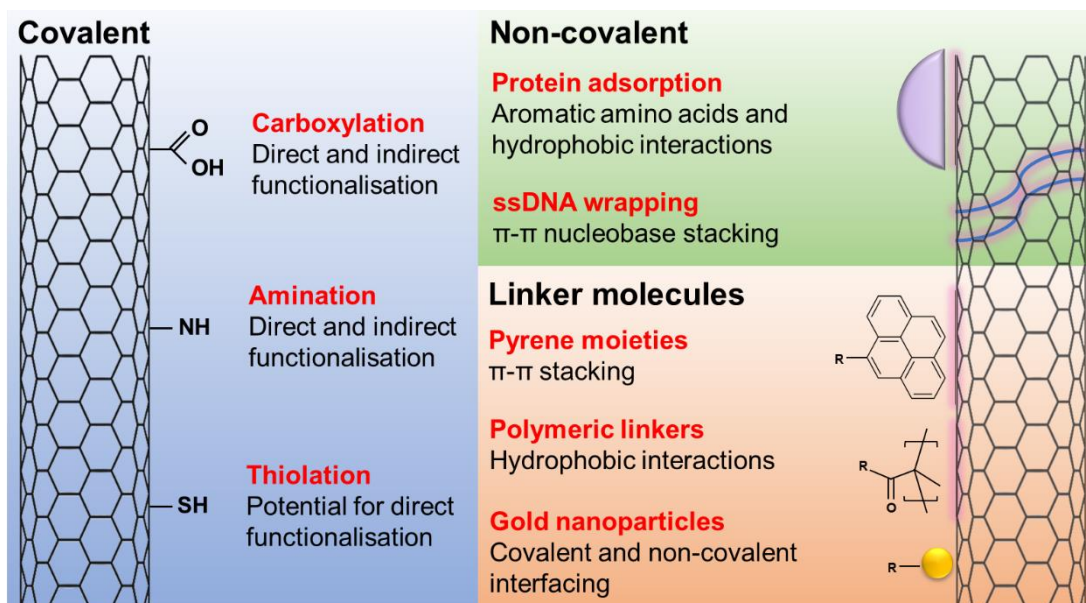
Figure 1.8 – Biocompatible nanocarbon functionalisation strategies. Covalent modification introduces functional groups directly into the carbon lattice, and these can conjugate biomolecules directly or indirectly (via attachment of linker molecule). Non-covalent functionalisation utilises hydrophobic interactions and π-π stacking of biomolecules to directly decorate the surface of nanocarbon. Linker molecules can

play an adaptor role; covalently or non-covalently interfacing with nanocarbon, whilst providing reactive biochemical handles for biomolecule conjugation. Modifications shown are not to scale. Figure copied with permission from Lee et al. (2022).

1.4.1.1 Covalent functionalisation

Covalent functionalisation of nanocarbon can be defined as the breaking of the sp^2 carbon lattice to create a new chemical bond. This represents a vast field of research (Dyke and Tour 2004; Mallakpour and Soltanian 2016; Schroeder et al. 2019), with reviews by Guy and Walker (2016) and Dubey *et al.* (2021) going into great detail on the wet and dry chemistry techniques behind these modifications. While charge mobility may be slightly hampered (Zeng et al. 2008), the flexibility and functionality of new chemical groups magnifies nanocarbon usefulness as a transistor. In particular, it offers NT-FETs discrete sites for direct and indirect biomolecule conjugation (Figure 1.8) so creating a spatially intimate environment for binding events to be monitored (Schasfoort et al. 1990). For these reasons, covalent functionalisation remains a popular strategy in NT-FET design, and a range of examples will be discussed below.

Carboxylation is one of the most common functionalisation techniques (Martín et al. 2013), as carboxyl groups make a prime target for further derivatisation. Oxygen-containing groups are typically introduced by a strong oxidising agent (Dyke and Tour 2004; Scaffaro et al. 2012; Guy and Walker 2016), and act as an anchor for direct and indirect biomolecule conjugation. EDC/NHS (1-Ethyl-3-(3-dimethylaminopropyl)carbodiimide/N-Hydroxysuccinimide) coupling is a popular choice for direct protein attachment (Huang et al. 2002; Jiang et al. 2004), with stable amide bonds formed between the free amines in the peptide backbone or side chain, and the activated NHS-ester (Gao and Kyratzis 2008). Indeed, this was the functionalisation method of choice in the recently developed SARS-CoV-2 antigen FET-biosensor. Polyclonal antibodies to the spike 1 protein were conjugated onto SWCNTs to achieve ultrasensitive levels of antigen detection (0.55 fg mL^{-1}) (Shao et al. 2021). This illustrates the potential NT-FETs have to modernise diagnostic techniques, replacing time consuming laboratory-based assays.

Amination is a less commonly employed functionalisation technique, but like carboxylation, it has the potential to react with native functional groups in biomolecules. As a proof of concept in graphene-based FETs, primary amines were

substituted for oxygen containing groups and conjugated to HIV antibodies via carbodiimide activation of native protein carboxylic acid groups (Ramanathan et al. 2005; Islam et al. 2019), proving a successful biosensor.

Thiolation is comparatively new to the field of nanocarbon functionalisation, and has only been used to attach biomolecules indirectly via gold substrates (Katz and Willner 2004; Spampinato et al. 2016). With a recent development in the fabrication of thiolated SWCNTs (Mao et al. 2018), there is potential for direct protein functionalisation via cysteine residues. This would be advantageous to carboxylation and amination because surface exposed cysteines with free thiol groups are relatively rare (compared to, for example, lysine), giving greater control over protein orientation. This is an exciting template for future NT-FET design.

1.4.1.2 Non-covalent functionalisation

Non-covalent functionalisation is the alternative strategy for interfacing SWCNTs with biomolecules. Hydrophobic interactions, electrostatic interactions or π-π stacking between the two species provide bioreactivity without compromising the structural or electrical integrity of nanocarbon (Zhou et al. 2019b). Whilst this has obvious advantages over covalent functionalisation, it is important to consider the factor of Debye length in the NT-FET design. Proteins, such as antibodies, are large in size, so the use of physiologically relevant high salt buffers can place the functional centres of these proteins beyond the sensing region of the biosensor (Schasfoort et al. 1990). The design, especially in terms of the interface site between the receptor and SWCNT, is therefore crucial to the success of non-covalently functionalised NT-FET.

Protein adsorption is the simplest method to directly functionalise SWCNTs, using π-π stacking from aromatic amino acids and general hydrophobic interactions from the protein surface. Some of the earliest attempts at interfacing proteins with nanocarbon used the adsorption of enzymes, such as glucose oxidase (Guiseppi-Elie et al. 2002) and α-chymotrypsin (Karajanagi et al. 2004). Whilst the former enzyme displayed evidence of electron transfer, the latter retained only 1 % of its activity due to it unfolding on SWCNT. Weak physical bonding between the protein and nanocarbon also contributes to a loss of protein immobilisation (Zhou et al. 2019b), meaning this strategy tends to be avoided in the design of modern NT-FETs. However, the importance of these early experiments will not be forgotten, as

they highlight the importance of protein structure and function in these hybrid systems.

In contrast to proteins, single stranded DNA (ssDNA) represents a biomolecule that's highly suited to non-covalent interaction with nanocarbon. The inherent structure of the polymeric nucleic acid complements SWCNTs; with planar nucleobases forming π-π stacking interactions with the side-walls, and the polar sugar-phosphate backbone providing sufficient torsion to wrap the nanotube (Zheng et al. 2003). Applications in NT-FETs are expansive, being used throughout SWCNT functionalisation techniques to disperse and control available surface area (Freeley et al. 2017; Freeley et al. 2021), directly as a DNA probe to sense for target sequences (Star et al. 2006) and indirectly, with additional chemistries incorporated to create a platform for further biomolecule attachment (Xu et al. 2018b).

1.4.1.3 Linker groups

Linker molecules represent the final category of SWCNT functionalisation and can be characterised through their bifunctional ability to covalently or non-covalently interact with nanocarbon, whilst simultaneously providing a reactive handle to covalently interface with a biomolecule. Coming under the same wing as non-covalent functionalisation, this approach again benefits from the undisrupted sp^2 network; but is at risk of pushing biomolecules beyond the Debye length (Schroeder et al. 2019; Xu et al. 2021).

Pyrene based linkers represent a significant class of linker, utilising their aromatic pyrene group to π-stack onto SWCNTs (Fernando et al. 2004). One of the most commonly employed is 1-pyrenebutanoic acid succinimidyl ester (PBASE), which uses the ester group in a nucleophilic substitution reaction with free amines on a protein (Chen et al. 2001; Kodali et al. 2011; Seo et al. 2020). To achieve better control over the protein—NT-FET interface, however, the linker attachment residue can be defined. Xu et al. (2021) demonstrate this, by selectively incorporating azide mutations into a receptor protein and reacting with a dibenzylcyclooctyne (DBCO)-based pyrene linker in a click-chemistry cycloaddition reaction. As a result, the receptor protein's orientation was systematically varied on the nanotube axis and differential electrostatic gating effects were observed.

Polymeric linkers are amphiphilic molecules typically consisting of a hydrophobic alkyl backbone with protruding polar groups for biofunctionalisation and water solubilisation (Richard et al. 2003). Acting in much the same way as pyrene-based

linkers, polymeric linkers are simply larger in size and can wrap helically around SWCNTs (Dubey et al. 2021). In an example of bio-optoelectronic control, bacteriorhodopsin was functionalised to an NT-FET via an amphiphilic polymer and showed evidence of charge transfer from light-induced proton pumping (Bakaraju et al. 2020). For this to occur via an indirect and non-covalent linkage is testament to the complex nature of optical doping in bionanohybrids.

Gold nanoparticles (NPs) are a final, popular example of linker molecule. Biocompatibility arises from their naturally high affinity to thiol groups (Uvdal et al. 1992) and easily modifiable surface for EDC/NHS chemistry (Jazayeri et al. 2016), while adaptability stems from their covalent and non-covalent SWCNT attachment methods (Han et al. 2007; Salice et al. 2014; Alim et al. 2018; Danielson et al. 2020). Another example from the narrow field of bio-optoelectronic nanocarbon-FETs used the immobilisation of photosystem 1 to gold NPs, where an increase in conductivity was recorded after red light irradiation (Nishiori et al. 2019). This highlights the potential biomolecules have at converting optical energy into electrical.

1.4.2 Functionalising biomolecules for SWCNT attachment

To consider the conjugation of biomolecules to nanocarbon from a different perspective, one can explore the functional chemistries that biomolecules themselves have to offer. Most examples discussed above exploit the native functional groups present in protein and nucleic acids, so these will be summarised briefly below. The newest trend, and most likely future direction, that biology is heading in is the use of synthetic biology. Combining *in silico* modelling with the ever-evolving methods of SWCNT functionalisation, new chemistries and new blueprints for biomolecule design can be incorporated at the genetic level to tackle some of the problems faced by NT-FETs (Figure 1.9).
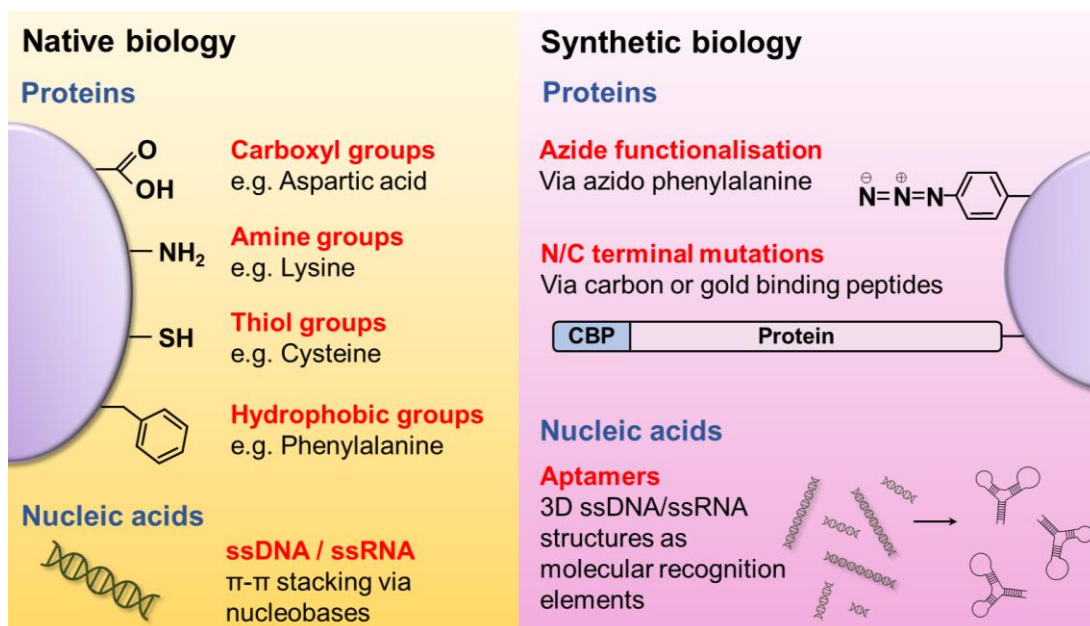
Figure 1.9 – Biomolecule functionalisation strategies. Native biomolecules have a range of functional chemistries at their disposal. Proteins can utilise carboxyl, amine, thiol, and hydrophobic groups as prospective SWCNT interfacing sites, whilst ssDNA and ssRNA (single stranded RNA) can stack via π-π interactions. Tweaking of biomolecules via synthetic biology introduces new capabilities for proteins, such as azide functionalisation sites and novel N/C terminal mutations to incorporate carbon or gold binding peptides. Aptamers constructed from ssDNA and ssRNA represent its own field of biochemistry but offers huge potential in NT-FET design. Figure copied with permission from Lee et al. (2022).

1.4.2.1 Native biology

When looking to attach biomolecules to nanocarbons, a plethora of functional groups already exist to mediate the conjugation. Proteins, if using the standard genetic code, can have up to twenty different side chains present, supplying a mixture of charged, polar, neutral, and hydrophobic properties. Carboxylic acids can be found on the side chains of aspartic acid and glutamic acid and can be targeted for carbodiimide activation to covalently crosslink a protein with available amine groups on SWCNTs (Awasthi et al. 2009; Islam et al. 2019). Subsequently in the reverse strategy, amine groups found on the side chains of lysine can be crosslinked to carboxylic acid groups present on SWCNTs via an EDC/NHS coupling reaction (Huang et al. 2002; Jiang et al. 2004). Cysteines offer an alternative conjugation site to gold NPs with their thiol group; assuming these are accessible and aren't pre-disposed in structural disulphide bonds or other functional

centres (Ljungblad 2009; Jazayeri et al. 2016). Finally, hydrophobic amino acids can mediate non-covalent protein adsorption through the aromatic side chains of phenylalanine and tryptophan, and aliphatic side chains of isoleucine, leucine, and valine (Gu et al. 2015).

Although native proteins are easier to generate and use, this does come with a lack of control over conjugation orientation. Target residues, such as glutamate and lysine, will be found commonly across the surface of proteins which risks multiple attachment orientations. Cysteine is affected to a lesser extent as it is the only amino acid offering a free thiol group and is present in proteins at a much lower frequency (Miseta and Csutora 2000). Nevertheless, any duplication of accessible, reactive side chains risks NT-FET function, e.g., by binding the SWCNT at its functional centre, or in its analyte binding region. This builds the case for selective, defined attachment residues.

Nucleic acids are better suited in their native form for SWCNT attachment than proteins. Single-stranded DNA or RNA can naturally wrap SWCNTs through the π-π interactions of the nucleobases (Zheng et al. 2003), providing an immediate template for hybridisation-based NT-FETs (Tran and Mulchandani 2016). Meanwhile, many of the biofunctionalised NT-FETs in the literature exploit ssDNA to aid SWCNT dispersion, control protein conjugation sites and mediate the non-covalent attachment of other biomolecules to the nanocarbon (Han et al. 2007; Freeley et al. 2017; Xu et al. 2018b; Freeley et al. 2021). These properties are thus highly desirable and will be used in NT-FETs for generations to come.

1.4.2.2 Synthetic biology

Synthetic biology offers considerable promise to the field of NT-FETs, with biomolecules systematically refined, repurposed, and rebuilt to introduce novel and useful functionalities. This can boost device performance by (i) controlling biomolecule orientation for maximum functionality, and (ii) defining a consistent biomolecule—SWCNT interface.

The first strategy uses azide functionalisation as a novel example of proteins instigating the biochemical link to SWCNTs. Here, the non-natural amino acid (nnAA) p-azido-L-phenylalanine (AzF) is incorporated into a recombinant protein at a defined residue through an expanded genetic code (Chin et al. 2002; Reddington et al. 2013b). Phenyl azide chemistry opens up two new routes to SWCNT functionalisation. The first, mentioned above, uses bio-orthogonal click chemistry to

attach the protein to a strained-alkyne linker. The second is a direct link between the protein and SWCNT via UV irradiation: the mechanism of choice for NT-FET functionalisation in this thesis. The advantage azide functionalisation brings over other strategies is selective control over the protein attachment residue, where protein orientation and functionality can be defined. Applications for this have been showcased by lab members past and present, and AzF chemistry will be discussed in further detail below (Reddington et al. 2013b; Freeley et al. 2017; Zaki et al. 2018; Thomas et al. 2020; Freeley et al. 2021; Xu et al. 2021; Gwyther et al. 2022).

A second strategy is the development of carbon or gold binding peptides as genetic fusions to the N- and/or C-terminus of a protein. Protein adsorption to SWCNTs is at the fundamental core of carbon binding peptide (CBP) design, as research groups exploited phage display technology (Parmley and Smith 1988) to selectively identify peptides and motifs with a strong affinity for SWCNTs (Wang et al. 2003; Su et al. 2006; Zheng et al. 2009). Coyle et al. (2013) then furthered the research by developing CBPs with differing affinities for sp^2 and sp^3 carbon, and eventually, gold binding peptides (Dunakey et al. 2019). By incorporating both the CBP and gold-binding peptides into sfGFP, a dual-material binding biomolecule was established (Dunakey et al. 2019). Meanwhile Kuang et al. (2010) showed CBPs were effective in NT-FETs for chemosensing, by fusing the peptide to a fragment of an insect receptor protein and detecting the chemical trinitrotoluene in both chemical vapour and liquid-gated configurations.

A final synthetic biology approach, and one set to revolutionise the design of biomolecules for NT-FETs involved in analyte sensing, is the aptamer. Single-stranded oligonucleotides (including DNA and RNA) undergo a systematic evolution process (Tuerk and Gold 1990) to generate a sequence that's capable of forming high affinity 3D structures to bind any target protein. Their significance in NT-FET design lies within their ability to mimic proteins without being a protein. Antibodies, for example, are perfectly crafted for ligand recognition, but their large size (10-15 nm) (Rudikoff and Potter 1976; Teillaud et al. 1983) risks any incoming analyte being beyond the Debye length and thus impossible to sense (So et al. 2005). This, paired with the ethical costs of antibody production from animals (Ruscito and DeRosa 2016), the functionalisation strategy needed for antibody conjugation and the risk of permanent denaturation from changing conditions, offers a challenging proposition for their continued use. Aptamers, being much smaller in size (1-2 nm) (So et al. 2005), cheaper to produce and arguably easier to functionalise, offer the perfect alternative (Maehashi et al. 2007). Considerations into aptamer use,

however, must include the presence of nucleases within clinical samples, as these can degrade the aptamers before any sensing can take place (Moon et al. 2008).

1.4.3 AzF functionalisation

1.4.3.1 Genetic reprogramming

As a nnAA, AzF requires genetic reprogramming for the cell to (i) recognise the site of AzF incorporation, and (ii) charge a compatible tRNA molecule with AzF. The genetic code can be expanded for this purpose by reprogramming the amber stop codon (UAG). This is the least used codon in the *E. coli* genome, terminating only 7.5 % of genes encoded by model *E. coli* strain K-12 (Blattner et al. 1997; Smolskaya and Andreev 2019). Repurposing this particular codon for AzF incorporation ensures the minimum possible number of read through events for endogenous TAG-terminated genes. Cell lines remain viable while AzF-containing proteins are expressed, albeit with a reduced yield due to competition with terminator of protein synthesis: release factor 1 (RF1; Chin 2017). For regular or large-scale expression of nnAA containing proteins, optimised *E. coli* strains should be considered. For example, Mukai et al. (2015) developed a strain which has recoded all endogenous amber stop codons for TAA, and has constitutive expression of RF1 switched off.

Repurposing the amber stop codon in practise requires a simple site-directed mutagenesis procedure to introduce the TAG mutation in the target gene sequence (Liu and Schultz 2010; Zitti and Jones 2023). The accompanying translational machinery then comes from a co-transformed vector, e.g., pDULE-cyanoRS, encoding a bio-orthogonal tRNA / aminoacyl tRNA synthetase pair from *Methanocaldococcus jannaschii* (Miyake-Stoner et al. 2010). The tRNA is engineered to recognise the UAG stop codon through a CUA anticodon ($tRNA_{CUA}$), while the tyrosol-tRNA synthetase is engineered to recognise tyrosyl derivative nnAAs (e.g., AzF) and catalyse the attachment to its cognate $tRNA_{CUA}$ (Blight et al. 2004; Chin 2017). Recombinant protein expression will then occur when the relevant induction molecules are present, and an exogenous supply of AzF is added to the culture (Figure 1.10).
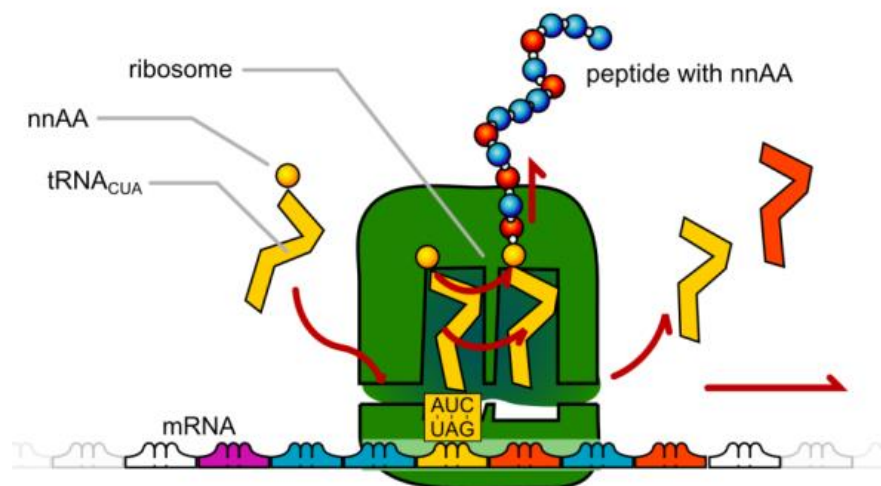
Figure 1.10 – Schematic of nnAA incorporation during translation. The mRNA transcribes the TAG mutation from the gene sequence as UAG. The engineered tRNA$_{CUA}$ recognises the UAG codon during mRNA translation and incorporates the nnAA (e.g., AzF) into the growing polypeptide chain, suppressing normal termination by RF1. Figure copied with permission from Bowen (2020).

1.4.3.2 Functionalisation chemistry

Once incorporated into the protein, AzF has various chemical pathways available due its highly reactive phenyl azide (Ph-N$_3$) group. The two routes relevant to SWCNT functionalisation are UV-induced photoreactivity and strain-promoted azide-alkyne cycloaddition via bio-orthogonal click chemistry (Figure 1.11).
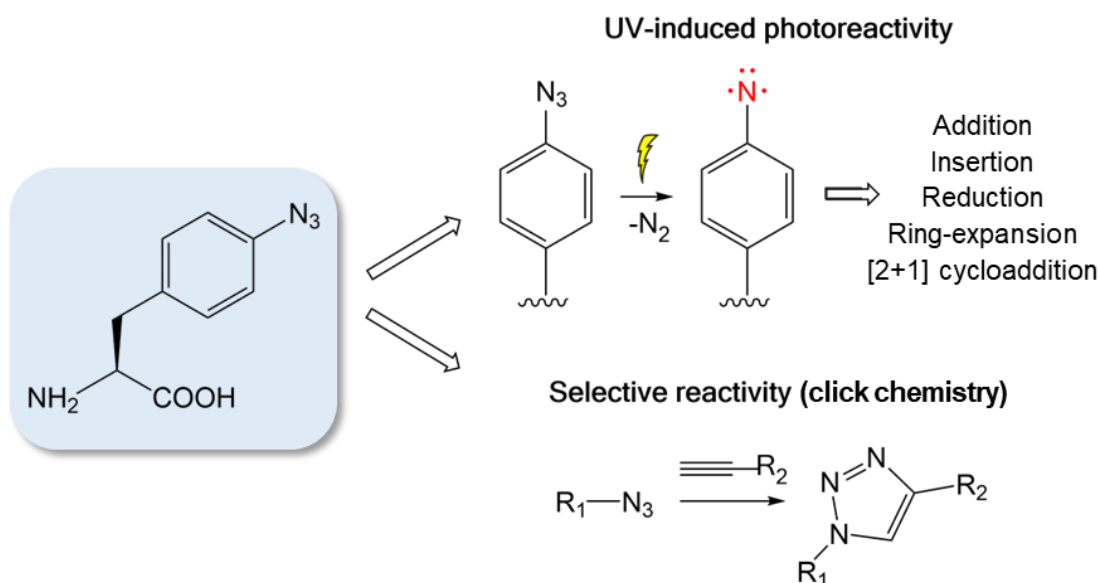
Figure 1.11 – Chemical pathways of AzF: photoreactivity and click chemistry.
UV-induced activation of the azide group can generate a highly reactive nitrene radical that can pursue numerous downstream reactions. [2+1] cycloaddition is used to covalently functionalise SWCNTs. Selective click chemistry reaction between the azide group and a target alkyne will form a triazole ring. A planar linker molecule with strained-ring alkyne moiety can be used in conjunction with AzF-containing proteins to non-covalently functionalise SWCNTs.

UV-induced photoreactivity causes the phenyl azide group of the AzF residue to decompose under short UV wavelengths (< 310 nm), releasing N_2 and generating a highly reactive nitrene radical (Figure 1.11; Chin et al. 2002). Depending on its chemical environment, the radical can insert into N-H or C-H σ-bonds, reduce into an amine or expand into the phenyl group to form a seven-membered ketenimine ring (Gritsan and Platz 2010; Reddington et al. 2013b; Hartley et al. 2016). In the presence of SWCNTs, however, a [2+1] cycloaddition reaction can take place to covalently link the AzF residue and SWCNT (Figure 1.12). The mechanism for this allows the nitrene radial to diverge into singlet-state or triplet-state, but both converge on attacking the π electron-rich side walls of SWCNTs to generate a three membered aziridine ring (Holzinger et al. 2004). This is a highly strained intermediate structure that is expected to open and re-hybridise into a hetero-bridged structure, e.g., losing the C-C bond and maintaining two C-N bonds, with the nitrogen and connecting 'R' group positioned perpendicularly above the nanotube (Setaro et al. 2017). The lone pair of electrons from the nitrogen atom is then thought to be donated to the π electron network, increasing electron density

and preserving SWCNT conductance (Setaro et al. 2017). In my joint 1st author paper (Thomas, Jamieson, Gwyther et al. 2020), I used this approach to covalently attach four different proteins to SWCNT side walls in a site-specific and defined manner. The protein—SWCNT interface was dictated by the attachment residue, and coupling between the two species could be observed from a change in single-molecule behaviour. This intimate and defined protein—SWCNT interface lends itself to the design of my protein-integrated NT-FETs, as I exploit protein function to modulate SWCNT conductance.
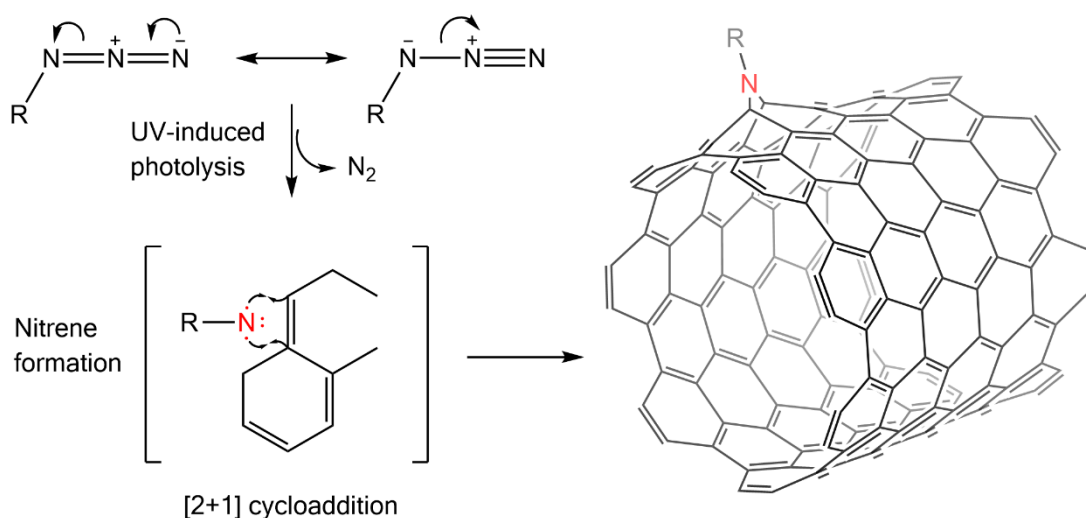
Figure 1.12 – Mechanism of AzF cycloaddition to SWCNTs. UV irradiation extrudes N_2 and generates a nitrene radical. The radical electrophilically attacks the SWCNT to form an intermediate aziridine ring, before relaxing into a hetero-bridged structure.

Azide-alkyne cycloaddition (AAC) is another chemical pathway AzF can pursue to attach SWCNTs, albeit indirectly via a linker molecule. The biorthogonal reaction between the azide in the protein and alkyne group of the linker is an example of the Nobel Prize winning 'click chemistry', considered modular by design, selective, high yielding and operating with a high thermodynamic driving force to reaction completion (Rostovtsev et al. 2002; Tornøe et al. 2002; Baskin et al. 2007). The reaction produces a five-membered triazole ring, and typically requires a copper (I) catalyst to proceed at room temperature (Bräse et al. 2005). As Cu^{+} ions are known to promote formation of reactive oxygen species which damage protein structure (Gaetke et al. 2014), a strain-promoted AAC (SPAAC) reaction is better suited to

biomolecules (Agard et al. 2004). A DBCO-pyrene linker molecule is well-positioned for this role (Figure 1.13 (A)), with DBCO comprising the strained alkyne moiety, and pyrene comprising a planar polycyclic structure, suitable for π-π stacking onto SWCNTs. We showed this to be an effective methodology for NT-FET functionalisation, as AzF-containing receptor proteins were conjugated to DBCO-pyrene linker molecules (Figure 1.13 (B)) that decorated the SWCNTs in a defined and homogenous manner (Figure 1.13 (C); Xu, Bowen, Gwyther et al. 2021). Receptor protein function remained intact and electrostatic gating was observed from exposure to analytes. This was seen to vary with receptor protein orientation, and consequently highlighted the importance of AzF location, as the protein anchor.
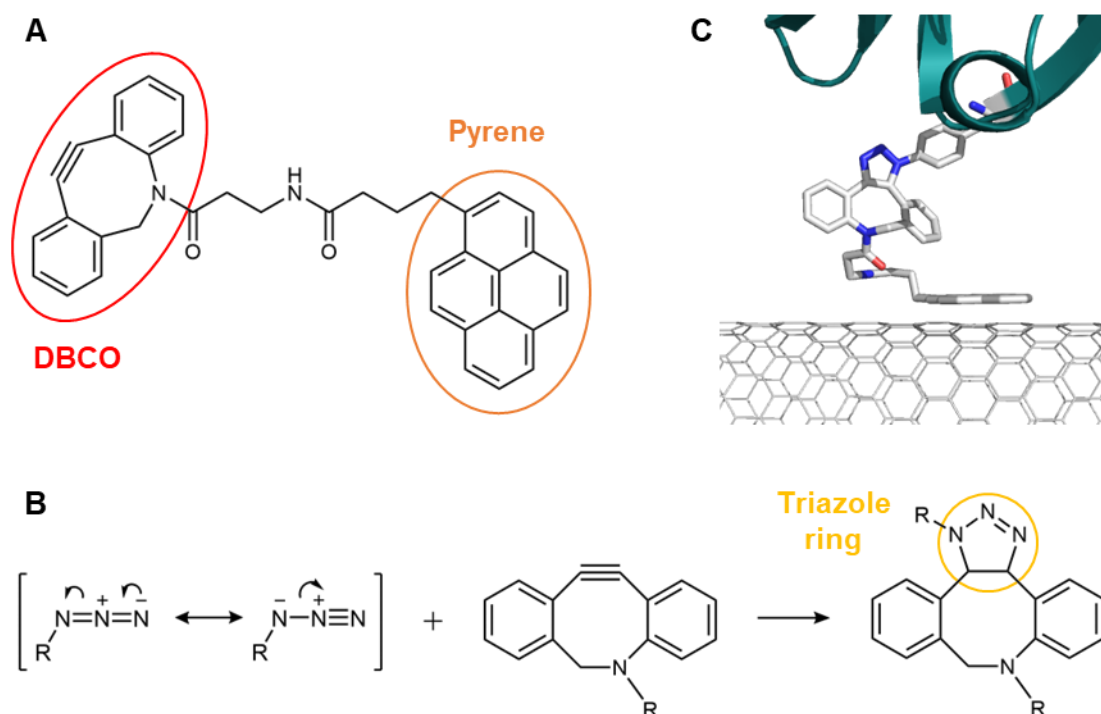
Figure 1.13 – SPAAC reaction and SWCNT functionalisation. (A) DBCO-pyrene linker molecule synthesised from DBCO-amine and 1-pyrenebutyric acid-NHS ester. (B) The azide group of AzF reacts with the strained-ring alkyne DBCO in a SPAAC reaction, forming a covalent triazole ring. (C) SWCNT functionalisation via the AzF-triazole-pyrene linker. A 3D representation of the linker group, optimised computationally via Prof. Alexander Nemukhin (Xu et al. 2021), demonstrates the π-π stacking of the pyrene group onto the SWCNT.

1.4.3.3 Conformational rotamers

Considering the importance of AzF location in anchoring proteins to SWCNTs (Thomas et al. 2020; Xu et al. 2021; Gwyther et al. 2022), one should also consider the conformational side chain rotamers AzF can occupy to better model the protein—SWCNT interface. A protein's amino acid side chains will regularly cycle through rotameric states, and their propensity can be influenced by a number of external factors: changes to the local backbone angle (φ and ψ), secondary structure, intramolecular bonding, and the physicochemical environment e.g., pH and electrostatic potential (Dunbrack 2002; Chamberlain and Bowie 2004). Understanding the rotamers of AzF and their propensity will help to optimise NT-FET design, as the orientation of the AzF anchor ultimately dictates the orientation of the protein on the SWCNT, and thus their ability to function.

To derive rotamers for AzF, a background in bond angles and structural constraints is essential. Rotamers arise from the conformational space available to them, with the backbone and side chain dihedrals defining the steric constraints: φ, between N and C_α, ψ, between C_α and C, ω, between C and N, and χ_n, between successive side chain atoms (Figure 1.14 (A)). Side chain dihedrals (χ_n) will generally cluster around -60° (gauche$^+$), 60° (gauche$^-$) and 180° (trans) in a sp^3—sp^3 bonded configuration as it allows the pi orbitals to stagger against their opposite atomic groups; lowering the potential energy (Dunbrack 2002). The gauche$^-$ configuration of the χ_1 angle is an exception to this, because the γ side chain atom is too close to the main chain atoms (C=O and N-H) for this conformation to be favourable. This means AzF is likely to favour the gauche$^+$ and trans states at χ_1, producing a large 120° swing between side chain rotamers (Figure 1.14 (B)), a trend mirrored by other symmetric aromatic residues (Ruvinsky et al. 2011). The χ_2 angle, by comparison, has little effect on AzF rotamers. C_β is bonded to the sp^2 hybridised C_γ, so dihedrals are limited to +/- 90°. This only twists the planar phenyl ring and will not induce global movement of the side chain. Considering both χ_1 and χ_2 constraints, I would anticipate AzF's major rotamers to be gauche$^+$ and trans as a function of χ_1.
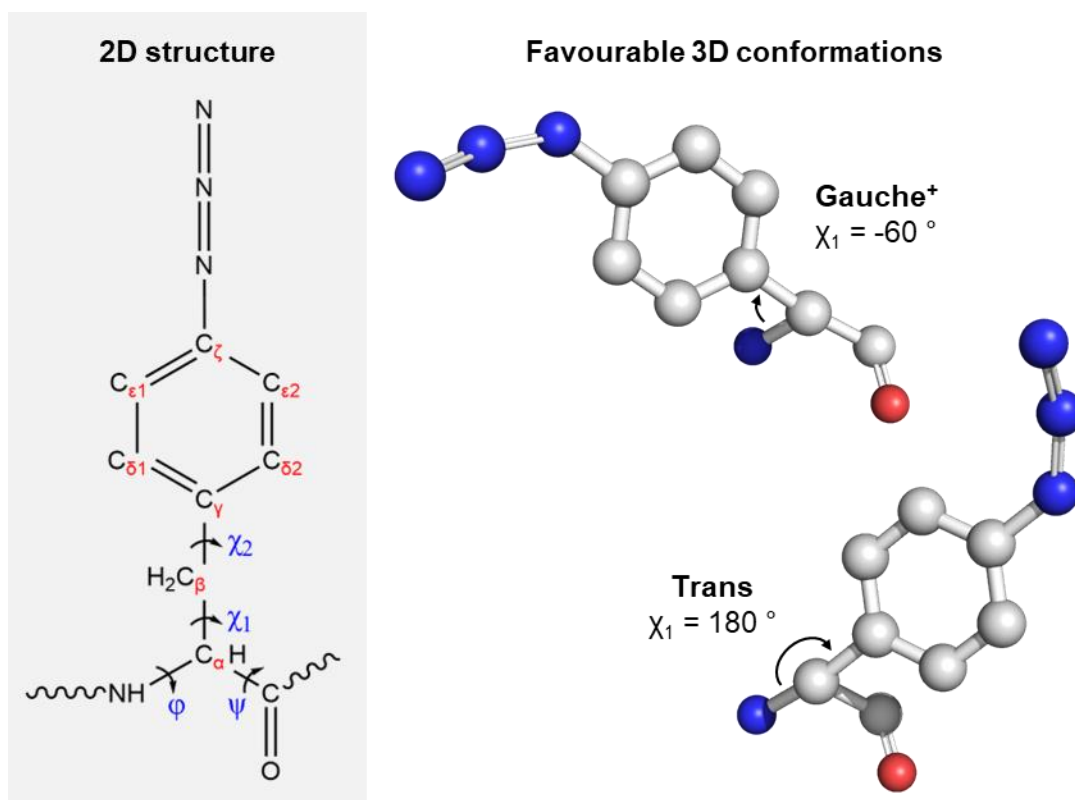
Figure 1.14 – 2D and 3D structural representations of AzF. The 2D structure details AzF nomenclature including the carbon naming order and dihedral angles φ, ψ, χ_1 and χ_2. The 3D representations illustrate the gauche+ and trans side chain conformations arising as a function of χ_1. AzF is viewed along the C_β and C_α bond, so C_α isn't visible from the 3D representations.

1.5 Exploiting protein function for NT-FET application

1.5.1 BLIP-II

The rise of antibiotic resistance (ABR) poses an unprecedented threat to public health (Baquero 2021). In the interest of designing an NT-FET as sensing platform for AMR, I look to use a receptor protein that can test for a distinguishable, but ubiquitous resistance marker. Alas, the natural variability of bacterial resistance mechanisms prevents this, so the NT-FET should instead target the most common marker: the β-lactamase.

The receptor protein chosen as bait for the β-lactamases is the aptly named β-lactamase inhibitor protein-II (BLIP-II). BLIP-II is a 28 kDa potent proteinaceous inhibitor of class A β-lactamases, arising from soil bacterium *Streptomyces exfoliatus* (Lim et al. 2001a). Its ability to interact with manifold β-lactamases in picomolar to femtomolar affinity arises from its inherent structure (Lim et al. 2001a;

Brown and Palzkill 2010; Brown et al. 2013b). BLIP-II appears highly symmetrical with a seven-bladed β-propeller structure (Figure 1.15 (A)); the apical β-turns and loops of which form the β-lactamase binding interface (Figure 1.15 (B)) (Lim et al. 2001a). The magnitude of affinity between BLIP-II and β-lactamases has been attributed to its concentric arrangement of hydrophobic and hydrophilic residues (the red and orange atoms in Figure 1.15 (A), respectively). Its central cluster of aromatic residues is responsible for mediating hydrophobic contacts to the conserved loop-helix region of β-lactamase, adjacent to the active site. The BLIP-II loop containing W53, N50 and D52 is then positioned to sterically block the active site, preventing the entrance of antibiotics (Lim et al. 2001a). This scaffold complements the O-ring hotspot hypothesis, which defines a hotspot as a residue which can cause a 2.0 kcal/mol loss in binding energy after alanine substitution (Bogan and Thorn 1998; Brown et al. 2011). Hotspots are typically aromatic, whilst the surrounding residues are hydrophilic, as depicted at BLIP-II's binding interface. Research by Brown *et al.* confirmed this, with W53, Y73, F74, W152, Y191 and W269 observed to have the greatest effect on binding affinity between BLIP-II and the β-lactamases TEM-1, KPC-2, Bla1 and CTX-M-14 (Brown et al. 2013b). The purpose of the surrounding hydrophilic residues is then to exclude solvent access to the binding interface. In addition to the complementary protein-protein interactions, the enthalpic and entropic component of BLIP-II's binding interface is key to it being one of the tightest protein-protein interactions ever recorded. Its structural rigidity prohibits any major conformational change when binding to a β-lactamase, minimising the entropic cost. This in turn favours an enthalpic decrease, as intramolecular interactions are not lost, and new non-covalent intermolecular interactions are formed, upon β-lactamase association (Brown et al. 2011).
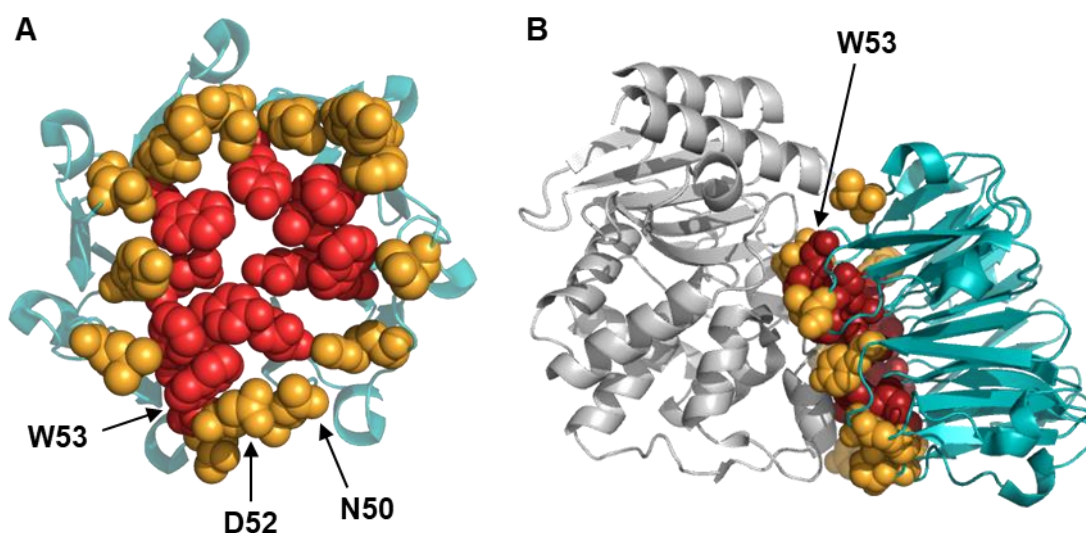
Figure 1.15 – Binding interface of BLIP-II. (A) Face-on view of BLIP-II's binding interface. The central ring of mostly hydrophobic residues (in red: W53, Y73, F74, N112, W152, Y191, I229, F230, E268, W269, N304) have been shown to have the biggest effect on BLIP-II's binding affinity. Meanwhile, the outer ring residues (in orange: N50, D52, T57, L91, Y113, D131, D167, S169, D170, D206, Y208, F209, Y248, R286) tend to contribute more to the binding specificity of BLIP-II. Residues N50, D52 and W53 have been highlighted as the residues responsible for sterically blocking the active site of incoming β-lactamases (grey), as seen in (B).

Considering the extreme affinity between BLIP-II and the β-lactamases, and its broad range specificity, the protein is well placed to function as a receptor to class A β-lactamases. The structure of BLIP-II lends itself to my AzF functionalisation strategy, with the repeating β-propeller structure offering regular protrusions from which to anchor BLIP-II by. This could offer distinct electrostatic surface sampling of incoming β-lactamases and would allow us to build a library of unique electrical signatures. The design, testing and modelling of my BLIP-II^AzF variants as receptor proteins in NT-FETs will be covered in Chapters 3 and 4.

To discuss the research timeline to date, the Jones group demonstrated covalent attachment of BLIP-II[41AzF] to SWCNTs in 2020 (Thomas, Jamieson, Gwyther et al. 2020). The TEM-1 β-lactamase was added after BLIP-II[41AzF] integration, and distinct increases in height were attributed to formation of the BLIP-II[41AzF]—TEM-1 complex on the SWCNT surface. In collaboration with the Palma lab at Queen Mary University London (QMUL), the first BLIP-II functionalised p-type NT-FETs were then developed in 2021 (Xu, Bowen, Gwyther et al. 2021). Functionalising the

SWCNTs non-covalently via a DBCO-pyrene linker, three BLIP-II^{AzF} variants (BLIP-II^{41AzF}, BLIP-II^{49AzF} and BLIP-II^{213AzF}) were attached via click chemistry. The BLIP-II^{41AzF} and BLIP-II^{213AzF} functionalised NT-FETs responded to increasing concentrations of TEM-1 by a real-time increase, and decrease, in conductance respectively. These measurements were linked to differential electrostatic gating by TEM-1 – as defined by BLIP-II orientation. This thesis will focus on the second generation of BLIP-II functionalised p-type NT-FETs, as I look to integrate BLIP-II covalently and explore device characteristics.

1.5.2 Class A β-lactamases

Underpinning the most prevalent form of ABR, the β-lactamase enzyme family have evolved to hydrolyse the four-membered ring of β-lactam antibiotics (Abraham and Chain 1940). The family is subdivided into four classes using the Ambler classification system (Ambler 1980). Class A, C and D evolved from the membrane-bound penicillin binding proteins, differentiating by specific sequence motifs but sharing the same serine-based hydrolytic mechanism (Massova and Mobashery 1998; Tooke et al. 2019). Class B is evolutionarily ambiguous, but is part of the metalloprotein superfamily and uses Zn^{2+} ion(s) in its hydrolytic mechanism (Carfi et al. 1995; Alderson et al. 2014; Mojica et al. 2016). There is considerable structural divergence associated with the two hydrolytic mechanisms, and consequently hydrolytic activity and inhibitor interaction varies between the classes (Kaderabkova et al. 2022).

As the general inhibition targets of BLIP-II, only class A β-lactamases will be produced and tested for in this body of work. However, the impact on ABR biosensing is still significant. Class A is the most diverse and abundant of all β-lactamase classes and contains many clinically concerning β-lactamases that would be beneficial to test for in a medical setting (Philippon et al. 2016; Furniss et al. 2022; Kaderabkova et al. 2022). The class A β-lactamases produced as analytes for my BLIP-II^{AzF}—NT-FETs are considered in detail below.

1.5.2.1 TEM-1

The most common plasmid-encoded β-lactamase of gram negative bacteria is TEM-1, causing resistance to key antibiotics including penicillins and cephalosporins (Shah et al. 2004). As a class A β-lactamase, TEM-1's catalytic mechanism uses a

triad of conserved residues: Ser70, Lys73 and Glu166 (Figure 1.16 (A)). The mechanism, in brief, involves Lys73 deprotonating the side chain hydroxyl group of Ser70 to give a charged oxygen atom (Figure 1.17). This acts as a nucleophile and attacks the carbonyl group of the β-lactam ring, breaking the amide bond and forming an acyl-intermediate. A water molecule coordinated in the active site is deprotonated by Glu166 to attack the acyl-intermediate, hydrolysing the β-lactam ring and completing the catalysis (Kaderabkova et al. 2022). Crucially, substitutions of residues proximal to the active site are known to broaden TEM-1's β-lactam substrate profile. Mutations such as E104K, R164S/H, M182T and G238S have arisen in response to oxyimino-cephalosporins, a form of extended-spectrum antibiotic introduced in the 1980s (Bush 2002; Salverda et al. 2010). The TEM extended spectrum β-lactamases are characterised by increased conformational flexibility at the active site, combatting the large and inflexible oxyimino side chain (Palzkill 2018). The prevalence and rapidly evolving substrate specificity of TEM-1 thus make for desirable analyte attributes, and testing with BLIP-II[AzF] functionalised NT-FETs will give valuable insight into the potential clinical usefulness.

As an analyte for NT-FETs, the electrostatic surface potential of TEM-1 has the potential to play a significant role in conductance doping. In Figure 1.16 (B), we can see the surface of TEM-1 is clustered with patches of negative and positive charge. The active site, shown in the 90° rotation, is characterised by a notably strong negative potential. However, pockets of polar charge are seen to vary uniquely across the 3D surface. The effect on conductance doping therefore will depend on the specific orientation TEM-1 adopts from binding BLIP-II, and if its overall positioning is successful at breaching the Debye length.
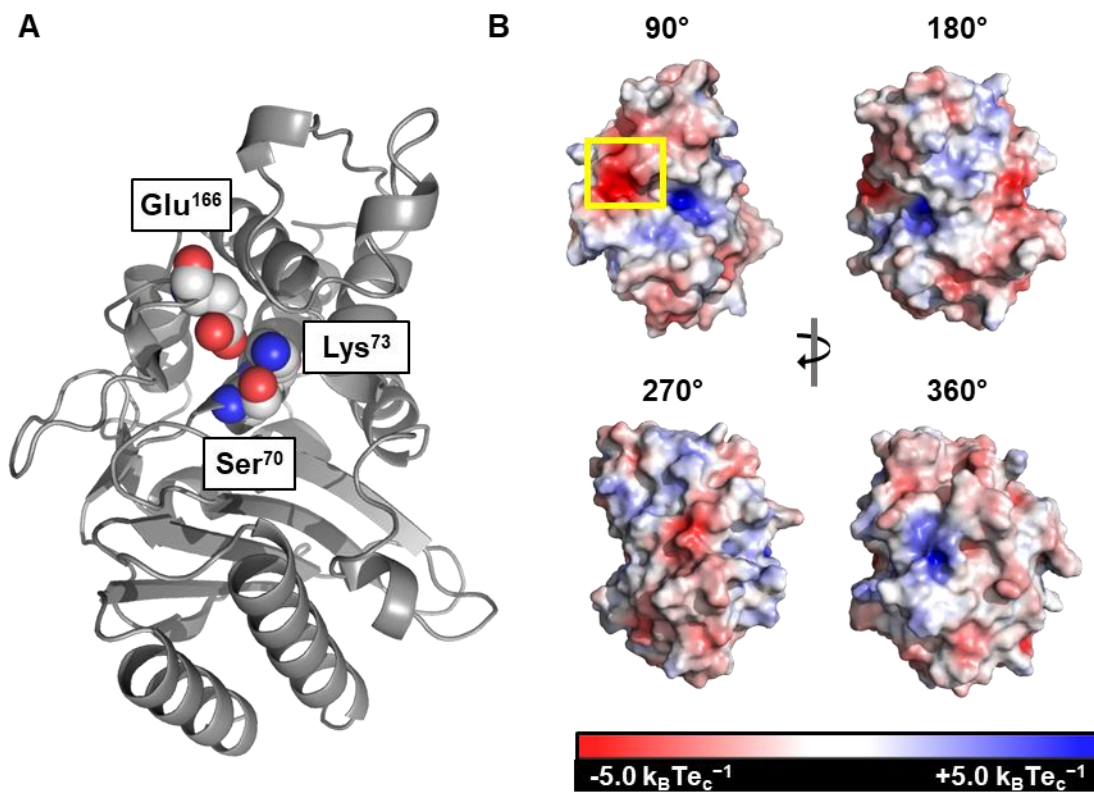
Figure 1.16 – TEM-1 structure and electrostatic profile. (A) The three key catalytic residues of TEM-1 are highlighted in a spherical form as Ser70, Lys73 and Glu166. (B) Electrostatic map of TEM-1, following a 360° rotation around its x axis. Yellow box highlights the active site region.
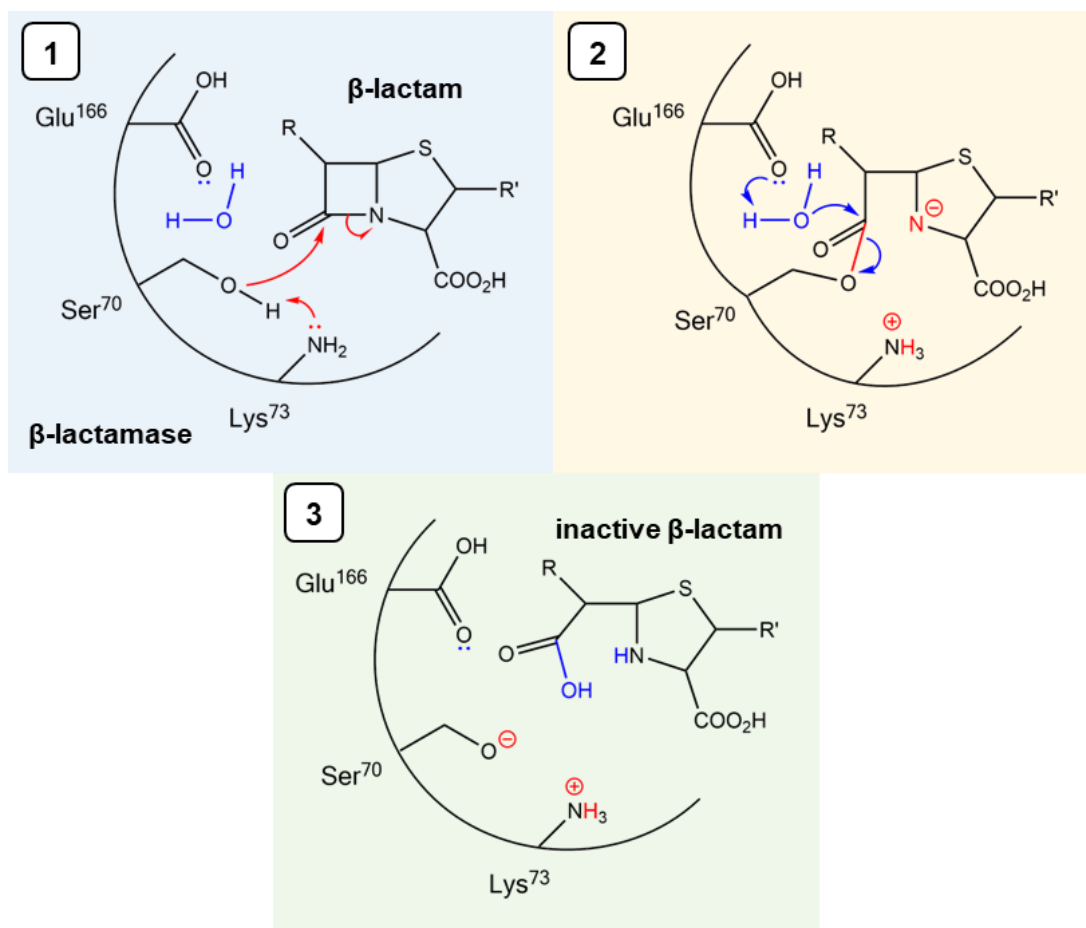
Figure 1.17 – Hydrolytic mechanism of serine β-lactamases. Lys[73] deprotonates the side chain hydroxyl of Ser[70] for the charged oxygen to acylate the β-lactam ring. In the subsequent de-acylation step, a coordinated water molecule is deprotonated by Glu[166] to hydrolyse the acyl-intermediate. The inactive β-lactam is then released, and the β-lactamase active site restored.

1.5.2.2 KPC-2

KPC-2 is a potent and highly evolved class A β-lactamase. With a broader substrate profile than TEM-1, KPC-2 can inactivate penicillins, cephalosporins and carbapenems (Papp-Wallace et al. 2010). Its carbapenemase activity, and ability to evade common β-lactamase inhibitors such as clavulanic acid, have contributed to the Centers for Disease Control and Prevention declaring KPCs a major threat to public health (Spellberg and Bonomo 2016). There is thus considerable clinical interest to test KPC-2 as an analyte for my BLIP-II functionalised NT-FETs.

As a class A β-lactamase, KPC-2 uses the same conserved residues as TEM-1 to hydrolyse β-lactam rings: Ser70, Lys73 and Glu166 (Figure 1.18 (A); Levitt et al.

2012). The difference in substrate profile comes from mutations around the active site, where a wider and shallower structure can accommodate bulkier β-lactams (Ke et al. 2007). KPC-2 and TEM-1 also share 45 % sequence homology which results in a similar tertiary structure. However, the electrostatic surface potential is notably different, with the overall charge appearing more positive for KPC-2, and more negative for TEM-1 (Figure 1.18 (B)). Polar charge is still seen to cluster across the KPC-2 surface, but the difference is apparent around key areas such as the active site, which is largely neutral in KPC-2 and strongly negative in TEM-1. Tailoring the orientation of the β-lactamases through systematic design of BLIP-II^{AzF} variants will therefore allow distinct electrical signatures to be generated.
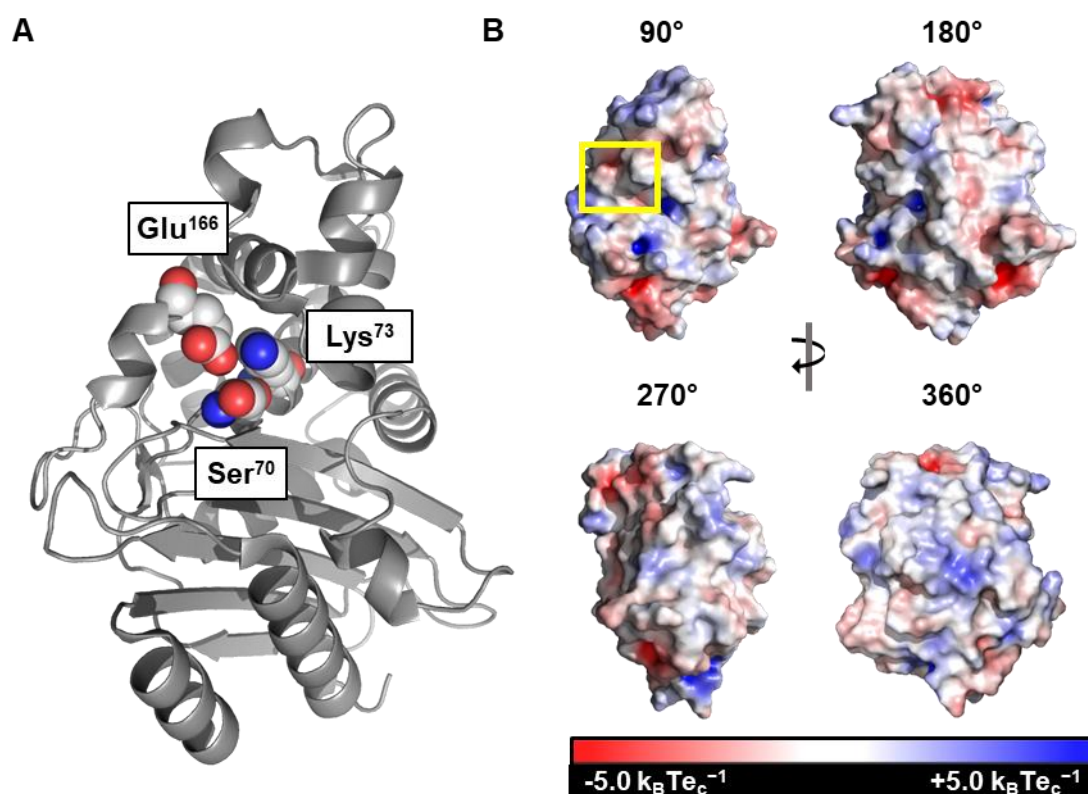
Figure 1.18 – KPC-2 structure and electrostatic profile. (A) The three catalytic residues of KPC-2 are highlighted in a spherical form as Ser70, Lys73 and Glu166. (B) Electrostatic map of KPC-2, following a 360° rotation around its x axis. Yellow box highlights the active site region.

1.5.3 sfGFP

The green fluorescent protein (GFP), first isolated from the jellyfish *Aequorea victoria*, was subject of the 2008 Nobel Prize (Shimomura et al. 1962). Its discovery and subsequent developments generated one of the most important tools for contemporary biological research as a genetically encoded autofluorescent probe (Chalfie et al. 1994). This yielded significant application for cell imaging, monitoring gene expression and aiding recombinant protein solubility (Tsien 1998; Zimmer 2009). Developments attributed to its widespread use include improved stability for culturing in cells at 37 °C, and shifting excitation and emission wavelengths to alter fluorescent properties (Heim et al. 1995; Cormack et al. 1996). The enhanced GFP variant (EGFP) boasted increased fluorescence through an improved quantum yield (Yang et al. 1996), while the superfolder GFP (sfGFP) variant was generated from EGFP several years later through a process of directed evolution. Appropriately named, sfGFP benefitted from rapid folding and maturation – even when fused to poorly folding proteins (Pédelacq et al. 2006; Wu et al. 2009). The sfGFP variant is therefore favoured in the Jones lab, and I will study it in this thesis as a means to investigate GFP's light-induced electron donor behaviour (Bogdanov et al. 2009). It is hypothesised that by integrating sfGFP into the NT-FET platform, I can mediate optoelectronic transduction through light absorption.

Distinct in structure, sfGFP is comprised of an eleven stranded β-barrel structure (Figure 1.19 (A). Its functional centre, the chromophore, resides in the middle of the barrel; shielded from solvent and held rigidly in place by hydrogen bonds and hydrophobic side chains (Remington 2011). The chromophore forms post-translationally as residues Thr^{65}, Tyr^{66} and Gly^{67}, in the presence of molecular oxygen, autocatalytically cyclise, dehydrate and oxygenate to form an extended delocalised π electron system: p-hydroxybenzylideneimidazolinone (Tsien 1998). The chromophore can exist in two protonation states: the less populated CroA, featuring a neutral protonated state on the phenol group of tyrosine 66 (λ_{max} = ~400nm), or the more fluorescent and highly populated CroB with a charged phenolate (λ_{max} = ~485nm); giving rise to its characteristic spectral properties (Figure 1.19 (B); Pédelacq et al. 2006). Following light absorption at either of the protonation states, an electron is promoted from the highest occupied to the lowest unoccupied molecular orbital (LUMO). Spontaneous transition back to the LUMO ground state then releases a photon at ~510 nm (Remington 2011).
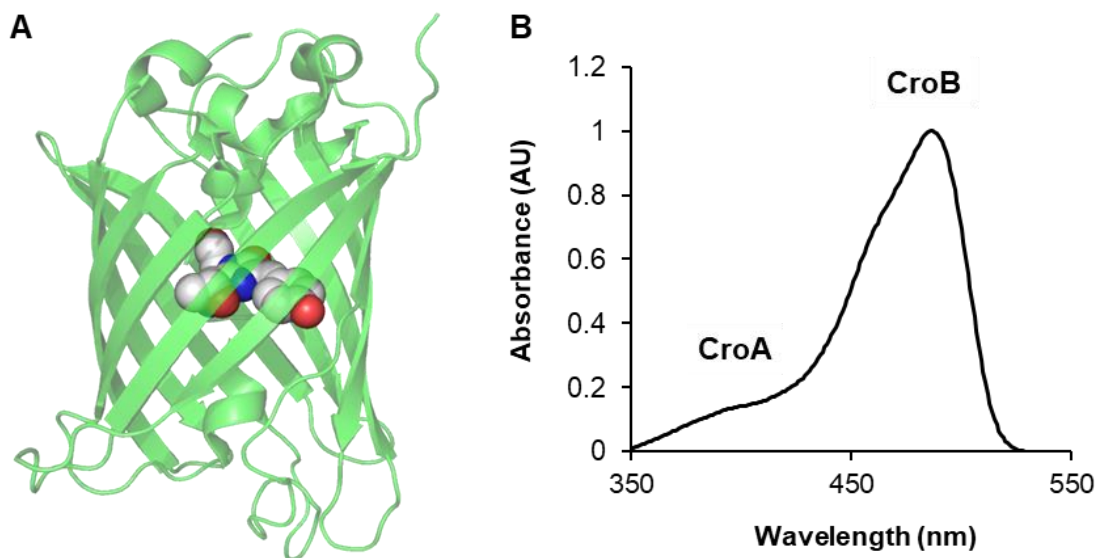
Figure 1.19 – Wild type sfGFP structure and absorbance properties. (A) sfGFP has an eleven stranded β-barrel structure, which shields an internal chromophore (coloured spheres) from solvent. (B) Characteristic absorbance spectrum of wild type sfGFP. The neutral protonated state of Tyr[66] (CroA) has a λ_{max} = ~400nm, whilst the predominant charged phenolate state (CroB) has a λ_{max} = ~485nm.

As part of the fluorescence mechanism, charge transfer can also occur. Excited state proton transfer (ESPT) was elucidated in the chromophore of wild type (WT) GFP to explain how the predominant CroA emits green light (~ 510 nm) while absorbing at 397 nm. The Boxer group identified CroA shifting to an intermediate state (CroI) following excitation, with a proton shuttling from the phenol group of Tyr[66] to Glu[222]. These two residues are connected by a 'proton wire', consisting of a water molecule and a hydrogen bond (Agmon 2005). Decay to ground state then emits the green photon, with the proton shuttling back to complete the photocycle (Chattoraj et al. 1996; Brejc et al. 1997). While these mechanisms have only been proven in WT GFP, a similar occurrence is anticipated for sfGFP which predominates in its deprotonated CroB form. Water molecules have been identified in the local chromophore environment, so it's possible that these may accept and / or transport the proton as the chromophore shifts from CroA to CroB (Arpino et al. 2012). Further proton shuttling routes have been identified by Shinobu and Agmon (2015) that link the chromophore with the external bulk solvent.

Considering charge transfer of the opposite polarity, enhanced GFP (EGFP; predecessor to the sfGFP variant) has been identified as an electron donor following excitation (Bogdanov et al. 2009). Electron acceptor molecules present in the

medium with EGFP were reduced after irradiation at 488 nm, proving direct electron transfer to an external oxidant. The Jones group also showed evidence of this when covalently integrating sfGFP to the side walls of a SWCNT (Thomas et al. 2020). A loss of fluorescence intensity upon UV irradiation was attributed to fewer photocycles, as electrons promoted to the LUMO were transferred to the SWCNT, rather than returning to ground state. Interestingly, an increase in photobleaching resistance was observed with the sfGFP[132AzF] variant, suggesting some feedback to individual sfGFP molecules was possible through a water-based charge transfer pathway. The coupling residue will therefore be of great significance as I look to electrically integrate sfGFP into my NT-FETs.

1.6 Computational methods to optimise NT-FET design

1.6.1 *In silico* modelling

A methodology central to all research chapters in this thesis is *in silico* modelling. Comparable to the experimental techniques of *in vitro* and *in vivo*, the term *'in silico'* is broadly defined as any form of computational experiment (Ekins et al. 2007). For the purpose of this thesis, however, I narrow that definition and use '*in silico* modelling' as a phrase to describe the study of 3D protein and carbon nanotube structure using the molecular visualisation software, PyMOL (Schrödinger and Delano 2015). This is a fundamental tool for macromolecule analysis and allows me to consider all aspects of structure and spatial dimension.

To give a few examples of application, the proteins first chosen to be integrated into NT-FETs would have their crystal structure studied *in silico* to locate compatible sites for AzF incorporation. Consideration would be given to a residue's accessibility, and inherent role in protein functionality and tertiary structure, before shortlisting for AzF substitution. The SwissSwidechain plugin (Gfeller et al. 2013) would then be used to selectively mutate the residue, introducing the non-natural AzF. In another example of application, manual docking of the AzF-modified protein with carbon nanotubes would allow me to replicate the NT-FET setup. This would yield particularly useful in Chapter 3 and Chapter 4, where incoming analyte proteins could be modelled against the BLIP-II—SWCNT complex, and distance could be measured to give insight on the likelihood of Debye length breaches. Finally, the Adaptive Poisson-Boltzmann Solver (APBS) is a useful plugin that exists within PyMOL to calculate electrostatic surface potential (Baker et al. 2001). Understanding the strength and polarity of charge that decorates a protein's surface

is key to elucidating potential sources of electrostatic gating and would find application in all research chapters of this thesis.

1.6.2 Molecular dynamics modelling

A methodology that complements and builds upon *in silico* modelling is molecular dynamics. This simulation-based study allows the movement of atoms in a protein to be predicted over time, rather than being studied through a static snapshot. Its valuable insight on dynamic processes, structural stability and conformational flexibility is well-placed to feature alone, or alongside wet-lab experiments, as recognised by a growing trend of top journal publications (Hollingsworth and Dror 2018). Its success today, however, is testament to the scientific advancements made over the last 70 years.

To give a brief history, molecular dynamic simulations were developed from early models of hard sphere interactions by solving classical equations of motion for each particle, simultaneously (Alder et al. 1957). This progressed to encompass liquid water molecules (Rahman et al. 1971) and eventually the first protein model: bovine pancreatic trypsin inhibitor (McCammon et al. 1977). Further developments throughout the 1980s and 1990s allowed algorithms to be refined, computing power to increase, and user-friendly software packages to be produced, improving simulation accuracy and accessibility (Ciccotti et al. 2022). The significance of molecular dynamics, and its contribution to science, was finally recognised by award of the 2013 Nobel Prize for Chemistry to laureates Martin Karplus, Michael Levitt and Arieh Warshel (Levitt and Warshel 1975; Warshel and Levitt 1976; Brooks et al. 1983). Through a combination of quantum and classical physics, their collaborative efforts were responsible for building the first computer programme to effectively model a biochemical process. This would form the foundation of many modern day simulation programs.

In this thesis, molecular dynamics will be used in Chapter 4 to study the effect of introducing AzF into BLIP-II. As a non-natural amino acid, AzF will be structurally and chemically diverse from the canonical amino acid it substitutes for (e.g., alanine in BLIP-II[41AzF], and threonine in BLIP-II[213AzF]). Key data to extract will therefore be around the structural stability of the protein, exploring the impact AzF has on local and global structure. The other major area for data extraction will be AzF conformation and flexibility. As the anchor residue in the NT-FET setup, understanding AzF's side chain rotamer propensity will provide valuable insight into

BLIP-II's likely binding conformation after UV irradiation. Representative structures will be extracted and manually docked to a SWCNT, using the known geometry of the [2+1] cycloaddition (Setaro et al. 2017). Downstream *in silico* modelling will then allow analyte proteins to align, and electrostatic potential to be calculated. If these models support the experimental data (Chapter 3), it will showcase molecular dynamics as an effective prediction tool to calculate biomolecular electrostatic gating; a synergistic example of dual-approach (computational and wet-lab) research.

1.7 Aims and objectives

Pushing the boundaries of biotechnology, this thesis encompasses synthetic biology and nanotechnology to develop protein-integrated NT-FETs with useful application. Chapter 3 builds on previous research by the Jones and Palma collaboration to develop a biosensor for antibiotic resistance. Our first prototype NT-FET used non-covalently functionalised BLIP-II to detect class A β-lactamase, TEM-1, via electrostatic gating (Xu et al. 2021). However, this setup is limited by the height of the DBCO-pyrene linker molecule and is more exposed to Debye screening effects. I therefore look to directly and covalently attach BLIP-II to the SWCNT channel of the NT-FET, via UV irradiation of the incorporated AzF moiety. I then investigate the sensing of two class A β-lactamases: TEM-1 and KPC-2. This chapter will cover the design, engineering, and production of BLIP-II^{AzF} variants and β-lactamase enzymes, followed by the characterisation, functionalisation, and β-lactamase sensing experiments with the NT-FET devices.

Chapter 4 builds on the experimental results from Chapter 3, modelling the BLIP-II^{AzF}—NT-FET interface to establish whether I can predict AzF mutation site success in mediating proximal analyte sensing. Using molecular dynamics to extract data on AzF side chain rotamer propensity, *in silico* modelling will be performed to align BLIP-II conformers onto a SWCNT bundle with interacting β-lactamase proteins. Distance and electrostatic potential will then be calculated to consider how likely electrostatic gating is to occur within the Debye length. A correlation between Chapter 3 experimental data and computational models would allow a new pipeline to be developed, where prototype BLIP-II^{AzF} variants can be assessed prior to production.

Chapter 5 diverts from biosensing NT-FETs to a focus on optoelectronic NT-FETs. In collaboration with the Bobrinetskiy lab, I look to exploit nature's own light-

responsive elements by covalently integrating sfGFP into an NT-FET platform, via UV irradiation of an incorporated AzF moiety. By exposing the device to different light wavelengths and intensities, I look to investigate if light can be effectively transduced as an electrical signal, and how this may vary through two different sfGFP attachment positions. This chapter will cover the design, engineering and production of sfGFP^{AzF} variants, followed by the characterisation, functionalisation, and light sensing experiments with the NT-FET devices.

2. Materials and Methods

2.1 Materials

2.1.1 Routine laboratory chemicals

For the following sets of methodologies, a standard range of chemicals were used. Product sources and related specification or preparation notes are detailed in Table 2.1. Stock solutions were prepared by dissolving chemicals in deionised water (dH2O).

Table 2.1 – Routine chemicals.

Chemical	Specification / Preparation	Product source
Acetic acid	≥ 99.5 % purity	Scientific Laboratory Supplies (SLS)
Acrylamide: Bis-Acrylamide	40 % (w/v) Acrylamide: Bis-Acrylamide 29:1	Geneflow
Agarose	Molecular biology grade	Appleton Woods
Ammonium persulphate (APS)	Prepared as 10 % (w/v) stock	Melford
L-Arabinose	≥ 98 % purity	Sigma-Aldrich
β-mercaptoethanol	≥ 99 % purity	Sigma-Aldrich
Bromophenol blue	Technical grade	Sigma-Aldrich
Coomassie blue	Coomassie Brilliant Blue R250	Thermo Fisher Scientific
Deoxyadenosine triphosphate (dATP)	Prepared as 10 mM stock	Promega
Deoxycytidine triphosphate (dCTP)	Prepared as 10 mM stock	Promega

Chemical	Specification / Preparation	Product source
Deoxyguanosine triphosphate (dGTP)	Prepared as 10 mM stock	Promega
Deoxythymidine triphosphate (dTTP)	Prepared as 10 mM stock	Promega
Dimethyl sulfoxide (DMSO)	≥ 99.5 % purity	Sigma-Aldrich
Ethanol	≥ 99.8 % purity	VWR
Ethidium bromide	Prepared as 10 mg mL^{-1} stock; ≥ 95 % purity	Sigma-Aldrich
Ethylenediamine-tetraacetic acid (EDTA)	EDTA disodium salt dihydrate; ≥ 99 % purity	Apollo Scientific
D-Glucose	Anhydrous	Melford
Glycerol	Analytical grade	Thermo Fisher Scientific
Glycine	Glycine free base	Melford
Imidazole	≥ 99 % purity	Sigma-Aldrich
Isopropyl β-d-1-thiogalactopyranoside (IPTG)	Prepared as 1 M stock	Melford
Isopropanol	≥ 99.5 % purity	Thermo Fisher Scientific
Lactose	≥ 98 % purity	Sigma-Aldrich
Magnesium sulphate	Analytical grade	Thermo Fisher Scientific
Methanol	≥ 99.8 % purity	Thermo Fisher Scientific
Sodium chloride	≥ 99.5 % purity	Thermo Fisher Scientific

Chemical	Specification / Preparation	Product source
Sodium dodecyl sulphate (SDS)	Prepared as 10 % (w/v) stock	Melford
Sodium hydroxide	Analytical grade	Thermo Fisher Scientific
Sodium phosphate monobasic	Monohydrate; ≥ 98 % purity	Melford
Sodium phosphate dibasic	Anhydrous; ≥ 98 % purity	Melford
Tetramethylethylene-diamine (TEMED)	≥ 99 % purity	Melford
Tris(hydroxymethyl) aminomethane hydrochloride (Tris-HCl)	≥ 99 % purity	Duchefa Biochemie
Tris(hydroxymethyl) aminomethane base (Tris-base)	≥ 99.5 % purity	Melford

2.1.2 Routine laboratory buffers

For the following sets of methodologies, a standard range of buffers and solutions were used. Buffer and solution composition is detailed in Table 2.2, with respective pH and filter sterilisation requirements. For the base solvent, dH2O was used for all buffers/solutions without filter sterilisation, and ultra-pure water (Select Fusion; Suez) was used for those with filter sterilisation.

Table 2.2 – Routine buffers, media and solutions. If no pH adjustment was required, '~' is denoted. Buffers purchased from external companies indicated by ('product source') and confidential materials / quantities denoted by '*'.

Buffer / Media / Solution	Composition	pH	Filter sterilised
Autoinduction media (Studier 2005)	1X 2x YT broth (see composition below)	7	✓
	1X trace metals (see composition below)		
	50 mM ammonium chloride		
	25 mM sodium phosphate dibasic		
	25 mM potassium phosphate monobasic		
	5 mM sodium sulphate		
	2 mM magnesium sulphate		
	0.5 % (v/v) glycerol		
	0.2 % (w/v) lactose		
	0.05 % (w/v) glucose		
	0.05 % (w/v) L-arabinose		
BugBuster (Merck)	Confidential *	~	✓
Coomassie destain buffer	40 % (v/v) methanol	~	✗
	10 % (v/v) acetic acid		
Coomassie stain buffer	40 % (v/v) methanol	~	✗
	10 % (v/v) acetic acid		
	0.1 % (w/v) R250 Coomassie blue		

Buffer / Media / Solution	Composition	pH	Filter sterilised
CutSmart buffer 10X (New England Biolabs)	50 mM potassium acetate 20 mM Tris-acetate 10 mM magnesium acetate 100 µg mL^{-1} recombinant albumin	7.9	✓
DC Protein Assay Reagent A	Alkaline copper tartrate solution *	13.6	✓
DC Protein Assay Reagent B	Dilute Folin reagent *	< 2.1	✓
Dulbecco's phosphate buffered solution (DPBS; Thermo Fisher Scientific)	8.0 g L^{-1} sodium chloride 2.16 g L^{-1} sodium phosphate dibasic 0.2 g L^{-1} potassium chloride 0.2 g L^{-1} potassium phosphate monobasic	7	✓
Gel loading dye no SDS 6X (New England Biolabs)	60 mM EDTA 19.8 mM Tris-HCl 15 % Ficoll®-400 0.12 % Dye 1 0.006 % Dye 2	8	✓

Buffer / Media / Solution	Composition	pH	Filter sterilised
GoTaq G2 Green Master Mix 2X (Promega)	400 µM dATP	8.5	✓
	400 µM dCTP		
	400 µM dGTP		
	400 µM dTTP		
	3 mM magnesium chloride		
	GoTaq G2 DNA polymerase *		
	Yellow dye *		
	Blue dye *		
Ion exchange elution buffer	1 M sodium chloride	8	✓
	50 mM Tris-HCl		
Lysogeny broth (LB) agar (Neogen)	10 g L^{-1} tryptone	~	✗
	5 g L^{-1} yeast extract		
	10 g L^{-1} sodium chloride		
	15 g L^{-1} agar		
Magnesium sulphate solution	5 mM magnesium sulphate	~	✓
N3 buffer (Qiagen)	4.2 M guanidium hydrochloride	4.8	✓
	0.9 M potassium acetate		
Ni affinity elution buffer	250 mM imidazole	8	✓
	50 mM Tris-HCl		
Ni affinity wash buffer	50 mM Tris-HCl	8	✓
	10 mM imidazole		

Buffer / Media / Solution	Composition	pH	Filter sterilised
P1 buffer (Qiagen)	50 mM Tris-HCl 10 mM EDTA 100 µg mL^{-1} RNase A 0.1 % (v/v) LyseBlue	8	✓
P2 buffer (Qiagen)	200 mM sodium hydroxide 1 % (w/v) SDS	~	✓
PB buffer (Qiagen)	5 M guanidium hydrochloride 30 % (v/v) isopropanol	~	✓
PE buffer (Qiagen)	100 mM sodium chloride 10 mM Tris-HCl 80 % (v/v) ethanol	7.5	✓
Periplasmic extraction buffer	50 mM Tris-HCl 20 % (w/v) sucrose 1 mM EDTA	8	✓
Q5 Reaction Buffer 5X (New England Biolabs)	Confidential *	8.5	✓
Q5 High GC Enhancer 5X (New England Biolabs)	Confidential *	~	✓

Buffer / Media / Solution	Composition	pH	Filter sterilised
Quick Ligase reaction buffer 2X (New England Biolabs)	66 mM Tris-HCl 10 mM magnesium chloride 1 mM dithiothreitol 1 mM adenosine triphosphate 7.5 % (v/v) polyethylene glycol; PEG600	7.6	✓
SDS-PAGE loading buffer	0.2 M Tris-HCl pH 6.8 10 % (v/v) β-mercaptoethanol 8 % (w/v) glycerol 2 % (w/v) SDS 0.04 % (w/v) bromophenol blue	~	✗
Sodium phosphate buffer	50 mM sodium phosphate dibasic / sodium phosphate monobasic	7	✓
Super optimal broth (SOB; Melford)	20 g L^{-1} tryptone 5 g L^{-1} yeast extract 0.5 g L^{-1} sodium chloride 2.4 g L^{-1} magnesium sulphate 0.186 g L^{-1} potassium chloride	7	✗
SDS-PAGE running buffer	192 mM glycine 25 mM Tris base 0.1 % (w/v) SDS	8.3	✗
Sodium hydroxide solution	1 M sodium hydroxide	~	✗

Buffer / Media / Solution	Composition	pH	Filter sterilised
TAE buffer	40 mM Tris-acetate	8.8	✗
	1 mM EDTA		
Trace metals 5000X	50 mM iron (III) chloride	~	✓
	200 µM calcium chloride		
	100 µM manganese chloride		
	100 µM zinc sulphate		
	20 µM cobalt chloride		
	20 µM copper chloride		
	20 µM nickel chloride		
	20 µM sodium molybdate		
	20 µM boric acid		
Tris buffer	50 mM Tris-HCl / Tris-base	8	✓
2x YT broth (Thermo Fisher Scientific)	16 g L^{-1} tryptone	7	✗
	10 g L^{-1} yeast extract		
	5 g L^{-1} sodium chloride		

2.1.3 Media

All media types (LB agar, SOB and 2x YT) were prepared with dH$_2$O as per the manufacturer's instructions and sterilised by autoclaving at 121°C for 15 minutes. Further media modifications then took place in a laminar flow cabinet (Microflow), sterilised by 70 % ethanol:

- LB agar was cooled to 50°C before selective antibiotic supplementation and plate pouring. Once set, the plates were sealed with Parafilm and stored at 4°C for up to 2 weeks.

- SOB was cooled to room temperature before supplementation with 4 % (w/v) glucose, sterilised by passing through a 0.22 µM syringe filter. This super

optimal condition (SOC) broth was then aliquoted in 500 µL volumes, into sterile 1.5 mL Eppendorf tubes and stored at -20°C until required.

- 2x YT was cooled to room temperature and stored until required. If the media was being taken forward for an autoinduction protocol, supplementary salts, sugars and trace metals were added, pre-inoculation, by passing through a 0.22 µM syringe filter.

2.1.4 Antibiotics

Antibiotics were prepared as 1000X stock solutions (except Tetracycline which was prepared to 200X), sterilised by filtration through 0.22 µM cellulose acetate syringe filters (Sartorius) and stored at -20°C. Table 2.3 details the antibiotics used, final working concentration, solvent and product source.

Table 2.3 – Antibiotic preparations.

Antibiotic	Working concentration	Solvent	Product source
Carbenicillin	50 µg mL^{-1}	dH$_2$O	Thermo Fisher Scientific
Chloramphenicol	35 µg mL^{-1}	Ethanol	Melford
Kanamycin	30 µg mL^{-1}	dH$_2$O	Duchefa Biochemie
Tetracycline	12.5 µg mL^{-1}	Ethanol	Duchefa Biochemie

2.1.5 Enzymes

Commercial enzymes were used for various molecular biology methods. Table 2.4 details the specific activity of these enzymes and their source company.

Table 2.4 – Enzyme parameters.

Enzyme	Activity	Product source
DpnI	20,000 units mL^{-1}	New England Biolabs

GoTaq G2 DNA polymerase (present in GoTaq G2 Green Master Mix)	Confidential	Promega	
Q5 High-Fidelity DNA Polymerase	2,000 units mL^{-1}	New England Biolabs	
Quick Ligase	Confidential	New England Biolabs	
RNase A	5,000 units mg^{-1}	Generon	
T4 Polynucleotide Kinase (PNK)	10,000 units mL^{-1}	New England Biolabs	

2.1.6 Bacterial strains

Two strains of *E.coli* bacteria were used for plasmid transformation and protein expression, and both are detailed in Table 2.5.

Table 2.5 – Bacterial strains.

Strain	Genotype	Proteins expressed	Product source
BL21(DE3) Competent *E. coli*	fhuA2 [lon] ompT gal (λ DE3) [dcm] ΔhsdS λ DE3 = λ sBamHIo ΔEcoRI-B int::(lacI::PlacUV5::T7 gene1) i21 Δnin5	BLIP-II TEM-1 KPC-2	New England Biolabs
One Shot™ TOP10 *E. coli*	F- mcrA Δ(mrr-hsdRMS-mcrBC) Φ80lacZΔM15 Δ lacX74 recA1 araD139 Δ(araleu)7697 galU galK rpsL (StrR) endA1 nupG	sfGFP	Thermo Fisher Scientific

2.1.7 Vectors for protein expression

A variety of plasmid constructs (Table 2.6) were used in this project to host the genes for recombinant protein expression.
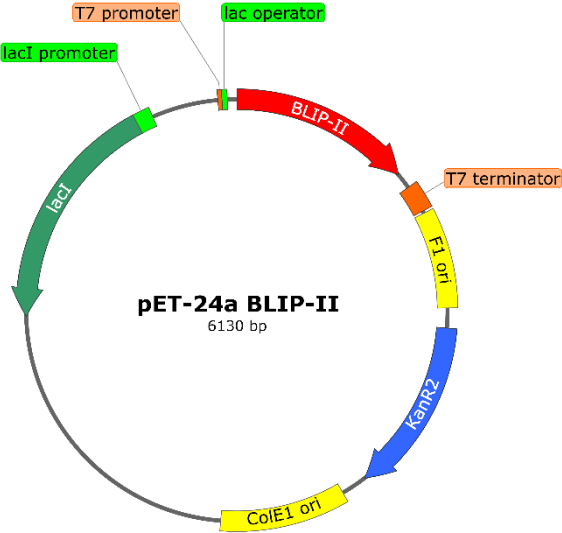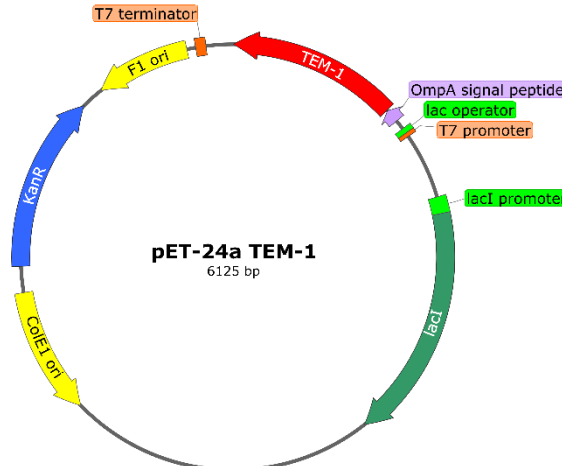
BLIP-II and TEM-1 proteins were both expressed using a pET-24a vector. This used IPTG to induce expression under the T7/lac promoter system and contained a selective kanamycin resistance gene. The BLIP-II vector was made and sourced from the Palzkill lab (Brown and Palzkill 2010) whilst the TEM-1 vector was made and sourced from the Makinen lab (Sosa-Peinado et al. 2000).

KPC-2 protein was expressed using a pTP123 vector, assembled and gifted by the Palzkill lab (Petrosino et al. 1999). This vector used a trc promoter system, a hybrid of tryptophan and lactose promoters, which used IPTG as the inducer molecule and contained a selective chloramphenicol resistance gene.

sfGFP protein was expressed using a pBAD vector. The vector contained the selective ampicillin resistance gene, and sfGFP expression was under the control of an arabinose inducible promoter. The plasmid was kindly donated by the DDJ lab (Reddington et al. 2012).

The introduction of nnAAs relied upon the vector pDULE-cyanoRS. It was designed by the Mehl lab (Miyake-Stoner et al. 2010), and contains a bio-orthogonal tRNA / aminoacyl tRNA synthetase pair from *Methanocaldococcus jannaschii*. The tRNA has been engineered to recognise the UAG stop codon, whilst the tyrosol-tRNA synthetase recognises tyrosine derivative ncAAs (e.g., AzF) and catalyses the attachment to the tRNA (Blight et al. 2004).

Table 2.6 – Plasmid constructs. Plasmid maps were generated by SnapGene software (Insightful Science 2022).

Plasmid map	Summary
	Vector: pET-24a **Protein expressed:** BLIP-II **Selective marker:** Kanamycin [R] **Source:** Palzkill lab (Brown and Palzkill 2010)
	Vector: pET-24a **Protein expressed:** TEM-1 **Selective marker:** Kanamycin [R] **Source:** Palzkill lab (Brown and Palzkill 2010)
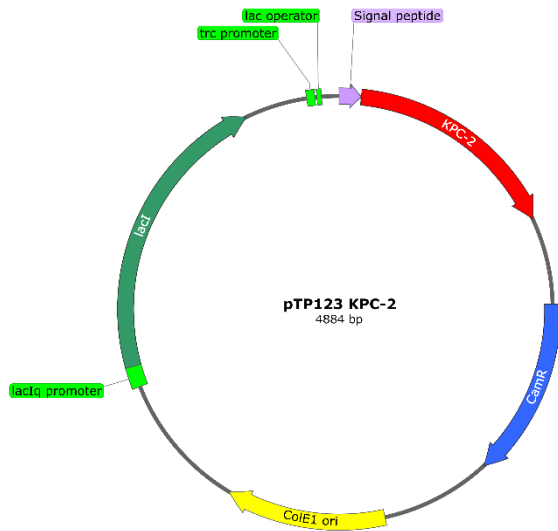
Vector: pTP123

Protein expressed:
KPC-2

Selective marker:
Chloramphenicol [R]

Source: Palzkill lab
(Petrosino et al. 1999)
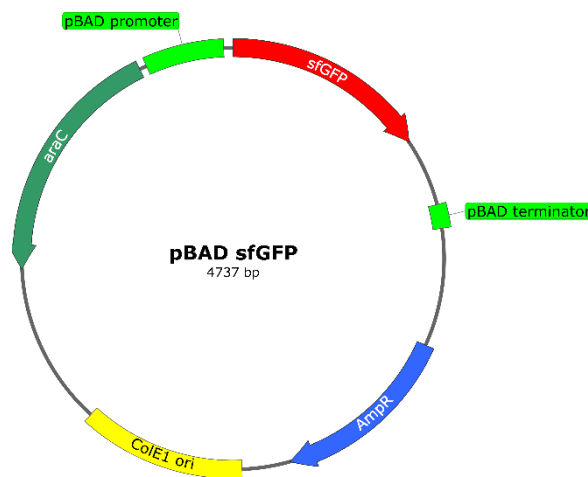
Vector: pBAD

Protein expressed:
sfGFP

Selective marker:
Ampicillin [R]

Source: Jones lab
(Reddington et al. 2012)
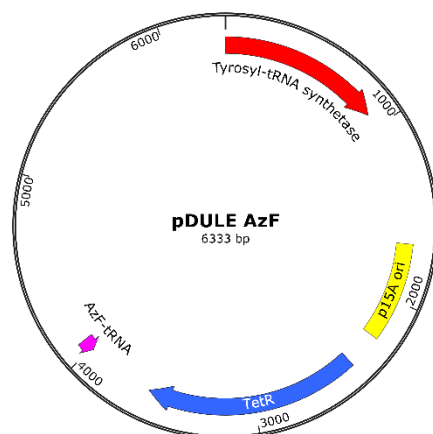
Vector: pDULE-
cyanoRS

Protein expressed:
Tyrosyl-tRNA synthetase

RNA transcribed:
Engineered AzF tRNA

Selective marker:
Tetracycline [R]

Source: Mehl lab
(Miyake-Stoner et al.
2010)

2.1.8 *p*-Azido-L-phenylalanine

Non-natural amino acid *p*-Azido-L-phenylalanine (AzF; Insight Biotechnology) was prepared by dissolving in a minimal volume of sodium hydroxide solution (Table 2.2). Once growth media reached an optical density (OD_{600}) of 0.6, AzF was added to a final concentration of 1 mM. Dark conditions were maintained throughout all stages to prevent premature photolysis of AzF.

2.1.9 Nitrocefin

The β-lactamase chromogenic substrate, nitrocefin (Stratech), was prepared fresh for the relevant assays. Dissolved in the minimal volume of DMSO, nitrocefin was then diluted for use with dH_2O. Concentration was determined by measuring the absorbance of nitrocefin in dH_2O, using a molar extinction coefficient (ε_{390}) of 17,700 M^{-1} cm^{-1}.

2.1.10 DBCO-Cy3

A fluorescent probe to test for azide incorporation, dibenzocyclooctyne-Cy3 (DBCO-Cy3) was prepared by dissolving in a minimal volume of DMSO and diluting to 2 µM with dH_2O. Concentration was determined by measuring absorbance at 548nm, with ε = 92,000 M^{-1} cm^{-1}. Aliquots were then stored at -20°C.

2.1.11 Single-walled carbon nanotubes (SWCNTs)

SWCNTs, purchased from Sigma-Aldrich, were ≥ 95 % semiconducting with a (7,6) chirality. To prepare the solution for casting, 0.1 mg of SWCNTs were suspended in 500 µL 1 % SDS solution and dispersed via 1 hour of bath sonication. The SWCNT solution was centrifuged at 15000 rpm for 1 hour, with the supernatant taken forward for a further 500X dilution in 1 % SDS solution.

2.2 Computational modelling and analysis

2.2.1 *In silico* modelling

All aspects of *in silico* modelling were performed using molecular visualisation software, PyMOL (Schrödinger and Delano 2015). Protein structures were downloaded as .pdb files from the Protein Data Bank (Table 2.7; Berman et al.

2000). CNT structures were downloaded as .pdb files from TubeGen (Frey and Doren 2011), after building to the specification used experimentally (Materials 2.1.11).

Table 2.7 – PDB files used for *in silico* modelling.

PDB code	Protein(s)	Reference
1JTD	BLIP-II and TEM-1	(Lim et al. 2001a)
3QHY	BLIP-II and Bla1	(Brown et al. 2011)
2OV5	KPC-2	(Ke et al. 2007)
2B3P	sfGFP	(Pédelacq et al. 2006)

2.2.2 AlphaFold

To generate starting structures for molecular dynamics (MD) analysis, a simplified version of AlphaFold (Jumper et al. 2021) v2.1.0 was used via the Google Colab notebook. Gene sequences were translated in Serial Cloner (Perez 2013), and copied into AlphaFold with signal sequences and the initiator methionine removed (Appendix Table 8.1). To predict the structure of the AzF variants, the desired mutation site was substituted with a tyrosine residue.

The predicted structure was then passed through the SWISS-MODEL (Waterhouse et al. 2018) structure assessment to check protonation states, with the processed co-ordinates taken forward as the starting structure for MD.

2.2.3 Molecular dynamics

2.2.3.1 GROMACS software

GROMACS (GROningen Machine for Chemical Simulations) is a free software package and was chosen to perform MD simulations (Bekker et al. 1993). Preparation of the topology file, energy minimisation and simulation analysis were carried out using GROMACS 2022.3, whilst the computationally demanding stages

of two-step equilibration and production MD were allocated to the Supercomputing Wales HAWK Server (project code SCW1631), using GROMACS 2021.5.

2.2.3.2 CHARMM36 forcefield

Forcefields are the backbone of MD simulations, using a collection of equations and constants to define the potential energy acting on the system. CHARMM36 was my forcefield of choice, being the most recently developed forcefield by the MacKerell group for general protein simulation (Best et al. 2012). Here, the potential energy function is described simply in Equation 2.1 (Croitoru et al. 2021). The sum of intermolecular (non-bonded) energy (U_{inter}) and intramolecular (bonded) energy (U_{intra}) determines the potential energy (U).

Equation 2.1 $$U = U_{inter} + U_{intra}$$

To break this down further, intermolecular energy is contributed by terms for electrostatic interaction and van der Waals forces, as detailed in Equation 2.2 (Croitoru et al. 2021). The electrostatic interaction term is described by Coulomb's law, where q_i and q_j denote the partial atomic charges assigned to a pair of atoms i and j, while r_{ij} is the distance between them. The dielectric constant, ε, describes the ability of the space between two atoms to hold an electrical charge, and in combination with the electrostatic function, it describes a scenario where increasing distance between two atoms will reduce the electric force between them. Van der Waals can arise between two atoms through attractive or repulsive forces, and this interaction is commonly represented through the Lennard-Jones (LJ) potential curve (González 2011). In this curve we observe potential interaction energy plotted against the distance between atoms i and j, and derive the point at which the minimum potential energy (ε_{ij}) is reached and its associated atom distance $R_{min,ij}$. The repulsive forces are then represented by the bracketed function with an exponent of 12, while attractive forces have the exponent of 6.

Equation 2.2

$$U_{inter} = \sum_{electrostatic} \frac{q_i q_j}{4\pi\varepsilon_0 r_{ij}} + \sum_{vdW} \varepsilon_{ij}\left(\left(\frac{R_{min,ij}}{r_{ij}}\right)^{12} - 2\left(\frac{R_{min,ij}}{r_{ij}}\right)^{6}\right)$$

The potential energy from intramolecular bonding in Equation 2.3 is contributed to by terms for bonds (b), valence angles (θ), Urey-Bradley (r), dihedral angles (ϕ) and improper dihedral angles (φ) (Croitoru et al. 2021). To consider the effect of geometrical deviations from atomic coordinates, these quadratic expressions take the calculated value for b, θ, r_{1-3} and φ and subtract the equilibrium value for b_0, θ_0, $r_{1-3;0}$ and φ_0, respectively.

Bond length (b) will take the distance between two bonded atoms in Å. Valence angles (θ) identifies the angle between three bonded atoms. Urey-Bradley (r_{1-3}) considers three linearly bonded atoms and will take the distance (Å) between the 1st and the 3rd atom, to account for angle bending as a result of non-bonded interaction (Simanouti 1949). Improper dihedral angles are included to ensure planar groups remain planar, and so consider four atoms, whereby atoms (j, k, l) are bound to a central atom (i). The angle (φ) is taken from the angle between two planes of atoms: (i, j and k) and (j, k and l). Each term also contains a corresponding force constant (K_b, K_θ, K_{UB} and K_φ), which is obtained through vibrational analysis studies, theoretically or experimentally.

The dihedral angle term is more complex and considers four sequentially bonded protein backbone atoms (a, b, c and d). Atoms b and c lie in the same plane, while a and d protrude in different directions, resulting in two planes of atoms: P_{abc} and P_{bcd}. The angle between these planes is defined as ϕ. As the bc bond rotates from -180° to +180°, atoms a and d move between favourable and unfavourable conformations, (energy minima and maxima). This periodic oscillation in dihedral potential energy is expressed as a cosine function: $K_n (1+cos(n\phi - \delta_n))$ where n is the multiplicity, e.g., the number of energy minima in a full 360° bond rotation, δ_n is the phase between each multiplicity (°), and the force constant, K_n, is the amplitude. To account for the periodicity of bc bond torsion, the dihedral term can be expanded up to six times in a Fourier series ($\sum_{n=1}^{N}$) to accurately model the most common torsion potential (Brooks et al. 2009). Finally, CMAP (crossterms and 2D dihedral energy grid

correction map) is an additional term employed by CHARMM36 to prevent the systematic biasing towards certain secondary structures (Mackerell et al. 2004).

Equation 2.3

$$U_{intra} = \sum_{bonds} K_b(b - b_0)^2 + \sum_{angles} K_\theta(\theta - \theta_0)^2 + \sum_{Urey-Bradley} K_{UB}(r_{1-3} - r_{1-3;0})^2$$

$$+ \sum_{dihedral} \sum_{n=1}^{N} K_n(1 + cos(n\phi - \delta_n)) + \sum_{improper} K_\varphi(\varphi - \varphi_0)^2 + CMAP$$

2.2.3.3 Parameterisation of amino acid *p*-Azido-L-phenylalanine

The parameterisation of AzF involved the definition of new atom types, bond lengths, dihedral angles and partial charges for the AzF residue. The structural coordinates of AzF were prepared by former lab member, Dr. Harley Worthy, and incorporated into PyMOL via a .pkl file using the SwissSidechain plugin (Gfeller et al. 2013; Schrödinger and Delano 2015). To derive the values for parameterisation, the AzF residue was saved as a .pdb file and input to the AnteChamber PYthon Parser interfacE (ACPYPE; Sousa Da Silva and Vranken 2012). Partial charges were derived using the bond charge corrections method, and bond lengths and dihedral angles were calculated. Parameterisation output values were written in a format compatible with the CHARMM36 forcefield, including the CHARMM specific atom names. A text editor was then used to introduce the values to the CHARMM36 forcefield parameter files, including the atom type (.atp), residue type (.rtp), bonded interactions (ffbonded.itp) and non-bonded interactions (ffnonbonded.itp) as detailed in Appendix Table 8.2 – 8.11. The hydrogen database was not amended as no new hydrogens were added, but an addition was made to the termini database (Appendix Table 8.12 – 8.15) for BLIP-II[41AzF], to account for the NH3$^+$ cap.

2.2.3.4 Input structure preparation

Starting structural coordinates were derived from AlphaFold and SWISS-MODEL (Methods 2.2.2). For the WT BLIP-II protein, no further adjustments were made. For the AzF variants of BLIP-II, the structural coordinates were loaded into molecular visualisation software, PyMOL (Schrödinger and Delano 2015), and using the SwissSidechain (Gfeller et al. 2013) plugin, the AzF was substituted in for tyrosine

at the desired mutation site. A new .pdb file was written, and this was taken forward as the input structure for MD.

Using GROMACS, the pdb file was converted to Gromos87 format (.gro), adding hydrogen ions where required. Parameters from the adapted CHARMM36 forcefield were used to inform GROMACS on AzF topology and charge, and the tip3p water model was employed. The unit cell was then defined, with the protein centred and kept at least 1 nm from the box edge in the dodecahedron cell. Next, the simulation box was solvated with spc216.gro, an equilibrated 3-point water model. Overall charge was calculated, and sodium ions were added in to neutralise the system.

2.2.3.5 Energy minimisation

In order to achieve the protein's most stable conformation before production MD, energy minimisation (EM) was performed. Here, steric clashes were relieved and potential energy was lowered using the steepest descent algorithm. The step size was set at 0.01 nm and the maximum number of steps was 50000. The minimisation had to converge under 1000 kJ mol^{-1} nm^{-1} to ensure simulation stability.

Interactions between atoms and their neighbours were also considered during EM, with a neighbour list updated every step using the Verlet cut-off scheme and grid framework. The Particle-Mesh Ewald (PME) algorithm helped to determine total electrostatic and van der Waals energy, with a 1.2 nm cut off chosen for both coulombs and van der Waals. Finally, periodic boundary conditions (PBC) were applied in *xyz* dimensions.

2.2.3.6 Two-step equilibration: temperature and pressure

Two-step equilibration follows EM to equilibrate the solvent around the protein. Parameters regarding PBC, atom neighbour finding, and atom interactions are maintained from EM, with the addition of a cubic interpolation for PME and 0.16 nm grid spacing for fast Fourier transformations, which finely balances the accuracy of electrostatics and van der Waals. The run control algorithm, however, changes from steep descent to leap-frog to integrate Newton's equations of motion. Equilibration was run for 100 ps for both temperature and pressure, with a 2 fs time step for integration.

Further parameters included are bond parameters. Here, the holonomic constraints employed to replace bond vibration are corrected for by a LINCS algorithm. This resets bonds to their correct length following rotation through one iteration and uses the highest order (4) constraints. All bonds to hydrogen atoms are further converted into constraints. To ensure a constant temperature (300 K), velocity-rescale temperature coupling is used for both protein and non-protein groups every 0.1 ps. Finally, no dispersion correction is applied for energy and pressure due to the use of the CHARMM36 forcefield.

Temperature and pressure equilibration do have parameters specific to their own simulation. For temperature, there is no pressure coupling and velocities are generated according to the Maxwell distribution using a random seed. For pressure, velocity generation is switched off, as it continues from the temperature equilibrated trajectory. Isotropic Berendsen pressure coupling is now employed to ensure a constant pressure every 2 ps, with a reference pressure of 1 bar and reference compressibility of water at 4.5×10^{-5} bar^{-1}.

2.2.3.7 MD production run

All parameters, topologies and trajectory coordinates from the pressure equilibration run were carried as input into the final MD production run. The only change saw the number of steps increase, to account for a 200 ns run with energies and coordinates being saved every 10 ps.

2.2.3.8 Post MD analysis

Once the simulation had reached completion, the trajectory file was converted to remove the water molecules and the molecular mass was centred in the box as treatment for the periodic boundary conditions. The structure was then fitted to the reference structure file by translation.

2.2.3.9 Structural stability analysis

For each repeat, RMSD data was extracted using an index file for the C_α atoms of the protein without the extended His tag (residues 41 – 310). Radius of gyration data was then extracted for the same structure but collected protein data rather than

C_a. Following structural stability analysis, the trajectory file had the first 10 ns trimmed to remove any data bias from 'warm up' phase of the simulation.

2.2.3.10 RMSF and B-factor

For each repeat, RMSF and B-factor data was extracted using an index file for the protein without the extended His tag. Using the trimmed trajectory file, values were calculated per residue. Data was collated from the three repeats, and average RMSF and B-factor values were then calculated. Average B-factor values were loaded into a BLIP-II structure on PyMOL to generate the cartoon putty figure.

2.2.3.11 RMSD of AzF residue

For each repeat, RMSD data was extracted for the AzF residue using the trimmed trajectory file. The first stage of the RMSD calculation required least squares fitting of the residue to the C_α, C_β and CO atoms in the supplied reference structure. Next, the RMSD calculation was performed on phenyl ring of AzF.

This data was plotted in an RMSD vs time plot, and additionally by population frequency analysis, which used a bin cut-off of 0.01 nm. Once peaks had been defined, modal groups were identified. A search of the RMSD data for points within these groups yielded specific timepoints, allowing a simple simulation frame extraction to correlate the modal group to a specific rotamer.

2.2.3.12 BLIP-II:SWCNT modelling with β-lactamases

Extracted BLIP-II structures with differing AzF rotamers were loaded into PyMOL with a SWCNT bundle. To model the β-lactamase binding, the BLIP-II:TEM-1 crystal structure was loaded into the session and aligned to the BLIP-II protein. For KPC-2, the crystal structure was loaded into the session, and aligned to the TEM-1 protein due to inherent homology and predicted binding to the same BLIP-II interface. To accurately represent the bonding geometry between AzF and a SWCNT, the protein was oriented to have AzF inserting into the bundle perpendicularly. The protein complex was then rotated about the SWCNT bundle (maintaining the perpendicular angle of the phenylazide group) until a minimum distance from the β-lactamase was

achieved. APBS electrostatics was finally performed on both TEM-1 and KPC-2 to reveal electrostatic surface potential (Baker et al. 2001).

2.2.4 Signal peptide prediction

The SignalP 5.0 peptide prediction software (Almagro Armenteros et al. 2019) was used to test the β-lactamase protein sequences, to ensure the correct fractionation protocol was applied after expression. For job submission, the protein sequence was entered in FASTA format, and the gram-negative organism group selected. The output file then contained a detailed breakdown of signal peptide probability, along with signal peptide type and the predicted cleavage site. If signal peptide probability was > 0.8, a periplasmic extraction protocol (Methods 2.4.4.4) was followed to isolate the protein.

2.2.5 Isoelectric point and molecular mass calculator

Two key protein parameters, isoelectric point (pI) and molecular mass, were essential to identify for downstream techniques such as ion exchange chromatography and SDS-PAGE analysis. Here, the online ExPASy server was used (Walker et al. 2005) by inputting the protein sequence in FASTA format and calculating the pI and molecular mass with average resolution.

2.3 Molecular biology and recombinant DNA methods

2.3.1 Oligonucleotide primers

Oligonucleotide primers were designed for site-directed mutagenesis and gene amplification (Table 2.8) using Serial Cloner software (Perez 2013), and optimised using AmplifX software (Jullien 2021). Melting temperature (Tm) was calculated using an online Tm Calculator (New England Biolabs 2022). Lyophilised primers were then ordered from Integrated DNA technologies and rehydrated as per manufacturer instructions.

Table 2.8 – Oligomeric primer sequences for gene amplification or target mutation sites. Mutations introduced are highlighted in red.

Gene/Mutation site	Forward Sequence	Reverse Sequence	Tm (°C)
T7 (sequencing)	TAA TAC GAC TCA CTA TAG GG	CTA GTT ATT GCT CAG CGG T	55
pBAD (sequencing)	ATG CCA TAG CAT TTT TAT CC	GAT TTA ATC TGT ATC AGG	51
BLIP-II Y73 TAG	AGG TGG TTA GTT TCA TGG GCT	GCA ATT GCA TCC ACA CCA CT	65
BLIP-II D131 TAG	CGG TAA CGA GTA GGG CCA AA	CCC CAA GCA ATC ACT TCC C	65
BLIP-II T135 TAG	AAA CTT AGG TGC CGG CCG A	GGC CAT CCT CGT TAC CGC	65
BLIP-II A138 TAG	CCC GTT CCG GTG TAG ATG CTA TT	CCT CCT ACG GCA CCG TAG TTT	61
BLIP-II Y191 TAG	TGG TGT GTA GTA CCG CGC T	CCA TCC AGC GCG GTC AC	65
BLIP-II N198 TAG	GTA AAA TAG GGT GGT GTT ATT GCG TG	TGC CAG CGC GGT ATA CA	67
BLIP-II E217 TAG	CCG GCG TAG GCT CAG T	CAC TGT GGT CTG GCC AAA ATA ATT ATC C	65
BLIP-II F230 TAG	GGC GCT GAA AGA TGG TAA AGT TAT T	AGG CTG TGC TAG ATG CCG	65

2.3.2 DNA amplification by polymerase chain reaction (PCR)

DNA amplification was performed as part of whole plasmid inverse PCR (for site-directed mutagenesis) and colony PCR protocols. For whole plasmid inverse PCR, a high-fidelity DNA polymerase was desirable to ensure the primers carrying the mutation for site-directed mutagenesis were accurately amplified into the plasmid DNA. Thus, the Q5 High-Fidelity DNA Polymerase kit (New England Biolabs) was purchased. The established reaction setup and PCR protocol used can be seen in Table 2.9.

Table 2.9 – Whole plasmid inverse PCR for site-directed mutagenesis. Tm denotes the melting temperature specified for primer pairs in Table 2.8.

Material	Volume in 50 µL reaction
Nuclease free water	13.5
5X Q5 Reaction Buffer	10
5X Q5 High GC Enhancer	10
Template DNA (1 ng µL^{-1})	10
Forward primer (10 µM)	2.5
Reverse primer (10 µM)	2.5
dNTPs (10 mM)	1
Q5 High-Fidelity DNA Polymerase	0.5

PCR conditions					
Initial denaturation	30 reaction cycles			Final extension	Hold
	Denaturation	Annealing	Extension		
98°C 30 seconds	98°C 10 seconds	Tm °C 30 seconds	72°C 30 seconds kb^{-1}	72°C 2 minutes	4°C Infinite

For colony PCR, a ready-to-use GoTaq G2 Green master mix containing GoTaq G2 polymerase (Promega) and all the necessary reaction components was favoured. Template DNA was prepared by picking colonies from transformed bacteria (Methods 2.3.8) and suspending the cells in 10 µL of nuclease free water. These were heated at 98°C for 10 minutes, then centrifuged for 3 minutes at 13000 rpm. The supernatant achieved constituted the template DNA, which was taken forward into the reaction mix. The complete reaction mix and PCR protocol are detailed in Table 2.10.

Table 2.10 – Colony PCR.

Material	Volume in 25 µL reaction
2X GoTaq G2 Green Master Mix	12.5
Template DNA	5
Nuclease free water	5
Forward primer (10 µM)	1.25
Reverse primer (10 µM)	1.25

PCR conditions					
Initial denaturation	30 reaction cycles			Final extension	Hold
	Denaturation	Annealing	Extension		
98°C 2 minutes	98°C 30 seconds	55°C 30 seconds	72°C 1 minute kb^{-1}	72°C 5 minutes	4°C Infinite

2.3.3 Agarose gel electrophoresis

To analyse DNA fragment sizes, 1 % (w/v) agarose gels were prepared by heating and dissolving 1 g of agarose in 100 mL TAE buffer. Ethidium bromide was then supplemented to a final concentration of 0.3 µg mL^{-1} and the gel cast. Once solidified, the gel was submerged in a tank (Cleaver) containing TAE buffer, and comb retracted. For sample preparation, DNA products from site-directed mutagenesis were mixed with 6X gel loading dye on Parafilm to achieve 1X concentration, while DNA products from colony PCR required no dye addition. Samples were loaded in 10 µL volumes and DNA ladder (1 kb / 1 kb plus; New England Biolabs) in a 2 µL volume. Electrophoresis was performed for 45 minutes at 140 V, with the separated DNA bands then visualised using the GelDoc-It UV-transilluminator (Ultra-Violet Products Ltd).

2.3.4 DNA purification

For DNA to be utilised in downstream applications e.g., cloning or sequencing, residual impurities must be removed. The QIAquick PCR purification kit (Qiagen) was used in this instance. To describe briefly, of the volume of DNA sample to be purified, 5 times that volume of PB buffer was used to mix in with the sample, and this was applied to the QIAquick spin column. The spin column was placed in a collection tube and centrifuged at 13000 rpm for 1 minute, binding the DNA to the silica membrane and allowing the impurities to be discarded in the flow-through. To wash the spin column, 750 µL of PE buffer was added and centrifuged for 1 minute at 13000 rpm two times, discarding the flow-through after each spin. Finally, the DNA was eluted in nuclease free water by moving the spin column to a sterile 1.5 mL tube and applying the desired volume of water. For recovery of PCR product, 10 µL was applied to the membrane, while recovery of plasmid from a miniprep used a larger volume of 50 µL. After waiting for 1 minute, the spin column was centrifuged at 13000 rpm for 1 minute, and the eluted sample taken as purified DNA. If the DNA wasn't for immediate use, it was placed in the freezer for long term -20°C storage.

2.3.5 DNA phosphorylation and ligation

The next step in the cloning process was to functionalise the plasmid DNA produced by PCR. For this, 5 µL of purified PCR product were combined with 10 µL of Quick Ligase reaction buffer, 2 µL of CutSmart buffer, 1 µL of DpnI and 1 µL of T4 PNK

(Table 2.4), and left to incubate for 30 minutes at 37°C. To ensure only the mutated DNA could be recircled, DpnI was used to recognise and degrade the methylated template. T4 PNK was then used phosphorylate the 5' terminus of DNA fragments, a prerequisite for ligation.

Once the first incubation had finished, the mixture was moved to room temperature conditions and 1 µL of Quick Ligase (Table 2.4) was added . This was incubated for 5 minutes to enable plasmid recircularisation. The mixture then underwent an additional DNA purification (Methods 2.3.4) step to remove the enzymes and buffer salts. DNA quantification (Methods 2.3.6) confirmed the concentration and purity, before taking the DNA forward for bacterial transformation (Methods 2.3.8).

2.3.6 DNA quantification

To confirm the quantity and quality of purified DNA, a quick check on the NanoDrop ND 1000 Spectrophotometer (Thermo Fisher Scientific) was carried out. Using the nucleic acids setting, a blank measurement was taken using 2 µL of nuclease free water. The pedestal was wiped clean using a lens tissue, and 2 µL of the DNA sample was then applied and measured. Absorbance (A_{260}) was measured using Equation 2.4.

To calculate DNA concentration, the Beer-Lambert equation was then used (Equation 2.5). The equation terms are defined as concentration (c), molar extinction coefficient (ε) and pathlength (l). The molar extinction coefficient uses the units (ng/µL)$^{-1}$ cm^{-1}, and the accepted value for double stranded DNA is 50 (ng/µL)$^{-1}$ cm^{-1}. The NanoDrop uses two different pathlengths of 1.0 mm and 0.2 mm.

From purified PCR constructs, a usable quantity was considered to be ≥ 10 ng µL^{-1}. Whereas plasmids from a miniprep required a concentration of ≥ 50 ng µL^{-1} before they could be sent for sequencing. The quality of DNA was also assessed from the curve of the absorbance vs wavelength plot. A desirable curve of purified DNA would show only one clear peak at 260 nm, while contaminants such as salt and protein produce additional peaks at 230 nm and 280 nm respectively.

Equation 2.4 $\qquad A_{260} = -log\left(\frac{Intensity_{sample}}{Intensity_{blank}}\right)$

Equation 2.5 $\qquad c = \frac{(A \times \varepsilon)}{l}$

2.3.7 Competent cell preparation

For the purposes of bacterial transformation, competent cells were bulk prepared, aliquoted and stored at -80°C. The preparation protocol was spread across two days, and all stages were completed in an ethanol sterilised laminar flow cabinet (excluding the incubation) using autoclaved materials and equipment. On the first day, 2 L of 10 % glycerol, 1 L of SOB in a two-litre growth flask, 10 mL of SOB in 50 mL growth flask, centrifuge bottles, 0.5 mL tubes, 400 µL and 200 µL filter tips were autoclaved at 121°C for 15 minutes. A starter culture (Methods 2.4.1) was set up using 10 mL of SOB and 100 µL of competent cells (Table 2.5) fresh from a new aliquot. No antibiotic was added, and the flask was sealed for 16 hours of incubation at 37°C and 200 rpm.

On the second day, 1 L of SOB was prewarmed to 37°C. The media was then inoculated with 1 mL from the starter culture, sealed and left to incubate at 37°C and 200 rpm. Periodic 500 µL samples were taken to check the OD_{600}. Meanwhile, centrifuge bottles were pre-chilled in ice and the centrifuge pre-cooled to 4°C. Once OD_{600} hit 0.6, the culture was immediately removed from the incubator and left to chill on ice for 15 minutes. The culture was then divided between centrifuge bottles and spun at 4°C and 5000 rpm for 15 minutes. The supernatant was poured off and 1 L of 10 % glycerol replaced the lost volume of media. Cells were resuspended through vortexing and centrifuged again at the same conditions. This supernatant removal, resuspension and centrifugation cycle was repeated once more with the second 1 L of 10 % glycerol. After the final centrifugation, the supernatant was removed, and the cells were resuspended in the residual glycerol. Aliquots of 50 µL were produced and flash frozen in liquid nitrogen, to be stored long term at -80°C.

Testing of the competent cells was necessary before experimental use. Cells were plated on LB agar plates (Materials 2.1.3) of all antibiotics and tested by electroporation with a known plasmid to confirm transformation ability. Working competent cells would be indicated by no colonies on the antibiotic plates, and colonies on the selective antibiotic plate of the tested plasmid.

2.3.8 Bacterial transformation and selection of electrocompetent *E. coli* cells

Plasmids were transformed into both *E. coli* BL21 and TOP10 (Table 2.5) cells through a process of electroporation. A 50 µL aliquot of competent cells was mixed

with 1 µL of plasmid DNA at concentration of 50 ng µL^{-1} (or the equivalent volume for ~50 ng of plasmid DNA) and chilled on ice for 5 minutes in the electroporation cuvette. In the case of double transformation, ~25 ng of each plasmid DNA was added to the cells. The cuvette was then placed in the Flowgen Cellject electroporator and given a short pulse at 2500 V, with 500 µL of SOC media added immediately after. The cells were transferred to sterile 1.5 mL tube and left to incubate for 1 hour at 37°C and 200 rpm.

After incubation, cells transformed with plasmid from PCR products were pelleted to achieve a higher cell density media for plating. This involved centrifugation for 1 minute at 13000 rpm, and 400 µL of the supernatant being removed. The cells were then resuspended in the remaining supernatant, and the entire volume spread onto the appropriate antibiotic plate (Materials 2.1.3). In the case of plasmids transformed from a stock, the lower cell density media was sufficient for plating, so 100 µL was spread directly on the selective antibiotic plate and the rest discarded. Plates were then left to incubate at 37°C overnight, and stored for a maximum of 2 weeks at 4°C.

2.3.9 Plasmid DNA extraction from bacterial cells

To extract plasmid DNA from a starter culture (Methods 2.4.1), the QIAprep Spin Miniprep kit was used. The kit is comprised of a series of buffers, which when used in a stepwise manner, facilitates the lysis of bacterial cells and DNA adsorption to the silica membranes of the QIAprep spin columns. A clean-up procedure, mirroring that of the QIAquick PCR purification protocol (Methods 2.3.4), completes the plasmid extraction.

To describe the protocol in brief, 10 mL of starter culture was centrifuged at 4000 rpm for 10 minutes to pellet the cells. The supernatant was removed, and the pellet resuspended in 250 µL of P1 buffer. Next, 250 µL of lysis (P2) buffer was added and incubated for 5 minutes at room temperature. To neutralise the alkaline solution and prepare the DNA for silica membrane adsorption, 350 µL of N3 buffer was added. The tube was inverted several times and then centrifuged hard at 13000 rpm for 10 minutes. The resulting supernatant contains the plasmid DNA and is added QIAprep spin column. The spin column is placed in a collection tube and centrifuged for 1 minute at 13000 rpm. The supernatant is discarded.

The plasmid DNA now undergoes the same clean-up protocol as in Methods 2.3.4 to remove residual salts and endonucleases. The only changes to the protocol are

the use of a set volume (500 µL) of PB buffer, and the continued use the QIAprep spin columns, not QIAquick. The eluted plasmid DNA was then quantified (Methods 2.3.6).

2.3.10 Sequencing

To sequence plasmids, the Eurofins TubeSeq service was used. Here, 20 µL samples comprising of 2 µL primer (forward or reverse, depending on the desired read) and 18 µL plasmid, were aliquoted. Plasmid DNA was diluted for use using nuclease free water, aiming for a concentration of 50 – 100 ng µL^{-1}. In the case of BLIP-II^{AzF} variants, a Power Read sequencing upgrade was purchased to account for the high GC percentage, which would otherwise result in poor sequencing results.

2.4 Recombinant protein expression and purification methods

2.4.1 Starter cultures

Starter cultures are the crucial first step in numerous downstream protocols, e.g., plasmid extraction and protein expression. Prepared in a sterile laminar flow cabinet, 10 mL of freshly autoclaved 2x YT media (Materials 2.1.3) was aliquoted into a sterile 25 mL universal tube, and the appropriate selective antibiotic(s) were added to their respective working concentrations (Table 2.3). A fresh colony was picked from the LB agar plate and expelled into media to inoculate it. The culture was then sealed and left to grow overnight at 37°C and 200 rpm.

2.4.2 Expression of AzF protein variants

To incorporate nnAA AzF into proteins, a dual-vector expression system was required. The first plasmid contained the mutated gene of interest with the TAG amber stop codon, and the second (pDULE-cyanoRS) carried the engineered tRNA / aminoacyl tRNA synthetase pair to facilitate AzF incorporation (Materials 2.1.7). A cell line was established through dual transformation of both plasmids (Methods 2.3.8) and successful colony growth on a double selection LB agar plate (Table 2.3). A single colony was then taken forward to set up a starter culture (Methods 2.4.1).

2.4.2.1 BLIP-II

BLIP-II^{AzF} variants were produced using the vectors pET-24a (BLIP-II) and pDULE-cyanoRS (Table 2.6) using *E. coli* BL21 cells. A 10 mL starter culture was used to inoculate 1 L of 2x YT media supplemented with kanamycin and tetracycline (Table 2.3) and incubated at 37°C and 200 rpm. Once an OD_{600} of 0.6 was reached, the growth flask was covered in foil and moved to the dark room. AzF was solubilised (Materials 2.1.8) and both IPTG and AzF was added to a final concentration of 1 mM. The culture was then incubated at 22°C for 16 hours. The next day, cells were pelleted at 5000 rpm and 5°C for 20 minutes in the Fiberlite^{TM} F9-6 x 1000 LEX rotor, with care being taken to not expose the cells to any light. The supernatant was removed, and the pellet resuspended in 30 mL of Tris buffer, before lysis by sonication to extract the expressed protein (Methods 2.4.4.2).

2.4.2.2 sfGFP

sfGFP^{AzF} variants were produced using the vectors pBAD and pDULE-cyanoRS (Table 2.6) using *E.coli* TOP10 cells. A 10 mL starter culture was used to inoculate 1 L of autoinduction media supplemented with carbenicillin and tetracycline (Table 2.3) and incubated at 37°C and 200 rpm. After 90 minutes of incubation, the growth flask was covered in foil and moved to the dark room. AzF was solubilised (Materials 2.1.8) and AzF was added to a final concentration of 1 mM. The culture was then incubated at 37°C for 16 hours. The next day, cells were pelleted at 5000 rpm and 5°C for 20 minutes in the Fiberlite^{TM} F9-6 x 1000 LEX rotor, with care being taken to not expose the cells to any light. The supernatant was removed, and the pellet resuspended in 30 mL of Tris buffer, before lysis by French press to extract the expressed protein (Methods 2.4.4.3).

2.4.3 Expression of β-lactamases

The β-lactamases are expressed into the periplasmic space but follow a similar protocol to that of the AzF variants. Differences become apparent in the downstream processes, where lysis and purification methodologies vary.

2.4.3.1 TEM-1

TEM-1 uses the vector pET-24a (TEM-I) to facilitate expression (Table 2.6) in *E.coli* BL21 cells. A 10 mL starter culture was used to inoculate 1 L of 2x YT media supplemented with kanamycin (Table 2.3) and incubated at 37°C and 200 rpm. Once an OD_{600} of 0.6 was reached, IPTG was added to a final concentration of 1 mM. The culture was then incubated at 22°C for 16 hours. The next day, cells were pelleted at 5000 rpm and 5°C for 20 minutes in the Fiberlite™ F9-6 x 1000 LEX rotor, and the supernatant removed. The pellet then underwent periplasmic extraction to carefully extract the protein, without lysing the whole cells (Methods 2.4.4.4).

2.4.3.2 KPC-2

KPC-2 uses the vector pTP123 to facilitate expression (Table 2.6) in *E.coli* BL21 cells. A 10 mL starter culture was used to inoculate 1 L of 2x YT media, and following protocol set by Mehta et al. (2015), the working concentration of chloramphenicol was reduced to 12.5 µg mL^{-1}. The culture was incubated at 37°C and 200 rpm, and once an OD_{600} of 0.6 was reached, IPTG was added to a final concentration of 1 mM. The culture was then incubated at 22°C for 16 hours. The next day, cells were pelleted at 5000 rpm and 5°C for 20 minutes in the Fiberlite™ F9-6 x 1000 LEX rotor, and the supernatant removed. The pellet then underwent periplasmic extraction to carefully extract the protein, without lysing the whole cells (Methods 2.4.4.4).

2.4.4 Cell lysis

There were numerous lysis techniques used to extract the proteins from the whole cell, or from specific cellular compartments. The methods chosen were based on the protein itself and culture volume.

2.4.4.1 BugBuster

Before protein was expressed on a large scale, 10 mL starter cultures would often be put through expression testing to identify the optimum conditions. In this

instance, BugBuster was chosen as the whole cell lysis technique, with the protocol as follows.

An aliquot (1 mL) was taken from culture before and after 3 hours of expression. The OD_{600} was read for both samples, and the volume of the post-expression sample was adjusted to ensure the cell density was equivalent to that of the pre-expression sample. The samples were then pelleted by centrifugation at 13000 rpm for 1 minute. Next, 100 µL of BugBuster was added and the cells were resuspended through pipetting. After leaving to incubate for 5 minutes at room temperature, the cells were centrifuged for 3 minutes at 13000 rpm.

The resulting mixture would resemble clear supernatant (the soluble fraction) atop a small white pellet (the insoluble fraction). The supernatant was removed and stored in a new tube, whilst 100 µL of Tris buffer (Table 2.2) was added to the insoluble fraction to resuspend the pellet. Both fractions were then taken forward for SDS-PAGE analysis.

2.4.4.2 Sonication

Sonication was the whole cell lysis technique chosen to purify BLIP-II^{AzF} variants. Under dark conditions, the resuspended cell pellet was emptied into a 50 mL beaker placed into an ice box and covered with foil. The probe sonicator was sterilised with 70 % ethanol, and the glass window covered with foil to stop light entering. The ice box was then placed in the sonicator (Sonics VCX 750), and the height adjusted until the probe was fully submerged but not touching the bottom of the beaker. The door was closed and the sonicator switched on for 30 sonication cycles of 10 seconds on at 225 W and 20 seconds off. Once complete, the ice box was re-covered with foil and the probe cleaned with 70 % ethanol. The lysed cells were then decanted into a centrifuge tube and spun at 4 °C and 25000 rpm for 1 hour in the Fiberlite^{TM} F21-8 x 50y rotor, with the supernatant generated containing the soluble BLIP-II^{AzF} proteins ready for purification.

2.4.4.3 French press

The French press was the whole cell lysis technique chosen to purify sfGFP^{AzF} proteins, as the yield with sonication was shown to be poor. Under dark conditions, the resuspended cell pellet was poured into the chilled French pressure cell and the piston fitted. The cell was mounted into the Aminco press, and pressure applied up

to 1250 psi. The lysed cells were collected in a foil-covered centrifuge tube and spun at 4°C and 25000 rpm for 1 hour in the Fiberlite™ F21-8 x 50y rotor, with the supernatant generated containing the soluble sfGFP^{AzF} proteins ready for purification.

2.4.4.4 Periplasmic extraction

Periplasmic extraction is an outer membrane lysis technique and was used to purify β-lactamase proteins from the periplasmic space. In brief, the cell pellet from inoculated culture was resuspended in 30 mL periplasmic extraction buffer (Table 2.2) and stirred slowly at room temperature for 10 minutes. The cells were then re-pelleted by centrifugation at 10000 x g at 4°C for 10 minutes, in the Fiberlite™ F21-8 x 50y rotor. Supernatant was discarded, and the cells resuspended in 30 mL chilled magnesium sulphate solution, being stirred slowly over ice for 10 minutes to release the periplasmic proteins. Next, the centrifugation step was repeated again, with the supernatant generated containing the soluble periplasmic proteins. This was then mixed in equal volumes with Tris buffer to prepare for column binding.

2.4.5 Protein purification

To purify protein from the lysed cell / membrane mixture, different purification columns were used to exploit the protein's physical and chemical properties. Flowgen HiFlow Nickel-NTA FPLC 5mL columns were used for nickel affinity chromatography, while the Cytiva Resource Q column and HiLoad™ 16/600Superdex™ S75 pg column were used for ion exchange and size exclusion chromatography, respectively. All columns were used with either an ÄKTA Prime Plus or ÄKTA Purifier FPLC system.

2.4.5.1 Nickel affinity chromatography

Nickel affinity chromatography was chosen to purify proteins with engineered 6X His tags at their N-terminus (e.g., BLIP-II) or C-terminus (e.g., sfGFP). The principle behind this technique uses coordination bonds formed between the immobilised nickel ions in the column matrix and the electron donor groups of histidine's imidazole ring (Bornhorst and Falke 2000), to anchor the proteins. Washing steps

follow to remove the unbound protein, while competitor compound imidazole is finally loaded onto the column to elute the His-tagged protein.

To describe the method in detail, the HiFlow Nickel-NTA column was first equilibrated through a run of 25 mL deionised water and 25 mL Ni affinity wash buffer (Table 2.2). The soluble supernatant obtained from cell lysis was then loaded onto the column at a flow rate of 1 mL min^{-1}. Wash buffer continued to flow while the absorbance was monitored at 280 nm for BLIP-II and 485 nm for sfGFP. When the absorbance returned back to baseline (typically ~40 mL after loading the sample), elution could begin.

Ni affinity elution buffer (Table 2.2) was run from a 0 – 100 % gradient over 30 mL, and the absorbance closely monitored to observe the anticipated peak from His-tagged proteins. Fractionation into 1.8 mL volumes began when the absorbance trace started to rise and ended when the trace hit baseline. For the AzF variants, monitoring was switched off as soon as a slight increase in absorbance was observed to prevent premature photolysis, and fractionation started and continued until the elution buffer hit 100 %. After the protein was eluted, the AKTA continued to pump 100 % elution buffer for 5 minutes clean the column, before switching back to a 25 mL water wash and 25 mL 20 % ethanol wash for storage purposes.

2.4.5.2 Ion exchange chromatography

Ion exchange chromatography was chosen to purify the proteins lacking an affinity tag, e.g., TEM-1 and KPC-2. The principle behind this technique is the use of environmental pH to control the ionisation of protein functional groups and thus their overall net charge. This is then exploited to trap a population of charged proteins in a matrix of oppositely charged resin, before eluting with an increasing salt gradient. In the case of the Resource Q anion exchange column, the stationary phase consisted of positively charged ammonium groups, so proteins had to be negatively charged to bind. The first stage of the protocol thus required the isoelectric point to be calculated (Methods 2.2.4), to ensure the Tris buffer was at least 0.5 pH units above pI to deprotonate the protein.

To begin the ion exchange protocol, the column was equilibrated with 30 mL dH$_2$O and 30 mL Tris buffer. Next, the periplasmic supernatant (mixed 50:50 with Tris buffer) was loaded on at a speed of 1 mL min^{-1}, with absorbance being monitored at 280 nm. At this stage, flow through was collected to ensure any protein failing to bind was caught. After absorbance returned to baseline, ion exchange elution buffer

(Table 2.2) could then be run from a gradient of 0 – 100 % over 30 mL, with fractionation in 1.8 mL volumes starting as soon as increase in absorbance was observed. Once the gradient had completed, the AKTA was washed sequentially in 30 mL dH$_2$O and 30 mL 20 % ethanol for storage purposes.

2.4.5.3 Size exclusion chromatography

Size exclusion chromatography was chosen as the follow up purification technique to nickel affinity and ion exchange, as not only did it help to remove contaminant proteins, but it simultaneously buffer exchanged out the excess salts. The principle behind this technique uses a protein's hydrodynamic volume to dictate the speed at which it can elute through a porous beaded matrix. Small proteins can access the total column volume by diffusing into the pores, while larger proteins are excluded and eluted in the column's void volume. The elution volume is thus specific to each protein and allows the careful separation into distinct fractions.

The HiLoad™ 16/600Superdex™ S75 pg column was the column of choice for all proteins purified, as they had a similar molecular weight range of 27 kDa – 32 kDa. To begin the protocol, the column was first washed with 120 mL dH$_2$O followed by 120 mL Tris buffer. Meanwhile, the protein sample to load was concentrated in a 10 kDa molecular weight cut off column (Fisher Scientific) at 4000 rpm, until the total protein volume reached 1 mL. Once the column was equilibrated, the protein sample was loaded and run at 1 mL min^{-1}, with absorbance being monitored at 280 nm, or 485 nm for sfGFP. All visible absorbance peaks were fractionated in 1.8 mL volumes and analysed by SDS-PAGE. Crucially, for the AzF variants, the wild type proteins were run first to identify the elution volume. This allowed UV monitoring to be switched off for their purification, and fractionation to occur around the estimated volume. Once all protein had been collected, the column was switched back to dH$_2$O for a 120 mL wash, followed by 20 % ethanol for a 120 mL wash and storage.

2.4.6 Protein analysis

2.4.6.1 Sodium dodecyl sulphate polyacrylamide gel electrophoresis (SDS-PAGE)

SDS-PAGE analysis was performed after protein expression trials, purification, and modification, to analyse any changes in protein composition. Based on LaemmLi's approach (LaemmLi 1970), protein samples were treated with SDS to coat

polypeptides with a negative charge, while β-mercaptoethanol and heat were applied to denature the proteins. Samples were then loaded into polyacrylamide gels to undergo electrophoresis. This resulted in protein being separated by molecular mass and produced a band pattern to be analysed.

To begin the SDS-PAGE protocol, 12.5 % resolving gels were produced in 5 mL volumes (Table 2.11) and poured into the 0.75 mm glass plate mould, topped with 500 μL isopropanol to burst any bubbles and flatten the gel. Once set, the isopropanol was drained off and 2.5 mL of stacking gel (Table 2.11) poured on, with a 10 or 15-well comb inserted. Meanwhile, the protein samples were mixed with the 5X SDS-PAGE loading buffer and heated at 98 °C for 5 minutes. Once the gel was set, the comb was removed, and the gel sealed in a cassette with a dummy plate. The cassette was then placed in the mini-PROTEAN 3 Cell (Bio-Rad) and submerged in SDS-PAGE running buffer.

BLUeye Pre-Stained Protein Ladder was loaded in the first well of each gel at a volume of 2 μL. Protein samples were then loaded into the others, at a volume of 5 μL for highly concentrated protein mixtures, or 10 μL for lesser concentrated. Gels were run at 200 V for 50 minutes, before being placed into 50 mL Coomassie stain buffer. The gel was heated in the microwave for 30 seconds and then left to incubate on a rocker for 10 minutes. The Coomassie stain was removed, and the gel rinsed in dH$_2$O. Finally, the gel was placed in 50 mL Coomassie destain buffer, sealed to prevent evaporation and left overnight on the rocker.

To record images, the gel was placed on a white tile and photos were taken with both my phone camera and the GelDoc-It, using the white light setting.

Table 2.11 – Composition of SDS-PAGE resolving and stacking gels. For the resolving gel, 1.5 M Tris-HCl pH 8.8 was used; for the stacking, 0.5 M Tris-HCl pH 6.8 was used.

Material	Resolving gel (12.5 %)	Stacking gel
dH$_2$O (v/v)	42.2 %	73.8 %
Acrylamide: Bis-Acrylamide (v/v)	31.3 %	13.0 %

Tris-HCl (v/v)	24.8 %	10.0 %
SDS (v/v)	1.0 %	2.0 %
APS (v/v)	0.5 %	1.0 %
TEMED (v/v)	0.2 %	0.2 %

2.4.6.2 Protein quantification: Bio-Rad DC assay

Once fractions had been collected from size exclusion chromatography and analysed with SDS-PAGE, the purest were pooled (and in some cases, further concentrated) before protein quantification. The Bio-Rad DC assay was used for proteins without a known molar extinction coefficient. This is a colorimetric assay which uses the reaction of amino acids (most notably tyrosine and tryptophan) to alkaline DC Protein Assay Reagent A, to reduce Cu^{2+} ions. Consequently, when mixed with DC Protein Assay Reagent B, Cu^+ reduces the Folin reagent which generates a spectrally detectable species proportional to the concentration of protein.

To describe the protocol in brief, a bovine serum albumin (BSA) standard curve was first prepared at five concentrations between 0.2 – 1.5 mg mL^{-1}. Protein standards or samples (20 µL) were combined with 100 µL of Reagent A in a disposable cuvette. Reagent B (800 µL) was then added to each cuvette and mixed by pipetting. The cuvettes were placed on a rocker and left to incubate for 15 minutes. Finally, absorbance was read at 750 nm on the Cary 60 spectrophotometer (Agilent) with a 1 cm pathlength, and the protein concentration of the standards plotted against absorbance to generate a standard curve. If the unknown protein sample had a concentration above the curve, the necessary dilution was performed, and experiment repeated.

2.4.6.3 Absorption spectroscopy

The Cary 60 spectrophotometer (Agilent) was used to record all absorption readings and UV-visible spectra in 1 cm pathlength cuvettes. Absorption readings were taken for cell density and DC assays in disposable cuvettes (Fisher Scientific). Spectral readings were taken for sfGFP in quartz cuvettes (Hellma), recording from 250 –

700 nm at a rate of 300 nm min^{-1}. Absorption spectroscopy also allowed protein concentration to be calculated for wild type sfGFP and its AzF variants if their molar extinction coefficient was known (Table 2.12). This was calculated using the Beer-Lambert law (Equation 2.5).

Table 2.12 – Molar extinction coefficients. Values used for protein concentration calculation at λ_{485}.

Protein variant	Molar extinction coefficient (M^{-1} cm^{-1})	Reference
sfGFP WT	49,000	(Reddington et al. 2013b)
sfGFP^{132AzF}	45,000	(Reddington et al. 2012)
sfGFP^{204AzF}	55,000	(Reddington et al. 2012)

2.4.6.4 Fluorescence spectroscopy

The Varian Cary Eclipse fluorescence spectrophotometer (Agilent) was used to record fluorescence spectra for wild type sfGFP and its AzF variants. Samples were placed in 101.057-QS quartz cuvettes (Hellma), pathlength 5 mm x 5 mm. Using a scan rate of 1200 nm min^{-1} and slit width of 5 nm, emission spectra were collected at 2 nm data intervals between 400-600 nm. A fixed wavelength was used to excite the sfGFP samples, namely 445, 470 or 590 nm.

2.4.6.5 Detection of AzF incorporation by Click Chemistry

To confirm whether AzF had been successfully incorporated into the protein and that the reactivity was still intact, DBCO-Cy3 was used in a strain-promoted azide-alkyne cycloaddition (SPAAC) reaction. Under dark conditions, 10 µM of purified protein in Tris buffer was mixed with a fivefold molar excess of DBCO-Cy3. The tube was then wrapped with foil and incubated on a rotation mixer for 1 hour at room temperature. Next, the samples were analysed via SDS-PAGE (Methods 2.4.6.1).

Before Coomassie staining could take place, the gel was imaged in the GelDoc-It under UV light. The fluorescent bands observed constituted dye-labelled protein,

while the excess dye can be seen further down the gel. Upon analysis by ImageJ (Abràmoff et al. 2004), the intensity ratio between these two bands allowed the concentration of clicked dye to be determined. The Coomassie stained protein band could then be compared with the fluorescent protein band to determine a Click efficiency.

2.4.7 Construction and analysis of protein functionalised NT-FETs

2.4.7.1 Fabrication of NT-FET devices (QMUL)

NT-FET devices were kindly prepared by collaborators at Queen Mary University London (QMUL; Dr. Mark Freeley and Dr. Chang-Seuk Lee) and the full methodology for device fabrication can be found here (Xu et al. 2018b).

To summarise briefly, device fabrication began with 400 nm of SiO_2 being grown onto a p-doped silicon wafer to form the base substrate. A combination of laser and electron beam lithography were used to apply a predesigned electrode pattern (Figure 2.1), followed by electron beam evaporation to apply a 5 nm adhesive layer of chromium and a 40 nm layer of gold. The devices were 10 mm x 10 mm in size and consisted of 2 sets of 8 electrodes, paired with a reference electrode and separated by a 300 nm gap. To connect the device to a voltage supply and electrical monitoring equipment (via the PS-100 probe station, Lakeshore), one contact pad was supplied per electrode pair, with the reference electrode on the reciprocal side.
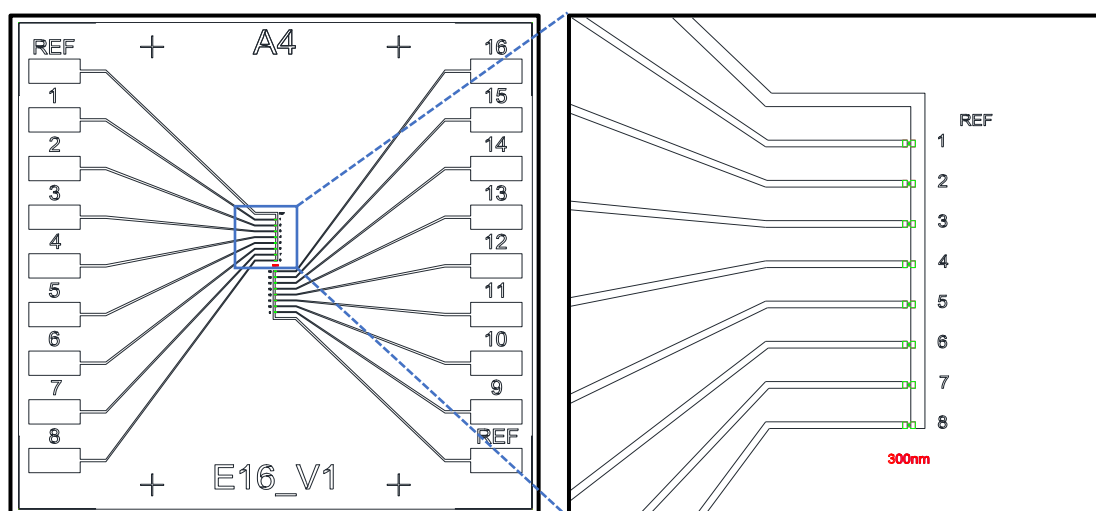
Figure 2.1 – NT-FET device (QMUL) electrode pattern. There are two sets of 8 electrodes (1-8 and 9-16) which are paired with the reference (REF) electrode. Each

electrode has a contact pad for electrical interfacing. Between the pairs, a 300 nm gap (highlighted in green) exists as the site for SWCNT dielectrophoresis.

To complete NT-FET assembly, the 300 nm gap between electrode pairs were bridged with the pre-prepared SWCNT solution (Figure 2.2), via a process of dielectrophoresis. Here, 5 µL of SWCNT solution was cast onto the device and probes were connected to a contact pad and reference electrode. An alternating current voltage was then applied between the electrodes (V_{p-p} = 2 V, frequency = 400 kHz) for 15 seconds. This created a nonuniform magnetic field to induce partial dipoles along the SWCNT fragments, with the established dielectrophoretic force pulling the SWCNTs down to the electrodes to bridge them (Tian et al. 2009). To confirm the successful deposition of SWCNTs, current voltage (I/V) characteristics were recorded via the semiconductor parameter analyser in a -1 – 1 V bias sweep before and after dielectrophoresis (Methods 2.4.7.6). AFM analysis (Methods 2.4.7.5) was then used to visually confirm the presence of SWCNTs and the quality of the junction.
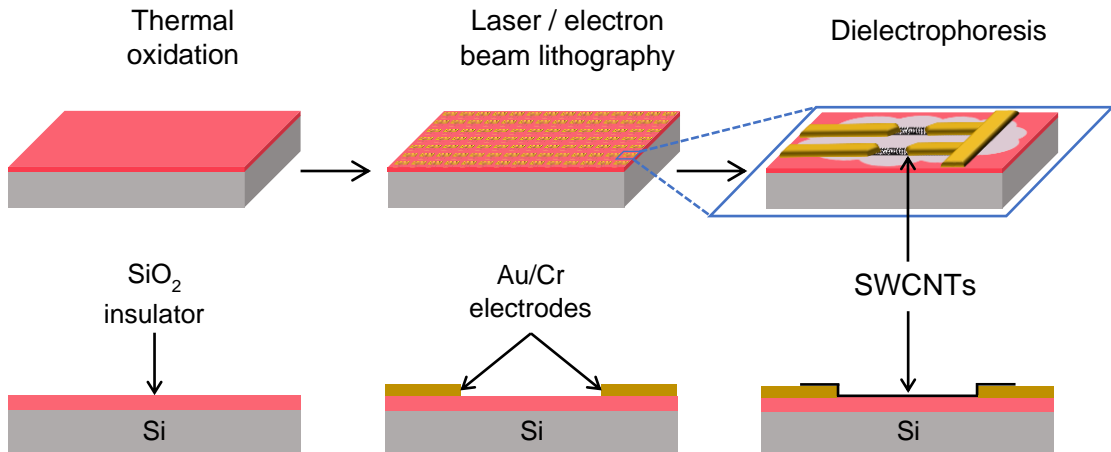
Figure 2.2 – Schematic diagram of NT-FET device (QMUL) fabrication. The base substrate is formed by thermal oxidation of the silicon wafer. A combination of laser and electron beam lithography then applied the predesigned electrode pattern, followed by casting of SWCNT solution and dielectrophoresis to bridge the electrodes with SWCNTs.

2.4.7.2 Fabrication of NT-FET devices (MIET)

NT-FET devices were kindly prepared by collaborators at the Moscow Institute of Electronic Technology (MIET; Nikita Nekrasov and Aleksei Emelianov), and the full methodology for device fabrication can be found here (Emelianov et al. 2021).

To describe in brief, a p-doped silicon wafer was thermally oxidised to grow a thin 300 nm layer of SiO_2 and form the base substrate. Thermal decomposition of ferrocene in the presence of carbon monoxide then triggered the growth and deposition of SWCNTs by gas-phase formation onto the cold silicon wafer. This process lasted only 15 seconds to ensure low density of SWCNT growth, averaging ~1 nanotube per 10 μm^2. Source and drain 100/15 nm Au/Ti electrodes and contact pads were then applied through a photolithographic lift-off process, with an interelectrode distance of 12 µm established (Figure 2.3). Femtosecond laser processing ensured only one SWCNT bridged the gap, while laser scribing isolated the individual devices. Finally, chips were cut to size around the perimeter of three devices and treated with acetone boiling and 250°C vacuum heating to eliminate any organic residuals or photoresist. To characterise the devices, I/V curves were recorded in a -0.5 – 0.5 V bias sweep before and after dielectrophoresis. AFM analysis then confirmed the successful deposition of a SWCNT across the junction (Figure 2.4).
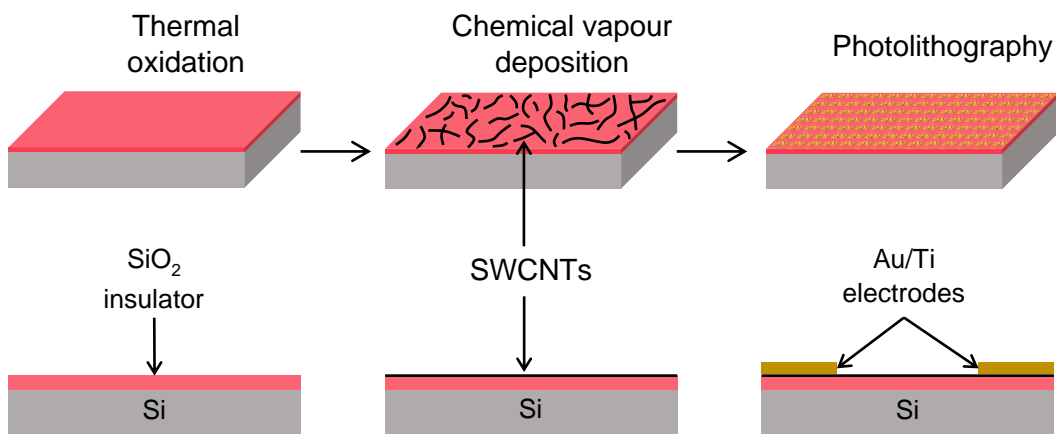
Figure 2.3 – Schematic diagram of NT-FET device (MIET) fabrication. The base substrate is formed by thermal oxidation of the silicon wafer. SWCNTs are then deposited via thermal decomposition of ferrocene, followed by photolithography to apply source and drain electrodes.

83
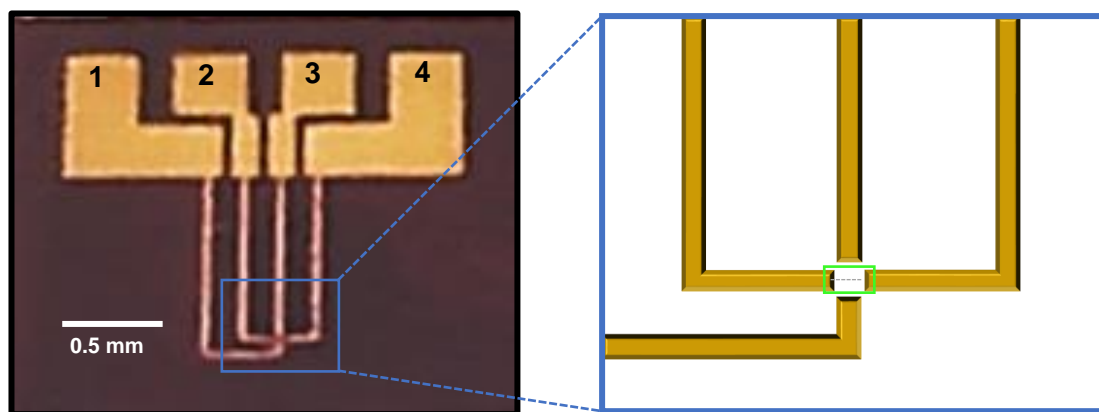
Figure 2.4 – Image of NT-FET device (MIET) and electrode junction schematic.
Each device comprised of four electrodes, with their respective contact pads
labelled 1-4. Of these electrodes, only two (2 and 4) were bridged by a SWCNT
across the 12 μm channel (highlighted in green).

2.4.7.3 UV photo-attachment of proteins to SWCNTs (QMUL)

The apparatus for photolysis was set up as shown in Figure 2.5. To ensure uniform
distance of the NT-FET from the 302 nm UV lamp (Analytik Jena), the chip was
placed on top of a lidded 6-well plate sandwiched between two Eppendorf racks,
with the UV lamp balanced across. This left a gap of approximately 5 mm between
the UV lamp and the chip. An argon flow was then fixed to the 6-well plate, with flow
directed at the chip, to minimise UV-light enhanced oxygen adsorption to the
SWCNTs (Muckley et al. 2016).

To begin the functionalisation protocol, 25 μL of 1 μM BLIP-II^{AzF} variants was drop
cast onto the centre of the chip under dark conditions. The UV lamp was then
switched on for 5 minutes of irradiation. Once complete, the chip was rinsed
thoroughly under a jet of 500 mL dH$_2$O to remove any unbound protein and then
dried under the argon flow.
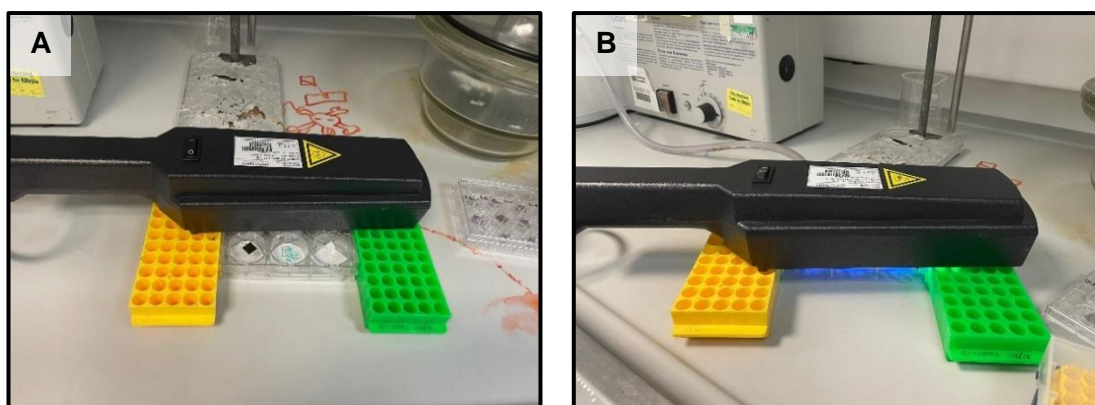
Figure 2.5 – Apparatus setup for NT-FET functionalisation. (A) The chip is placed on top of a lidded 6-well plate, while sandwiched between two Eppendorf racks. **(B)** An argon flow is affixed to the side of the 6-well plate and UV lamp switched on to induce photolysis.

2.4.7.4 UV photo-attachment of proteins to SWCNTs (MIET)

To attach protein to the chips sent by MIET, an initial sterilisation took place to remove any impurities that may have accumulated during transportation. The chips were thus soaked in ethanol for 1 hour, followed by a 60 second rinse under deionised water and dried under a nitrogen flow.

Meanwhile, the photolysis apparatus was set up. An airtight lockbox with a nitrogen source and drain was placed inside a purpose-built glovebox. A 305 nm light emitting diode (LED; intensity 18 W m^{-2}) was affixed to the roof of the lockbox and a stage was mounted beneath to hold the chip. Once all experimental components were placed inside the box, gloves were attached to the holes of the glovebox and the nitrogen flow was switched on (Figure 2.6). Humidity was reduced to 10 % before the nitrogen flow was slowed and hands could slowly be placed inside the glovebox to close the lid of the lockbox. When humidity reached 1 %, the lockbox was reopened to drop cast 25 µl of 100 nM sfGFP^{AzF} variant onto the centre of the chip. The lockbox was then reclosed, and the LED switched on for 5 minutes of irradiation. Once complete, the LED was switched off and rinsed thoroughly under a jet of 500 mL dH$_2$O to remove any unbound protein and dried under the nitrogen flow.
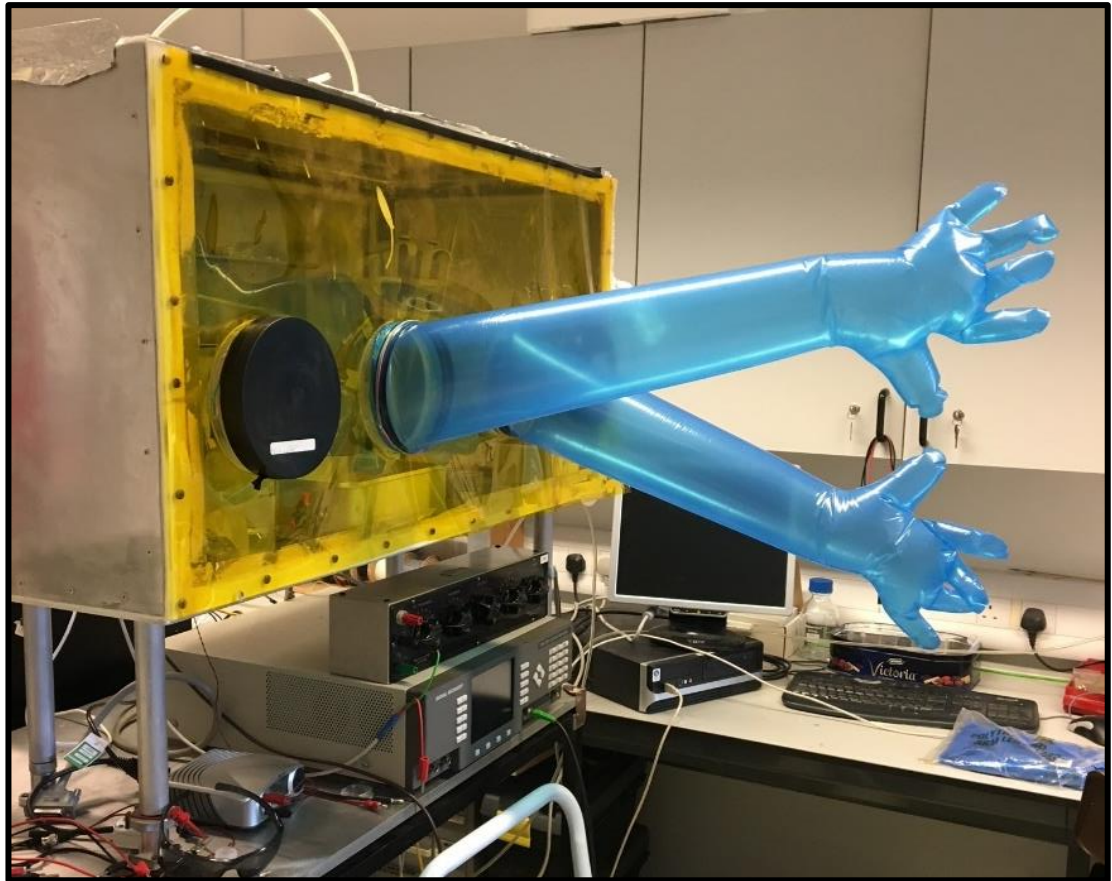
Figure 2.6 – Glovebox for protein attachment. Transparent yellow sheeting
minimises the ambient and UV light from passing through, while nitrogen gas floods
the chamber to displace the oxygen.

2.4.7.5 Atomic force microscopy

To analyse the fabrication of protein-functionalised NT-FET devices, atomic force
microscopy (AFM) was carried out. AFM works to produce a topographical image of
a 3D surface using the reflection of a laser from a sharp-tipped cantilever as it raster
scans across the sample. The cantilever bends in response to the tip contacting the
surface and this is detected by the photodiode (Figure 2.7).
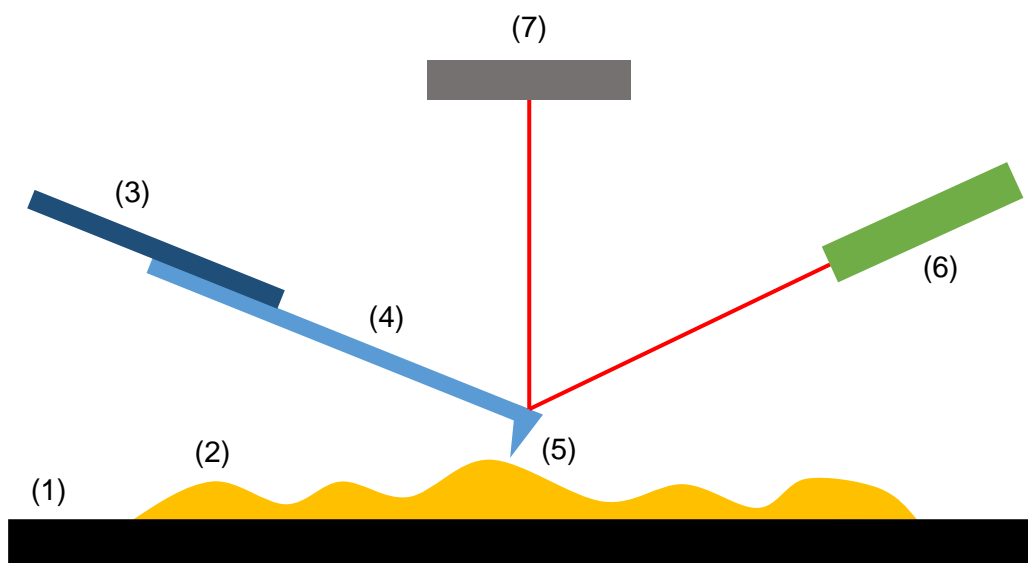
Figure 2.7 – AFM schematic. The stage (1) holds the sample / chip (2), while the piezo (3) oscillates the cantilever (4) tip (5). The deflection of the tip as it moves across the surface is monitored by the reflection of the laser beam (6) from the cantilever onto the photodiode detector (7).

The AFM systems used were a Bruker Dimension Icon AFM at QMUL (Figure 2.8) and a NT-MDT Solver Pro AFM at MIET. Samples were measured using tapping mode in air and under ambient conditions. The probe (tip) attached to the cantilever differed between the AFMs, with a ScanAsyst silicon nitride probe used with the Bruker and a pure silicon ScanSens probe used with the NT-MDT. The probes had a spring constant of 0.4 N m^{-1} and 3.5 N m^{-1}, respectively. Quick 2 Hz scans would initially be performed over a 10 µm^2 scan area to identify an NT-FET junction, before zooming in to ~ 1.5 µm^2 and slowing the scan rate to 1 Hz per line, with a set point of 0.03 V.

AFM measurements were taken after dielectrophoresis, after BLIP-II^{AzF} / sfGFP^{AzF} functionalisation, and in the case of the sensing experiments, after β-lactamase binding. The appearance of new globular objects or an increase in height after functionalisation was taken as a successful attachment of protein. A large increase in height was not expected following β-lactamase addition due to the anticipated lateral binding. Analysis took place with NanoScope Analysis software (Bruker Corporation 2015), with images flattened, cropped (if necessary) and sections taken to extrapolate the height profiles of proteins on and along the SWCNT. Using Origin

(OriginLab Corporation 2022), average height profiles were then built and compared to observe the height difference after protein addition.
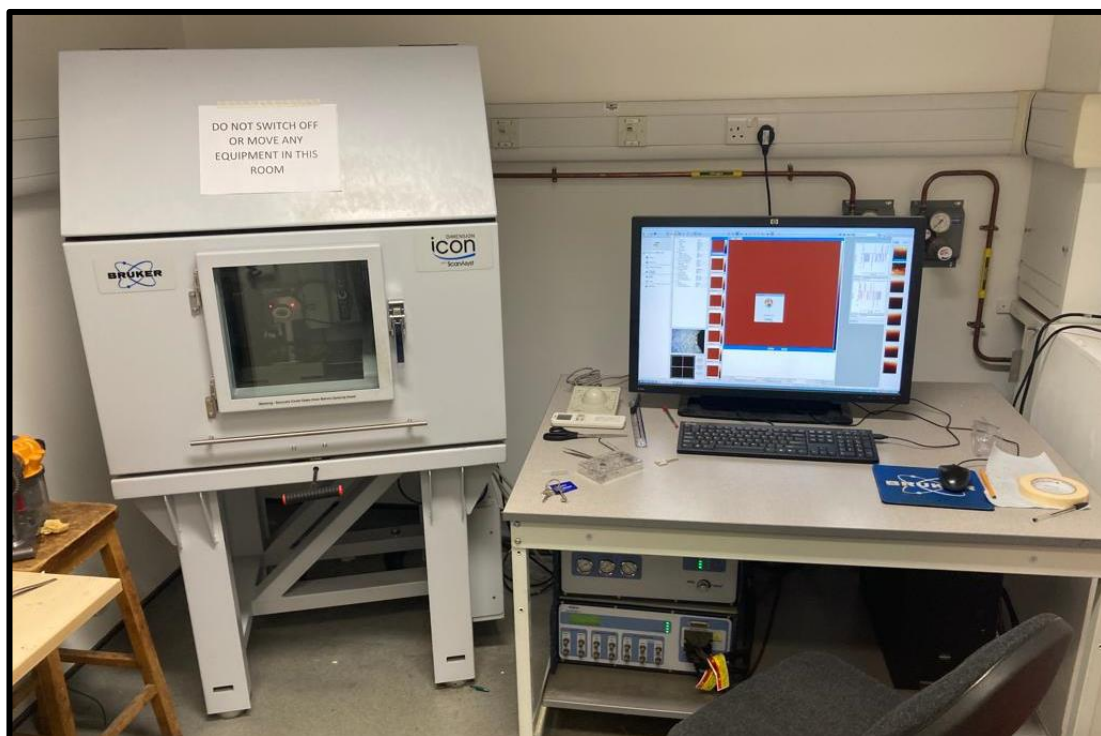
Figure 2.8 – Bruker Dimension Icon AFM. The AFM (left) is sat within an acoustic hood on an air table, to minimise the effect of environmental vibrations. This connects to the adjacent computer, where the AFM is controlled, and samples are visualised.

2.4.7.6 Electrical measurements

Electrical measurements were performed at QMUL using a PS-100 probe station (Lakeshore) connected to a 4200-SCS semiconductor parameter analyser (Keithley). At MIET, measurements were recorded with a homemade probe station connected to a semiconductor parameter analyser (IPPP 1/5, MNIPI).

For the I/V characteristics, the NT-FET chips were placed in the probe station chamber (Figure 2.9), with the source probe connected to an individual electrode contact pad and the drain probe to the common reference electrode. The source probe was set to bias sweeping mode (-1 V to 1 V for QMUL, -0.5 to 0.5 V for MIET) at a step of 0.05 V, while the drain probe and silicon gate electrode were grounded. The I/V characteristics were recorded at room temperature before dielectrophoresis,

after dielectrophoresis, after protein functionalisation, and after incremental β-lactamase additions. For the β-lactamase sensing experiment, the electrical setup was kept the same, while 10 μL of DPBS buffer was pipetted onto the NT-FET chip and left for 100 s. I/Vs were recorded in a -1 V to 1 V bias sweep and this baseline reading would be normalised to for all the following readings. 10 μl of analyte was added every 100 s, mixed by pipetting and a 10 μl volume removed. After the 100 s, I/Vs were recorded and the next analyte addition could take place. This process took place with eight incremental concentrations of DPBS doped with β-lactamase: 2, 10, 20, 100, 400, 700, 1000 and 2000 nM. The experiment concluded after waiting 100 s from the final analyte addition, and recording the final I/V.

For the real-time sensing experiments, the source and drain probe were connected as above. A fixed voltage of 0.1 V was applied to the source, while the reference and gate electrode were grounded. The analyser was then set to record current as a function of time. To initiate the experiment, 10 μL of DPBS buffer was pipetted onto the NT-FET chip and left for 100 s for the baseline to settle. To ensure the volume of buffer / analyte remained the same throughout the analyte additions, analyte was added in a 10 μL volume every 100 s (or 200 s if the current was unsettled), mixed by pipetting and then a 10 μL volume was removed. This process took place with eight incremental concentrations of DPBS doped with β-lactamase: 2, 10, 20, 100, 400, 700, 1000 and 2000 nM. The experiment concluded after waiting 100 s from the final analyte addition. Results were plotted in Origin (OriginLab Corporation 2022).

For the illumination experiments, a small patch of SiO_2 was scratched off to allow a third probe to connect to the underlying gate electrode. Here, a negative $V_{GS} \leq -10$ V was applied so the device could reach V_T and thus its operational state in the p-type region; opening the FET channel and allowing current to flow from the source to drain electrodes. V_{DS} was set to 1 V. Irradiation of the sfGFP-modified SWCNT transistors took place with 445, 470 and 590 nm light emitting diodes (LEDs) mounted on a fixed holder. LED intensity and time intervals varied with individual experiments. LEDs were switched off to allow device recovery, but in situations of no observable recovery in the dark, a gate voltage sweep from -15 to 15 V was employed to reset the device.
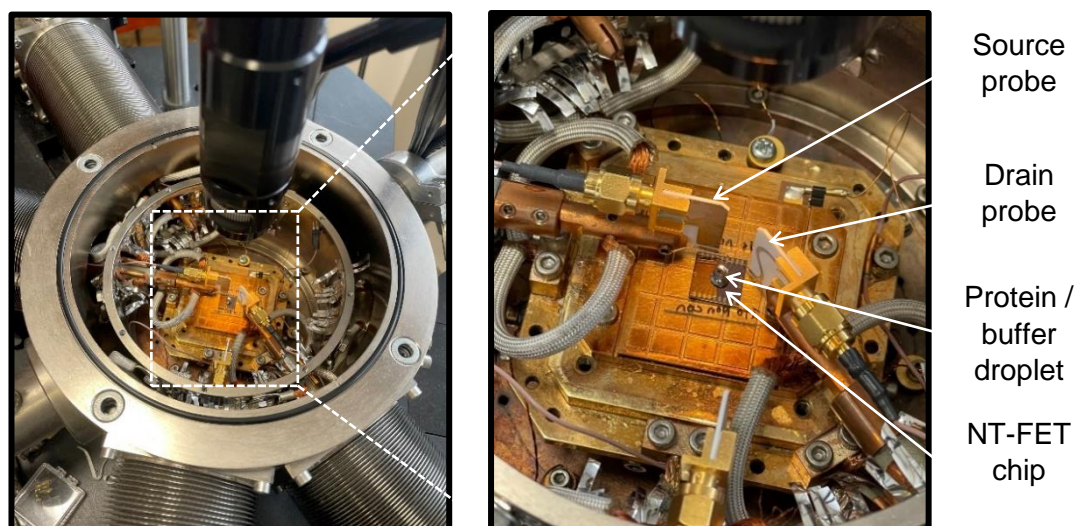
Figure 2.9 – Probe station setup. In real-time sensing experiments, the source probe is connected to the individual electrode, and the drain to the reference. The protein / buffer droplet is pipetted onto the electrode junctions at the centre of the NT-FET chip.

2.4.7.7 Raman spectroscopy

Raman spectra were carried out on micro-Raman spectrometer Centaur HR (Nanoscan Technology). The SWCNTs across the NT-FET were characterised before and after sfGFP functionalisation, using a ×100 objective at 532 nm (Cobolt), a beam spot of ~1 μm^2 and laser power of 1 mW.

3. Building a biosensor: Covalent integration of BLIP-II^{AzF} into a NT-FET device for β-lactamase sensing

Work in this chapter contributed to a published, peer-reviewed paper where I am joint 1st author. With permission from the publisher, figures have been taken and adapted for my thesis.

Thomas, S., Jamieson, W., **Gwyther, R.**, Bowen, B., Beachey, A., Worthy, H., Macdonald, J., Elliott, M., Castell, O. and Jones, D., 2020. Site-Specific Protein Photochemical Covalent Attachment to Carbon Nanotube Side Walls and Its Electronic Impact on Single Molecule Function. *Bioconjugate Chemistry*, 31(3), pp.584-594.

Statement of work

Work in this chapter was performed in collaboration with the Palma lab at QMUL. I collected all the data shown except the AFM and electrical measurements of the NT-FETs, which required the specialist assistance of Dr. Mark Freeley or Dr. Chang-Seuk Lee. All data presented in this chapter has been plotted and analysed by me.

3.1 Introduction

The rise of antibiotic resistance (ABR) is one of the greatest threats to modern day society. Misuse and overuse of mainstream antibiotics has applied a selective pressure to bacteria, encouraging their evolution into novel resistant strains (Bell and MacLean 2018). One source of this is blind antibiotic prescription, where patients are prescribed an antibiotic without diagnosing (i) if the infection is bacterial, or (ii) if the infection is harbouring ABR. In these scenarios, conventional diagnostic testing is seen as a tedious and time-consuming process, taking up to 60 hours for bacterial culturing and phenotypic testing (Mayrhofer et al. 2008; Burnham et al. 2017). If rapid, point-of-care diagnostic tools could be developed to replace these practises, then the accuracy of antibiotic prescriptions would improve significantly; buying crucial time for research and development into alternative antibiotic therapies.

In the context of ABR, carbon nanotube-based field-effect transistors (NT-FETs) offer the perfect platform for the development of rapid diagnostic tools. These electrical sensing devices are solid-state, miniaturised and label-free (Luo and Davis

2013; Sadighbayan et al. 2020), comprising of a receptor and transducer in an electrical circuit. The receptor is typically a biomolecule (e.g. DNA or protein) which takes on the molecular recognition role. The transducer is a semiconducting material which connects the receptor to the circuit, and converts biomolecular events (e.g. protein binding) into a measurable electrical signal. Single-walled carbon nanotubes (SWCNTs) are well-suited for this role, being compatible in size to biomolecules, having multiple functionalisation routes for biomolecule interfacing, and semiconducting at specific chiralities (Dresselhaus et al. 1995; Jariwala et al. 2013). Their success in a wide range of biosensing FET applications has shown they are prime candidates for use in my FET (Allen et al. 2007; Deng et al. 2022).

For my NT-FET to effectively detect ABR, the receptor element – and its target analyte – is crucial to its function. ABR operates through a variety of mechanisms, and as such, there is no ubiquitous marker to target. The NT-FET will therefore focus on the most common marker: the β-lactamase. This enzyme family has arisen in response to the most prescribed antibiotic class, the β-lactams (Dolk et al. 2018). Subdivided into different classes, class A β-lactamases are the most abundant (Philippon et al. 2016) and thus would have a large influence clinically if targeted by my NT-FET receptor. As such, two of the most prevalent enzymes in this class: TEM-1 and KPC-2, have been produced recombinantly as analytes for my NT-FET (Eiamphungporn et al. 2018). To find a receptor capable of binding to these proteins, competitive bacterial evolution has yielded several natural inhibitor proteins. One of these, β-lactamase inhibitor protein-II (BLIP-II), demonstrates picomolar affinity to a diverse range of class A β-lactamases (Brown and Palzkill 2010) and would be the perfect bait in my NT-FET setup, offering rapid and selective binding.

In order to attach my receptor protein to the transduction material, either BLIP-II or the SWCNTs must undergo a functionalisation process to introduce the novel chemistry required to facilitate an interaction between the two species. My joint 1st author peer-reviewed review with Dr. Chang-Seuk Lee goes into great detail on the methodologies available (Lee et al. 2022), with the non-natural amino acid (nnAA) p-azido-L-phenylalanine (AzF) chosen for my NT-FET approach. The approach works by incorporating AzF into a recombinant protein at designed residue positions through an expanded genetic code and utilising the inherent photochemistry of the phenyl azide group (Introduction 1.4.3.2; Chin et al. 2002; Reddington et al. 2013b). UV irradiation generates a nitrene radical from the phenyl azide to facilitate an electrophilic attack on electron-rich surfaces via a [2+1] cycloaddition; a process

shown to work with an alternative allotrope of carbon, graphene (Freeley et al. 2017; Zaki et al. 2018). The key benefit of this approach is that I can define protein attachment. By systematic design, I tether the protein through a single mutation site that ensures the analyte binding-site is accessible, that an incoming analyte wouldn't sterically clash with the SWCNTs and that the analyte will be in close enough proximity to influence the conductance of the SWCNT. This design ensures consistent analyte sampling, a marked departure from early biosensing FETs which used random receptor interfacing via lysine/arginine residues (Figure 3.1; Huang et al. 2002). Hoping to build from the latest results in the Jones and Palma collaboration (Xu et al. 2021), AzF will be used in BLIP-II to test covalent functionalisation of the SWCNTs. Extensive covalent functionalisation (e.g., by chemical oxidation) is known to damage inherent electrical conductance, but a valuable study by Setaro et al. (2017), highlighted the potential for azide-mediated [2+1] cycloaddition mechanisms to preserve the sp^2 electronic network upon SWCNT functionalisation. Through restricted covalent functionalisation events, AzF will facilitate intimate binding between BLIP-II and the SWCNTs without damaging the electrical integrity, and will mediate analyte binding proximal to the SWCNT surface.
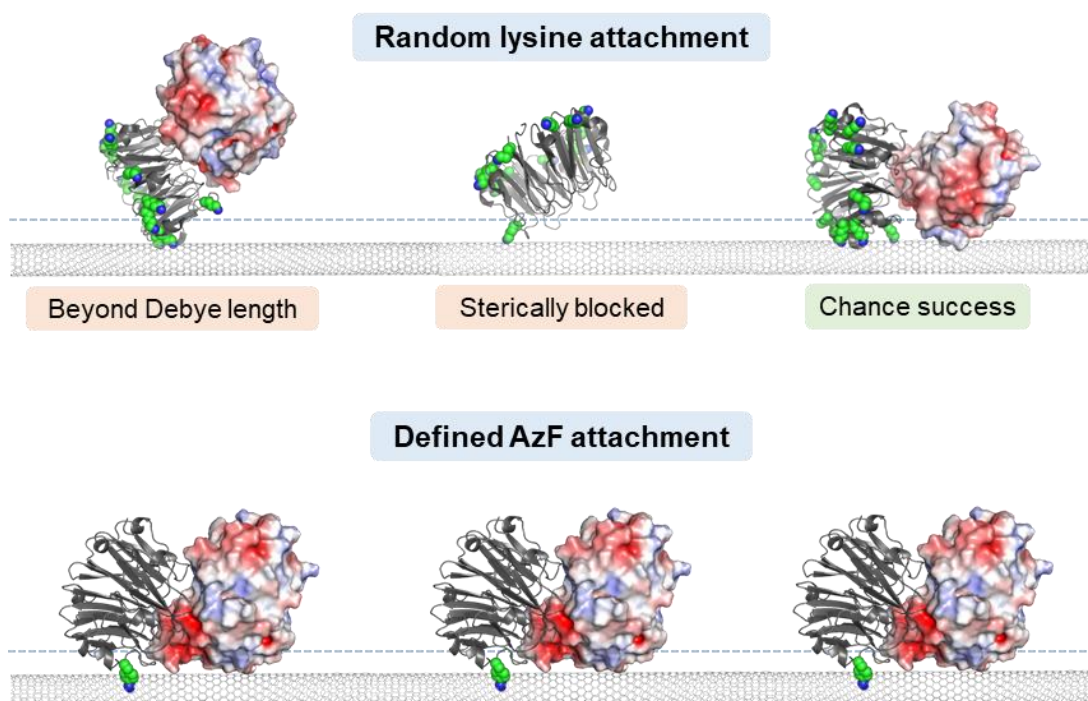
Figure 3.1 – Random vs defined protein-SWCNT interfacing approaches.
Random lysine attachment can lead to no signal being produced if the receptor protein (grey) binds unfavourably. Defined receptor attachment through a singular

AzF residue ensures regular analyte binding (multi colour) with consistent signal transduction.

The type of signal transduced upon receptor-analyte interaction is dependent on the analyte itself. Proteins can impart a gating effect across the semiconducting SWCNT channel and change the charge carrier population within it, by their own uniquely charged surface potential. The electrostatic distribution varies by a protein's tertiary structure and charged amino acid population, conferring distinct electrostatic 'signatures' to individual analytes. For protein-protein binding events to be effectively transduced, however, the electrostatic surface potential (ESP) must come within one Debye length (Introduction 1.3.3; Stern et al. 2007). This is a parameter which describes the screening ability of ions in an aqueous solution to counter the surface charge of a biomolecule, and dictates from the buffer in my NT-FET setup that a biomolecule must come within 0.7 nm of the SWCNTs to induce a gating effect (Israelachvili 1991; Xu et al. 2021). Once it comes within this distance, the net electrostatic charge can either increase or decrease current, depending on the n- or p-type nature of the semiconducting channel. My NT-FET device utilises p-type SWCNTs, which use positively charged holes as the majority charge carrier. Here, a positive gate voltage will deplete the charge carrier population and reduce conductance (Figure 3.2), while a negative gate voltage causes an accumulation of charge carriers and will increase conductance (Lee et al. 2009). When testing my NT-FET against specific β-lactamase analytes, I will study the change in conductance to try and establish the gating mechanisms at play.

Positive electrostatic surface potential

Negative electrostatic surface potential
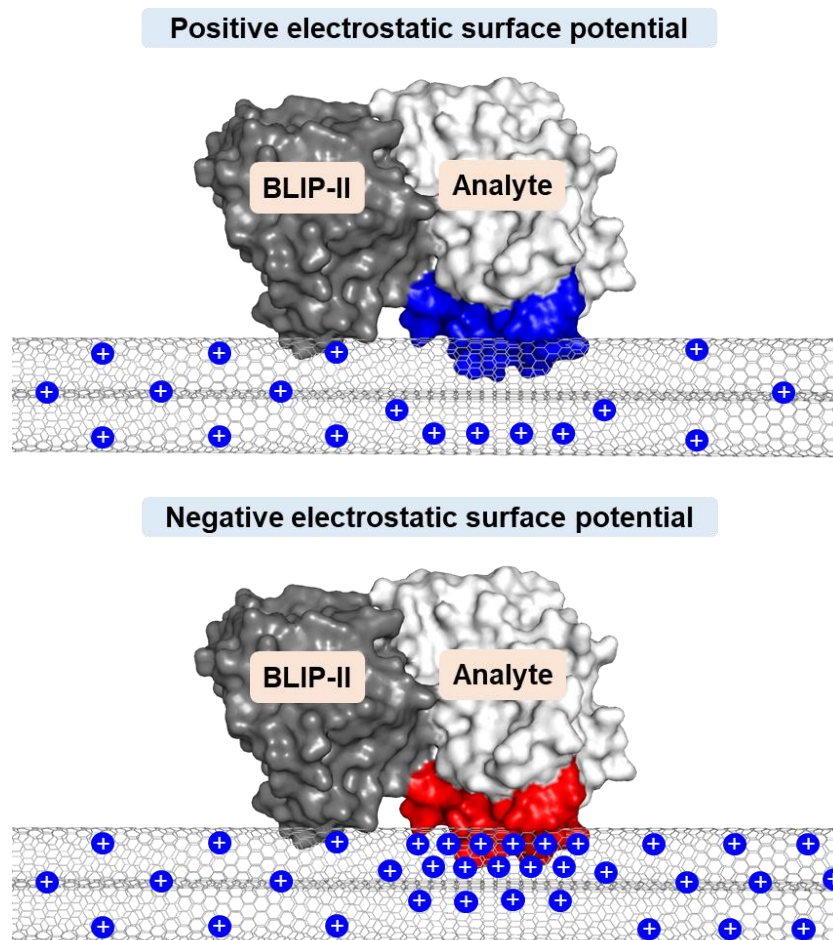
Figure 3.2 – Schematic diagram of p-type SWCNTs influenced by a gating voltage. Incoming positive electrostatic potential (blue) depletes holes at the SWCNT surface, reducing current flow. Meanwhile, incoming negative electrostatic potential (red) causes an accumulation of holes, increasing current flow.

This chapter aimed to further develop the NT-FETs produced by the Jones and Palma collaboration (Xu et al. 2021) by testing new methodologies. In my approach, I designed new BLIP-II^{AzF} variants to functionalise the NT-FETs via UV-induced covalent attachment. Experiments into the impact of covalent functionalisation revealed the [2+1] cycloaddition of BLIP-II^{AzF} to the SWCNTs defied the dogma and boosted electrical conductance across the NT-FETs, possibly through a gating mechanism. The defined attachment position of BLIP-II, as mediated by AzF, then ensured the receptors were acting in unison to provide a clear and consistent electronic signal upon analyte binding. Tested against prevalent β-lactamases: TEM-1 and KPC-2, the BLIP-II variants showed that signal strength depended on the location of the AzF mutation, and that electrical conductance varied with the type of β-lactamase present. Finally, in silico modelling was performed to identify

potential electrostatic surface potential on incoming β-lactamases that could be inducing a gating voltage.

3.2 Results and Discussion

3.2.1 *In silico* design of BLIP-II^{AzF} variants

To construct a highly sensitive NT-FET, the receptor element (BLIP-II) must be interfaced in a precise manner, with the β-lactamase binding site unobstructed and near the SWCNT surface. Ultimately, the location of the protein anchor (AzF) will dictate this, so *in silico* modelling was performed with BLIP-II to identify potential mutation sites. Surface-exposed residues were prioritised over buried residues to minimise any possible conformational change as a result of the AzF substitution, and to reduce the risk of steric clash between BLIP-II and SWCNT. An array of potential mutation sites was selected, and Figure 3.3 highlights these as yellow spheres. Here, A41, G49 and T213 were chosen to continue on from previous research, with AzF substitutions at A41 and T213 shown to mediate electrostatic gating from TEM-1 with our non-covalently BLIP-II^{AzF} functionalised NT-FET (Xu et al. 2021). G49 was designed as a control protein, with AzF substituted in at the β-lactamase binding interface. This would prevent BLIP-II from binding a β-lactamase when integrated into the NT-FET. Six further residues (T135, A138, T174, N198, G210 and E217) were then selected after *in silico* rotation of the BLIP-II—TEM-1 complex. Parallel alignment of BLIP-II—TEM-1 to the SWCNT highlighted the fundamental differences in height between the two proteins (~4 nm vs ~5 nm; Figure 3.3), so AzF mutations were introduced along the flattest part of the BLIP-II—TEM-1 axis to reduce the chance of steric obstruction.
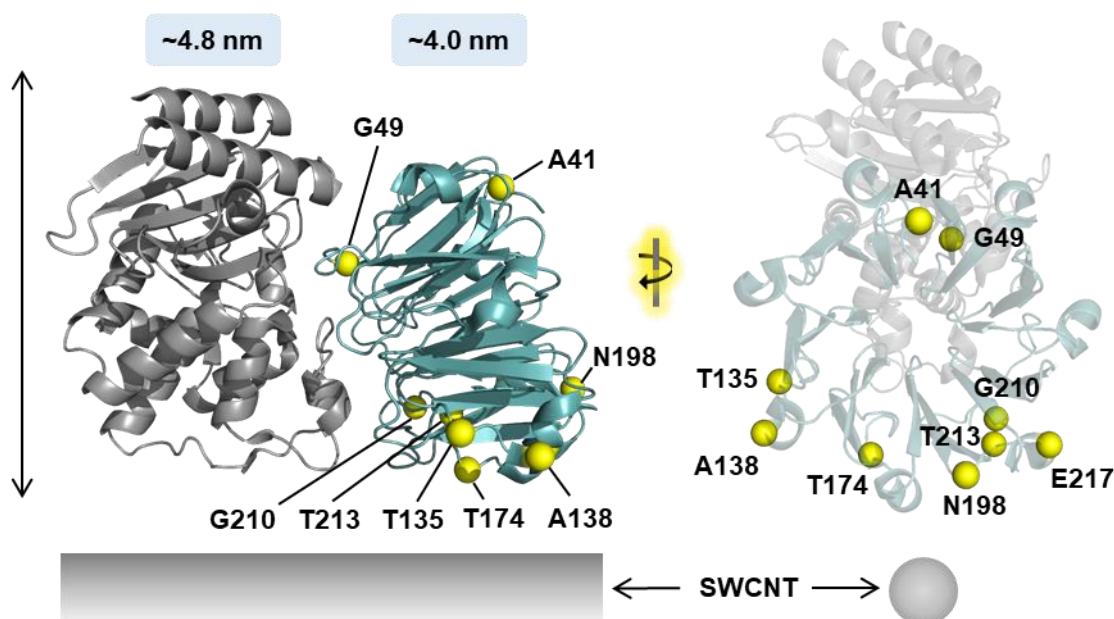
Figure 3.3 – BLIP-II^AzF variants. BLIP-II (blue) interfaced with TEM-1 (grey). Yellow spheres indicate AzF mutation sites. Sites were chosen to be surface exposed, with the β-lactamase binding site parallel to the SWCNT.

3.2.2 Site-directed mutagenesis to introduce the TAG mutation

To provide BLIP-II with the functionality to covalently bind SWCNTs, AzF was incorporated into BLIP-II using an expanded genetic code (Chin et al. 2002; Reddington et al. 2013b). Here, the amber stop codon (TAG) is repurposed to code for AzF, while the complementary translational machinery is transformed into the cell line before recombinant protein expression (Introduction 1.4.3.1; Miyake-Stoner et al. 2010). The BLIP-II gene was optimised for the repurposed amber stop codon with the terminal codon encoded as TAA rather than TAG. Plasmids encoding the TAG codon at A41, G49 and T213 had already been prepared by Dr. Ben Bowen, but new primers were designed to introduce the TAG codon mutations at gene positions equivalent to T135, A138, T174, N198, G210 and E217. A range of annealing temperatures were then tested (62°C, 65°C and 68°C) to maximise the chance of whole plasmid inverse PCR working. Successful plasmid amplification was observed for all variants, as illustrated by the fluorescent bands at ~6 kb on the agarose gel (Figure 3.4). T174 showed the weakest amplification, with only a faint band at 65°C, so several PCR runs were needed to generate sufficient DNA for ligation. N198 was another notable variant, requiring new primers to be designed

after failing the first round of PCR. These primers were more successful, as evidenced by the strong fluorescent band at ~6kb.
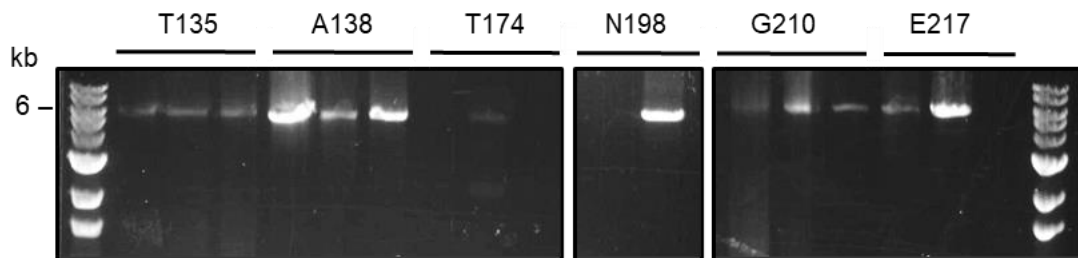
Figure 3.4 – Site-directed mutagenesis of wild type BLIP-II to introduce TAG mutations. Different annealing temperatures were tested for each variant, and bands at 6 kb represent successful amplification of the pET-24a plasmid. Gels were 1 % w/v agarose and had 10µl samples loaded.

Following site-directed mutagenesis PCR, the products were purified, phosphorylated, ligated and eventually transformed into *E. coli* BL21 (DE3) competent cells. Colony PCR was then performed to check the cloning process, using primers which flanked the gene insertion site (Figure 3.5). The presence of a full length gene encoding BLIP-II would produce a band of ~1.1 kb, so colonies 1, 2 and 5 were taken forward from T135, while only colony 4 was taken forward from A138. Band sizes greater than 1.1 kb would suggest an unidentified DNA fragment was present, while some colonies failed to produce any bands at all, suggesting the BLIP-II gene or flanking primer sequences weren't present. These colonies were abandoned. Successful colonies were cultured overnight and underwent plasmid extraction for sequencing. Four of the six variants had TAG successfully incorporated: T135, A138, N198 and E217.
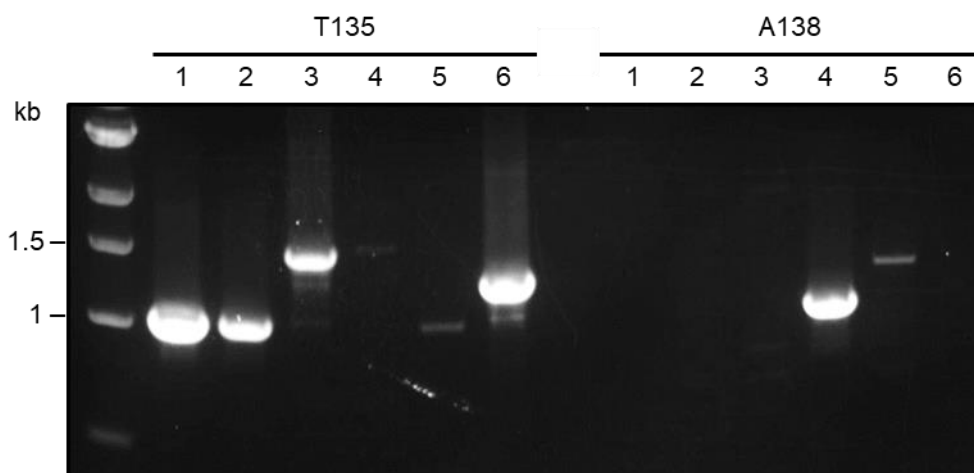
Figure 3.5 – Colony PCR of transformed BLIP-II TAG (pET-24a) plasmids.
Colonies were picked to test gene insertion success using T7 primers flanking the gene insertion site. Following amplification, bands appearing ~1.1 kb in size had their colony taken forward for plasmid miniprepping and sequencing.

3.2.3 BLIP-II^{AzF}: Expression, functionality testing and purification

Once the BLIP-II TAG plasmids (pET-24a) had been verified through sequencing, *E. coli* BL21 (DE3) cells were co-transformed with pET-24a and pDULE-cyanoRS (Miyake-Stoner et al. 2010). The latter plasmid encoded the AzF translational machinery essential for nnAA incorporation (Introduction 1.4.3.1). Six out of the nine total BLIP-II^{AzF} variants were successfully co-transformed for recombinant protein expression (BLIP-II^{41AzF}, BLIP-II^{135AzF}, BLIP-II^{138AzF}, BLIP-II^{198AzF}, BLIP-II^{213AzF}, BLIP-II^{217AzF}). As identical methodologies were followed for all BLIP-II^{AzF} variants, a general discussion of expression, functionality testing and purification will be considered below, with specific BLIP-II^{AzF} variants identified from the representative figures and graphs.

Transformed colonies of pET-24a and pDULE-cyanoRS were used to inoculate 2 L flasks of liquid broth, with the appropriate selective antibiotics added. When optical density reached 0.6 AU, AzF and IPTG were added, and the culture was left to grow in dark conditions overnight. The following day, a 1 mL sample was fractionated by the detergent BugBuster, and the soluble supernatant tested for BLIP-II^{AzF} functionality using a nitrocefin assay (Figure 3.6). Nitrocefin is a substrate of TEM-1 β-lactamase and is pale yellow in colour, turning red when hydrolysed. If BLIP-II^{AzF} was present in the soluble supernatant, it would inhibit TEM-1 and prevent a colour change from yellow to red. All six BLIP-II^{AzF} variants (BLIP-II^{41AzF}, BLIP-II^{135AzF}, BLIP-

II^{138AzF}, BLIP-II^{198AzF}, BLIP-II^{213AzF}, BLIP-II^{217AzF}) had their inhibitory functionality confirmed through a nitrocefin assay with TEM-1, with no observable colour change from yellow to red.
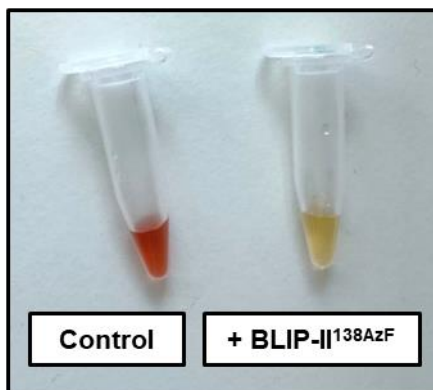
Figure 3.6 – Colourimetric nitrocefin assay. TEM-1 β-lactamase (1 µM) was mixed with soluble cell supernatant of BLIP-II^{138AzF} (or 20 mM Tris for the negative control) and incubated for 30 minutes. Nitrocefin (10 µM) was then added, and the image taken after 30 minutes.

Following the colourimetric verification of BLIP-II^{AzF}'s presence and functionality, the whole culture was sonicated, and fractionated into soluble and insoluble fractions by centrifugation. The soluble supernatant was then taken forwards for the first purification step: Ni affinity chromatography. BLIP-II^{AzF} has a His tag at its N-terminus which allows it to coordinate to the Ni ions embedded in the chromatography matrix. Figure 3.7 (A) shows the elution profile of BLIP^{138AzF} during this process, monitoring the absorbance at 280 nm. A large peak between 0 – 30 mL represents the flow through, with the other soluble proteins failing to stick to the column. Once the absorbance dropped back to zero, a gradient of Ni affinity elution buffer (Table 2.2) was applied. At this stage, UV monitoring was switched off to prevent premature AzF photolysis and all fractions were collected between 65 – 85 mL. As a known error of our AKTA purifier, this reports the UV trace to be at its maximum absorption limit (6 AU) rather than its minimum (0 AU), as highlighted in yellow in Figure 3.7 (A). All fractions were then analysed by SDS-PAGE (Figure 3.7 (B)) to identify those containing BLIP-II^{138AzF}. The flow through lane shows a mix of protein bands, while the adjacent elution fractions are dominated by a band ~ 30 kD. BLIP-II^{138AzF} was matched to this band as its molecular mass was calculated to be ~ 28.5 kD (Walker et al. 2005). This process was repeated for the five remaining

BLIP-II^{AzF} variants, each of them showing near identical elution profiles and protein band sizes from SDS-PAGE.
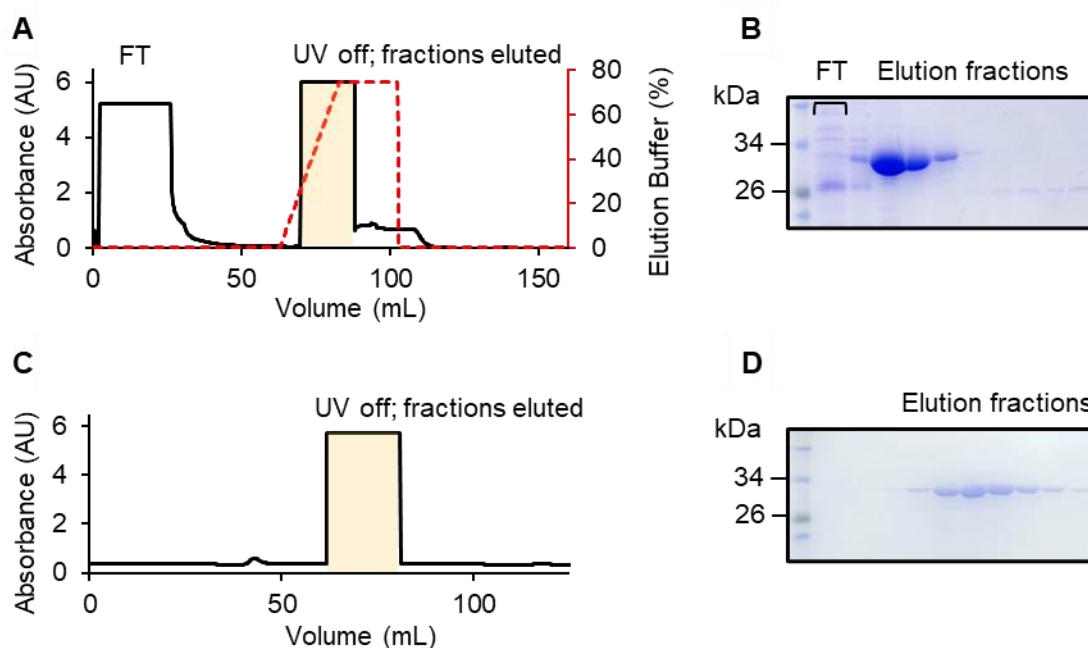
Figure 3.7 – Purification of BLIP-II^{135AzF}. Soluble cell lysate was injected onto a Ni-NTA column and treated sequentially with Ni affinity wash and Ni affinity elution buffer (Table 2.2), with any flow through (FT) collected. Absorbance was monitored at 280 nm (A), and as soon as the absorbance started to increase, the UV was switched off and fractions were collected. 10 µl samples were then loaded on a gel and analysed by SDS-PAGE (B). Once fractions containing BLIP-II^{135AzF} were identified, they were concentrated and run on the SEC column (C). Fractions collected from SEC were analysed by SDS-PAGE and BLIP-II^{135AzF} was seen as clean, purified band at ~30 kDa (D).

To remove protein impurities and buffer exchange the BLIP-II^{AzF} protein into Tris buffer (Table 2.2), the fractions containing BLIP-II^{AzF} were taken forward for a second purification step using the Superdex 75 size exclusion chromatography (SEC) column. Fractions were pooled and concentrated to 1 mL, before loading onto the SEC column. The UV was switched off when an increase in 280 nm was detected (~ 65 mL), and fractions were collected blindly (Figure 3.7 (C)). SDS-PAGE analysis revealed high purity protein bands from the SEC fractions, suitable for downstream photochemical attachment to SWCNTs (Figure 3.7 (D)). Pooling and concentrating the fractions to a volume of ~1 mL achieved a yield of 0.93 mg

mL^{-1} for BLIP-II^{135AzF}, with a yield range of 0.66 – 1.76 mg mL^{-1} across the other five BLIP-II^{AzF} variants. Aliquots were then prepared at 10 μM and 1 μM, and flash frozen in liquid nitrogen for long term storage at -80°C.

To test AzF reactivity in the BLIP-II^{AzF} variants, a click chemistry assay was performed with the fluorescent DBCO-Cy3 dye. This was an important test of the purification process to assess whether photolysis had occurred from any ambient light exposure. Incubating BLIP-II^{AzF} in a 1:5 ratio with DBCO-Cy3 allowed the excess strained alkyne group of DBCO to react with any available azide group and form a protein—dye complex. Separation with SDS-PAGE and gel irradiation with UV revealed a fluorescent signal for each protein band (Figure 3.8 (A)). Fluorescence intensity was non-uniform across the BLIP-II^{AzF} variants despite the same concentration of BLIP-II^{AzF} being mixed with DBCO-Cy3. This observation appears counterintuitive as all variants were designed to be surface exposed, and thus more accessible for DBCO-Cy3 conjugation. However, previous research from our lab identified the charged microenvironment local to the AzF residue to be a contributing factor towards labelling efficiency (Reddington et al. 2012). Conformational freedom has further input, with the direction of side chain protrusion dictated by the backbone dihedral angles. This could favour the AzF side chain to face internally (Dunbrack and Cohen 1997). Alternatively, its possible protein samples were exposed to some visible light during the purification process, reducing the yield of unreacted AzF.

The efficiency of BLIP-II^{AzF} conjugation to DBCO-Cy3 can be compared across the variants. BLIP-II^{213AzF} had the highest fluorescence intensity of all variants (Figure 3.8 (A)), but its total protein band (Figure 3.8 (B)) was shown to be greater. Originally measured from a different standard curve, BLIP-II^{213AzF} was rechecked and clarified to be at 18 μM. This was corrected going forward, and the relative fluorescent intensities were plotted per μM in (Figure 3.8 (C)). Here, BLIP-II^{41AzF} was shown to have the highest fluorescent intensity at 1 AU μM^{-1}, whilst BLIP-II^{198AzF} and BLIP-II^{135AzF} had the lowest, 0.22 AU μM^{-1} and 0.25 AU μM^{-1}, respectively. It is important to note that the difference in click efficiency is not indicative of photochemical efficiency as they are two different reactions.
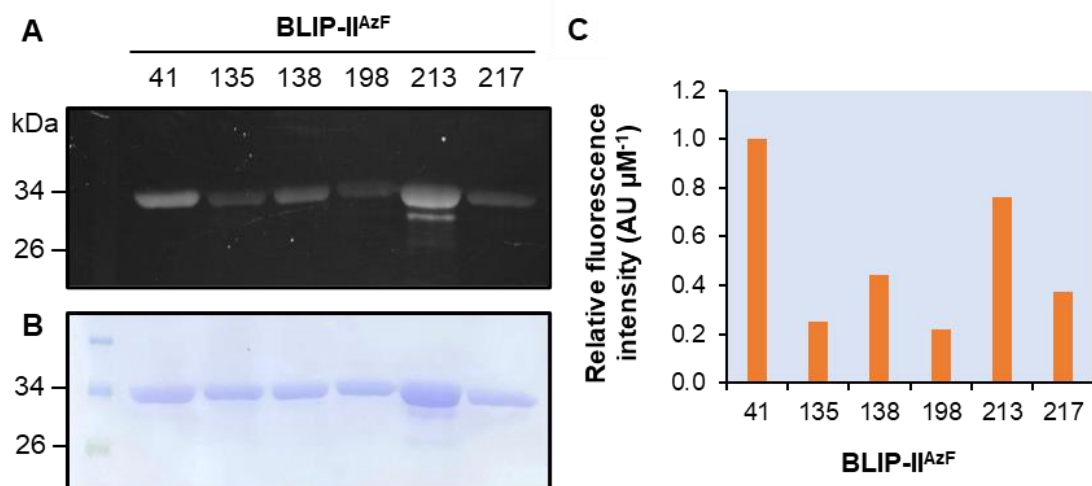
Figure 3.8 – Testing AzF reactivity in BLIP-II^AzF variants with DBCO-Cy3 assay.
(A) UV irradiated polyacrylamide gel. 10 µM samples of BLIP-II[41AzF], BLIP-II[135AzF], BLIP-II[138AzF], BLIP-II[198AzF], BLIP-II[213AzF] and BLIP-II[217AzF] were incubated in 50 µM DBCO-Cy3 for 1 hour, and 20µl samples were then analysed with SDS-PAGE. The gel was irradiated with UV and the image captured after a 13 second exposure. (B) Coomassie stain of the polyacrylamide gel, displaying the total protein loaded. (C) Relative fluorescent band intensity. ImageJ analysis generates a histogram from the distribution of grey pixels in each gel lane, the area of each peak was normalised to the highest intensity variant per µM (BLIP-II[41AzF]) and plotted in a bar graph.

3.2.4 β-lactamase: Expression, functionality testing and purification

To produce analytes for ABR sensing experiments, two β-lactamases were chosen for expression: TEM-1 and KPC-2. Both of these enzymes use an N-terminal Sec signal sequences for translocation and folding in the periplasmic space (Kaderabkova et al. 2022). Isolation of these enzymes from the periplasm therefore required an adapted purification protocol. As near-identical methodologies were followed for TEM-1 and KPC-2, a general discussion of β-lactamase expression, functionality testing, and purification will be considered below. Specific differences will be highlighted, and the β-lactamase variants identified from the representative figures and graphs.

A small-scale expression trial for β-lactamase was performed prior to a scaled expression. Here, pre-expression samples were fractionated into whole cell soluble and whole cell insoluble fractions, and post-expression samples underwent periplasmic extraction, followed by separation of the cytoplasm into soluble and insoluble fractions (Figure 3.9 (A)). The most significant change from the pre- to

post-expression samples was the presence of an intense band at ~28 kD in the periplasmic fraction, highlighted by the arrow. This fitted with the predicted molecular mass of KPC-2 (27.5 kDa), and a similar band was observed for TEM-1 (28.5 kDa; Walker et al. 2005). β-lactamase functionality was then tested using a nitrocefin assay without BLIP-II (Figure 3.9 (B)). Here, KPC-2's β-lactamase activity was confirmed through immediate nitrocefin hydrolysis to its red product. TEM-1 showed identical functionality.
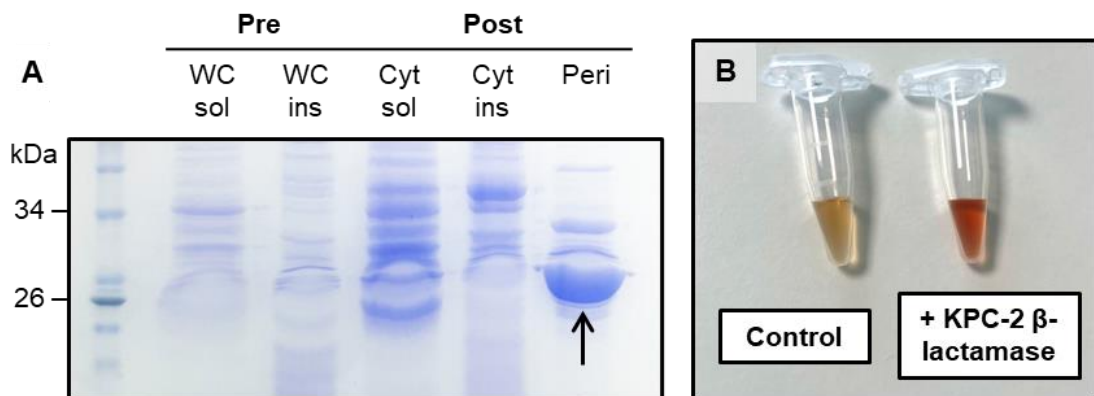
Figure 3.9 – KPC-2 β-lactamase expression test. A small-scale culture of *E. coli* BL21 cells expressing KPC-2 was grown to 0.6 OD, before IPTG induced expression for 3 hours at 22°C. 1 mL samples were taken pre and post induction, with the OD adjusted to match. Pre-induction samples were lysed using BugBuster and fractionated into whole cell (WC) soluble and insoluble fractions. Periplasmic proteins were then extracted from the post-induction sample, while BugBuster separated the remaining cell pellet into cytosolic (Cyt) soluble and insoluble fractions. SDS-PAGE analysis (A) showed a clear expression band (see arrow) at ~28 kDa in the periplasmic fraction. The nitrocefin assay (B) then proved KPC-2 β-lactamase activity, by instantly hydrolysing nitrocefin to its red coloured product.

With the periplasmic extraction protocol optimised, 2 L cultures were inoculated with *E.coli* BL21 cells transformed with the relevant β-lactamase plasmid. Expression was induced at 0.6 OD with IPTG, and the temperature lowered to a more favourable protein folding temperature (22 °C). The periplasm was extracted the following day and taken forward for a two-stage purification process. Both TEM-1 and KPC-2 lacked an affinity tag, so ion exchange was first used as a method for removing contaminating proteins. The isoelectric point for each protein was calculated as 5.46 and 6.98, respectively, so anion exchange was deemed a

suitable methodology. Here, our Resource Q column had a positively charged matrix, so my periplasmic fraction was dissolved in Tris buffer (pH 8) to give the β-lactamase a net negative charge. The purification had varying success, with TEM-1 binding well to the column, but KPC-2 failing to immobilise. This is evident in Figure 3.10 (A) and (B), where three successive flow through fractions were collected, and SDS-PAGE revealed them to contain the ~28 kD KPC-2 band. As KPC-2's isoelectric point was only one pH point away from the Tris buffer, it's likely it was weakly ionised, and the net charge was insufficient to bind the column. However, as a means of separating out contaminating proteins, this method still worked well. Rather than taking the ion exchange elution fractions, the flow through containing KPC-2 was instead collected and concentrated for SEC. In contrast, TEM-1 fractions were collected normally after elution in a gradient of ion exchange elution buffer (Materials 2.1.2).

The second purification technique used for the β-lactamases was SEC via the Superdex 75 column. This aimed to remove any further contaminating proteins by separating the proteins by molecular mass, and simultaneously remove the high levels of salt that accompanied the ion exchange elution. The elution profile of KPC-2 showed minor peaks either side of 50 mL, and a major peak recorded at ~65 mL (Figure 3.10 (C)). Proteins elute in order of molecular mass, and this can be seen in Figure 3.10 (D). The first few fractions contain a mix of three protein bands, which resolve to become the sole KPC-2 band at ~28 kD. These final fractions were the purest, and were hence pooled, concentrated and quantified via the Bio-Rad DC assay. TEM-1 followed the same SEC procedure and was eluted at the same volume as KPC-2 (~65 mL) due to its similar molecular mass. Identical pooling, concentration and quantification procedures then followed. Once a concentration for the β-lactamases had been established, 2 µl aliquots of 100 µM protein were prepared and snap frozen in liquid nitrogen. These highly concentrated aliquots were necessary for β-lactamase sensing experiments, because the β-lactamase would be diluted into Dulbecco's phosphate buffered solution (DPBS) buffer for the sensing experiments.
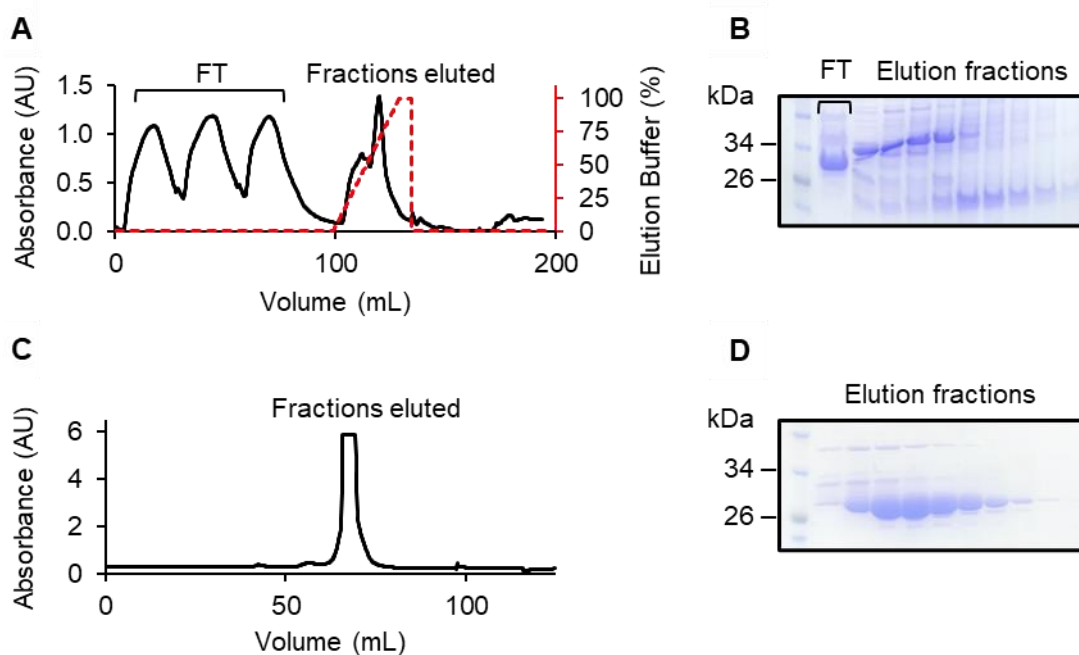
Figure 3.10 – Purification of KPC-2 β-lactamase. The periplasmic fraction was mixed in equal volumes with Tris 50 mM buffer before loading onto Resource Q column. Absorbance was monitored at 280 nm, and flow through (FT) was collected for any unbound protein. KPC-2 was eluted here, due to its isoelectric point being too close to Tris buffer pH. A gradient of ion exchange elution buffer was then applied to elute the bound protein and fractions were collected for SDS-PAGE analysis (B). With the fractions containing target protein identified, these were concentrated and run on the SEC column (C). SDS-PAGE revealed KPC-2 as a clean, purified band at ~28 kDa (D).

3.2.5 NT-FET device fabrication

With both the receptor protein (BLIP-II) and analytes (TEM-1 and KPC-2) prepared, only the NT-FET devices were left to fabricate. Collaborators at QMUL (Dr. Mark Freeley and Dr. Chang-Seuk Lee) followed the protocol described in Methods 2.4.7.1 to construct the devices. To describe in brief, 10 x 10 mm silicon chips had a predesigned electrode pattern applied through a combination of laser and electron beam lithography (Figure 3.11 (A)). SWCNTs were then deposited across transistor channels by a process of dielectrophoresis. This process is verified by measuring the I/V characteristics across the source and drain electrode in a -1 to 1 V bias sweep (Figure 3.11 (C)). A signal is confirmed by the current increasing with increasing voltage; while an unbridged junction would show no change. AFM was then used to check the quality of the electrode junction. Figure 3.11 (B) illustrates

the optimal SWCNT bridge, with only a couple of SWCNT bundles crossing the channel. Despite keeping dielectrophoresis conditions the same, the NT-FET channel will have an inherent variability in SWCNT distribution and bundle height. AFM is crucial to maintaining NT-FET channel 'uniformity', by choosing channels of a similar morphology and topography. These channels are then taken forward for sensing experiments.
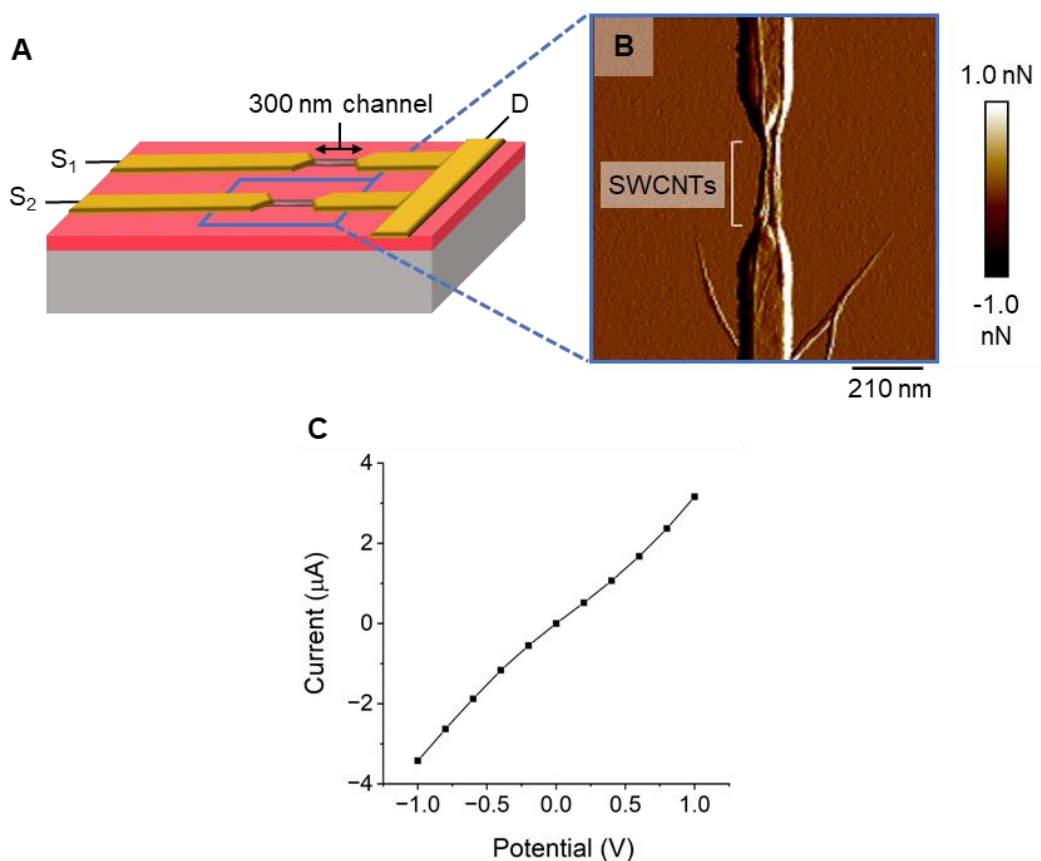
Figure 3.11 – NT-FET transistor channel and I/V characteristics. (A) Schematic diagram illustrating the source (S_1 and S_2) electrode connected to the drain (D) electrode, after SWCNTs have been deposited by dielectrophoresis. (B) AFM image of the SWCNT bundle bridging the source and drain electrode, in peak force error mode. (C) Representative I/V characteristics across the source and drain electrode after SWCNT dielectrophoresis in a -1 – 1 V bias sweep.

3.2.6 UV photo-attachment of BLIP-II^{AzF} to NT-FET devices and β-lactamase sensing

With the NT-FET devices prepared, the nanocarbon could be functionalised with the BLIP-II^{AzF} variants. Due to limited time and resources, only three BLIP-II^{AzF} variants

were attached to the silicon chips. BLIP-II[41AzF] and BLIP-II[213AzF] were selected, as these results would build upon the previously published research: Thomas et al. (2020) who covalently bound BLIP-II[41AzF] to SWCNTs dispersed across a glass coverslip, and Xu et al. (2021), who used click chemistry to attach BLIP-II[41AzF] and BLIP-II[213AzF] non-covalently to NT-FET devices, via a pyrene linker. This would allow me to compare how different attachment processes could affect NT-FET conductance characteristics. BLIP-II[49AzF] (prepared by Dr. Ben Bowen) was then chosen as the third variant, acting as a control protein. Cross-linking 49 AzF to the NT-FET would sterically block β-lactamase interaction and prevent a change in conductance, providing a suitable comparison to changes observed through BLIP-II[41AzF] and BLIP-II[213AzF] NT-FET devices. The other prepared BLIP-II[AzF] variants remain frozen at QMUL to be subject to future experiments.

UV photo-attachment of the BLIP-II[AzF] proteins took place as described in Methods 2.4.7.3, with one BLIP-II[AzF] variant assigned to each silicon chip. A silicon chip would comprise of up to sixteen NT-FET channels, depending on how many were deposited during dielectrophoresis. The effect of protein functionalisation on the NT-FET channels were characterised through their topography and electrical properties and is covered in sections 3.2.6.1 and 3.2.6.2.

3.2.6.1 AFM analysis

AFM is a powerful tool for analysing topographical changes. This analysis will cover two experiments used to investigate BLIP-II[AzF] covalently binding SWCNTs. Our inaugural study in 2020 showcased the covalent integration of BLIP-II[41AzF] to individual SWCNTs by site-specific photochemical attachment (Thomas et al. 2020). SWCNTs were suspended through sonication and drop cast on a glass coverslip, and BLIP-II[41AzF] was attached via UV irradiation. As the SWCNTs were approximately 1 nm in height, individual photochemical attachment events could be observed through AFM analysis (Figure 3.12 (A)). TEM-1 was then drop-cast to allow the protein complex to form *in situ* (Figure 3.12 (B)). Absolute protein height was calculated for both events by subtracting the height of the underlying SWCNT. BLIP-II[41AzF] height ranged between 1.5 – 2.5 nm, while the BLIP-II[41AzF]—TEM-1 complex height was estimated as 3.5 – 5 nm (Figure 3.12). These results are only slightly lower than the theoretical protein dimensions, with BLIP-II[41AzF] measured *in silico* as ~2.5 nm by ~4 nm, and TEM-1 measured as ~3 nm by ~5 nm. Some loss of height is expected when a soft substrate is sampled by AFM in tapping mode.

This is due to several factors. Firstly, the force imparted from the oscillating probe can compress the proteins, effectively squashing them and reducing their apparent height (Yang et al. 2007). The finite dimensions of the tip radius can hamper the perception of features smaller than the tip, with the height measured being a convolution of the feature itself plus the surrounding surface; generally resulting in height loss (Santos et al. 2011; Lai et al. 2015). Finally, long-range attractive forces, a type of van der Waals interaction, can arise between the tip and surface features, inducing apparent height loss (García and Pérez 2002; Lai et al. 2015). While the height gain observed is strong evidence for protein attachment and protein complexing, it is difficult to infer the exact binding position of TEM-1 relative to BLIP-II, e.g., if TEM-1 is binding adjacently to BLIP-II, or on top of it. This is due to the glass coverslip being removed mid-experiment for TEM-1 drop casting. Thousands of SWCNTs are immobilised to the coverslip in a random distribution, so the locating the same SWCNT after protein complexing is a near-impossible task.
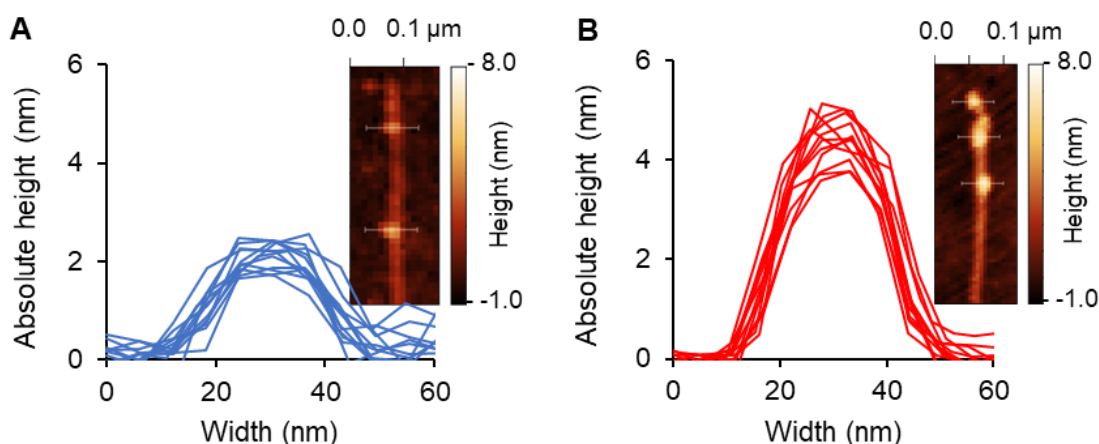
Figure 3.12 – Absolute protein height profiles from individual SWCNTs. Adapted from (Thomas et al. 2020), cross-sectional height data was taken from individual SWCNTs drop cast on glass coverslips, and functionalised with BLIP-II[41AzF]. Absolute height profiles for BLIP-II[41AzF] and the BLIP-II[41AzF]—TEM-1 complex are shown in (A) and (B) respectively, after the height of the bare SWCNT regions were subtracted.

The second experiment investigated covalent attachment of BLIP-II[41AzF] and BLIP-II[213AzF] in a more structured setup, as I attached the proteins across the SWCNT channel of my fabricated NT-FETs. Changes to the topography could be easily observed, as the bulk of the analysis was centred around SWCNT channel. Several

rounds of AFM analysis were performed: (i) after NT-FET device fabrication, (ii) after covalent functionalisation with BLIP-II[AzF] and (iii) after the β-lactamase sensing experiments.

The first application of AFM was after NT-FET device fabrication, when the electrodes were bridged with SWCNTs following dielectrophoresis. Here, AFM was performed to locate channels with an optimal morphology and topology. Figure 3.13 illustrates such channel, with small CNT bundles (~15 nm in height) connecting the source and drain electrode. This topography is ideal for biosensing applications, as the bundles have a good surface area to volume ratio for BLIP-II[AzF] functionalisation, and thus β-lactamase binding. A high surface area maximises the field-effect of incoming analytes on the NT-FET channel. However, the ratio to SWCNT channel volume has a fine balance; bundles too small and there will be significant noise across electrical measurements, bundles too large and incoming analytes will have less of an effect on SWCNT conductance. Another feature common to the NT-FETs are the peripheral SWCNTs branching off the source electrode (Figure 3.13). As they fail to contact the drain electrode, these won't directly affect the current passing through the NT-FET channel. However, they are still free to bind BLIP-II[AzF] and this becomes a powerful analysis tool for single molecule imaging by AFM. Proteins can only be seen individually if SWCNTs are 1-2 nm in height (e.g., smaller than the proteins themselves), so peripheral SWCNTs provide opportunity to analyse this.
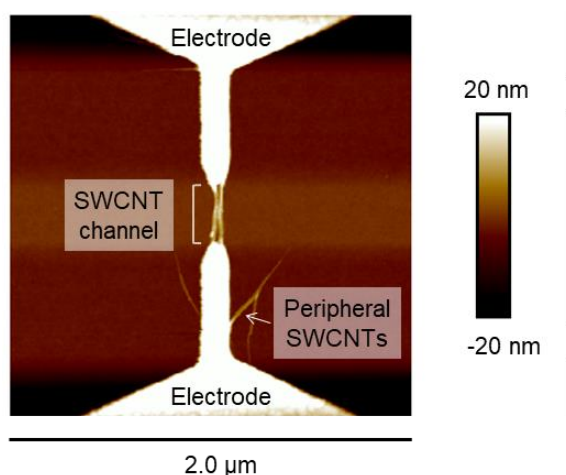
Figure 3.13 – NT-FET channel after dielectrophoresis. SWCNTs are deposited as a bundle between the source and drain electrodes, while some peripheral SWCNTs have sprouted from the source without making contact.

The second and third applications of AFM took place after BLIP-II^{AzF} variants were covalently attached to the NT-FET, and after the β-lactamase sensing experiments. The images taken at this stage allowed me to study the transistor channel's topography, by monitoring the change in height (Figure 3.14 and Table 3.1). The first observation was the variation in the baseline channel height, with both BLIP-II^{41AzF} functionalised NT-FETs averaging ~30 nm, whilst BLIP-II^{213AzF} was functionalised on smaller bundles of SWCNTs, averaging ~10 nm. This variation is intrinsic to the dielectrophoresis process, and of all eight NT-FET channels studied, this baseline height was kept between 10-40 nm. At the higher end of this scale, monitoring protein attachment does become more difficult, as a wider spread of SWCNTs ultimately leads to a more uneven surface with potential to mask protein attachment. This trend is observed in Figure 3.14 (A) and (C) which show a modest increase in height upon BLIP-II^{41AzF} attachment and is averaged across all NT-FET devices to 1.5 nm. By contrast, Figure 3.14 (B) and (D) show a more obvious increase in height from BLIP-II^{213AzF} attachment, but the smaller scale of the graph is deceptive, with the average height increase still only recorded as 1.9 nm across all NT-FET devices. After exposure to the β-lactamases, all NT-FETs demonstrated a minor increase in channel height; with BLIP-II^{41AzF} functionalised channels increasing from 1.5 nm to 2.1 nm and 1.8 nm for TEM-1 and KPC-2 respectively, and BLIP-II^{213AzF} functionalised channels increasing from 1.9 nm to 2.3 nm for both TEM-1 and KPC-2. This relatively small increase (0.3 – 0.6 nm) is sufficient to prove protein complexing, but it is in contrast to the height gain observed by addition of TEM-1 to BLIP-II^{41AzF} in the first study (~ 2 nm; Figure 3.12). KPC-2 has roughly the same dimensions as TEM-1 (~3 nm by ~5 nm) and I would anticipate a similar height gain when interfaced with either BLIP-II^{41AzF} or BLIP-II^{213AzF}. However, a key distinguishment to make between these two experiments is the underlying SWCNT(s). In Figure 3.12, the SWCNT was approximately ~1 nm in height, while the baseline SWCNT channel heights observed across Figure 3.14 were 10-40 nm. There is considerably more error in extrapolating absolute protein height from the latter method, as SWCNT bundles have a variable topography and can easily mask protein attachment. Experimental variability can also occur from the different AFM microscopes used to collect this data. The Veeco Multimode Nanoscope III was used to collect the data in Figure 3.12 at Cardiff University's School of Physics, while the Bruker Dimension Icon AFM was used to collect the data in Figure 3.14 at QMUL.

A **BLIP-II 41 AzF + TEM-1**

778 nm
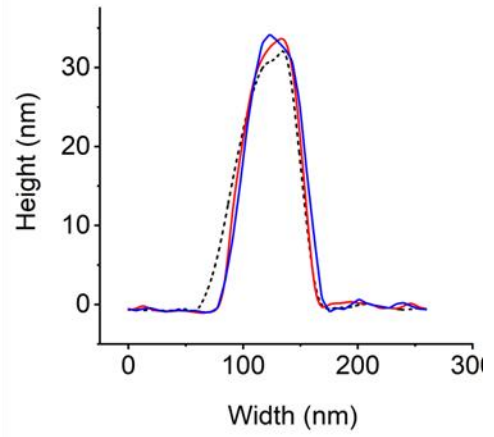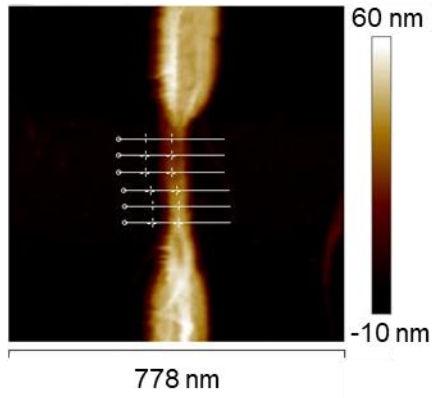
B **BLIP-II 213 AzF + TEM-1**

772 nm
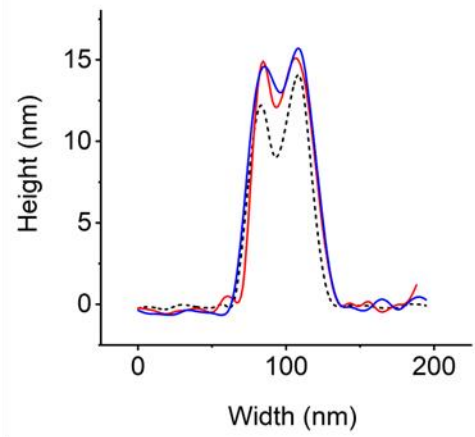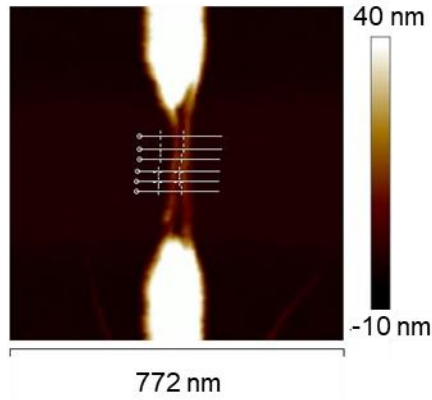
C **BLIP-II 41 AzF + KPC-2**

901 nm
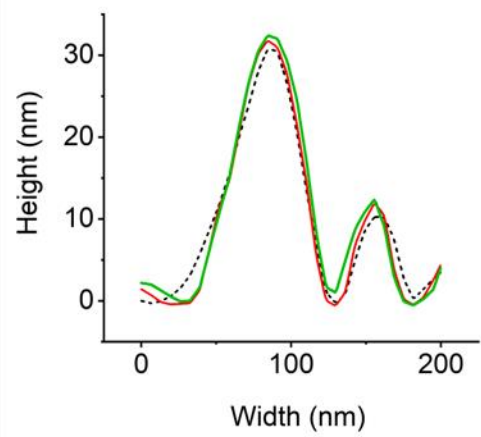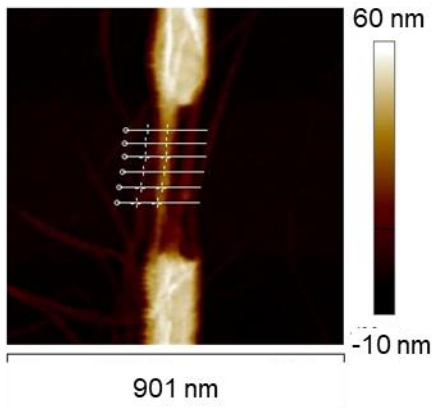
D **BLIP-II 213 AzF + KPC-2**

785 nm

112
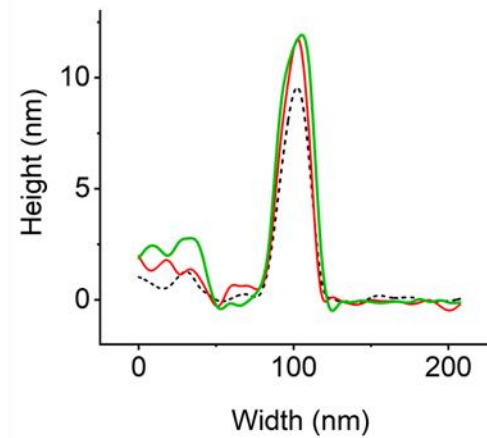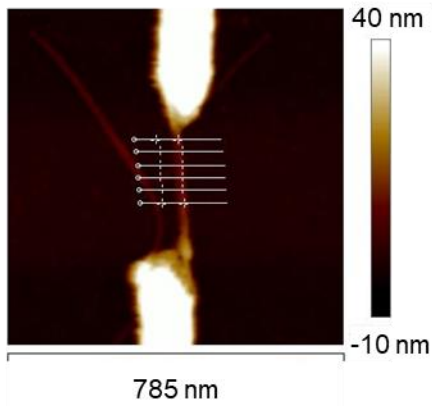
Figure 3.14 – AFM analysis of the NT-FET transistor channel. AFM images on the left show the functionalised transistor channel, with the overlaid horizontal white lines indicating six cross sections taken for height analysis. An average cross section was calculated for the channel before and after BLIP-II^{AzF} functionalisation, and again following β-lactamase sensing, and are plotted in the graphs on the right. Height profiles are seen for SWCNTs (black dashed), BLIP-II^{AzF} variant (red), TEM-1 (blue) and KPC-2 (green).

Table 3.1 – Average protein height extrapolated from AFM images. Six transverse cross sections were taken from eight NT-FET channels, comprising of two replicates for each BLIP-II^{AzF} variant with either TEM-1 or KPC-2. BLIP-II^{AzF} and BLIP-II^{AzF}—β-lactamase heights were calculated by subtracting the height of the underlying SWCNT bundle, and the height averaged across replicates. Standard deviation denoted by (±), n = 4 for BLIP-II^{AzF}, n = 2 for BLIP-II^{AzF}—β-lactamase.

	BLIP-II^{41AzF}	BLIP-II^{213AzF}
BLIP-II^{AzF}	1.5 ± 0.2 nm	1.9 ± 0.2 nm
BLIP-II^{AzF} + TEM-1	2.1 ± 0.0 nm	2.3 ± 0.4 nm
BLIP-II^{AzF} + KPC-2	1.8 ± 0.2 nm	2.3 ± 0.1 nm

Aside from studying the height of the NT-FET channel, AFM provides a valuable insight to peripheral SWCNTs that branch off larger bundles. These small-scale nanotubes offer potential to visualise single molecule attachment, with the ~2-5 nm sized proteins notable against single SWCNTs (~1 nm). Figure 3.15 (A) shows the clearest example of this, with three light-coloured spots (see white arrows) appearing at the end of a SWCNT after BLIP-II^{41AzF} attachment. The light colour indicates a localised increase in height, while the round shape is consistent of a protein. Considering the NT-FET was taken through a thorough washing step following protein attachment, I presume these species to be BLIP-II^{41AzF} proteins rather than adsorbed contaminants. The same SWCNT was then located after the sensing experiment with KPC-2, where the light-coloured spots appear to have multiplied with new spots appearing adjacent to the original. This could suggest KPC-2 has bound adjacently to BLIP-II^{41AzF}, rather than in a top-down formation.

The extracted height profiles (Figure 3.15 (B)) support this hypothesis, with the defined protein peaks from BLIP-II[41AzF] functionalisation broadening and gaining further height after complexing with KPC-2. This is an important insight into protein binding morphology.
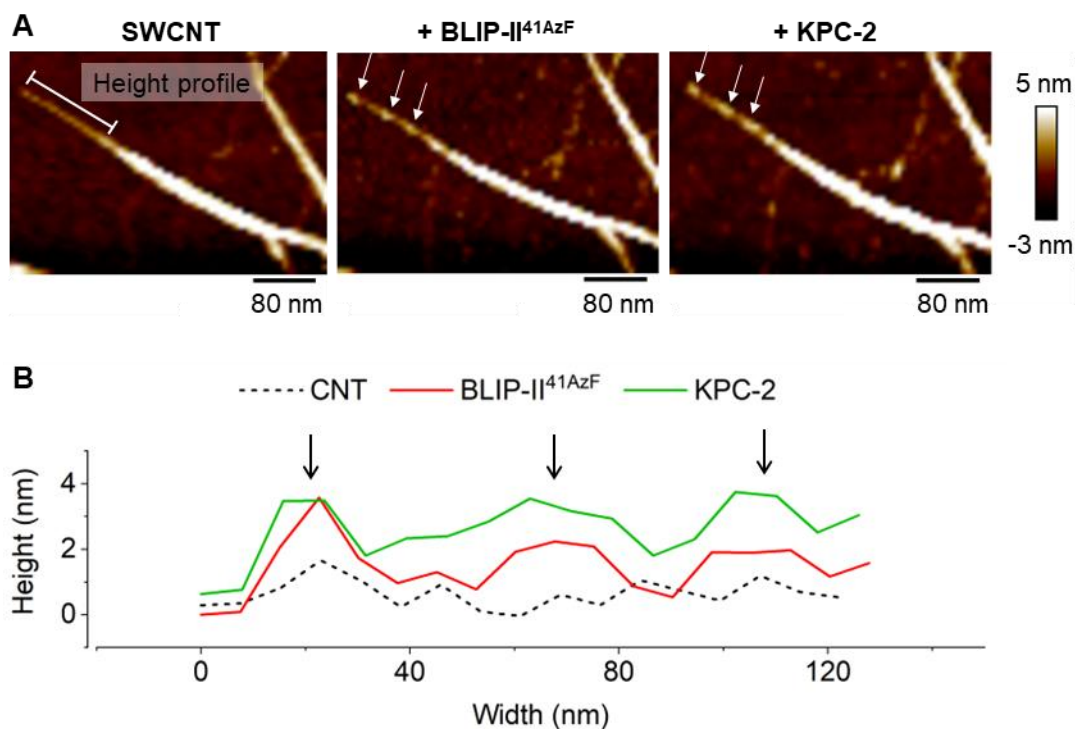
Figure 3.15 – Visualising single molecule attachment. (A) AFM analysis of single / double SWCNT bundles branching off the main transistor channel reveals individual BLIP-II[41AzF] proteins attaching along the length of it. Following the sensing experiment, KPC-2 proteins appear to bind adjacently. (B) Extracted height profile before and after BLIP-II[41AzF] functionalisation, and after KPC-2 sensing. Arrows identify speculative protein peaks.

3.2.6.2 Electrical measurements

Following the successful fabrication of BLIP-II[AzF] functionalised NT-FET devices, β-lactamase sensing experiments could take place to investigate whether the analytes could be detected through a change in conductance, and if sensing varied in respect to the azide mutation site. There are several methods available to test this,

including by collecting I/V characteristics or by monitoring the real-time current passing between the source and drain electrode.

To build on work by (Xu et al. 2021), real-time measurements were initially pursued as the method of choice. Here, the NT-FET device was connected to the probe station with a 0.1 V fixed voltage applied to the source electrode, and the drain electrode grounded. Higher voltages were avoided due to the potential damage to SWCNT bundles. As the experiment focused on measuring the electrostatic gating effect of incoming β-lactamases, the gate electrode was also grounded. The β-lactamase sensing experiment could then be carried out, as detailed in Methods 2.4.7.6. This began with casting 10 µl of DPBS buffer onto the device, and then adding eight incremental concentrations (2, 10, 20, 100, 400, 700, 1000 and 2000 nM) of β-lactamase every 100 seconds, or 200 seconds if the current was unsettled. To ensure buffer volume remained the same throughout the experiment, β-lactamase additions were accompanied by 10 µl buffer removal, after mixing the two liquids together.

Example output from the preliminary real-time studies showcases a BLIP-II[213AzF] functionalised NT-FET device exposed to increasing concentrations of KPC-2 (Figure 3.16). One of the most notable features here is the consistent drop in current throughout the experiment, and this was observed across all real-time experiments with BLIP-II[AzF] functionalised NT-FETs. For real-time data to be interpreted accurately, the baseline current (NT-FET with only DPBS buffer cast) should be allowed to stabilise to a plateau before exposure to analytes. However, the preliminary real-time experiment, as depicted in Figure 3.16, was poorly designed and did not account for this, allowing only 100 seconds for baseline stabilisation. It is evident that current continues to drop at 100 seconds, but lack of experience led myself and my collaborator to begin incremental analyte casting from 100 seconds onwards. This meant the continued downwards trajectory of the current could not be confidently linked to increasing analyte concentrations, so all the real-time data collected became unusable. Hindsight would have us increase the baseline stabilisation time, but a lack of time and resources led us to pursue an alternative method for assessing β-lactamase exposure to BLIP-II[AzF] functionalised NT-FET devices.
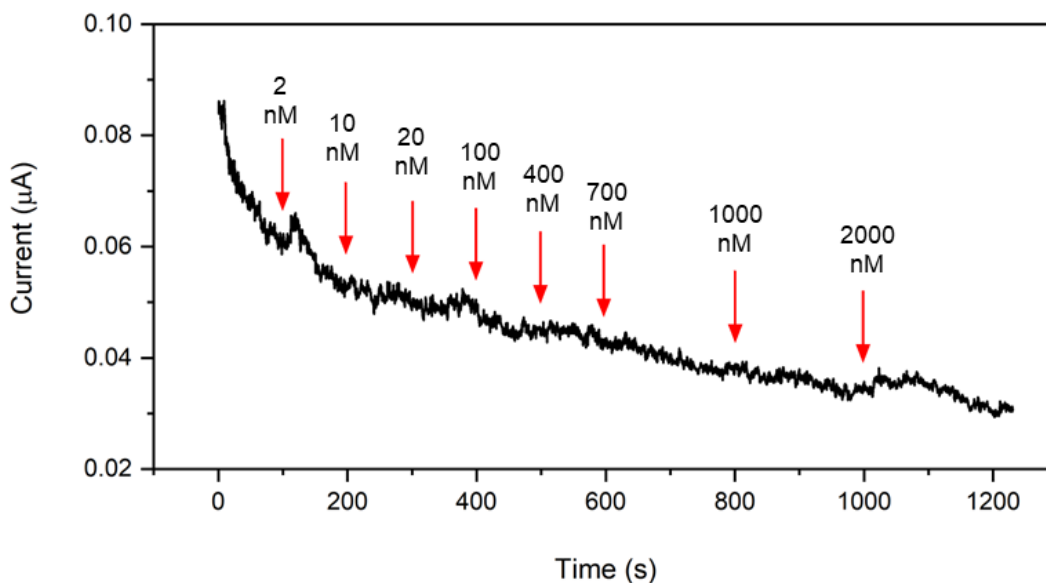
Figure 3.16 – Example output from preliminary real-time studies. BLIP-II[213AzF] functionalised NT-FET, doped with increasing concentrations of KPC-2 every 100 s or 200 s (red arrows).

Collecting I/V characteristics for individual NT-FET junctions was originally intended as a methodology for testing NT-FET device viability, but the data has additional value, providing insight into how conductance changes between two electrodes. To make this relevant to my experiment, voltage is supplied through the source electrode and grounded through the drain, so current can be measured as it passes through the SWCNT transistor channel. By recording I/V characteristics at different experimental phases, I can observe the effect of BLIP-II[AzF] on conductance as it covalently binds the SWCNT bundle, as well as any possible gating effects from increasing the β-lactamase concentration. The benefit of this data collection method is that up to 16 electrode junctions can be tested at each experimental phase. Real-time sensing, however, is limited to one junction at a time, as data must be recorded continuously throughout the β-lactamases sensing experiment. While it's still feasible for data to be collected across 16 different junctions, the dielectrophoresis > protein attachment > β-lactamase sensing protocol must be carried out individually for each junction, drastically reducing time and resource efficiency.

To begin the analysis, I/V data was collected before and after BLIP-II[AzF] functionalisation to investigate whether the covalent cross-linking to SWCNTs would have a noticeable effect on conductance. The I/Vs collected before BLIP-II[AzF] attachment are taken from post-SWCNT dielectrophoresis. These had to be

116

normalised to 1 to allow for data comparison, as the current would vary between 0.1 ~ 10 µA between individual electrode junctions. This variation is normal, and correlates to SWCNT bundle height, with a larger bundle having greater capacitance. The I/Vs collected after BLIP-II^{AzF} attachment were then normalised to the SWCNT bundle they were attached to, allowing the data to be compared across all electrode junctions. Figure 3.17 illustrates the change in I/V characteristics after functionalisation of the NT-FET with BLIP-II^{41AzF} (A) and BLIP-II^{213AzF} (B). The I/Vs pre-functionalisation display ohmic behaviour; with a linear relationship between current and voltage. This is to be expected with pristine SWCNTs, as their semiconducting nature allows them to carry the charge between electrodes with no change in resistance. By covalently attaching BLIP-II^{AzF}, I anticipate an increase in resistance across the NT-FET channel, due to the disruption of the π electron network (Jeon et al. 2011). However, the results are surprising, with Figure 3.17 suggesting resistance has dropped after both BLIP-II^{AzF} variants have been attached. When 1 V is supplied to the source electrode, current is seen to increase on average by 54 % for BLIP-II^{41AzF}, and 79 % for BLIP-II^{213AzF}. It is important to note that a fewer number of data points were collected for BLIP-II^{213AzF} and could be resulting in the greater standard error. Nevertheless, this trend is significant and corroborates experiments carried out by Setaro et al. (2017), who managed to maintain the π electron network upon covalent functionalisation with aromatic nitrenes. Here, the formation of an aziridine ring was proven to minimally distort the carbon π orbitals, highlighting the importance of the reactive group (in this case, the azide) to form a favourable cycloaddition product.
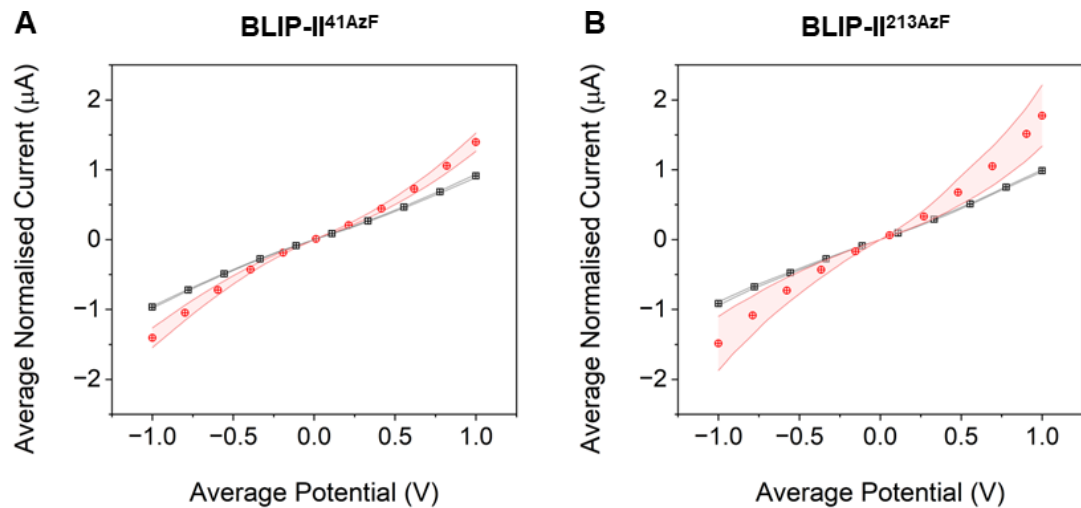
Figure 3.17 – Effect of BLIP-II^{AzF} covalently functionalising NT-FET device. I/Vs recorded between the source and drain electrode before BLIP-II^{AzF} attachment (black) were normalised to 1 and averaged. I/Vs recorded after BLIP-II^{AzF} attachment (red) were adjusted for normalisation and averaged. For BLIP-II^{41AzF} (A; n=15) and BLIP-II^{213AzF} (B; n=8). Standard error of the mean is plotted either side of the average measurements.

While the Setaro et al. (2017) hypothesis explains how conductivity can be maintained, the increase in current is novel and is most likely attributed to BLIP-II^{AzF} itself. Being covalently bound to the SWCNT, a portion of BLIP-II^{AzF} will automatically be within the Debye length. This provides scope for this area to induce gating across the NT-FET channel, if significant electrostatic surface potential (ESP) is present. Figure 3.18 illustrates the ESP surrounding the AzF mutation sites in BLIP-II^{41AzF} (A) and BLIP-II^{213AzF} (B). In BLIP-II^{41AzF}, AzF is located on the edge of BLIP-II's cylindrical profile, with a heavily acidic face to the left of it, and a partially basic face on the right. As the exact binding conformation at the SWCNT interface is unknown, there is scope for either of these areas to come within the Debye length. For BLIP-II^{213AzF}, there is less variability as AzF is positioned perpendicularly to a flat surface. Here, the surrounding ESP is weakly acidic. As both proteins elicit an increase in current, it suggests BLIP-II^{41AzF} is presenting a similarly acidic face to the SWCNT, where the net negative charge would have the effect of stabilising a higher concentration of holes within the NT-FET channel (Zheng et al. 2016b; Xu et al. 2021). The increase in holes equates to an increase in charge carriers in the p-type SWCNTs, explaining the observed increase in current after BLIP-II^{AzF} attachment.
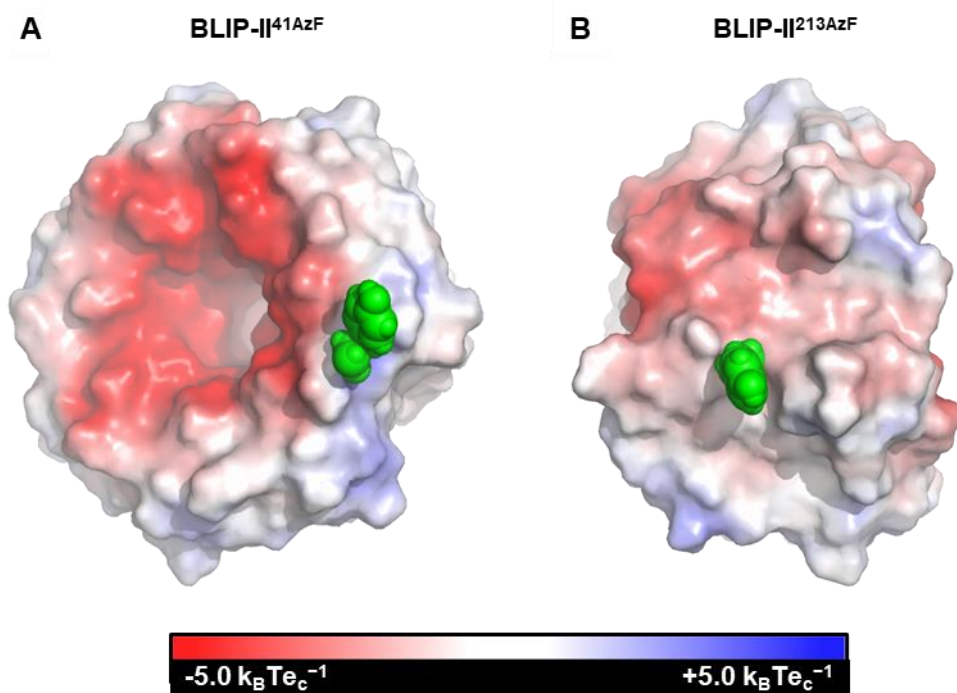
Figure 3.18 – Electrostatic surface potential of BLIP-II⁴¹ᴬᶻᶠ and BLIP-II²¹³ᴬᶻᶠ.
Sites of azide incorporation are highlighted as green spheres in BLIP-II⁴¹ᴬᶻᶠ (A) and
BLIP-II²¹³ᴬᶻᶠ (B), while the surrounding protein surface is coloured by electrostatic
surface potential.

With the I/Vs recorded following BLIP-II^{AzF} functionalisation of the SWCNTs, the β-
lactamase sensing assay could take place. Here, the experiment was adapted from
the real-time studies take discrete I/V measurements every 100 seconds, rather
than a continuous collection of real-time current data. To initiate the experiment, 10
µl of DPBS buffer was added to the NT-FET device and I/Vs were recorded after
100 seconds as the baseline measurement. Incremental β-lactamase
concentrations (2, 10, 20, 100, 400, 700, 1000 and 2000 nM) were then applied
every 100 seconds with I/Vs recorded between each addition. Current was
extracted from the I/Vs at 0.1 V (the same voltage applied in the real-time studies)
and plotted against β-lactamase concentration in Figure 3.19 and Figure 3.20. The
concentrations are different to those described above because they've been
adjusted for dilution with the liquid present on the device; an ever-changing
composition of DPBS buffer and increasing β-lactamase concentration.

Figure 3.19 plots the results of two control experiments; a non-functionalised NT-
FET device with pristine SWCNTs (A), and control protein BLIP-II⁴⁹ᴬᶻᶠ (B). The
pristine SWCNT control allows me to test whether TEM-1 or KPC-2 could affect the

passing current through protein adsorption. SWCNTs are hydrophobic in nature so any incoming hydrophobicity from the β-lactamase surface has the potential to adsorb to the SWCNT surface via hydrophobic or π-π interactions. From the results shown, TEM-1 was shown to have no effect on current, with average change staying consistently around 0.0 µA. KPC-2 was also shown to have little effect, resembling a minor dose-response at the highest concentrations (750 – 1350 nM), as current dropped from 0.0 µA to -0.09 µA.

The BLIP-II[49AzF] control (Figure 3.19 (B)) was used to test the NT-FET device setup without the ability to bind analytes, as anchoring the protein through the β-lactamase binding site sterically hindered any interaction. This ensured that any measurable change in current from BLIP-II[41AzF]/ BLIP-II[213AzF] functionalised NT-FETs could be linked the BLIP-II—β-lactamase interaction, rather than non-specific binding or protein adsorption. From the results shown, there are minor fluctuations in current upon increasing concentrations of both TEM-1 and KPC-2. TEM-1 hovers between -0.03 µA and 0.09 µA, whilst KPC-2 stays between -0.06 µA and 0.05 µA. As there is no clear trend to this data, these fluctuations can be put down to inherent experimental variation, e.g., the disturbance caused by pipetting to the local field effect, and taken together, these controls suggest a range of -0.1 – 0.1 µA would be an appropriate cut-off for baseline NT-FET variation.
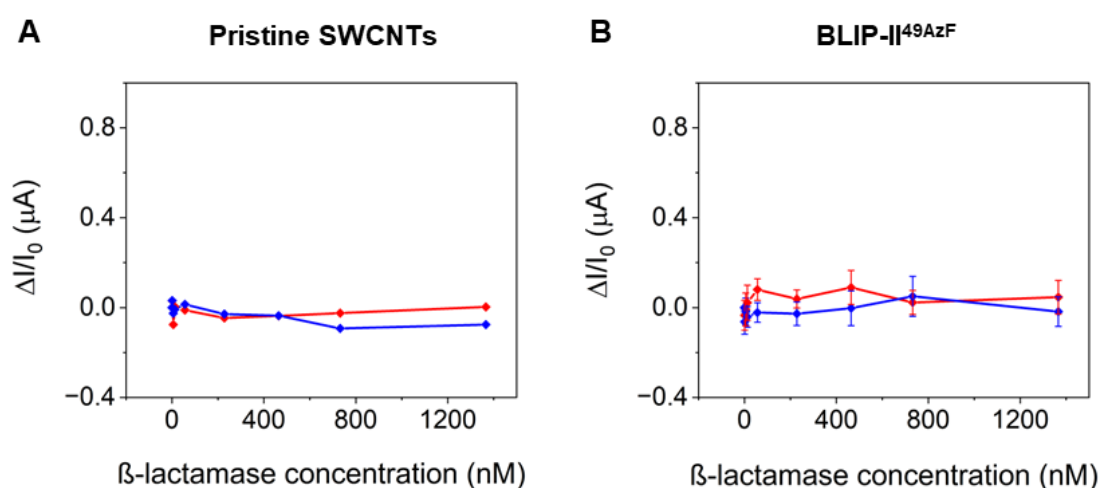
Figure 3.19 – β-lactamase sensing assay: control NT-FET devices. The assay was performed with non-functionalised NT-FET devices (e.g., pristine SWCNTs) (A; n=1) and the control protein BLIP-II[49AzF] (B; n=3). The average change in normalised

current is plotted against increasing concentrations of TEM-1 (red) and KPC-2 (blue) with a source-drain bias of 0.1 V.

Figure 3.20 shows the experimental results of BLIP-II[41AzF] (A) and BLIP-II[213AzF] (B) functionalised NT-FET devices against increasing β-lactamase concentration. For BLIP-II[41AzF], an increase in current accompanied TEM-1 concentrations between 0 – 450 nM. Above 450 nM, current was seen to plateau at 0.19 µA. When doped with KPC-2, a minor increase in current was observed between 0 – 50 nM, before dropping to a plateau of -0.1 µA. With the baseline variation for BLIP-II[AzF] functionalised NT-FETs set to -0.1 – 0.1 µA, only TEM-1 achieved a change in conductance that corresponded to effective β-lactamase sensing. Using the gating hypothesis, this small increase in current induced by TEM-1 could be explained by a weak patch of negative ESP breaching the Debye length to increase the number of holes within the NT-FET channel. However, this signal isn't particularly strong, and suggests BLIP-II[41AzF] may be unfavourably anchored; with poor signal linked to both β-lactamases binding beyond the Debye length.

By comparison, BLIP-II[213AzF] functionalised NT-FETs appear to show a much stronger signal upon β-lactamase exposure (Figure 3.20 (B)). For TEM-1, current jumped from 0 to 0.46 µA after only 50 nM, and continued to increase until 450 nM, where it plateaued at 0.64 µA. For KPC-2, a minor increase in current was observed between 0 – 50 nM, before dropping down and plateauing around -0.25 µA. This pattern is unusual and mirrors that seen in BLIP-II[41AzF] functionalised devices. One possible explanation is that the analyte concentration between 0 – 50 nM is below the device's minimum sensitivity level. From my knowledge on the BLIP-II[AzF]—NT-FET interface, I anticipate the change in current to have a linear relationship with increasing β-lactamase concentrations, as the binding orientation (and thus ESP presented) should stay the same. However, this is only observed above 50 nM concentrations. Below 50 nM and the device could be susceptible to baseline variation (-0.1 – 0.1 µA), explaining the minor increases observed in both NT-FET devices. An additional observation to pick up on is the plateauing of the signal by 450 nM in both BLIP-II[AzF] devices, as it suggests all BLIP-II[AzF] binding sites have been saturated. This would give a sensitivity range of 50 – 450 nM, or 0.5 pmol – 4.5 pmol. BLIP-II[213AzF] functionalised devices are overall shown to work more effectively than BLIP-II[41AzF], as the signal obtained from β-lactamases is much stronger. This suggests BLIP-II[213AzF] has attached in a more favourable conformation to the NT-FET, with both β-lactamases binding within the Debye

length. Based on the gating hypothesis, TEM-1 is thought to present a strongly negative ESP, while KPC-2 may offer a positively charged ESP; repelling the holes in the NT-FET channel and slowing the passage of current.
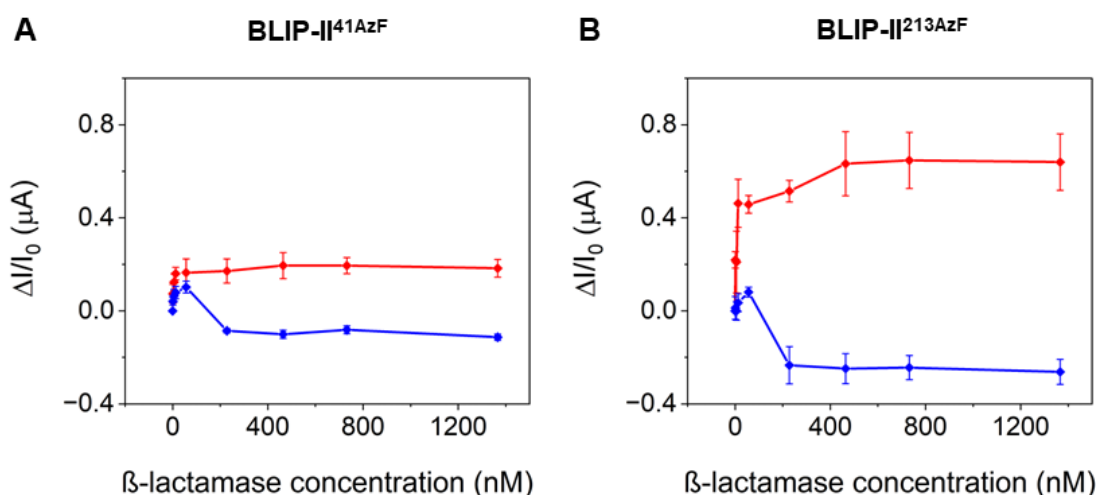
Figure 3.20 – β-lactamase sensing assay: BLIP-II⁴¹ᴬᶻᶠ (A) and BLIP-II²¹³ᴬᶻᶠ (B) NT-FET devices. The average change (n=3) in normalised current is plotted against increasing concentrations of TEM-1 (red) and KPC-2 (blue) with a source-drain bias of 0.1 V. Standard deviation is plotted through error bars.

To test the electrostatic gating hypotheses against computer generated electrostatic profiles of the β-lactamase surface, the crystal structure of the BLIP-II:TEM-1 protein complex and KPC-2 was loaded into molecular visualisation software, PyMOL. A SWCNT was aligned to the AzF mutation site and APBS electrostatics was performed on the β-lactamases. The outputted profiles can then be seen in Figure 3.21. These images are taken from the viewpoint of the SWCNT, allowing us to see the ESP which directly projects onto it. For BLIP-II⁴¹ᴬᶻᶠ, I observe a large spread of negatively charged potential ($\sim$ -3 $k_BTe_c^{-1}$) above the SWCNT for TEM-1, which supports the small increase in current measured in Figure 3.20 (A). Arguably, the change in current isn't as strong as the observed cluster of negative potential, which could suggest that TEM-1 is on the fringes of the Debye length, possibly fluxing in and out due to the flexibility of the N-terminal 41 AzF residue. Chapter 4 will study these models in further depth, using molecular dynamics to better predict the attachment conformation of BLIP-II⁴¹ᴬᶻᶠ and BLIP-II²¹³ᴬᶻᶠ, and consequently β-lactamase interaction within or beyond the Debye length. In comparison to TEM-1, KPC-2 has a fairly neutral ESP above the SWCNT, with one basic patch.

Experimentally, current was observed to drop slightly upon increasing KPC-2 concentrations, but this stayed within the baseline variation range of the NT-FET devices. Surface potential was either not strong enough to have induced significant gating or was pushed beyond the Debye length.

For BLIP-II[213AzF], different faces of the β-lactamase project towards the SWCNT. When interfaced with TEM-1, a mixed ESP is presented, with a notably strong patch of negative ESP (~ -5 $k_B Te_c^{-1}$) at the BLIP-II:TEM-1 interface. As the gating effect is expected to be a summation of all electrostatic potential presented, the overall charge presented from TEM-1 would be considered negative. This corroborates well with the large increase in current observed in Figure 3.20 (B), where gating is anticipated to increase the number of holes. When interfaced with KPC-2, a positive ESP dominates above the SWCNT. While the heatmap is showing only a slight positive charge (~ 1.5 $k_B Te_c^{-1}$), this covers a significant area of the protein. Gating by depleting holes in the NT-FET channel is anticipated and fits the data well in Figure 3.20 (B), where conductance is observed to drop with increasing KPC-2 concentrations.
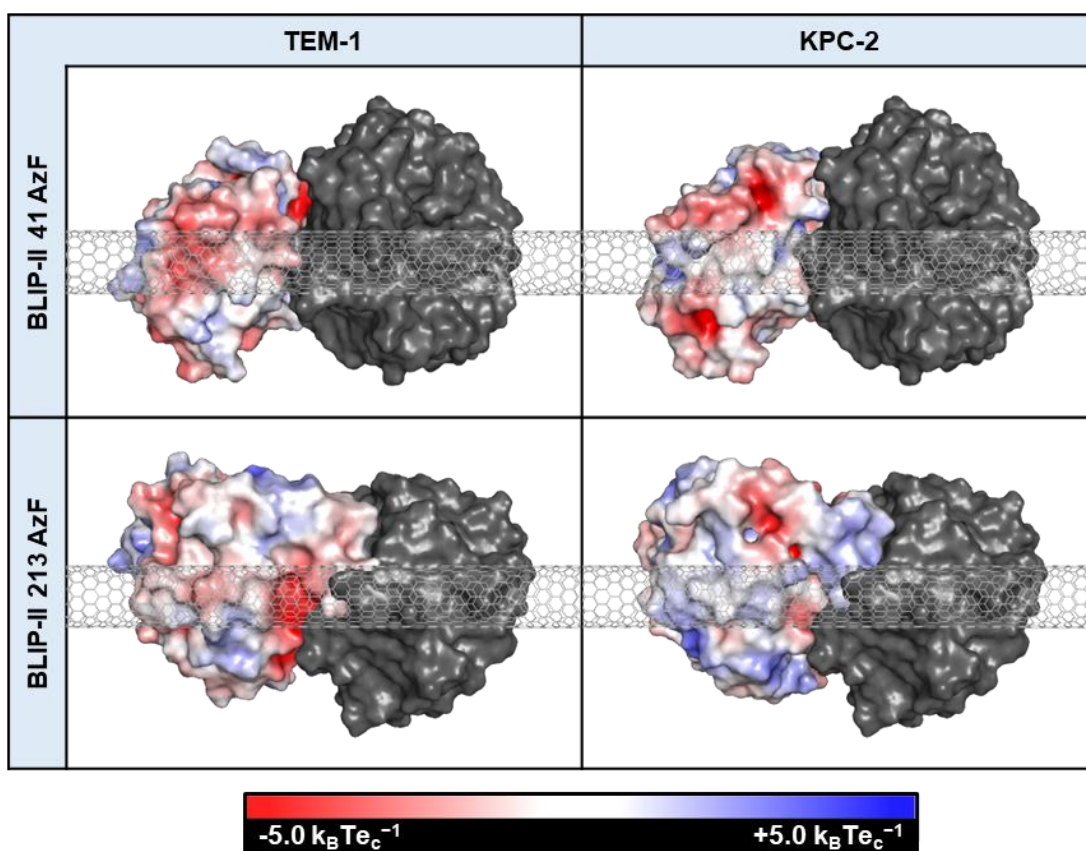
Figure 3.21 – Predicted electrostatic surface potential projection. BLIP-II[AzF]

(dark grey) was modelled onto a SWCNT and crystal structures of TEM-1 and KPC-2 were aligned. APBS electrostatics generated a heatmap of the β-lactamases to represent electrostatic surface potential.

3.3 Conclusions and Future Perspectives

To summarise the key results from this chapter, I successfully produced a repertoire of BLIP-II^{AzF} variants, of which three (BLIP-II^{41AzF}, BLIP-II^{213AzF} and BLIP-II^{49AzF}) were used to covalently functionalise my NT-FET devices. Protein attachment was confirmed by an increase in height across the NT-FET transistor channel, and I/V data was collected for electrical insight. Remarkably, covalent functionalisation of the SWCNTs with BLIP-II^{41AzF} and BLIP-II^{213AzF} was shown to increase conductance across the NT-FET channel, a feat explained in part by the compatible hetero-bridged structure (Setaro et al. 2017) and in part by gating induced by BLIP-II ESP. Sensing experiments against prevalent β-lactamases: TEM-1 and KPC-2, revealed the BLIP-II^{41AzF} and BLIP-II^{213AzF} devices could successfully discriminate between the two proteins by changes in current which corresponded to their ESP. Finally, BLIP-II^{213AzF} functionalised NT-FETs were shown to transduce a larger signal, suggesting BLIP-II^{213AzF} was more favourably oriented to transduce analyte binding events; a closer inspection of which will be pursued in Chapter 4.

To delve deeper into some of these key outcomes, the success of AzF in mediating protein-SWCNT interaction will first be considered. Functionalisation of SWCNTs is often the source of much debate, with covalent and non-covalent methodologies both offering distinct advantages (Lee et al. 2022). Covalent attachment offers a permanent anchor for biomolecules, with the close physical proximity between the SWCNT and receptor increasing the chance of incoming analytes passing within the Debye length. Non-covalent attachment offers what, typically, covalent attachment proteins cannot: a pristine sp^2 carbon network, with receptors adsorbed to the SWCNT surface. The resolution then, that anchoring proteins via AzF has all the benefits of covalent attachment without damaging the sp^2 network (Setaro et al. 2017), is a significant development in the field of protein-functionalised NT-FETs. Aside from the physical benefits to SWCNT conductance, the implementation of AzF anchoring offers an element of systematic control to achieve the most effective signal transduction. By studying the ESP of established receptor-analyte complexes, I can target the AzF mutation site to anchor the receptor in a favourable way, bringing the analyte close to the SWCNTs and presenting a strong

electrostatic surface potential. The accessibility, then, of these proteins to be produced commercially, must be considered. Once the receptor protein and AzF anchor site has been identified, a single mutagenesis step would introduce the required TAG codon. A dual-plasmid transformation would prime the expression cell line, and a standard protein production protocol would be followed, with AzF added in exogenously. This procedure is virtually the same as any other recombinantly produced protein, and places AzF-containing proteins in good stead for use in commercially produced NT-FETs.

Another key outcome to discuss is the diagnostic potential of these NT-FET devices and how the technology can be improved in the future. From the electrical measurements I have established that BLIP-II^{213AzF} functionalised NT-FETs elicited a stronger response to the β-lactamases than BLIP-II^{41AzF}, which highlights the importance of the AzF mutation site in the receptor protein. The change in conductance was linked to the ESP of incoming β-lactamases, and their gating potential (Heller et al. 2008). Schottky barrier modifications weren't considered in this experimental setup as no transfer characteristics were collected, so this mechanism of signal transduction remains unaccounted for. The sensitivity of the BLIP-II^{41AzF} and BLIP-II^{213AzF} functionalised NT-FETs was between 50 – 450 nM, or 0.5 – 4.5 pmol. This is similar to the sensitivity achieved in our non-covalent BLIP-II NT-FET prototype (Xu et al. 2021), which reached a minimum of 10 nM or 0.1 pmol. However, these results are not directly comparable as I used different data collection methods. It is possible that greater sensitivity could be achieved from my covalently functionalised BLIP-II^{41AzF} and BLIP-II^{213AzF} NT-FETs if real-time sensing was performed successfully, or if transfer characteristics were collected, but this will be an avenue for future research. With further BLIP-II^{AzF} variants developed in the inaugural stages of this research, it would also be valuable to test these alternative receptor proteins and consider their electrical outputs. Not only could they produce a stronger signal, but it would allow us to sample a different portion of analyte ESP, which feeds into the ultimate design aim of a multiplexed diagnostic device. In such device, multiple data inputs are processed at once, so if each input (e.g., individual NT-FET channel) hosted an alternative BLIP-II^{AzF} receptor protein, you could systematically sample the ESP of the entire analyte, allowing accurate identification of the ABR protein present. For this prototype to be developed, a library of β-lactamase ESP would have to be created. This marks another future research direction, by testing these devices against all known class A β-lactamases (> 550) – or at least the 114 representative enzyme families (Bush and Fisher 2011; Philippon

et al. 2016), to build a thorough database. Expanding on this, it would also be crucial to test the sensitivity of these devices to β-lactamases suspended in clinical fluids (e.g. blood serum or urine). Xu et al. (2021) reported success when testing their non-covalently functionalised BLIP-II NT-FETs against TEM-1 doped serum, so one would hope for a similar response in ours.

Considering the commercial potential for my NT-FET devices, I must also look at establishing better uniformity across the transistor channels. My channel height varies between 10-40 nm, despite using the same dielectrophoresis parameters, which has knock-on effects for the signal to noise ratio, and sensitivity to β-lactamases. There is little I can do to improve this, but I could try different methodologies such as drop-casting and dip-coating. Small-scale immobilisation of SWCNTs, generally, though, remains a challenge for the entire field; particularly in scaling up for commercial production (Lee et al. 2022). A final research direction for us to pursue is improving the reusability of NT-FET devices. Denaturation cannot be used to remove β-lactamases, as the process would simultaneously damage the receptor proteins. Therefore, the dissociation rate of β-lactamase from BLIP-II needs to be addressed. Currently, BLIP-II exhibits femtomolar affinity for KPC-2, which gives the BLIP-II—KPC-2 complex a half-life of ~ 10 days (Brown et al. 2013a). I could increase this dissociation rate by introducing alanine mutations at the BLIP-II—β-lactamase interface, as demonstrated by Brown et al. (2013b). If single alanine mutations were able to increase the rate 10 to 100-fold, a combinatorial approach could boost this even further. An alternative approach would be to use different β-lactamase inhibitor proteins (e.g. BLIP or BLIP-I), as they naturally exhibit lower affinity for the β-lactamases (Eiamphungporn et al. 2018). However, this would require us to restart all synthetic biology work to first optimise expression, and then design new AzF variants.

Overall, my BLIP-II[AzF] covalently functionalised NT-FETs were paramount in proving the success of AzF to mediate covalent attachment of proteins to SWCNTs in a non-destructive manner. The ability to sense and transduce incoming β-lactamases not only highlights the potential for ABR biosensing but sets a blueprint for future NT-FET design.

4. Molecular dynamics modelling to predict p-azido-L-phenylalanine mutation site success in BLIP-II^{AzF} functionalised NT-FET devices

Work in this chapter is contributing to an upcoming research article where I am joint 1st author. The current working title is referenced below.

Gwyther, R., Lee, C.S., Côte, S., Ramakrishnan, K., Palma, M., Jones, D., 2023. Optimising CNT-FET Biosensor Design: Predictive Modelling of Biomolecular Electrostatic Gating and its Application to Beta-Lactamase Detection. *Pending publication.*

Statement of work

All data presented in this chapter has been collected, plotted, and analysed by me.

4.1 Introduction

Developing commercially viable diagnostic devices in the 21st century requires an extensive device portfolio. In biosensing applications, a device must be highly selective towards the analyte, sensitive at low concentrations, label-free, rapid and simple to use (Carpenter et al. 2018). Carbon-nanotube based field-effect transistors (NT-FETs) go a long way to fit these criteria, and there has been an explosion of biosensing prototypes developed over the last 20 years (Allen et al. 2007; Yao et al. 2021). As the repertoire grows, researchers are continually striving to better NT-FET performance by tackling device limitations. The Debye length represents one such of these; an electrochemical parameter dictating the maximum distance an analyte can be from the transduction channel before ionic screening counters their gating effect (Stern et al. 2007). In physiological strength buffers, this distance is estimated at 0.7 nm (Xu et al. 2021; Lee et al. 2022), placing key receptor proteins such as antibodies (~ 10 nm in size) well-beyond this distance (Zheng et al. 2021). *In silico* modelling goes some way to indicate receptor protein suitability, but further computational studies to help us understand the precise mechanism of receptor protein—NT-FET interfacing would go a long way to help us to understand the likely binding conformation of analytes, and their proximity to the transistor channel.

In light of this, I looked to use my β-lactamase inhibitor protein-II p-azido-L-phenylalanine (BLIP-II^{AzF}) functionalised NT-FETs as the model system to replicate. The non-natural amino acid (nnAA), AzF, was introduced into receptor protein BLIP-

II to covalently anchor the proteins to single-walled carbon nanotubes (SWCNTs) through photochemical excitation (Chapter 3). The geometry of this reaction is crucial for our understanding of the BLIP-II[AzF]—NT-FET interface, so the mechanism is illustrated in Figure 4.1. On exposure to UV light (<310 nm), the azide group converts to a nitrene radical with the release of N_2. The nitrene radical then electrophilically attacks the π electron-rich side walls of SWCNTs to form a covalent hetero-bridged structure (Chin et al. 2002; Setaro et al. 2017). The C-N bond connecting the protein and SWCNT is seen to project perpendicularly and will dictate the binding position of BLIP-II with regards to the AzF side chain rotamer.
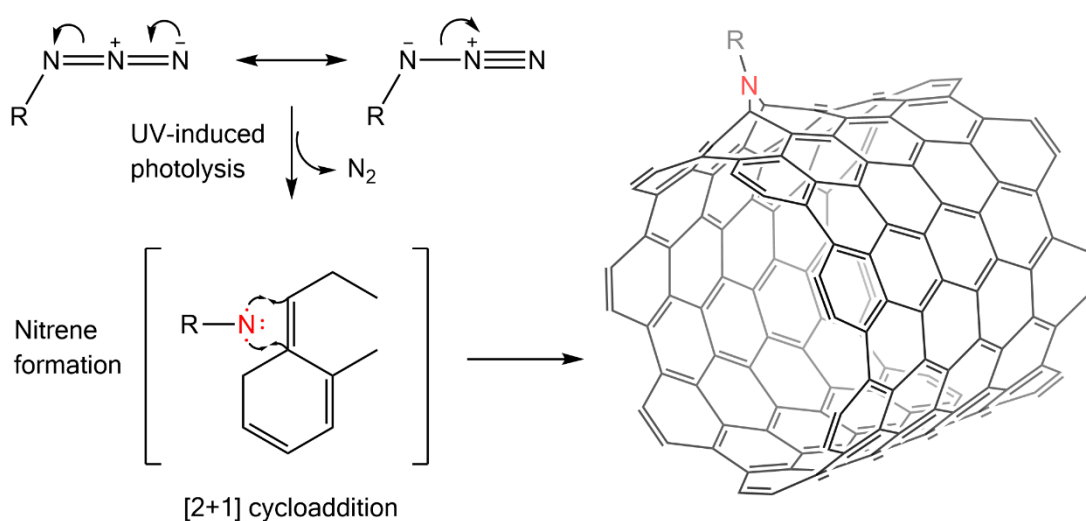
Figure 4.1 – Mechanism of AzF cycloaddition to SWCNTs. UV irradiation extrudes N_2 and generates a nitrene radical. The radical electrophilically attacks the SWCNT to form an intermediate aziridine ring, before relaxing into a hetero-bridged structure.

Amino acid side chains regularly sample different rotamers, which could vary (i) the probability of AzF being sterically available for SWCNT interfacing, and (ii) the compatibility of the BLIP-II[AzF] anchor to mediate proximal analyte sensing. Rotamers are largely dictated by their side chain dihedrals (χ_n), of which AzF has two: χ_1, between C_α and C_β, and χ_2, between C_β and C_γ. The χ_1 angle is anticipated to have the biggest effect on AzF's rotamers, with the favoured gauche[+] (-60°) and trans (180°) configurations resulting in a 120° swing of the phenyl azide group. The χ_2 angle, meanwhile, is limited by the sp^2 hybridised C_γ and can only induce twists to the phenyl ring. Nevertheless, the χ_1 angles are sufficient to change the binding orientation of BLIP-II[AzF] to SWCNTs, and this is exemplified by BLIP-II[213AzF] in Figure

4.2. Here, the gauche$^+$ configuration has the β-lactamase binding face positioned adjacently to the SWCNT, allowing for intimate binding of β-lactamases within the Debye length. The trans configuration, on the other hand, has the β-lactamase binding face angled away from the SWCNT, accessible to analytes but well-beyond the Debye length.
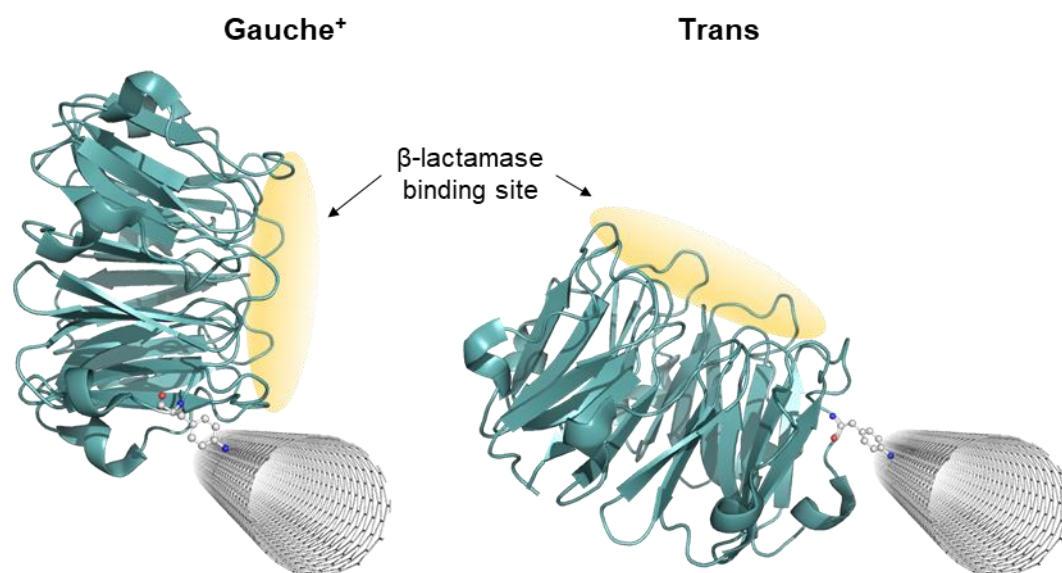
Figure 4.2 – Effect of χ₁ dihedral on BLIP-II[213AzF] binding conformation.
Gauche$^+$ configuration places the β-lactamase binding site adjacent to the SWCNT, while the trans configuration has it pointing away.

Elucidating the gauche$^+$ and trans rotamer states of AzF is a good first step to modelling the BLIP-II[AzF]—SWCNT interface, but external factors influencing their propensity cannot be ignored. Changes to the local backbone angle (φ and ψ), secondary structure, intramolecular bonding, and the physicochemical environment e.g., pH and electrostatic potential, can all influence rotameric disposition (Dunbrack 2002; Chamberlain and Bowie 2004). Rotamer libraries have been built to largely account for these, but as a nnAA, AzF has no reference (Dunbrack and Karplus 1993; Lovell et al. 2000; Scouras and Daggett 2011). Replicating BLIP-II[AzF] through molecular dynamic studies was therefore the only solution to acknowledge these external factors.

Extracting data on rotamer dynamics can be done via several methodologies. Directly collecting data on χ angles has allowed rotamers to be analysed by time (Engh et al. 1986; Das et al. 2016), population (Watanabe et al. 2013), principle

component analysis (Altis et al. 2007) and by rotamer libraries (Haddad et al. 2019). However, this can be a time-consuming process if there are multiple χ angles to consider, and for novices in the MD field, classifying side chain rotamers from the χ angles may not be immediately obvious. Clustering is an alternative technique that can be applied to individual amino acids. It aims to group molecular subsets based on conformational similarity, and a variety of algorithms have been developed (Shao et al. 2007). While it's perfect in premise, there is scope for considerable user bias, for example in choosing the appropriate cluster count, choosing an appropriate cut-off value, or assigning the atoms to use in a pairwise comparison. Complex statistical assessment is required to derive non-biased values, and this may not be accessible to all MD users. A final methodology is the use of root mean squared deviation (RMSD) to derive protein conformers. RMSD is calculated by aligning the trajectory structure to the starting structure, measuring the distance between the two, and plotting against time to link global changes in protein structure to specific RMSD values (Amusengeri et al. 2020; Sanyanga and Tastan Bishop 2020; Amusengeri et al. 2022). Only recently has this method been applied to individual amino acids, where Riziotis et al. (2022) used it demonstrate residue flexibility at the active site of proteins; offering a simple, unbiased approach to side chain rotamer analysis. This will form the basis of my analysis approach.

This chapter aimed to take a closer look at the BLIP-II[AzF]—NT-FET interface and establish whether I could predict AzF mutation site success in mediating proximal analyte sensing. In my approach I used AlphaFold (Jumper et al. 2021) to generate replicate protein structures of the gene sequences translated *in vitro* (BLIP-II[41AzF] and BLIP-II[213AzF]). These structures were fed into the molecular dynamics software GROMACS (Bekker et al. 1993), while the simulation parameters were set by an AzF-modified CHARMM36 forcefield (Best et al. 2012). Simulations were run for 200 ns, and three repeats were performed for each BLIP-II[AzF] variant. Data was extracted on backbone flexibility and AzF RMSD, to build a cohesive picture on AzF dynamicity. Side chain rotamer propensity was established and structures were extracted to perform *in silico* modelling with a SWCNT bundle. Successful rotamers (e.g., where no steric clash was recorded between BLIP-II and the SWCNTs) had crystal structures of analyte β-lactamase proteins aligned to assess their distance from the SWCNT bundle and whether they would pass through the Debye length. APBS electrostatics was finally performed to consider what electrostatic surface potential could be present, and how this could induce gating effects.

4.2 Results and Discussion

4.2.1 BLIP-II starting structures

For MD analysis to be performed on a protein, a starting structure must be provided in the form of a .pdb (protein data bank) file. Typically, this is published crystal structure, but for analysis of BLIP-II[41AzF] and BLIP-II[213AzF], representative structures had to be built. BLIP-II has three crystal structures: 1JTG, 3QI0 and 3QHY (Lim et al. 2001b; Brown et al. 2011). AzF could have been substituted into any of these structures to generate BLIP-II[41AzF] or BLIP-II[213AzF] models, but this wasn't necessarily the most accurate representation of the protein produced *in vitro* because there are slight differences in the translated sequences. One of these differences is the starting N-terminal residue. The gene sequence in my BLIP-II pET-24a plasmid encodes an N-terminal residue of Ala[41] while the crystal structures 1JTG and 3QI0 have either Val[39], or Thr[42] / Ser[43], respectively (Lim et al. 2001b; Brown et al. 2011). As I plan on studying the effect of AzF incorporation at the N-terminal residue (BLIP-II[41AzF]), neither of these crystal structures would simulate the conformational freedom associated with an N-terminal AzF[41] residue. The 3QHY structure, by comparison, did have Ala[41] as its N-terminal residue, and arguably this could have been substituted for AzF[41] and used as the starting structure (Brown et al. 2011). However, my protein sequence *in vitro* also included an extended His tag from the C-terminal. While the extended His tag has no relevance to the research question being asked, the computational model should be as representative as possible of the exact BLIP-II[AzF] variants investigated in Chapter 3. Therefore, I decided to generate my starting structures using AlphaFold, as it would create a geometrically optimised structure which factored in the Ala[41]/AzF[41] N-terminal residue and the extended C-terminal His tag (Jumper et al. 2021).

The AlphaFold protein structures were generated according to Methods 2.2.2, with the starting structure assembled in PyMOL to incorporate AzF (Methods 2.2.3.4; Gfeller et al. 2013; Schrödinger and Delano 2015). The starting structures for BLIP-II[41AzF], BLIP-II[213AzF] and control protein WT BLIP-II were aligned to the BLIP-II 3QHY crystal structure to investigate structural similarity and achieved all atom-alignment RMSD of 0.039 nm, 0.038 nm and 0.040 nm, respectively. This confirmed the AlphaFold models were representative of the BLIP-II crystal structure. The final starting structures are depicted in Figure 4.3, where the extended His-tag is visible as the long 'tail' protruding from the bottom of the protein. In BLIP-II[41AzF], AzF is located at the start the beta-sheet adjacent to the His-tag. In BLIP-II[213AzF], AzF is located further from the His-tag, and sits on an axis perpendicular to 41 AzF

mutation. WT BLIP-II has been included as a control, modelling the protein without the AzF residue.
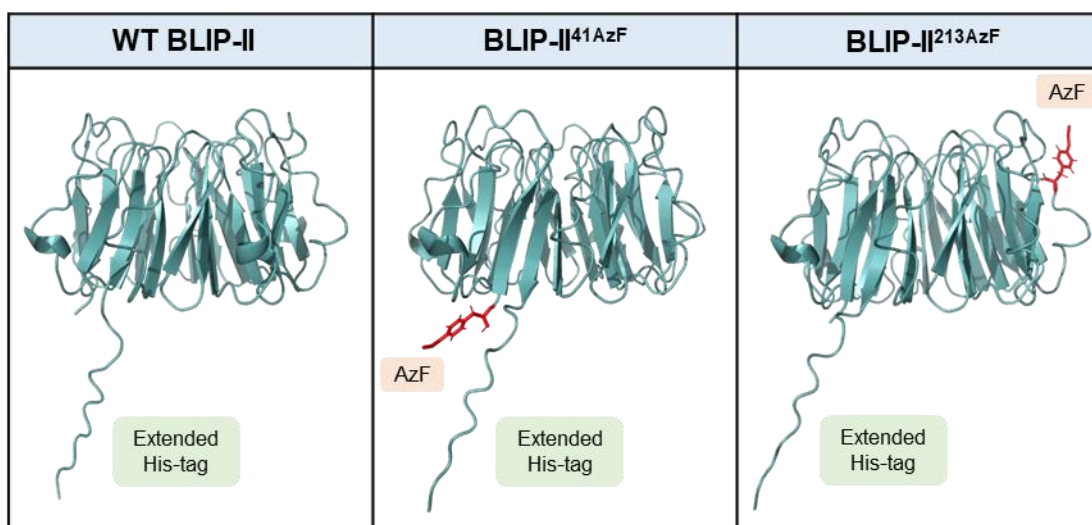
Figure 4.3 – BLIP-II starting structures. Structures were generated for each variant using the translated gene sequence of BLIP-II using AlphaFold (Jumper et al. 2021). The outputted .pdb files were then edited in PyMOL to incorporate the AzF residue (highlighted in red), generating the starting structure for the BLIP-II^{AzF} variants.

4.2.2 Parameterising AzF into CHARMM36 forcefield

To model the MD of a nnAA-containing protein, the topology and charge of the non-natural element must be defined within the simulation forcefield. Forcefields inform the molecular dynamics software, GROMACS, on the parameters associated with a molecule's time evolution (Methods 2.2.3.2; Bekker et al. 1993). Through a process of parameterisation, the CHARMM36 forcefield was adapted for this purpose (Methods 2.2.3.3; Best et al. 2012). In brief, an AzF structural file prepared by former lab member Dr. Harley Worthy, was submitted to ACPYPE to derive values for bond lengths, dihedral angles and partial charges (Sousa Da Silva and Vranken 2012). The values were then manually input into the CHARMM36 forcefield files, with the relevant changes detailed in Appendix Table 8.2 – Table 8.15. Atom types were assigned to AzF using the CHARMM naming convention, with new atom types defined for the azide group (Figure 4.4).
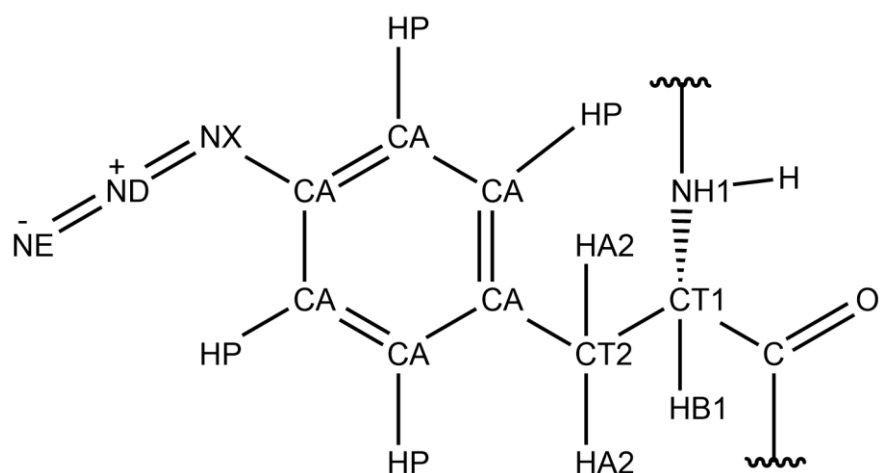
Figure 4.4 – AzF atom types in the adapted CHARMM36 forcefield. Atom types were assigned based on the CHARMM naming convention, but new atom types had to be defined for the azide group: NX, ND and NE.

4.2.3 MD simulation

Following the assembly of the BLIP-II starting structures, and construction of the AzF-compatible CHARMM36 forcefield, the files were submitted to GROMACS for simulation (Bekker et al. 1993). Energy minimisation was performed on the structures until convergence was reached, 'relaxing' the protein and removing any possible steric clash that may have occurred following AzF incorporation in BLIP-II[41AzF] and BLIP-II[213AzF] (Methods 2.2.3.5). A two-step temperature and pressure equilibration then followed, with the solvent adjusted around the protein to the parameters defined (Methods 2.2.3.6). Finally, a 200 ns MD production run was launched (Methods 2.2.3.7). Each protein variant had three repeated simulation runs, producing 600 ns of data, with energies and structural coordinates being collected every 10 ps.

4.2.4 Simulation control checks: RMSD and radius of gyration

To assess the simulation success, the structural stability of the protein models was analysed using whole protein RMSD of the C_α backbone and the radius of gyration. Whole protein RMSD has long been recognised as measure of conformational stability, as it compares each structure from the simulation trajectory against the reference starting structure (Kabsch 1976). A stable protein structure will have a low RMSD score as there is a high degree of similarity. According to literature, this

RMSD range is placed between 0.15 – 0.25 nm for RMSD alignment along the C_α backbone (Bolhuis 2006; Arnittali et al. 2021). If RMSD values are much higher than this, it could suggest the protein has unfolded. The radius of gyration is also a measure for a protein's structural stability and considers its compactness. A stable protein will maintain a steady radius, whilst an unstable, unfolding protein, will have an increasing radius (Arnittali et al. 2019).

Preliminary analysis was carried out to identify the range of residues that should be defined as the whole protein. RMSD collected on the C_α backbone for WT BLIP-II showed a huge disparity when the His tag was included and excluded from this definition (Figure 4.5). The His-tag, extended by serine and glycine repeats, is designed to be flexible so it can access and coordinate to the nickel atoms in the affinity purification column. However, these degrees of freedom skew the protein's C_α backbone RMSD to make it look more unstable than it is. For these reasons, analysis performed on the whole protein will exclude the His tag by use of an index file that will specifically extract data on residues 41 – 310.
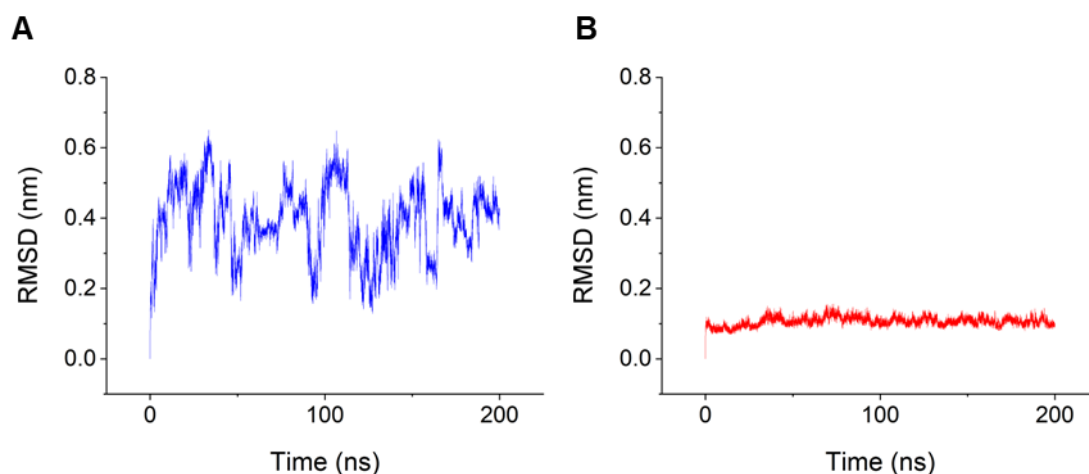
Figure 4.5 – Whole protein RMSD with and without C-terminal His tag. (A) WT BLIP-II RMSD data collected from C_α backbone which included the extended His tag (residues 41 – 322), and (B) which excluded the His tag (residues 41 – 310).

Whole protein RMSD data was extracted for all 3 protein variants across 3 repeats, using the newly defined index file (Figure 4.6 (A – C)). RMSD remained consistent across all protein variants, ranging between 0.09 – 0.15 nm. Radius of gyration (Figure 4.6 (D – F)) stayed constant, with values largely between 1.73 – 1.76 nm. The static nature of these parameters suggests the proteins remained stable over

the 200 ns simulation and could be taken forward for further analysis. The first 10 ns of each repeat, however, will be discarded, as the data produced in this time is considered part of the 'warm up' phase and could skew the total data if included. All further analysis will therefore take place with the latter 190 ns of the simulation.
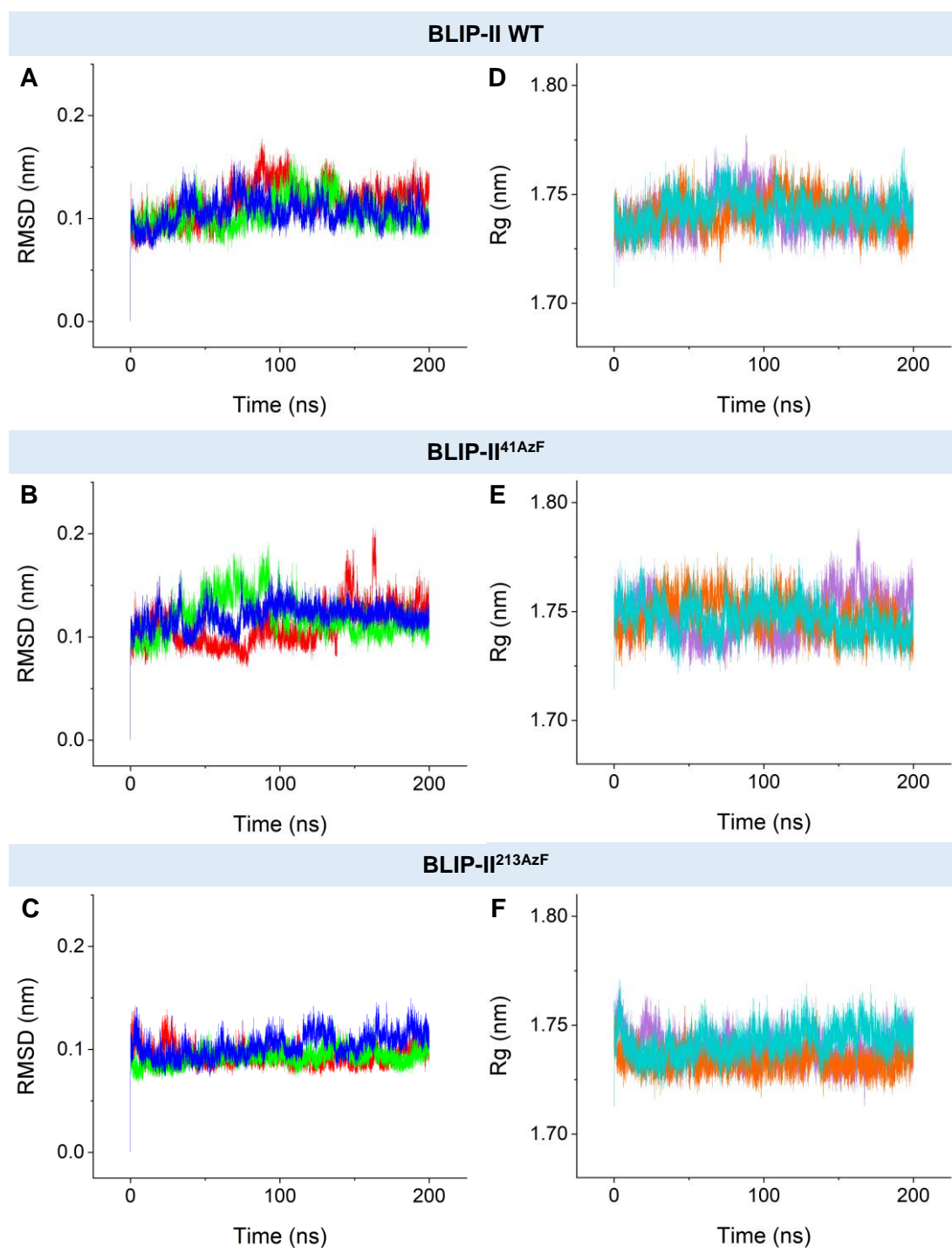
Figure 4.6 – Whole protein RMSD and radius of gyration. Data was extracted for residues 41 – 310, with RMSD data collected from C_α backbone and radius of

gyration (Rg) collected from all protein atoms. RMSD graphs (A – C) are coloured red, green and blue for repeats 1 – 3, respectively. Radius of gyration graphs (D – F) are coloured lilac, orange and turquoise for repeats 1 – 3, respectively.

4.2.5 BLIP-II[41AzF] MD analysis

4.2.5.1 RMSF and B-factors

To assess the effect of the AzF mutation at residue 41, an average root mean squared fluctuation (RMSF) value was calculated for each residue across the three repeats of WT BLIP-II and BLIP-II[41AzF] (Figure 4.7). RMSF is a measure of a residue's individual flexibility and motion. Where RMSD is calculated as the average positional difference between a reference and trajectory structure as a function of time, RMSF is calculated as the average atomic variation of individual residues over the whole trajectory, as a function of the residue (Arnittali et al. 2021).

With only one residue mutated, it was unsurprising that most of the RMSF values of BLIP-II[41AzF] aligned closely with the WT BLIP-II. However, one notable difference is the shift in RMSF at residue 41. Located at the N-terminus, this residue will typically have a higher mobility than those constrained by secondary or tertiary protein structure (Arnittali et al. 2021). However, the introduction of AzF at this location has more than doubled the RMSF to ~0.4 nm. This difference can be attributed to the side chains of the residues, as the phenyl azide is much larger than the methyl group of alanine in WT-BLIP-II, and a larger area will be covered when undergoing flux.
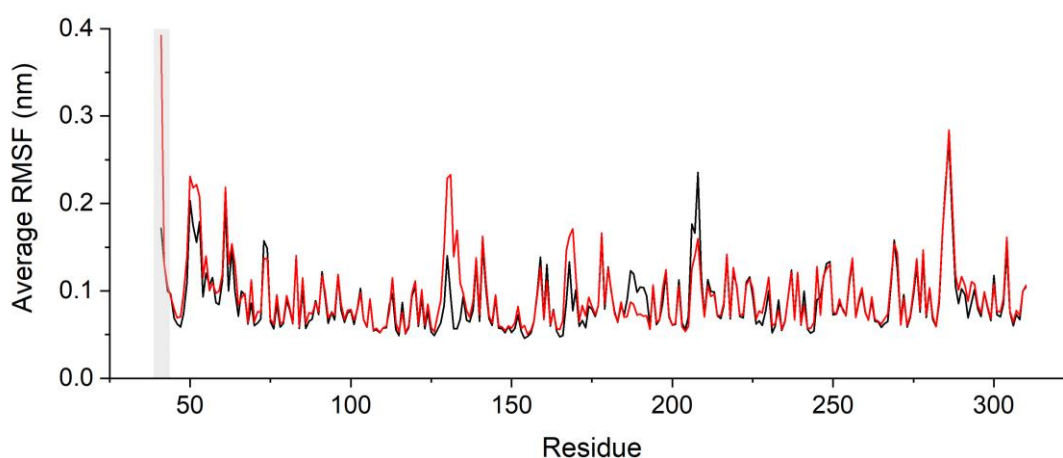
Figure 4.7 – Average RMSF of WT BLIP-II and BLIP-II[41AzF]. RMSF was calculated for each residue (all atoms) over the 190 ns simulation and averaged across the

repeats. WT BLIP-II is shown in black, BLIP-II[41AzF] in red, and residue 41 is highlighted in grey.

RMSF is also seen to vary by up to 1.0 nm around residues 50, 131, 167, 188 and 207. As observed in the literature, these residues and those adjacent, are heavily involved in BLIP-II's binding interface, predominating at apical β-turns and loops (Brown et al. 2013b). The surface-exposed nature of these residues permits a higher degree of freedom and space for rotamers to occupy, so the observed differences between the wild-type and BLIP-II[41AzF] are likely to be a factor of rotamer population in the simulation, rather than an indirect effect of AzF introduction.

These residues can be mapped onto the protein structure (Figure 4.8) by converting the RMSF values to B-factors. More commonly associated with crystallographic atomic displacement, B-factors are the measure of a structure's vibrational energy (Debye 1913; O'Connor 1975). The conversion of RMSF (in nm) to B-factors (in Å^2) allows PyMOL to plot a residue's fluctuation in three dimensions, where increased cartoon putty thickness and warmer heatmap colouring denote high flexibility. The AzF residue has the highest B-factor score, while the apical β-turns are next most prominent, indicative of their flexibility and function.
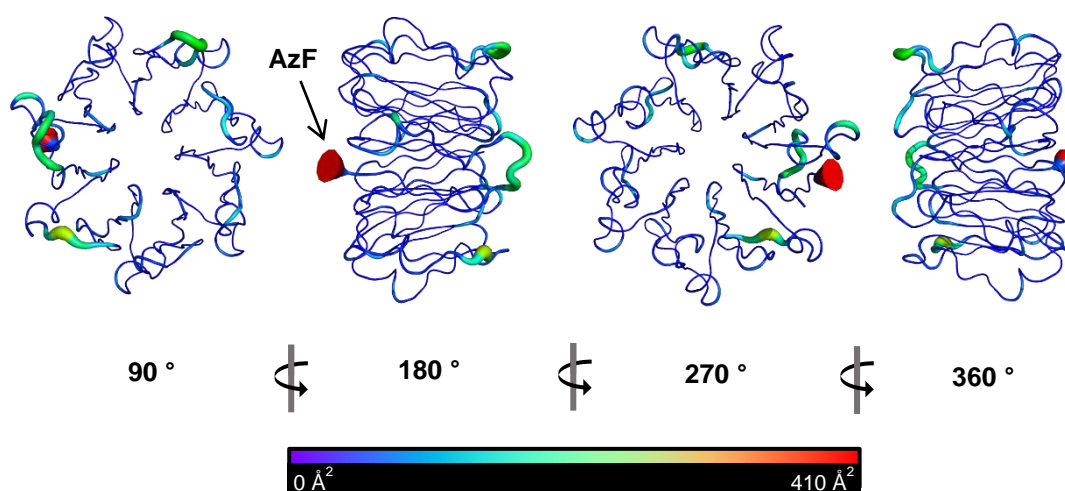
Figure 4.8 – Average B-factors of BLIP-II[41AzF]. B-factors calculated for the whole protein (residues 41 – 310) across the 190 ns simulation, averaged across the three repeats, and plotted per residue.

4.2.5.2 AzF rotamer analysis

To identify key rotamers of AzF, RMSD analysis was used. In this two-step approach, the protein structure was fitted through a least squares alignment to the C_α, C_β and CO of AzF in the reference structure. These atoms were chosen to account for backbone flexibility and to capture the changes in the χ_1 angle. The distance moved by the phenyl ring was then recorded every 10 ps. As the phenyl ring is planar to the azide group, I can assume the shift in RMSD applies to the phenylazide side chain. This analysis was performed for each repeat, with repeat 1 shown in Figure 4.9.

When RMSD is plotted against time, rotameric states can be identified by clustered RMSD values as it implies the phenylazide consistently deviates a particular distance from the reference structure. In repeat 1, these values centre around ~0.50 nm RMSD, but fluctuate to values of 0 – 0.20 nm (Figure 4.9 (A)). This data can be portrayed through a frequency distribution plot to identify specific phenylazide rotamer populations (Figure 4.9 (B)). Calculated as a percentage of the total number of data points extracted, 76 % of the structures were grouped into the rotamer 1 population which had an RMSD range of 0.34 – 0. 59 nm and modal group at 0.53 nm. Meanwhile, 18.9 % of the structures were identified as rotamer 2 which had an RMSD range of 0.14 – 0.33 nm and modal group at 0.22 nm. There is no clear population peak between 0 – 0.15 nm, and whilst this could represent a subpopulation of rotamer 2, it hasn't been quantified as part of it. The shape of the distribution provides further insight, with the flatter, skewed population between 0 – 0.33 nm suggesting an ill-defined cluster of rotamers, and the tall, symmetrical peak of rotamer 1 suggesting a well-defined population with a normal distribution. To assess the structural implications of rotamers *in silico*, protein structures corresponding to the RMSD modal groups at 0.53 nm (rotamer 1; red) and 0.22 nm (rotamer 2; green) were extracted (Figure 4.9 (C)). The χ_1 angle was identified to be trans for rotamer 1, and gauche[+] for rotamer 2. A frame stack of the simulation then allowed me to compare the rotamer populations against the global protein structure. Rotamer 1 matched the concentrated cluster of residues which projected parallel to bulk BLIP-II[41AzF] structure, but rotamer 2 was more difficult to discern. While the 120° swing in χ_1 angle was evident, rotamers projected widely about this angle. This observation is supported by the flat and broad RMSD population distribution between 0 – 0.33 nm, which suggested an ill-defined cluster of rotamers. An important note to add here is that in the frame stack, BLIP-II[41AzF] structures were superimposed through a whole protein alignment. Rigid structural elements, e.g.,

the repeating β-propellor structures, were tightly aligned to, while the more flexible regions (e.g., the N-terminus) showed greater variation. This could therefore exaggerate the spread of phenylazide rotamers associated with the N-terminal residue (AzF[41]) in Figure 4.9 (C).

Figure 4.9 – AzF[41] RMSD analysis: Repeat 1. (A) RMSD of phenylazide over 190 ns. (B) Frequency distribution plot of phenylazide RMSD over 190 ns, with bins set to 0.01 nm. (C) Frame stack of the simulated protein every 2 ns, aligning to the protein in the first frame. Rotamers were identified by the modal group of peaks identified in (B).

In repeat 2, I see a similar pattern emerging (Figure 4.10 (A) and (B)). The RMSD values centred around ~0.45 nm but fluctuated to values of 0 – 0.25 nm. These

numbers are arbitrary and cannot be compared to the RMSD values in Figure 4.9 because the reference structure is unique to each repeat. However, the distribution can be compared, and it follows a similar pattern. A major population peak (rotamer 1) centred around the modal group of 0.45 nm is flatter and broader than repeat 1, with an RMSD range of 0.27 – 0.58 nm. However, it represents a similar proportion of the population: 80.2 %. The minor peak (rotamer 2) centred around the modal group of 0.20 nm is narrower and sharper than repeat 1, with an RMSD range of 0.15 – 0.26 nm. This represented 12.0 % of the rotamer population. The small population between 0 – 0.14 nm was again present branching off the rotamer 2 population, but this was not quantified with rotamer 2, nor as its own peak. In Figure 4.10 (C), structures of rotamer 1 and 2 were extracted and compared to the frame stack of the simulation. The χ_1 angle was identified to be trans for rotamer 1, with the concentrated cluster of residues projecting the phenylazide in a direction parallel to the bulk BLIP-II[41AzF] structure. Rotamer 2 exhibited the gauche[+] χ_1 angle and predominantly projected the phenylazide into the bulk solvent. In an interesting development, the residues proximal to rotamer 2 appeared more ordered than in repeat 1, which is likely due to the better-defined subpopulation between 0 – 0.14 nm.
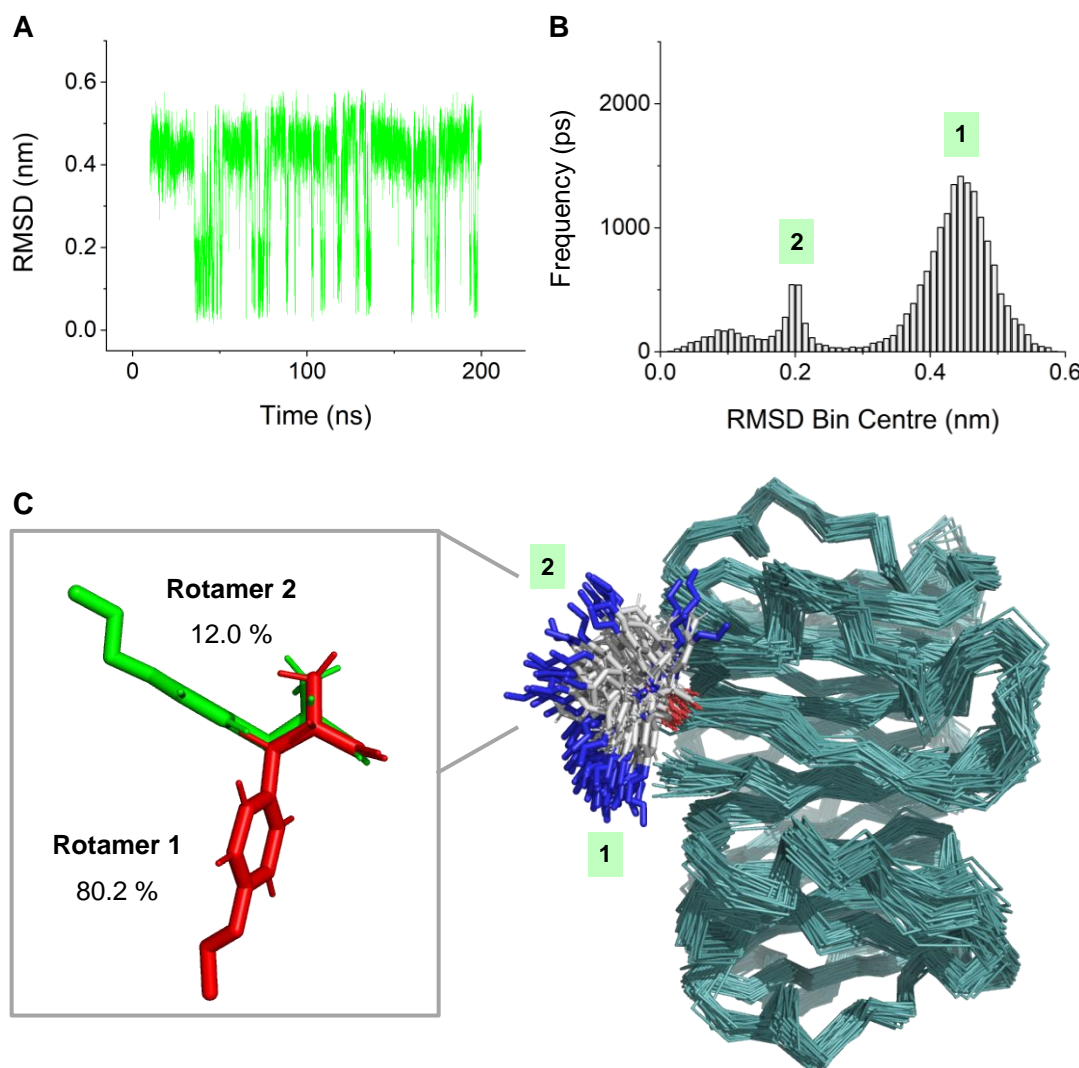
Figure 4.10 – AzF[41] RMSF analysis: Repeat 2. (A) RMSD of phenylazide over 190 ns. (B) Frequency distribution plot of phenylazide RMSD over 190 ns, with bins set to 0.01 nm. (C) Frame stack of the simulated protein every 2 ns, aligning to the protein in the first frame. Rotamers were identified by the modal group of peaks identified in (B).

In repeat 3, the outcomes were much the same as the other two runs; indicative of consistent and reliable results. RMSD values were centred around ~0.50 nm but fluctuated to values between 0 – 0.20 nm (Figure 4.11 (A)). The population distribution showed a large symmetrical peak for rotamer 1, with a modal group at 0.49 nm and RMSD range of 0.30 – 0.58 nm (Figure 4.11 (B)). This represented 78.0 % of the population. The minor peak of rotamer 2 totalled 12.3 % of the rotamer population and was centred around the modal group 0.21 nm, with an RMSD range of 0.16 – 0.29 nm. There was an additional data shoulder protruding

from the rotamer 2 peak between 0 – 0.15 nm, but this was not quantified due its ill-defined population. In Figure 4.11 (C), structures of rotamer 1 and rotamer 2 were compared to the simulation frame stack. Rotamer 1 residues were heavily clustered, with the identified trans χ_1 angle projecting the phenylazide in a direction parallel to the bulk BLIP-II[41AzF] protein. Meanwhile, the 120° swing of the χ_1 angle allowed gauche[+] rotamer 2 residues to project the phenylazide into the bulk solvent, in a fairly ordered but less populated manner.
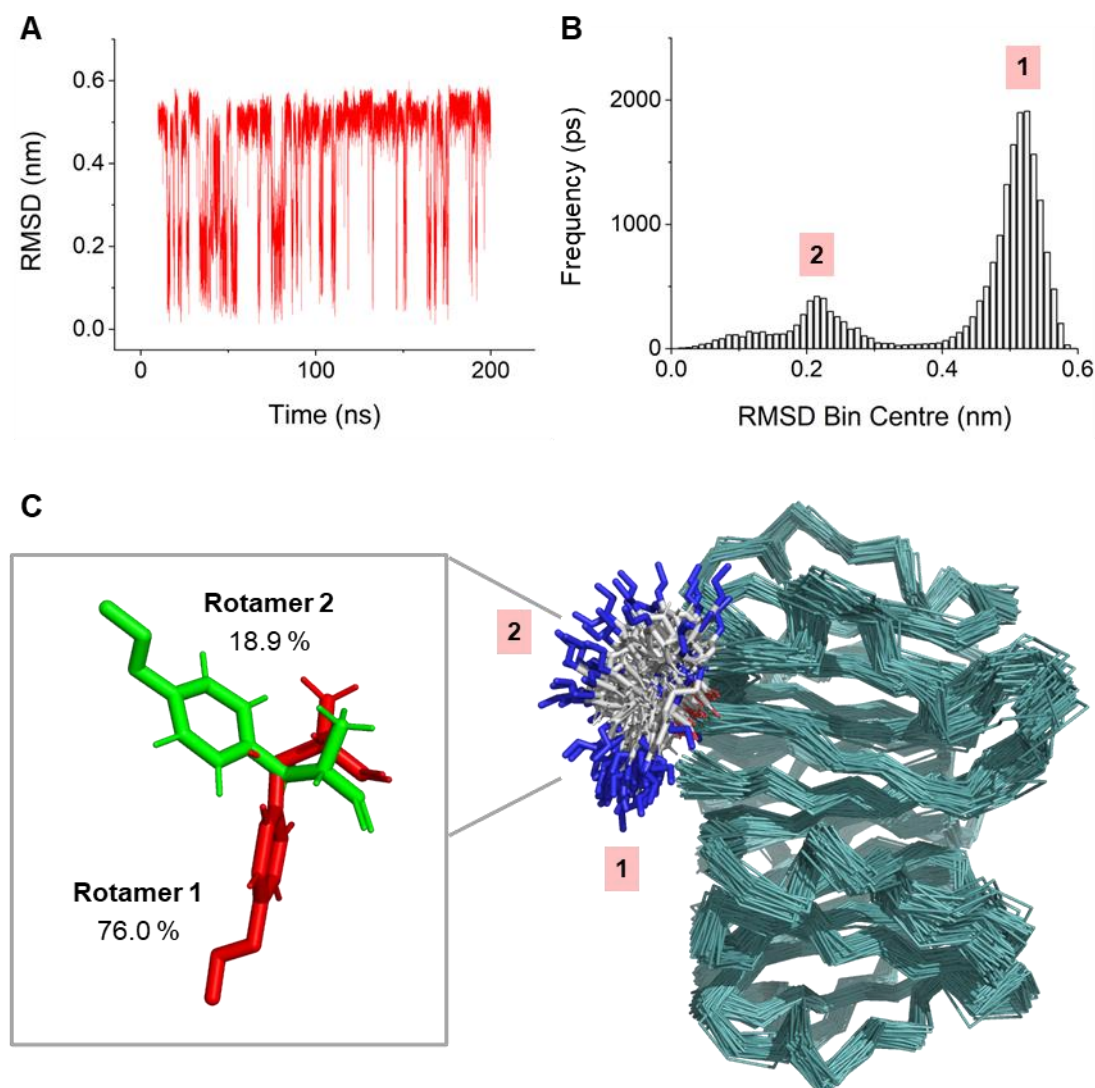

Figure 4.11 – AzF[41] RMSD Analysis: Repeat 3. (A) RMSD of phenylazide over 190 ns. (B) Frequency distribution plot of phenylazide RMSD over 190 ns, with bins set to 0.01 nm. (C) Frame stack of the simulated protein every 2 ns, aligning to the protein in the first frame. Rotamers were identified by the modal group of peaks identified in (B).

To summarise the data collected from the repeats, Figure 4.12 combines all defined rotamers and aligns the BLIP-II protein along the β-sheet connecting to AzF: residues AzFTSSV. Through this alignment, it is evident that both rotamers aligned consistently across all the repeats. The trans χ_1 angle of rotamer 1 projected the phenylazide in a direction parallel to the bulk BLIP-II[41AzF]. Meanwhile, the gauche+ χ_1 angle of rotamer 2 projected the phenylazide outwards, perpendicular to the protein and facing the bulk solvent. These rotamers were therefore taken forward for *in silico* modelling with SWCNT bundles, to identify any possible steric clash and prospective binding orientations.
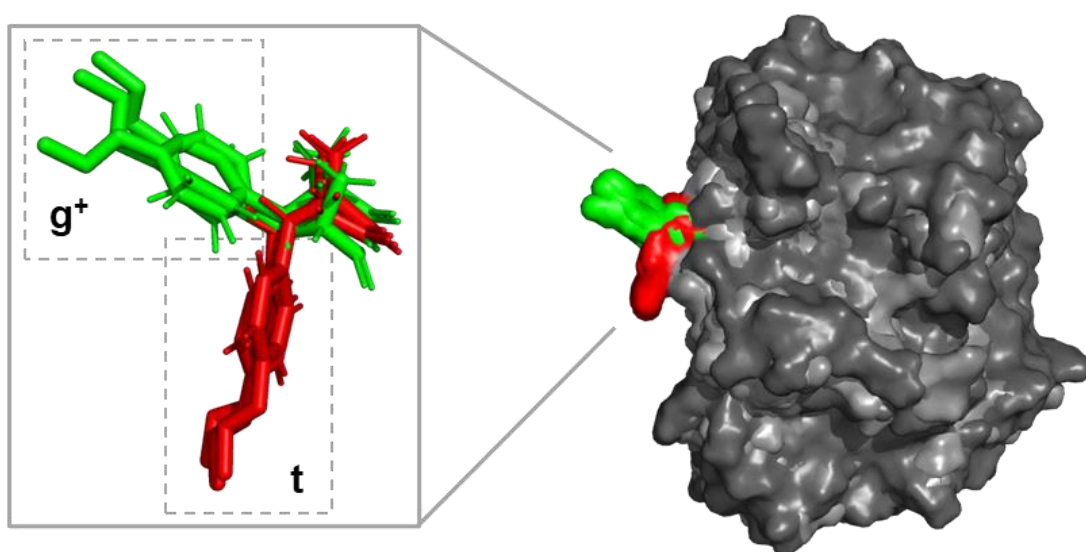
Figure 4.12 – Summary of BLIP-II[41AzF] rotamers. Frames extracted to illustrate rotamer 1 and 2 of AzF have been combined from repeats 1 – 3 and aligned along residues AzFTSSV. Rotamer 1 is red and rotamer 2 is green. The χ_1 angles are denoted as g+ = gauche+, and t = trans.

4.2.6 BLIP-II[213AzF] MD analysis

4.2.6.1 RMSF and B-factors

To assess the effect of the AzF mutation at residue 213, an average RMSF value is calculated for each residue across the three repeats of WT BLIP-II and BLIP-II[213AzF] (Figure 4.13). The RMSF values were similar for both protein variants, with the most significant change again arising from the substitution at residue 213. BLIP-II[213AzF] has an RMSF of 0.25 nm at this position, while WT BLIP-II reaches only 0.1 nm. While this is much lower the RMSF value observed for residue 41 in BLIP-II[41AzF], it

was to be expected because AzF in BLIP-II[213AzF] is constrained between two residues and doesn't have the flexibility of an N-terminal residue. The 2.5-fold increase in RMSF is therefore testament to the size and flexibility of the AzF side chain, which is compared to threonine at residue 213 in WT-BLIP-II.

RMSF was also seen to vary by up to 1.0 nm around residues 73, 208, 269 and 286. As noted in BLIP-II[41AzF] RMSF analysis, there are a cluster of amino acids on BLIP-II's apical face which play a key role in β-lactamase binding and these residues form part of this cluster (Brown et al. 2013b). The surface exposed nature and freedom to adopt different rotamers result in changeable populations; a paradigm linked to each individual simulation and the potential energy available to it.
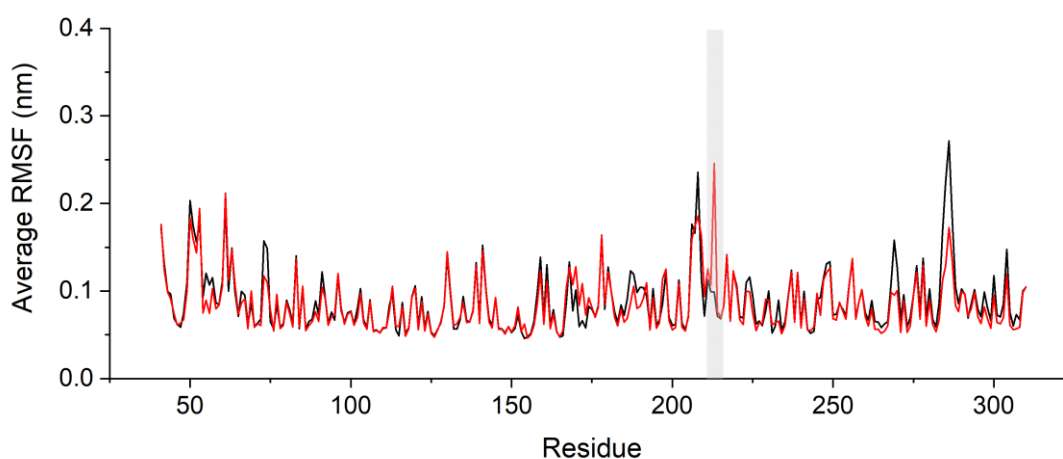
Figure 4.13 – Average RMSF of WT BLIP-II and BLIP-II[213AzF]. RMSF was calculated for each residue (all atoms) over the 190 ns simulation and averaged across the repeats. WT BLIP-II is shown in black, BLIP-II[213AzF] in red, and residue 213 is highlighted in grey.

To map this data on a protein structure, B-factors were extracted from each repeat and averaged to generate Figure 4.14, using the same cartoon putty thickness and colour heatmap scale as Figure 4.8. While no residues were coloured yellow/orange/red, B-factors were still significant across the protein. Residue 213 (AzF) scored the highest at 167 $Å^2$, while other regions of high RMSF included BLIP-II's apical face and surface exposed loops and turns. The centre of the protein appeared to have the lowest B-factors, with residues likely constrained by the regimented β-barrel structure.
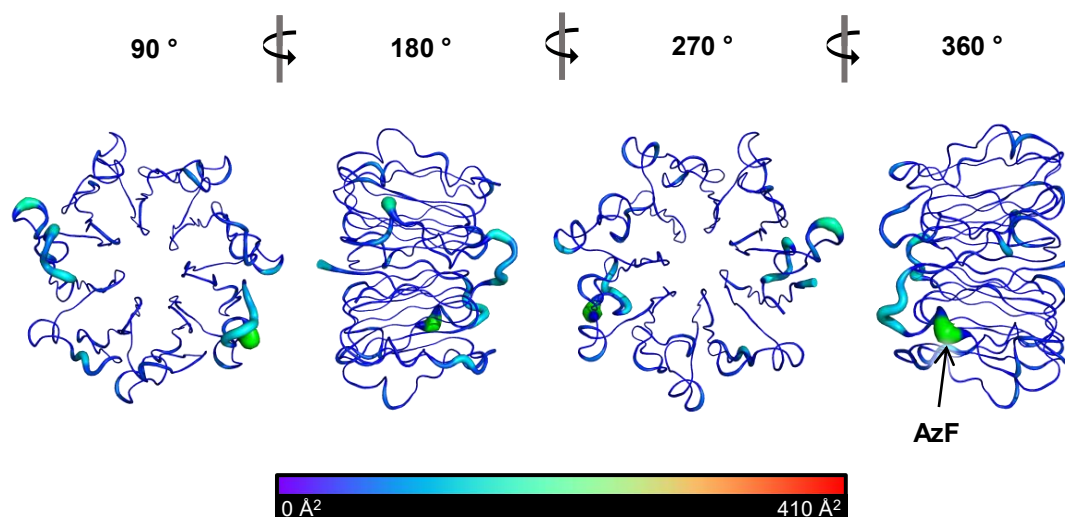
Figure 4.14 – Average B-factors of BLIP-II²¹³ᴬᶻᶠ. B-factors calculated for the whole protein (residues 41 – 310) across the 190 ns simulation, averaged across the three repeats, and plotted per residue.

4.2.6.2 AzF rotamer analysis

To analyse the rotamers dominating across the BLIP-II²¹³ᴬᶻᶠ simulations, the same two-step RMSD analysis was performed on AzF. This comprised of a least squares fit to C_α, C_β and CO, while the displacement of the phenyl ring from the reference structure was measured every 10 ps. As mentioned previously, the phenyl ring is planar to the azide group so I can assume the shift in RMSD corresponds to the entire phenylazide group.

In repeat 1 of BLIP-II²¹³ᴬᶻᶠ (Figure 4.15 (A)), phenylazide RMSD progressed through several chronological stages. Starting off at 0.20 nm, RMSD shifted at 8 nanoseconds to its majority population at ~0.45 nm. Towards the end of the simulation, RMSD shifted again to ~0.50 nm, with the RMSD range narrowing from ~0.40 – 0.53 to ~0.48 – 0.53 nm. When plotted as a population distribution (Figure 4.15 (B)), the overriding weakness of this analysis approach was revealed: only two peaks were present when three RMSD phases were identified in (Figure 4.15 (A)). This ultimately comes down to the measurement of the phenylazide from the reference structure, as movement is quantified in any direction, e.g., 0.5 nm forwards and 0.5 nm backwards would appear in the same peak of a population distribution. Naturally, dihedral angles constrain what rotamers are available to amino acid side chains, but an unfortunate reference structure (e.g., positioned halfway between two rotamers) would result in two rotamers being masked into one.

This is why the frame stack in (Figure 4.15 (C)) is so crucial to the analysis, double checking the rotamers identified in (Figure 4.15 (A)) correspond to those observed throughout the simulation. Here, rotamer 1 (red) was identified from the modal group at 0.20 nm and represented 4.4 % rotamer population. Rotamer 2 (green) had the highest population, representing 83.5 % of the population. Its structure was identified from the modal RMSD group arising from its defined simulation period (18 – 176 ns). The structure for rotamer 3 (blue) was identified using the same method, with its defined simulation period of 176 – 200 ns, and represented 12.1 % of the total rotamer population. Interestingly, closer inspection of the rotamers revealed the χ_1 angles to be gauche$^+$ for rotamer 1, trans for rotamer 2, and gauche$^-$ for rotamer 3. The gauche$^-$ configuration is rare for amino acid side chains to adopt because of the steric hindrance between C_γ and the main chain CO and NH groups. This suggests that an intermolecular interaction may be occurring between rotamer 3 and the bulk BLIP-II^{213AzF} protein to offset the steric hindrance.
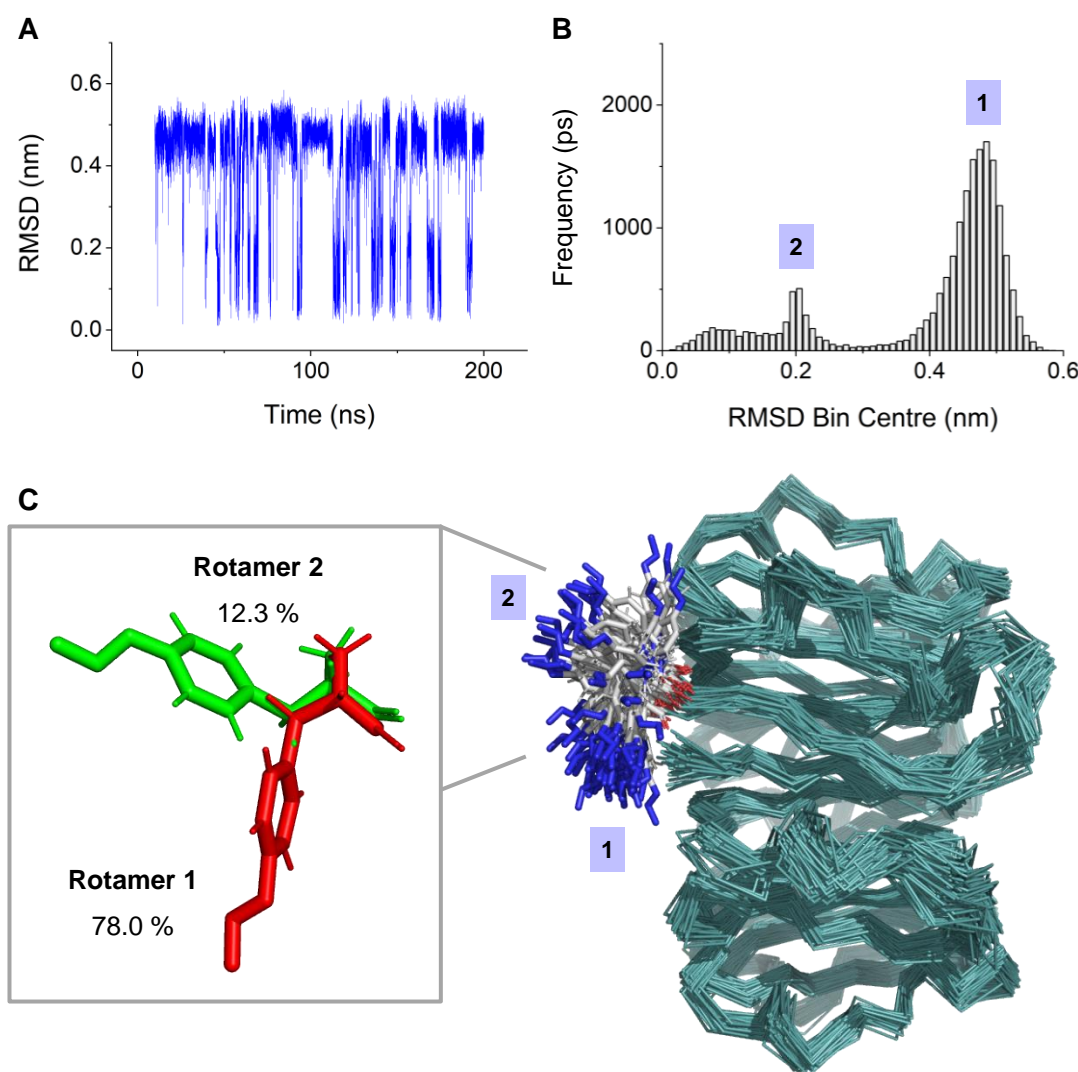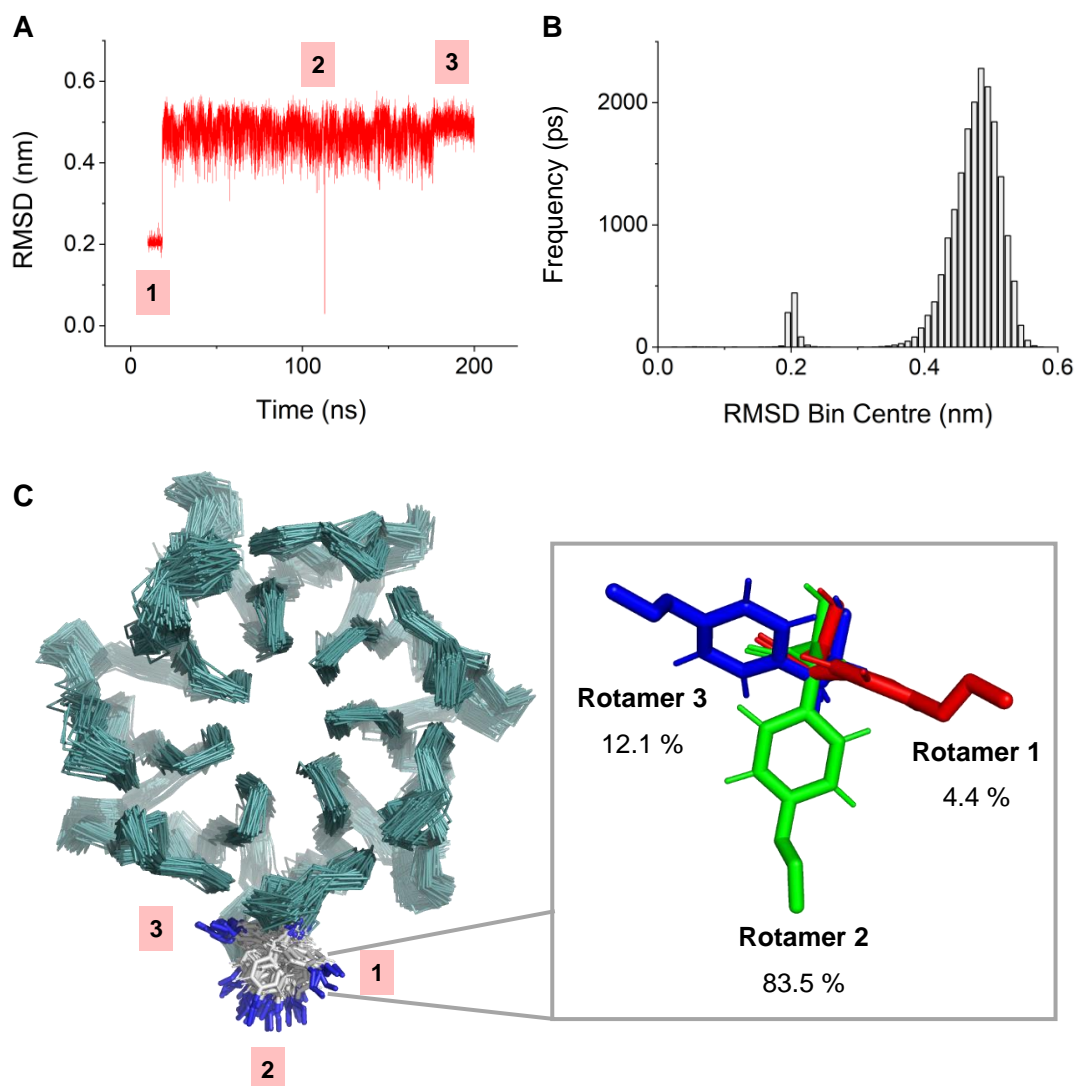
Figure 4.15 – AzF[213] RMSD analysis: Repeat 1. (A) RMSD of phenylazide over 190 ns. (B) Frequency distribution plot of phenylazide RMSD over 190 ns, with bins set to 0.01 nm. (C) Frame stack of the simulated protein every 2 ns, aligning to the protein in the first frame. Rotamers were extracted from the modal group of the regions identified in (A).

Repeat 2 is shown in Figure 4.16 and presented very differently to repeat 1. RMSD consistently fluctuated between two values at ~0.10 nm and ~0.20 nm, before shifting to ~0.45 nm after ~135 ns of simulation (Figure 4.16 (A)). When converted to a population distribution, three defined populations emerged (rotamers 1 – 3) with modal groups at 0.07 nm, 0.21 nm and 0.48 nm (Figure 4.16 (B)). Rotamers 1 and 3 were broader peaks, each with an RMSD range that spanned approximately 0.15 nm. Rotamer 2 had a restricted population distribution, but a modal group that achieved a frequency of nearly 2000 ps. This suggested variance within rotamer 2

structures would be minimal. To consider the rotamer structures *in silico¸* the extracted modal group structure was compared to a frame stack of the simulation (Figure 4.16 (C)). Here, a side on view of BLIP-II was taken to best highlight the rotamer differences. Rotamer 1 was marginally the most populous, dominating for 36.9 % of the simulation. Rotamer 2 was seen as an extension of rotamer 1 and represented 29.7 % of the total rotamer population. Interestingly, both rotamer 1 and 2 exhibited the gauche[+] χ_1 angle, but it was hypothesised that intermolecular interaction between the rotamers and the bulk BLIP-II[213AzF] protein may have stabilised slight variations of this which led to the two rotamer populations observed. Rotamer 3, by contrast, exhibited the trans χ_1 angle, swinging the phenylazide group 120° from its rotamer 1 or 2 structure. It occupied this conformation for the remaining 33.4 % of the simulation.
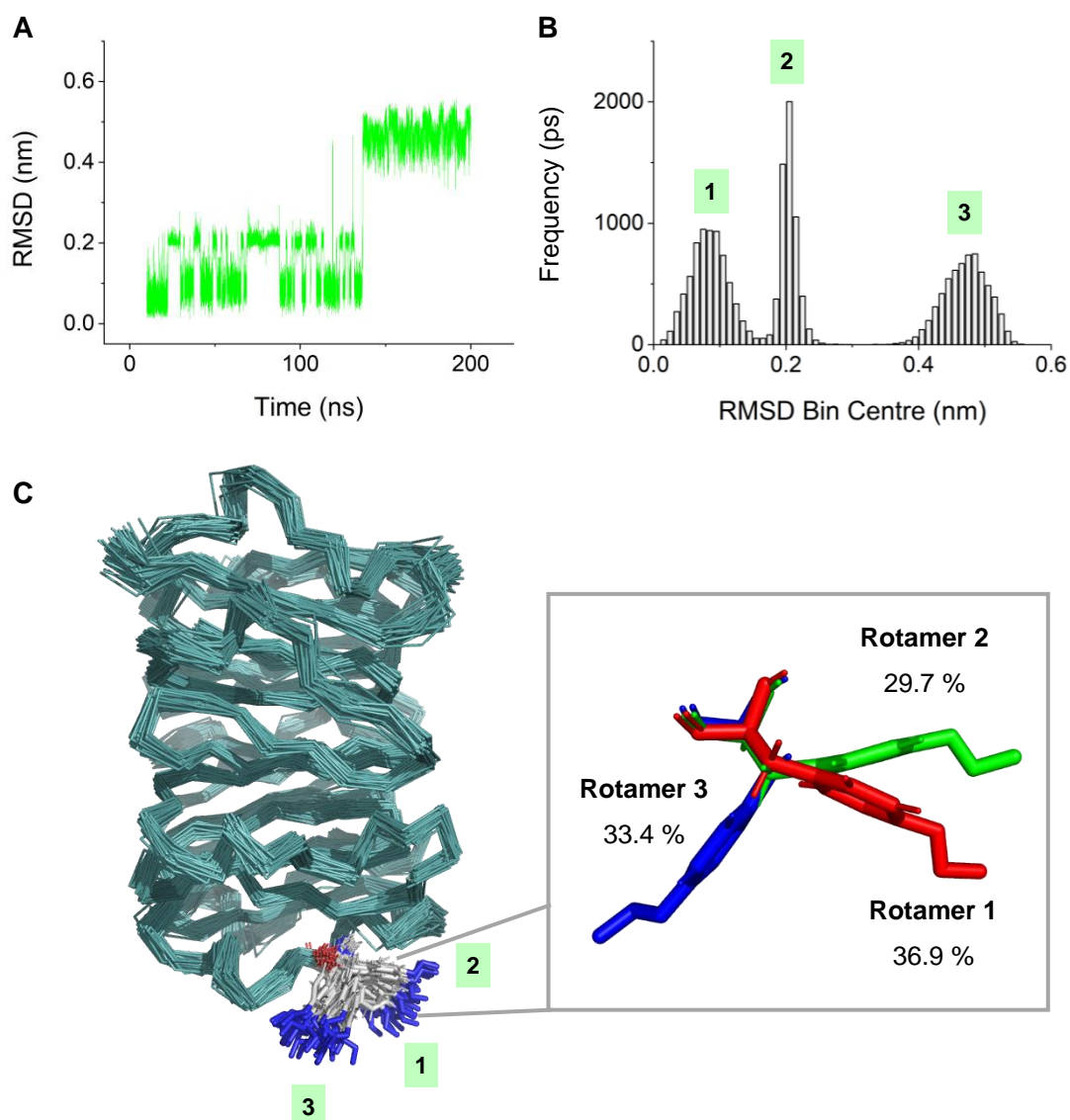
Figure 4.16 – AzF²¹³ RMSD analysis: Repeat 2. (A) RMSD of phenylazide over 190 ns. (B) Frequency distribution plot of phenylazide RMSD over 190 ns, with bins set to 0.01 nm. (C) Frame stack of the simulated protein every 2 ns, aligning to the protein in the first frame. Rotamers were identified by the modal group of peaks identified in (B).

Repeat 3 again presented differently to the other two repeats; with notably only two rotamers identified. RMSD fluctuated between two similar values, ~0.10 nm and ~0.20 nm, with very occasional shifts to ~0.50 nm (Figure 4.17 (A)). The rapid switch between ~0.50 nm and ~0.20 nm suggested this was a temporary state and not worthwhile to quantify. Plotting this data through a population distribution produced two interestingly shaped peaks (Figure 4.17 (B)). The peak centred at 0.12 nm (rotamer 1) had a prominent data shoulder to the left of it, broadening the peak to cover rotamers between 0 – 0.17 nm and thus 54.8 % of the simulation. Meanwhile, rotamer 2 was centred at 0.22 nm, and had a restricted population distribution between 0.18 – 0.31 nm. Rotamer 2 accounted for 43.6 % of the total rotamer population. The lack of a distinct gap between the peaks of rotamer 1 and 2, and the constant fluctuation between states in (Figure 4.17 (A)) suggested these rotamers were structurally similar and easy to switch between. Indeed, the extracted modal rotamer structures (Figure 4.17 (C)) bore a remarkable resemblance and correlated well to the concentrated cluster of AzF residues in the frame stack. Further inspection revealed both rotamer 1 and 2 were gauche⁺ for χ_1, so the constant switching between rotameric states was likely a factor of intermolecular interaction arising from the bulk BLIP-II²¹³ᴬᶻᶠ protein.
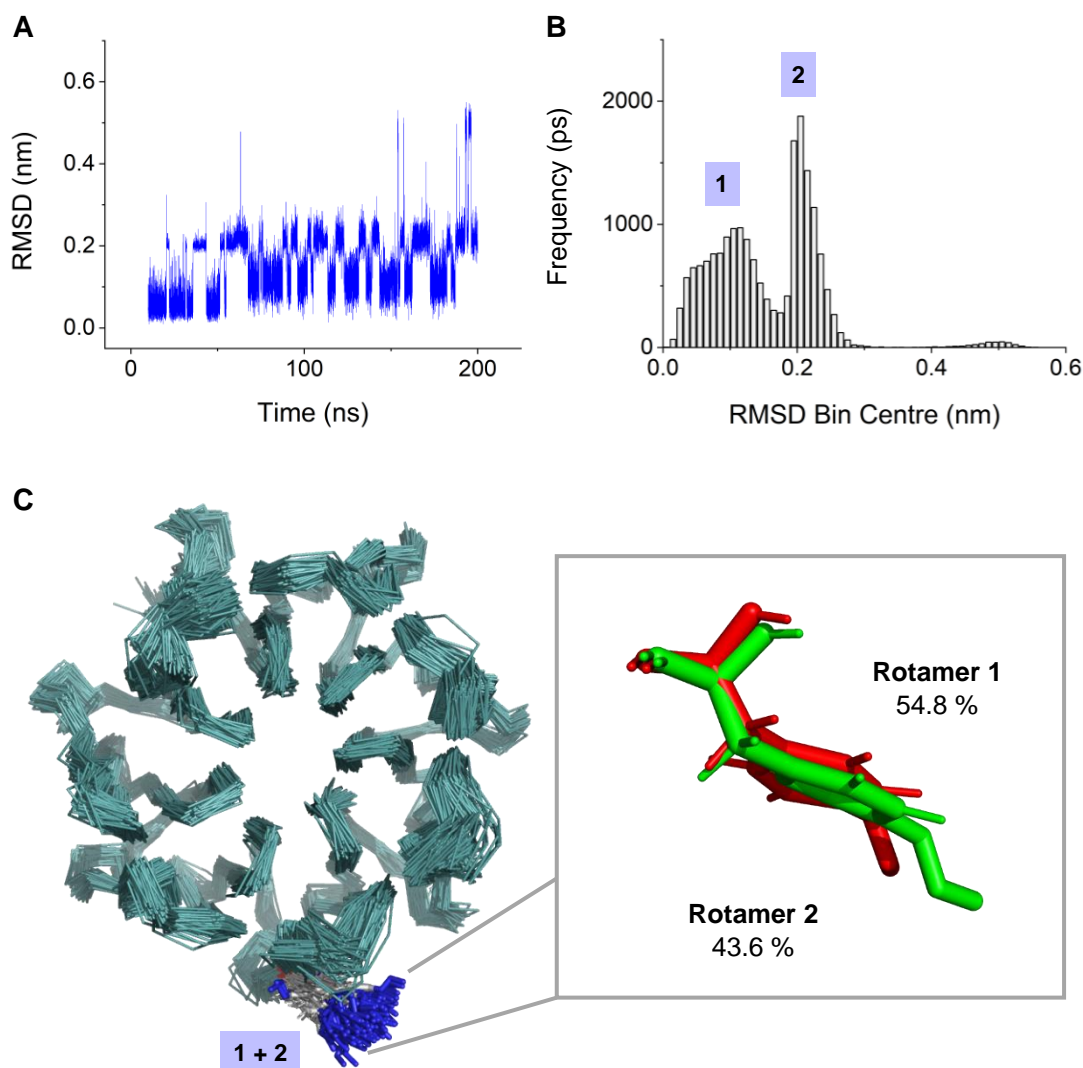
Figure 4.17 – AzF[213] RMSD analysis: Repeat 3. (A) RMSD of phenylazide over 190 ns. (B) Frequency distribution plot of phenylazide RMSD over 190 ns, with bins set to 0.01 nm. (C) Frame stack of the simulated protein every 2 ns, aligning to the protein in the first frame. Rotamers were identified by the modal group of peaks identified in (B).

To analyse the rotamer outputs across all three repeats, it was necessary to combine the structures and align them to the residues adjacent to AzF: QTAzFVP (Figure 4.18). The difference in χ_1 angles allowed for easy distinction between the rotamer structures, but new rotamer groups would be assigned based on structural homology and ability to interface with a SWCNT bundle without steric clash (Table 4.1). For these reasons, the gauche+ population were split into two. The majority of gauche+ rotamers showed close structural homology and were defined as the new rotamer group 1 (red). However, one of the gauche+ rotamers identified in repeat 2

had its χ_1 angle extended, possibly stabilised through an intermolecular interaction with the bulk BLIP-II[213AzF] protein. The resulting conformation caused the AzF rotamer to align closer to the bulk BLIP-II[213AzF] protein, rather than projecting into the solvent. As the mechanism of [2+1] AzF cycloaddition relies upon AzF to integrate perpendicularly to the SWCNT (Introduction 1.4.3.2), the extended gauche+ rotamer would likely induce steric clash between the protein and SWCNT, and would be unfeasible for SWCNT binding. This rotamer was therefore assigned to the speculated steric clash group: new rotamer group 3* (blue). The trans χ_1 population was also a rotamer group divided into two. The residue highlighted in green was assigned to the new rotamer group 2 as it projected straight into the bulk solvent with no suggestion of steric clash. Meanwhile, the extended trans χ_1 variant from repeat 2 was perceived to project in a direction that would induce steric clash and was therefore assigned to new rotamer group 3*. There was only one rotamer occupying the gauche⁻ χ_1 configuration, and this aligned adjacently to the BLIP-II[213AzF] protein. In anticipation of steric clash, this rotamer was also assigned into new rotamer group 3*. These new rotamer groupings were then taken forward for *in silico* modelling with SWCNT bundles, to identify any possible steric clash and prospective binding orientations.
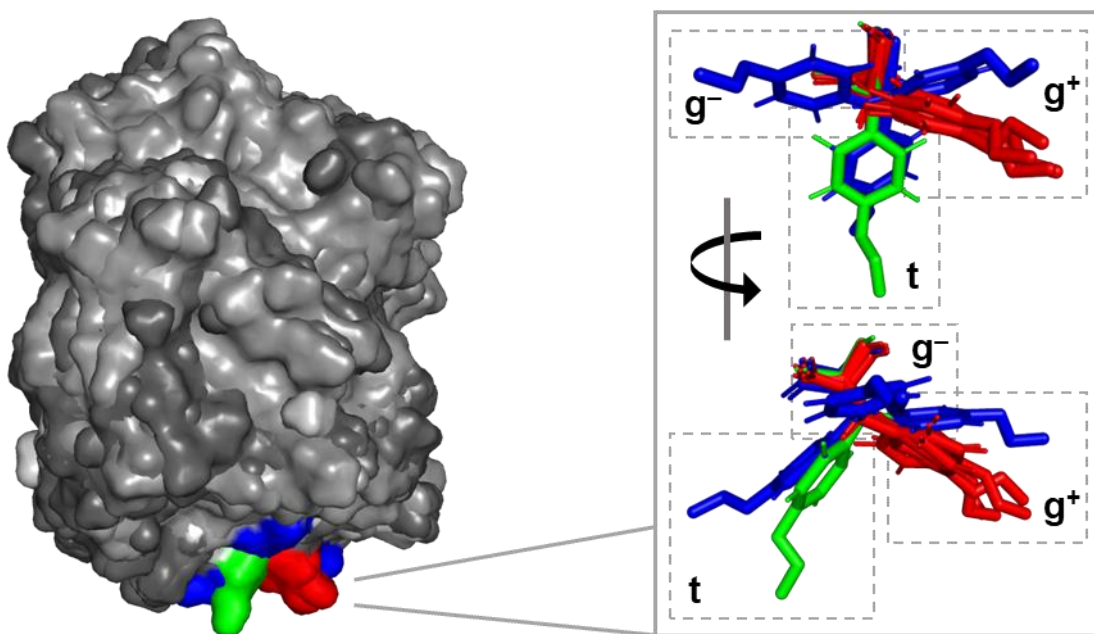
Figure 4.18 – Summary of BLIP-II[213AzF] rotamers. Frames extracted to illustrate all rotamers from repeats 1 – 3 and aligned along residues QTAzFVP. Rotamers are assigned by their properties (defined in Table 4.1) with rotamer groups 1, 2 and 3*

coloured red, green and blue respectively. The χ_1 angles are denoted as g^+ = gauche$^+$, g^- = gauche$^-$ and t = trans.

Table 4.1 – Assignment of new rotamer groups in BLIP-II[213AzF]. Groups were assigned by structural homology (rotamers 1 and 2) or potential for steric clash (3*).

Repeat	Rotamer	χ_1	New rotamer
1	1	gauche$^+$	1
	2	trans	2
	3	gauche$^-$	3*
2	1	gauche$^+$	1
	2	gauche$^+$	3*
	3	trans	3*
3	1	gauche$^+$	1
	2	gauche$^+$	1

4.2.7 BLIP-II[41AzF]: *in silico* modelling with SWCNT bundle

Having identified my modal AzF rotamers and extracted representative BLIP-II structures, *in silico* modelling with a SWCNT bundle was performed using PyMOL. Here, the protein was rotated about the SWCNT until the phenyl azide group was perpendicular to it, to represent the covalent bonding geometry (Introduction 1.4.3.2).

4.2.7.1 Rotamer 1: steric clash

Rotamer 1 models have been extracted from simulation repeats 1 – 3 and interfaced with a SWCNT bundle in Figure 4.19, with the excess SWCNTs hidden from view. All three repeats showed BLIP-II would be affected by steric clash if attempting to bind the SWCNT. This is due to AzF running parallel to the edge of BLIP-II (Figure 4.12), as it's intruding on a plane of residues which project from neighbouring loops and turns. There are five residues common to all observed clashes: S290, S291, S294, G295 and K310. In particular, the loop extending from P289-V296 bore a major constraint on the BLIP-II—SWCNT interface, with a

combination of these residues providing further clash in repeats 1 and 3. The variety of clash will be linked to the dynamism of the loop in that particular frame, but its constant presence suggests BLIP-II[41AzF] would be more likely to crosslink with a nearby residue than interface with the SWCNT when photoactivated.
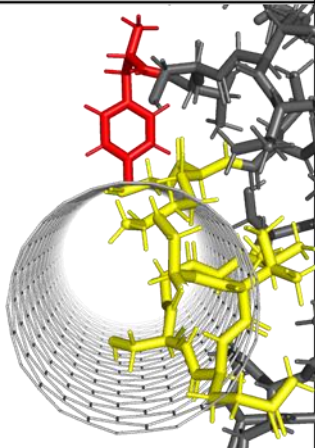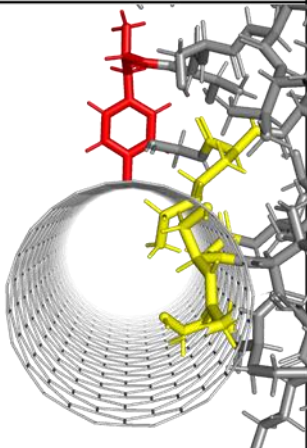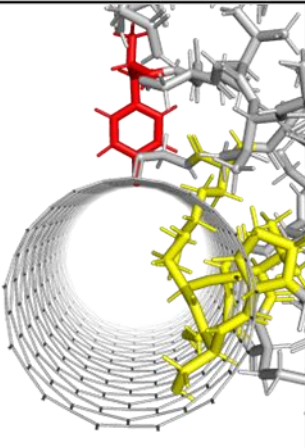
	Repeat 1	Repeat 2	Repeat 3
Residue clash	9 residues S290, S291, V292, Q293, S294, S295, V296, K310, G311	5 residues S290, S291, S294, G295, K310	7 residues P289, S290, S291, V292, S294, G295, K310
Cross section			

Figure 4.19 – BLIP-II[41AzF]: Rotamer 1 interfaced with SWCNT across repeats 1 – 3. AzF (red) is shown inserted into the SWCNT, while sterically clashing residues are highlighted in yellow.

4.2.7.2 Rotamer 2: modelling with TEM-1 and KPC-2

Rotamer 2 looked more promising for SWCNT attachment as it was seen to protrude perpendicularly away from the rest of the BLIP-II protein (Figure 4.12). Indeed, the *in silico* modelling with the SWCNT bundle proceeded seamlessly, with no steric clash (Figure 4.20). The alignment with the β-lactamases, however, suggested the rotamer wasn't the most successful anchor. With TEM-1 aligned to BLIP-II[41AzF], there was a 13.6 Å gap between the β-lactamase and the SWCNTs, while the gap was reduced slightly for KPC-2 to 11.8 Å. For an NT-FET to effectively monitor protein-protein interactions, the incoming analyte must be within the Debye length. This distance is determined by the electrolyte solvating the analyte, and the

DPBS buffer used in chapter 3 had a calculated Debye length of 7 Å. With both β-lactamases positioned beyond this distance, my modelling suggested they would be unable to induce an electrostatic gating effect. This somewhat correlated to the experimental observations because the BLIP-II[41AzF] functionalised NT-FETs failed to sense KPC-2 and transduced only a weak signal for TEM-1 (section 3.2.6.2). If we assume the BLIP-II[41AzF] and TEM-1 models have sufficient dynamicity to occasionally breach the Debye length, it's possible that TEM-1 could impart a weak gating effect on the SWCNTs. As electrostatic potential is known to decay exponentially from the charged molecule (Israelachvili 1991), gating from the cusp of the Debye length would require a strong ESP to affect SWCNT conductance. APBS analysis suggested TEM-1 had a strong negatively charged surface (~ -3 $k_B T e_c^{-1}$), while KPC-2 had a mix of weaker electrostatic surface potential. The ESP presented by TEM-1 may therefore have been sufficient to weakly increase the population of holes, and thus conductance, in the p-type SWCNTs (Artyukhin et al. 2006).

Figure 4.20 – BLIP-II[41AzF]: Rotamer 2 interfaced with SWCNT bundle and β-lactamases. BLIP-II is coloured dark grey, while TEM-1 and KPC-2 have been processed with APBS electrostatics and coloured by electrostatic potential.

4.2.7.3 Rotamer orientation viability

To summarise the data above, Table 4.2 has been compiled. The percentage time for each rotamer was calculated by averaging the individual rotamer propensity across repeats 1 – 3. Rotamer 1 was the most dominant, existing for 78.1 % of the simulations, but was not considered a viable option for SWCNT interfacing due to the extent of steric clash. Rotamer 2 was only present for 14.4 % of the simulation but could effectively bind the SWCNT bundle. The alignment with the β-lactamases, however, suggested they would be placed beyond the Debye length, and unable to impart a change in SWCNT conductance. These results generally correlated well with experimental observations, as BLIP-II[41AzF]—NT-FETs failed to transduce KPC-

2, and TEM-1 was only transduced through a weak increase in conductance (~ 0.19 µA; section 3.2.6.2). As mentioned previously, it is possible that inherent protein dynamicity could result in temporary breaches of the Debye length for TEM-1, where its strong negative ESP could impart a weak gating effect. One factor in particular that could contribute to Debye length breaches is the inherent flexibility of the N-terminal backbone. AzF[41] was shown to have the highest RMSF of all residues (Figure 4.7), and its extreme backbone mobility may sample configurations that shift the relative position of the BLIP-II[41AzF]—TEM-1 complex on the SWCNT. The N-terminal backbone flexibility is also responsible the relatively high population of unclassified rotamers (7.5 %). The flexibility and spatial freedom that accompanies AzF[41] encourages broad rotamer sampling which could have the potential to fit into any category e.g., sterically clashing with the SWCNT, or viable binding to the SWCNT with analytes binding within / beyond the Debye length. For these reasons, my molecular dynamics modelling of BLIP-II[41AzF] provides a good level of insight into the ability of AzF to mediate proximal analyte sensing, but the flexibility of the N-terminal residue introduces variables that aren't fully accounted for by the model.

Table 4.2 – BLIP-II[41AzF] rotamer summary.

Rotamer	Time	Steric clash?	TEM-1 in Debye length?	KPC-2 in Debye length?
1	78.1 %	✓	n/a	n/a
2	14.4 %	✗	✗	✗

4.2.8 BLIP-II[213AzF]: *in silico* modelling with SWCNT bundle

4.2.8.1 Rotamer 1: modelling with TEM-1 and KPC-2

Rotamer 1 of BLIP-II[213AzF] yielded the most promising results of all BLIP-II[AzF] models in terms of rotamer attachment configuration to mediate proximal β-lactamase sensing. It's orientation in Figure 4.18 showed the rotamer protruding diagonally away from the BLIP-II protein, and when it was aligned perpendicularly to the SWCNT (Figure 4.21), it resulted in the β-lactamase binding face tilting down towards the SWCNT. Alignment with TEM-1 and KPC-2 then brought the β-

lactamases within 1.6 Å and 2.0 Å of the SWCNT, respectively. These distances put both β-lactamases within the Debye length and would allow their ESP to electrostatically gate the SWCNT bundle. ESP, it is important to note, will vary considerably across a protein surface. The complex macromolecular structure will have both charge polarities, varying charge densities and varying charge distances from the SWCNT, due to the 3D protein surface. When coming to the qualitative decision on the average ESP presented, all of the above factors were considered. For example, TEM-1 was marbled with negative and positive patches underneath the SWCNT, but there was a notably strong acidic patch (~ -5 $k_BTe_c^{-1}$) at the BLIP-II—TEM-1 binding interface. Measured by PyMOL, this patch came within 5.1 Å of the SWCNT and was within the Debye length. On balance, I thus concluded BLIP-II was presenting a negatively charged face. KPC-2, on the other hand, appeared largely dominated by basic patches, so I predicted a positively charged face (~ 1.5 $k_BTe_c^{-1}$) to be presenting towards the SWCNT. From an experimental design standpoint, this insight on ESP is a valuable addition to the modelled protein—NT-FET interface, as it could allow you to target charge hotspots via different mutation sites, inducing a bigger change in NT-FET signal. To compare this model to the experimental results (section 3.2.6.2), BLIP-II[213AzF] functionalised NT-FETs recorded a conductance change of up to +0.64 μA for TEM-1 sensing, and -0.25 μA for KPC-2. The electrostatic gating hypothesis explains an increase in p-type SWCNT conductance as a response to negative gating potential, such as the -5 $k_BTe_c^{-1}$ charge presented by TEM-1. Meanwhile, a loss of p-type SWCNT conductance is explained by a positive gating potential, such as the 1.5 $k_BTe_c^{-1}$ charge presented by KPC-2 (Artyukhin et al. 2006). The magnitude of conductance change in this case appears to match strength of ESP presented.
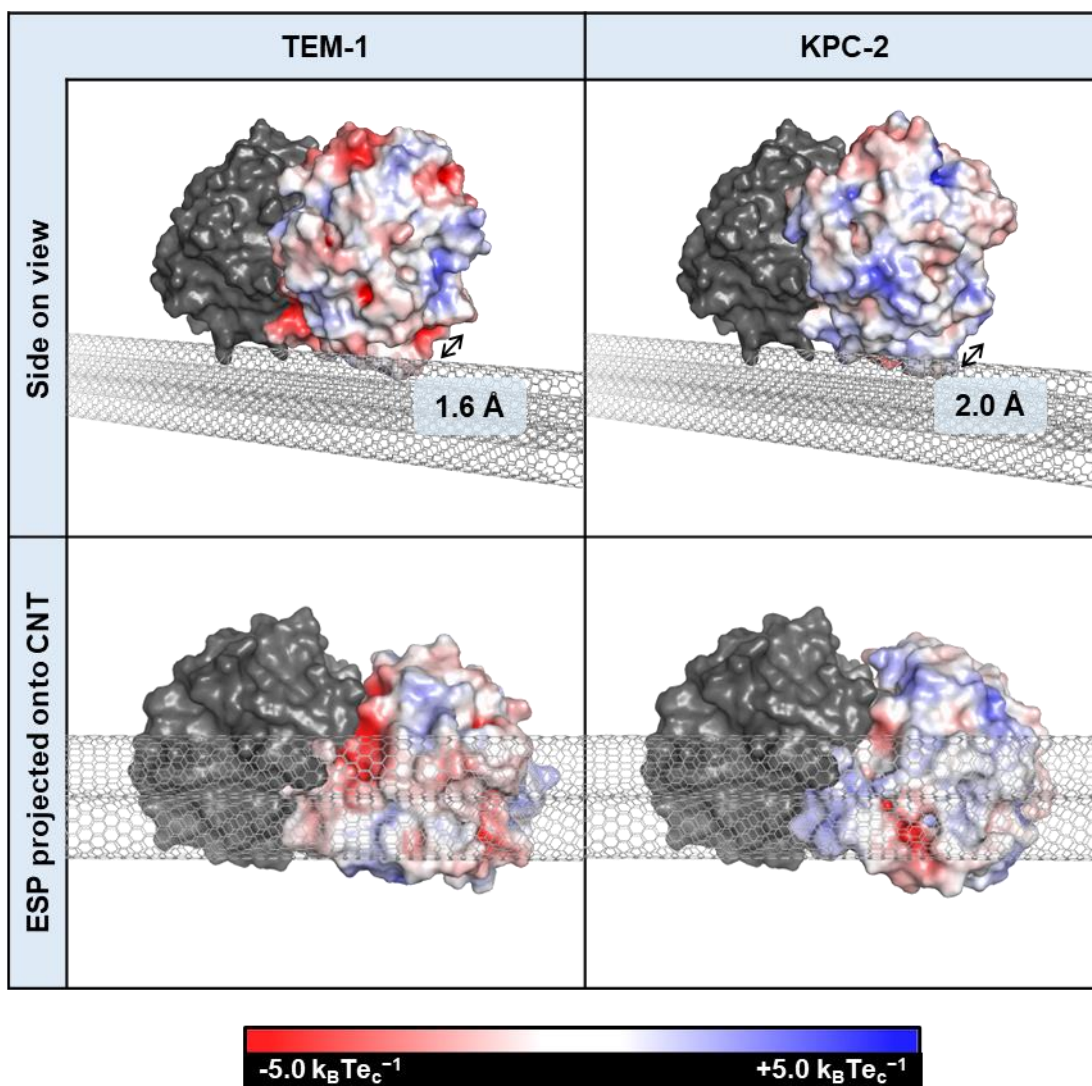
Figure 4.21 – BLIP-II[213AzF]: Rotamer 1 interfaced with SWCNT bundle and β-lactamases. BLIP-II is coloured dark grey, while TEM-1 and KPC-2 have been processed with APBS electrostatics and coloured by electrostatic potential (ESP).

4.2.8.2 Rotamer 2: modelling with TEM-1 and KPC-2

Rotamer 2 could easily be modelled onto the SWCNT bundle, with the rotamer protruding straight down away from the bulk BLIP-II[213AzF] protein (Figure 4.18). When this was perpendicularly aligned to the SWCNT, it became apparent that the β-lactamase binding site would be angled away from the bundle. Figure 4.22 shows the effect of this, as TEM-1 was measured 19.9 Å from the SWCNT, and KPC-2 was measured at 21.4 Å. Both proteins presented a strong ESP towards the SWCNT, but placement beyond the narrow 7 Å Debye length suggested the rotamer would be unsuccessful at inducing conductance across along the SWCNTs.
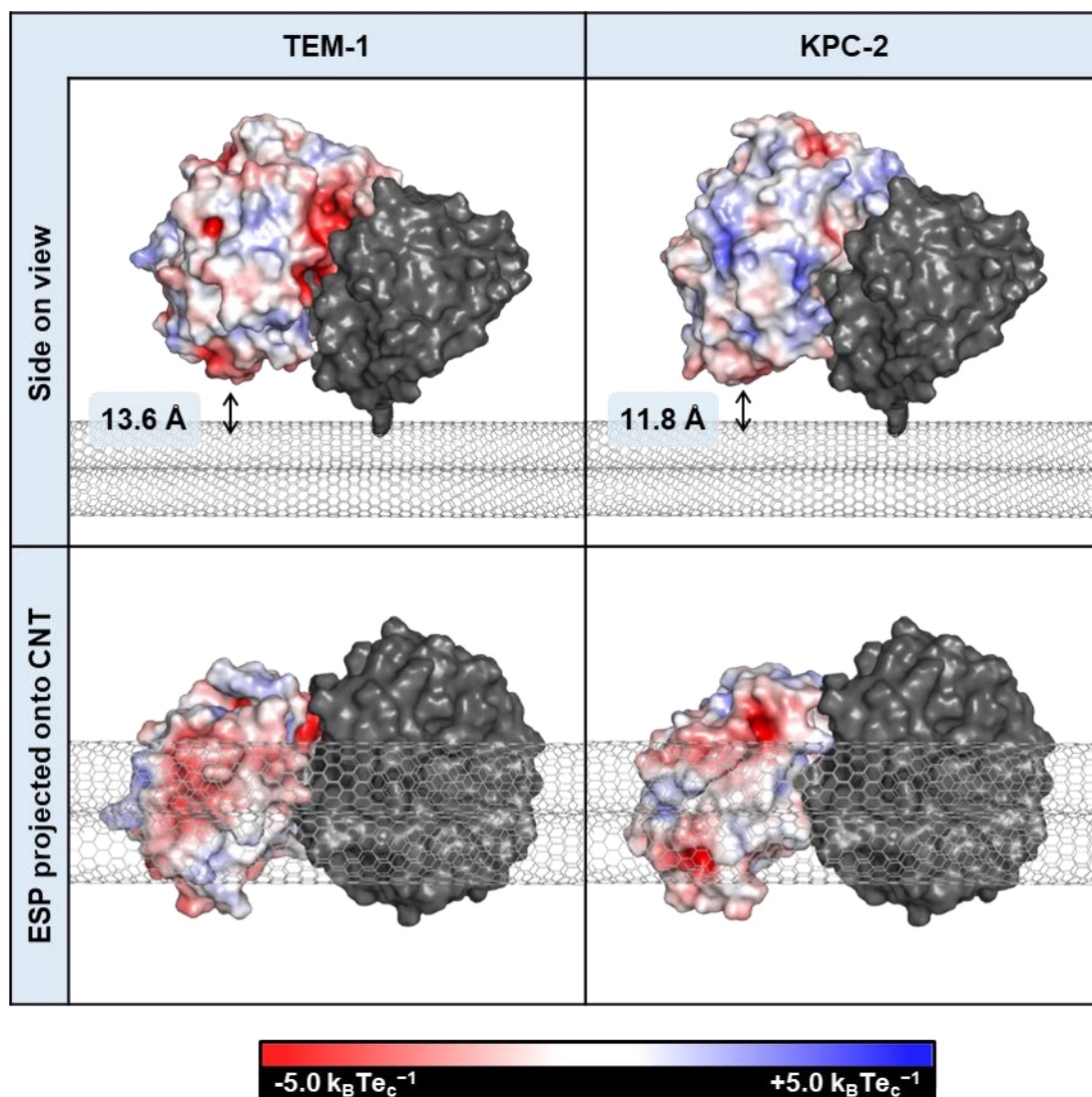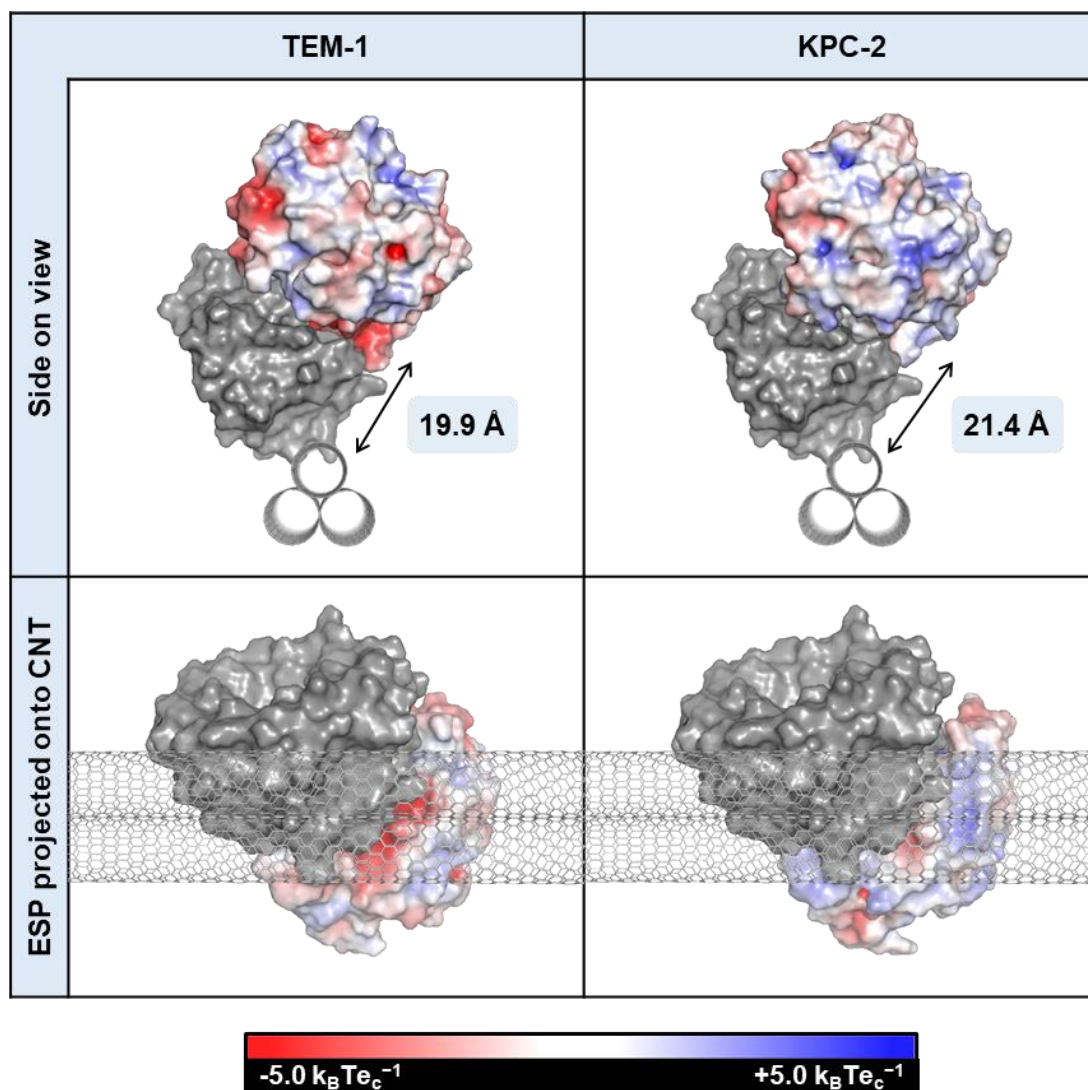
Figure 4.22 – BLIP-II²¹³ᴬᶻᶠ: Rotamer 2 interfaced with SWCNT bundle and β-lactamases. BLIP-II is coloured grey, while TEM-1 and KPC-2 have been processed with APBS electrostatics and coloured by electrostatic potential (ESP).

4.2.8.3 Rotamer 3*: steric clash

Rotamer 3* represented a group of rotamers that appeared almost parallel to surface of the BLIP-II protein (Figure 4.18). The direction of rotamer projection was a function of their gauche⁺, gauche⁻ and trans χ_1 angle, but their planar nature in relation to the bulk BLIP-II²¹³ᴬᶻᶠ protein ensured that perpendicular alignment to the SWCNT would result in steric clash from the surrounding protein residues (Figure 4.23). R1R3, the gauche⁻ variant, achieved the highest levels of steric clash, with thirteen residues intruding into the SWCNT. Attachment from this position would be impossible as AzF cannot access the nanocarbon surface.

R2R2 (the gauche+ variant) and R2R3 (the trans variant) saw less steric clash, with only two or one residue conflicts, respectively. Protein dynamics could arguably see these residues fluctuate in and out of steric clash zones, so one can still consider the possible β-lactamase binding conformations in relation to the SWCNT bundle. As an extended variant of rotamer 1 (Figure 4.21), the R2R2 rotamer generates similar results when modelled with the SWCNT bundle (Figure 4.24). The β-lactamase binding face is positioned only 2.4 Å from the SWCNT and TEM-1 presents a similar ESP. If the sterically clashing residues N207 and Y208 were caught in a favourable conformation, I could anticipate similar electrostatic gating to that observed in Figure 4.21. R2R3, meanwhile, is considered an extended variant of rotamer 2 (Figure 4.22). When this rotamer was modelled with the SWCNT bundle (Figure 4.24), BLIP-II ended up tilting further backwards, pushing any incoming β-lactamase even further from the SWCNT (~ 21.0 Å). As a result, favourable shifting of sterically clashing residue A216 wouldn't change the ESP presented. While the rotamer 3* group have been ruled out as viable binding orientations, it is important to consider these results in a dynamic context to ensure all possible ESP is accounted for.

	R1R3	R2R2	R2R3
Residue clash	**13 residues** Y206, F209, K239, A242, A243, G244, D245, N246, R247, T251, T252, V253, L258	**2 residues** N207, Y208	**1 residue** A216
Cross section			

Figure 4.23 – BLIP-II213AzF: Rotamer 3* interfaced with SWCNT. The simulation source for each rotamer has been acronymised to R#R# (repeat number and

rotamer number). AzF (blue) is shown inserted into the SWCNT, while sterically clashing residues are highlighted in yellow.
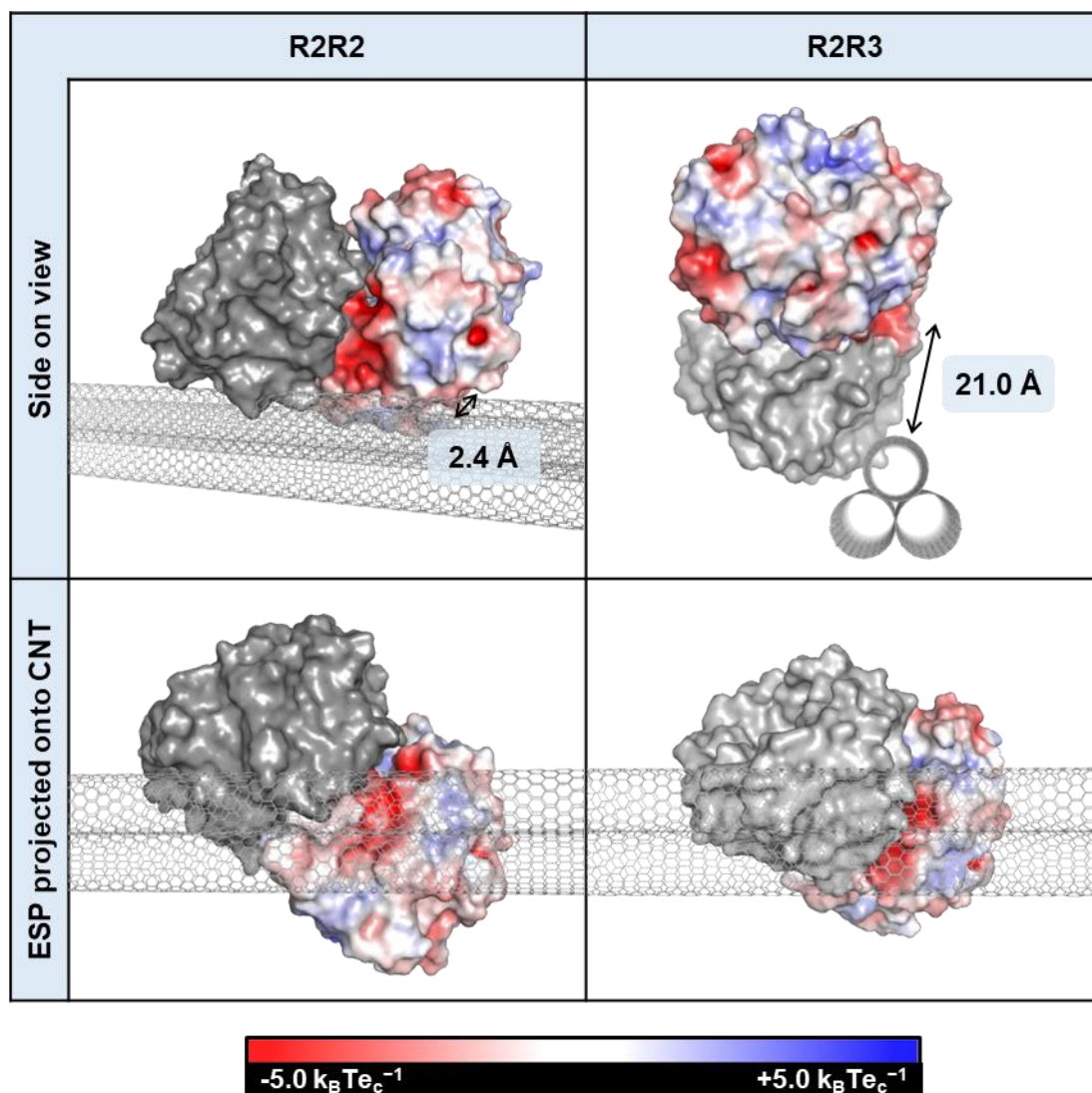
Figure 4.24 – BLIP-II[213AzF]: Rotamer 3* ignoring the steric clash. Rotamers R2R2 and R2R3 were modelled with the SWCNT bundle and TEM-1 was aligned. BLIP-II is coloured grey, while TEM-1 has been processed with APBS electrostatics and coloured by electrostatic potential (ESP).

4.2.8.4 Rotamer orientation viability

To summarise the data above, Table 4.3 has been compiled. The percentage time for each rotamer was calculated by averaging the individual rotamer propensity across repeats 1 – 3. Rotamer 1 was the majority population at 48.6 % and was predicted to be the most successful rotamer, with both β-lactamases aligning within

the Debye length. Crucially, the ESP presented was shown to correlate to the conductance changes measured from TEM-1 and KPC-2 sensing experiments (section 3.2.6.2). Conductance increased by up to 0.64 µA in TEM-1 sensing, which suggested a negative gating potential had been applied. From the computational model, I identified TEM-1 to be presenting a strong negative ESP (-5 $k_BTe_c^{-1}$) within the Debye length. Meanwhile, the experimental results for KPC-2 showed conductance to decrease by -0.25 µA, which suggested a positive gating potential had been applied. Again, the computational model supported this hypothesis, with KPC-2 presenting a positive ESP (~ 1.5 $k_BTe_c^{-1}$). Interestingly, the magnitude of conductance change was shown to be similar to the strength of ESP presented. Boosting signal transduction could therefore aided by stabilisation of rotamer conformations. To consider the other rotameric populations, rotamer 2 accounted for 27.8 % and could viably bind the SWCNT bundle. However, BLIP-II[213AzF]'s orientation would not permit incoming β-lactamases from influencing SWCNT conductance, as they were suspended ~20 Å above the nanocarbon surface. Inherent protein flux and dynamics from the BLIP-II[213AzF]—TEM-1 complex would be unlikely to mediate a Debye length breach. Finally, rotamer 3* grouped all the remaining rotamers by their planar proximity to BLIP-II[213AzF]'s surface (25.1 %). This was observed to cause steric clash when aligned perpendicularly to the SWCNT surface, rendering them non-viable for SWCNT attachment. However, this was taken with a pinch of salt, because R2R2 and R2R3 only experienced minor steric clash which could vary with protein dynamicity.

Table 4.3 – BLIP-II[213AzF] rotamer summary.

Rotamer	Time	Steric clash?	TEM-1 in Debye length?	KPC-2 in Debye length?
1	46.6 %	✗	✓ - strongly negative ESP	✓ - positive ESP
2	27.8 %	✗	✗	✗
3*	25.1 %	✓	n/a	n/a

4.3 Conclusions and Future Perspectives

To summarise the key results from this chapter, I used MD simulation to investigate AzF rotamers in BLIP-II[41AzF] and BLIP-II[213AzF]. Residue flexibility was measured by RMSF and B-factors, and both BLIP-II[AzF] variants recorded an increase from WT BLIP-II at the AzF mutation site, indicative of the side chain's freedom and flux. Side chain rotamers were identified through AzF RMSD studies, with BLIP-II[41AzF] grouping 92.5 % of the simulation into two rotamer groups and BLIP-II[213AzF] grouping 99.5 % of the simulation into three rotamer groups. Modal structures of the rotamer groups were extracted and *in silico* modelling was performed to assess if AzF was sterically available for covalent binding, and what distance the analytes would be from the SWCNT surface. Only one of BLIP-II[41AzF]'s rotamers were viable for SWCNT binding, and modelling with the SWCNT bundle suggested incoming β-lactamase proteins would bind just beyond the Debye length.. For BLIP-II[213AzF], both rotamer groups 1 and 2 were viable for SWCNT binding, but only rotamer group 1 allowed incoming β-lactamases to bind BLIP-II within the Debye length. ESP analysis of these β-lactamases correlated to the experimental results from Chapter 3, with positive ESP linked to hole depletion and negative ESP linked to hole accumulation.

The success of this modelling method ultimately comes down to physical NT-FET construction and experimental results from β-lactamase sensing assays. I therefore retrospectively compare my modelling data to the electrical results produced in Chapter 3. Here, BLIP-II[41AzF] recorded a weak electrical response to increasing concentrations of TEM-1 and KPC-2, with only TEM-1 breaching NT-FET baseline variation (-0.1 – 0.1 μA) to record a slight increase in current to 0.19 μA. The small gating effect observed isn't fully explained by my modelling data, where only rotamer 2 (representing 14.4 % of the population), allows TEM-1 to bind 13.6 Å from the SWCNT, beyond the Debye length. The high RMSF for 41[AzF] and inherent N-terminal backbone flexibility, however, had the potential to induce global shifts in the positioning of the AzF residue, as there is sufficient spatial freedom and flux. This could feasibly bring the BLIP-II[41AzF]—TEM-1 complex to the cusp of the Debye length, where the strong ESP presented by TEM-1 (-3 $k_B Te_c^{-1}$) could induce weak gating of the SWCNT. In addition to this, there is an unclassified rotamer population which represents 7.5 % of the population. It is possible that rotamers from this could contribute to the weak electrostatic gating, with a small proportion of TEM-1 binding through unidentified configurations that breach the Debye length. In comparison, BLIP-II[213AzF] recorded a stronger electrical response to increasing concentrations of

TEM-1 and KPC-2. Against TEM-1, current was seen to increase to 0.64 µA, while KPC-2 induced a drop to -0.25 µA. The gating effects observed here correlate to my modelling data. BLIP-II^{213AzF} had three rotamer groups identified, but only one (representing 46.6 % of the rotamer population) allowed β-lactamases to bind within the Debye length. When modelled against the β-lactamases, TEM-1 was shown to present a strong negative charge, up to -5 $k_B Te_c^{-1}$, while KPC-2 presented 1.5 $k_B Te_c^{-1}$. The strong negative ESP presented by TEM-1 is expected to significantly increase the number of holes within the SWCNT, while the slight positive charge of KPC-2 would slightly deplete holes, correlating to observed electrical results (Artyukhin et al. 2006). Overall, my modelling analysis has allowed me to derive two key parameters: (i) the viable rotamer population that permits β-lactamase binding within the Debye length, and (ii) the strength of ESP presented within the Debye length via APBS electrostatics. This systematic study has provided reasoning for the different electrical responses recorded by BLIP-II^{41AzF} and BLIP-II^{213AzF} functionalised NT-FET devices, and I deem this method to be a successful prediction of AzF mutation site success.

While the modelling and experimental data has fitted together nicely, the analysis techniques are still open to critical evaluation. One limitation that became apparent throughout this process is the use of AzF RMSD to analyse AzF at the N-terminus. Flexibility of the backbone at N- and C-termini is typical in protein structure, and there is an established link between backbone flexibility and the extent of conformational freedom experienced by side chain groups (Friedland et al. 2008; Havranek and Baker 2009). The histograms representing rotamer population in the N-terminal 41 AzF mutation failed to completely converge into defined rotamer peaks, and I hypothesise this is due to extensive rotamer sampling. This prevents me from classifying 7.5 % of the population, losing vital rotamer viability data and potential β-lactamase ESP. Another limitation linked to this methodology is the reference structure constraint. Before calculating the RMSD, the trajectory frame is compared to the default reference structure (the first frame collected). If your reference structure is halfway between two rotamer groups, the directionless measure of RMSD cannot distinguish between the groups and both rotamers will be plotted as part of the same population – as seen in the first repeat of BLIP-II^{213AzF}. To counter this, a superimposition frame stack of the entire trajectory was included for every AzF RMSD analysis performed. This allowed me to verify the actual number of rotamers and identify which RMSD peaks they were associated with. A final limitation associated with this method is the complexity surrounding

CHARMM36 forcefield amendments. Working with non-natural systems requires the forcefield to be adapted to recognise the non-natural element, in my case, the AzF residue. Other NT-FETs may also use unusual functionalisation chemistry to link together the biomolecules and SWCNTs, and so a certain level of knowledge will be required to alter the forcefield for these systems.

Aside from these limitations, there are a few other areas of improvement to target in future modelling approaches. Incidences of steric clash cause whole rotamer populations to be written off, regardless of the number of clashing residues. This could be considered unfair, as proteins are constantly undergoing dynamic flux, and may not sample continuous clashing. In future analysis attempts, I could consider setting a lower limit for steric clash (e.g. ≤ 3 residues), and in these situations, a bigger population sample could be taken to estimate steric clash probability and model the incidences where steric clash does not occur. Another opportunity for model improvement is inspired by Côte et al. (2021), who used advanced modelling to quantitively investigate the molecular origin of electrostatic gating from lysozyme on SWCNTs. This was a sophisticated approach to predicting ESP and could be used to more accurately link patches of ESP on the β-lactamase surface to experimental electrical results.

Overall, using MD to inform me of AzF rotamer propensity has yielded successful results, considering the observed electrical measurements in Chapter 3 and its correlation to applied *in silico* models of BLIP-II^{AzF}—NT-FET transistor channels. As with most methodologies, there are limitations associated with using AzF RMSD, but these have generally been countered with using additional analysis techniques or have been earmarked as future development opportunities. This, and other computational techniques, will be crucial for more effective NT-FET designs; building a pipeline for prototype AzF mutation models, through rotamer dynamicity assessment and *in silico* modelling.

5. Differential bio-optoelectronic gating of semiconducting carbon nanotubes by varying the covalent attachment residue in sfGFP

Work in this chapter contributed to a published, peer-reviewed paper where I am joint 1st author. With permission from the publisher, text and figures have been taken and adapted for my thesis.

Gwyther, R., Nekrasov, N., Emelianov, A., Nasibulin, A., Ramakrishnan, K., Bobrinetskiy, I. and Jones, D., 2022. Differential Bio-Optoelectronic Gating of Semiconducting Carbon Nanotubes by Varying the Covalent Attachment Residue of a Green Fluorescent Protein. *Advanced Functional Materials*, 32(22), p.2112374.

Statement of work

Work in this chapter was performed in collaboration with the Bobrinetskiy lab at MIET. I carried out the initial workload by producing and characterising the sfGFP^{AzF} variants, functionalising the NT-FETs and organising delivery to MIET. Dr. Aleksei Emilianov and Dr. Nikita Nekrasov were then responsible for downstream data collection, including NT-FET characterisation and photoresponse experiments. All data presented in this chapter has been plotted and analysed by me, unless explicitly referenced in the figure caption.

5.1 Introduction

The global depletion of non-renewable resources has catalysed the need for more sustainable technology. Optoelectronic devices represent a key market to target, as their ability to detect, modulate or emit light shows parallel functionality to many photoactive biomolecules. If these biomolecules could be substituted for their inorganic and finite counterparts e.g. silicon or gallium arsenide (Miller 1995; Xu et al. 2018a), a new generation of eco-friendly and low-cost bionanohybrids could be borne (Ou et al. 2021).

Nature has created a myriad of proteins capable of interacting with and responding to light at various wavelengths across the UV-visible region of the electromagnetic spectrum (Arnesano et al. 1999; Palczewski et al. 2000; Jordan et al. 2001). Fluorescent proteins (Zimmer 2009; Rodriguez et al. 2017) are the favoured candidate for bio-based optoelectronic FET development, as light-induced electrical excitation of the chromophore has the potential to be reciprocally coupled to conductance (Fernández-Luna et al. 2018; Nishiori et al. 2019). Fluorescent

proteins also have a structural advantage over smaller photoactive biomolecules, because an external protein shell protects the chromophore from the environment and fine-tunes the electronic properties through long-range charge transfer pathways (Bogdanov et al. 2009). These properties have led to the green fluorescent protein (GFP; Tsien 1998) being successfully trialled in molecular electronic setups, finding applications in light-harvesting and energy transfer (Zajac et al. 2018), BioLEDs (Fernández-Luna et al. 2018), solid-state protein lasers (Gather and Yun 2014), and optically gating gold substrates (Korpany et al. 2012). This puts us in good stead for using the superfolder variant of GFP (sfGFP; (Pédelacq et al. 2006)) as our light-responsive element in optoelectronic FET design.

For sfGFP to operate in an optoelectronic device, it must be interfaced with a compatible electronic material to allow light-induced charge transfer (Du et al. 2020). Nanocarbons, such as single-walled carbon nanotubes (SWCNTs) or graphene, offer an appropriate foundation, with their semiconducting properties and ability to be chemically modified (Karousis et al. 2010; Georgakilas et al. 2012; Norizan et al. 2020) allowing easy functionalisation with proteins (Calvaresi and Zerbetto 2013; De Leo et al. 2015; Marchesan and Prato 2015). SWCNTs tend to be favoured over graphene, as their cylindrical structure is more compatible with protein interfacing, and the diameter of 1 – 2 nm matches well with sfGFP dimensions (~3 nm x 5 nm; Figure 5.1(A)). Graphene, meanwhile, has a large hydrophobic surface which has been shown to induce protein unfolding and loss of function (Calvaresi and Zerbetto 2013).
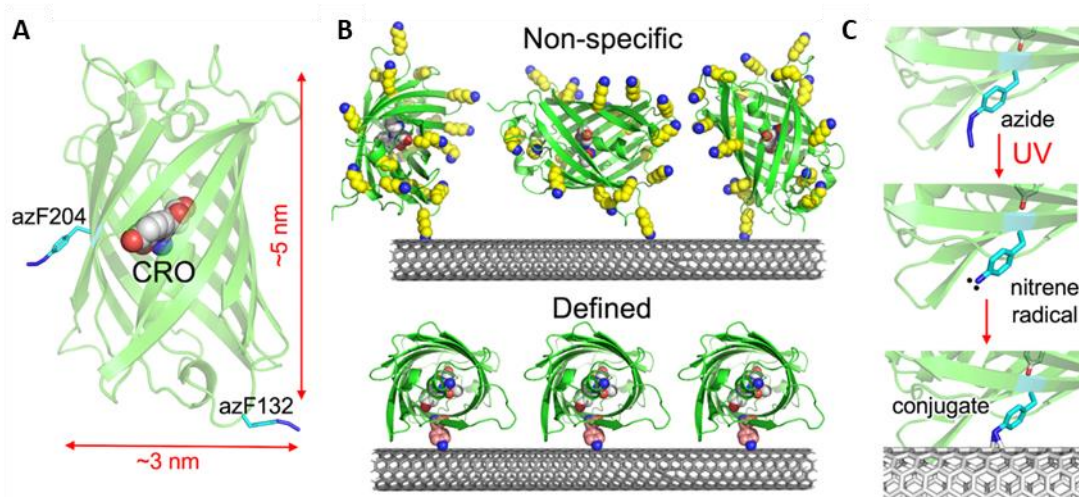
Figure 5.1 – Attachment of sfGFP to SWCNTs. (A) The structure of the superfolder version of GFP (Pédelacq et al. 2006) mutated *in silico* to contain *p*-azido-L-phenylalanine (AzF) at residues 132 or 204 (cyan and shown as sticks). The chromophore (CRO) is shown as grey spheres with relative dimensions shown in red. (B) Schematic outline illustrating non-specific attachment of GFP by, for example, primary amine chemistry via lysine residues (shown as yellow spheres) and defined, single-site attachment via genetically encoded phenyl azide photochemistry (shown as pink spheres). (C) SWCNT attachment using phenyl azide photochemistry. Illumination with UV light (305 nm) generates a nitrene radical that can covalently crosslink to the electron-rich SWCNT across a C=C bond. Figure copied with permission from Gwyther et al. (2022).

By coupling sfGFP to SWCNTs, we have the potential to tune optoelectronic SWCNT-FET (NT-FET) properties by exploiting single fluorescent protein molecule function (Wang et al. 2012; Freeley et al. 2017; Thomas et al. 2020; Ghasemi and Moth-Poulsen 2021). Previous examples of NT-FETs and graphene-FETs functionalised with photosensitive proteins have shown some promise, with an enhancement of photocurrent response, and wavelength-selective photodetection (Lu et al. 2012; Bakaraju et al. 2020; Tong et al. 2020). However, these approaches are limited in their potential because they do not allow the attachment site to be defined and systematically varied to optimise and/or alter the protein-dependent conductance characteristics. If Tong et al.'s (2020) primary amine conjugation chemistry approach was applied to sfGFP, there would be 19 potential lysine residues to mediate SWCNT attachment (Figure 5.1 (B)). With each attachment interface offering an alternative charge transfer pathway (Freeley et al. 2017;

Thomas et al. 2020), the summative response would be collective and unpredictable. Therefore, we look to mediate sfGFP attachment at a designed residue, to generate a defined, stable, intimate, and homogenous interface with optimal transduction between the two.

We have recently shown that proteins, including sfGFP, can be site-specifically covalently attached to graphene (Zaki et al. 2018) and SWCNTs (Chapter 3; Thomas et al. 2020) using genetically encoded phenyl azide photochemistry (Figure 5.1 (C)). The attachment mechanism is shown in Figure 5.1 (C) and involves irradiation with UV light, which converts the phenyl azide into a nitrene radical (Reddington et al. 2013b) that can then covalently link to the electron-rich side walls of a SWCNT (Thomas et al. 2020). Phenyl azide photochemistry makes generating bionanohybrids easier and more precise as the new abiotic chemistry is incorporated site-specifically at one single location by design (Chin et al. 2002; Reddington et al. 2013a). Furthermore, the phenyl azide moiety can easily be moved to different residues in a protein, changing the nature of the protein-SWCNT interaction and thus the transduction process.

In this work, we demonstrate the use of NT-FETs photochemically modified with two different phenyl azide containing variants of sfGFP (Figure 5.1 (A)) for the development of optoelectronic devices. Changing the protein's interfacing residue altered the properties of the NT-FET device. We demonstrate that the light-dependent electron-donating nature of sfGFP decreased the conductivity of p-type semiconducting SWCNT by circa an order of magnitude upon light illumination close to the peak absorbance wavelength for GFP. To the best of our knowledge, this is the first-time individual carbon nanotube-based transistors have been photochemically modified with a protein and shown direct orientation-specific effects on conductance modulation.

5.2 Results and Discussion

5.2.1 Expression and purification of sfGFP^{AzF} variants

To generate optically gated NT-FETs via covalently linked sfGFP, the attachment configuration will be crucial to its success. We have previously engineered sfGFP to contain the non-natural amino acid p-azido-L-phenylalanine (AzF) at either residue 132 (sfGFP^{132AzF}) or 204 (sfGFP^{204AzF}) (Reddington et al. 2012; Thomas et al. 2020). The sfGFP^{132AzF} variant is termed the long axis variant as the SWCNT attachment residue is positioned at the end of the β-barrel GFP structure distal from the

functional centre, the chromophore (Figure 5.1 (A)). The estimated distance between the chromophore and AzF is ~2.5 nm. The sfGFP[204AzF] variant is termed the short axis variant as residue 204 is positioned on the side of the β-barrel close to chromophore, resulting in a shorter distance between the chromophore and the attachment site (~1 nm). Both variants have been attached to SWCNTs in previous studies and have shown evidence of charge transfer and communication (Freeley et al. 2017; Thomas et al. 2020), so based on empirical knowledge, we anticipate similar mechanisms will be at play when employed in our NT-FET.

The sfGFP[AzF] variants were produced by recombinant expression in TOP10 *E. coli*. A dual-vector system of pBAD and pDULE-cyanoRS were used, with pDULE-cyanoRS encoding the engineered tRNA / aminoacyl tRNA synthetase pair to recognise the amber stop codon in sfGFP and incorporate AzF (Reddington et al. 2013a). The cells were cultured under dark conditions to prevent AzF photolysis, fractioned into soluble cell lysate via French press and purified by a two-step process. The first purification made use of an intrinsic C-terminal His-tag, coordinating sfGFP to Ni ions in a Ni-NTA chromatography matrix while endogenous proteins passed through (Figure 5.2 (A)). Increasing concentrations of imidazole in the Ni affinity elution buffer then forced sfGFP to elute, appearing as intense proteins bands between 26 – 34 kDa on the SDS-PAGE fractional analysis (Figure 5.2 (B)). It should be noted that the lower ~26 kDa band is a protein degradation band, due to a partial break in the polypeptide backbone within the chromophore. Fractions containing sfGFP were pooled and concentrated to 1 mL before loading onto the Superdex 75 column for purification via size exclusion and buffer desalting (Figure 5.2 (C)). sfGFP was eluted between ~70 – 90 mL and analysed with SDS-PAGE (Figure 5.2 (D)) to reveal a clean, intense band at ~30 kDa.
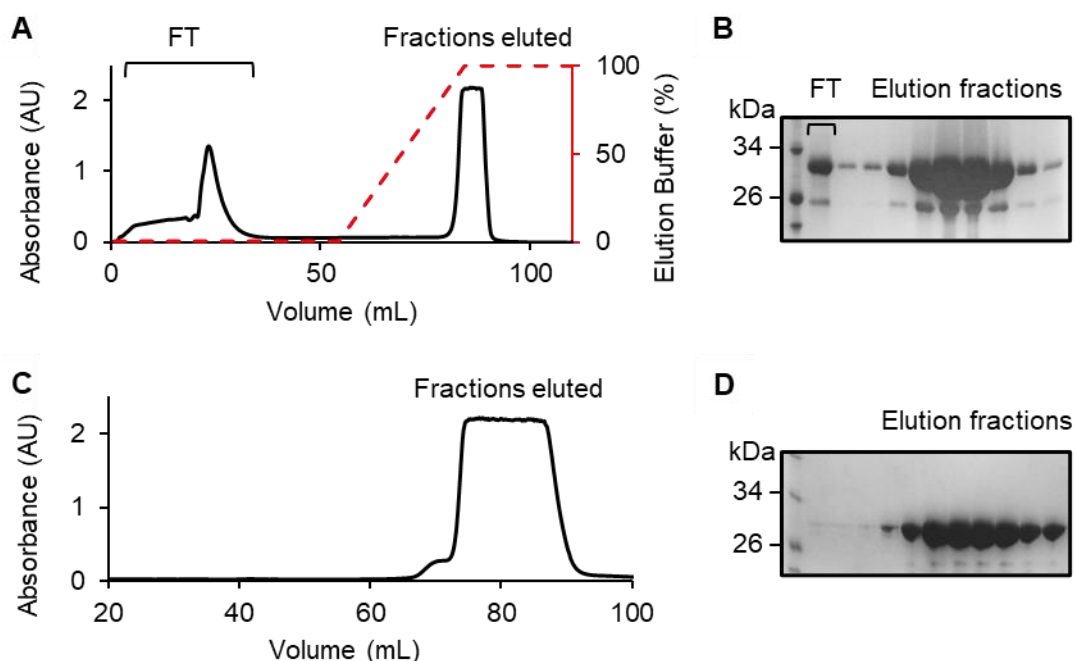
Figure 5.2 – Purification of wild type sfGFP. Soluble cell lysate was injected onto a Ni-NTA column and treated sequentially with Ni affinity wash and Ni affinity elution buffer, with any flow through (FT) collected. Absorbance was monitored at 485 nm (A), and as soon as the absorbance started to increase, fractions were collected. 10 µL samples were then loaded on a gel and analysed by SDS-PAGE (B). Once fractions containing sfGFP were identified, they were concentrated and run on the SEC column (C). Fractions collected from SEC were analysed by SDS-PAGE and sfGFP was seen as clean, purified band at ~30 kDa (D).

5.2.2 Characterisation of sfGFP^{AzF} variants

To characterise the sfGFP^{AzF} variants, protein concentration was calculated by measuring absorbance at λ_{max} (485 nm) and using the Beer-Lambert law (Equation 2.5), with the molar absorption coefficients detailed in Table 2.12. Absorption and fluorescent spectra were then recorded with sfGFP^{AzF} variants free in solution. Both sfGFP^{132AzF} and sfGFP^{204AzF} were shown to have characteristic absorbance (Figure 5.3 (A)) and fluorescence spectra (Figure 5.3 (B – D)), similar to unmutated, wild type (WT) sfGFP. This confirmed that AzF had not affected sfGFP protein structure and function was largely the same, with the highest emission intensity arising from excitation close to λ_{max}. Excitation wavelengths (445 nm, 470 nm and 595 nm) correspond to those used in the NT-FET photoresponse experiments (*vide infra).*

Aliquots of the protein were then prepared at 100 nM or 1 µM, flash frozen and stored at -80 °C.
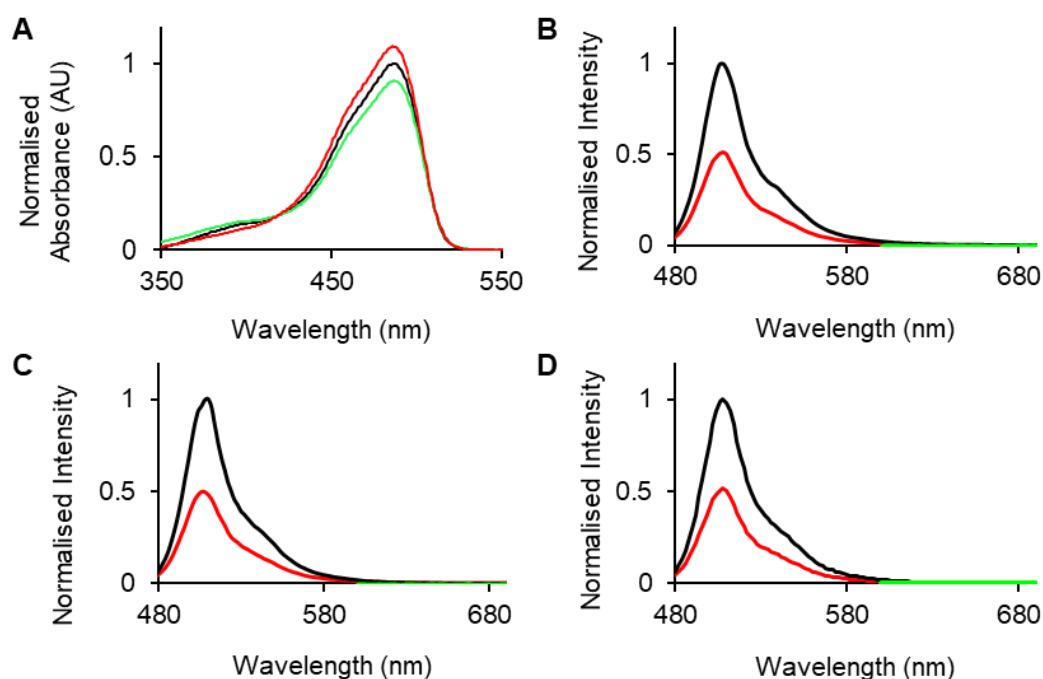
Figure 5.3 – Absorbance and fluorescence spectra of WT sfGFP and the sfGFP^{AzF} variants. (A) Absorbance spectra of 5 µM WT sfGFP (black line), sfGFP^{132AzF} (green line) and sfGFP^{204AzF} (red line). Spectra were normalized to the WT sfGFP. (B – D) Fluorescence emission spectra on excitation at 445 nm (red line), 470 nm (black line) and 590 nm (green line): (B) WT sfGFP, (C) sfGFP^{132AzF}, (D) sfGFP^{204AzF}. Figure adapted with permission from Gwyther et al. (2022).

Before sfGFP^{AzF} variants were taken forward for NT-FET device modification, AzF functionality was tested with fluorescent probe, DBCO-Cy3, in a strain-promoted azide-alkyne cycloaddition reaction. Here, WT sfGFP, sfGFP^{132AzF} or sfGFP^{204AzF} were incubated in a five-molar excess of DBCO-Cy3 and dye attachment was analysed via SDS-PAGE (Figure 5.4 (C)). Conjugation of the probe to sfGFP appeared as fluorescent bands when irradiated with UV (Figure 5.4 (A)) and provided evidence for AzF being chemically reactive. There was a notable difference, however, in labelling efficiency, with sfGFP^{204AzF} clicking five times more efficiently than sfGFP^{132AzF} (Figure 5.4 (B)). This behaviour has been observed previously by Reddington et al. (2012), and attributed to the 204 AzF

microenvironment promoting DBCO-Cy3 conjugation through hydrophobic interactions and limited side chain freedom. The 132 AzF microenvironment is surface exposed and dynamic, with some surrounding acidic residues. These differences may be responsible for hindering DBCO-Cy3 conjugation. No fluorescence was observed for WT sfGFP, which acted as a control for the selective DBCO-Cy3—azide reaction. It is important to note here that the difference in click efficiency is not indicative of photochemical efficiency, as they are two different reactions. The click reaction was used to prove the phenylazide chemistry remained present after an extensive purification protocol.
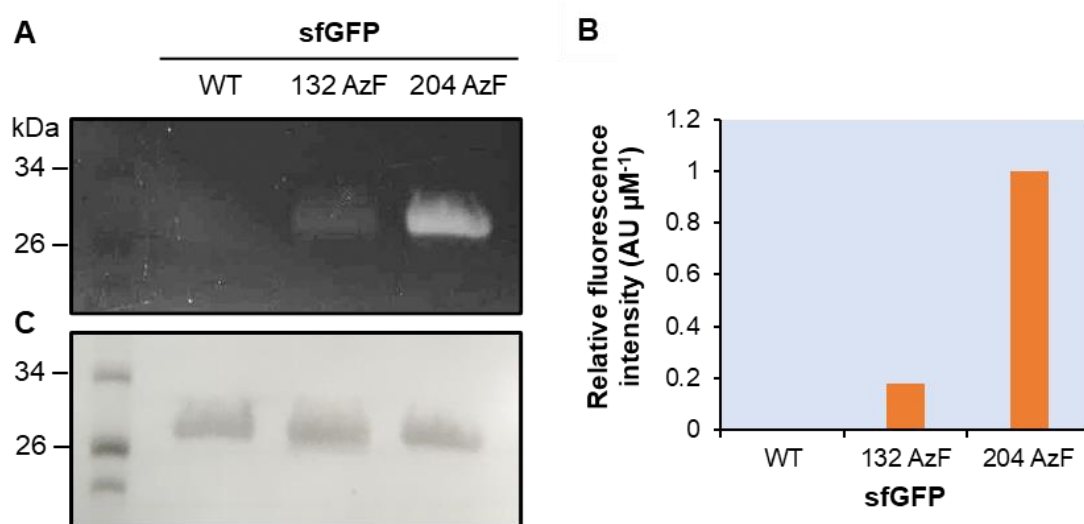
Figure 5.4 – Testing AzF Functionality in sfGFP variants with DBCO-Cy3 assay. (A) UV irradiated polyacrylamide gel. 10 µM samples of WT sfGFP, sfGFP^{132AzF} and sfGFP^{204AzF} were incubated in 50 µM DBCO-Cy3 for 1 hour, and 20µl samples were then analysed with SDS-PAGE. The gel was irradiated with UV and the image captured after a 13 second exposure. (B) Fluorescent band intensity. ImageJ analysis generated a histogram from the distribution of grey pixels in each gel lane, which was normalised and plotted as a bar graph. (C) Coomassie stain of the polyacrylamide gel, displaying the total protein loaded.

5.2.3 Photo-attachment of sfGFP^{AzF} variants to NT-FETs

NT-FETs were fabricated by Dr. Aleksei Emilianov and Dr. Nikita Nekrasov at MIET using the methodology outlined in 2.4.7.2. To functionalise the NT-FETs with the sfGFP^{AzF} variants, the UV irradiation mechanism shown in Figure 5.1 (A) was used. The published methodology (Zaki et al. 2018; Thomas et al. 2020) is described in

detail in Methods 2.4.7.4, but in brief, 100 nM of the sfGFP^{AzF} variant was drop cast onto the working area of the NT-FET device (Figure 5.5) and irradiated for 5 minutes with a 305 nm LED to trigger AzF photolysis. This decomposition formed a nitrene radical, which electrophilically attacked the π-electron rich sidewalls of the SWCNT to covalently bind sfGFP to the NT-FET device. Here, a low protein concentration was employed to ensure that proteins would be relatively well spaced on the SWCNT sidewall. The devices were washed thoroughly with deionised water and dried under a stream of nitrogen gas, before being taken forward for characterisation studies.
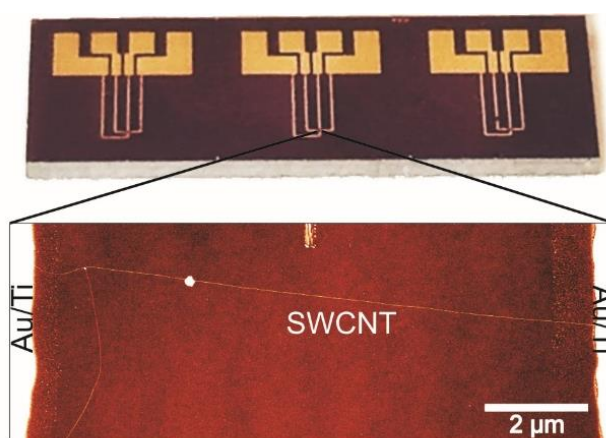
Figure 5.5 – Working area of NT-FET device. Optical image of a typical chip used (top), and an AFM image of the SWCNT transistor channel spanning between two Au/Ti electrodes (bottom). Figure adapted with permission from Gwyther et al. (2022).

5.2.4 Spectroscopic characterisation of sfGFP^{132AzF}—NT-FET and sfGFP^{204AzF}—NT-FET

Raman spectral analysis was performed to investigate the chemical structure of the SWCNTs after sfGFP^{AzF} functionalisation. Spectra for individual pristine SWCNT channels are shown in Figure 5.6 (A) and (C) in black. Analysis of the observed E_{33} optical transition revealed that the SWCNT corresponded to a (11, 10) semiconducting SWCNT with a diameter of 1.42 nm (Satco et al. 2019). Spectra for SWCNTs after functionalisation with sfGFP^{132AzF} and sfGFP^{204AzF} are shown in Figure 5.6 (A) and (C) in red. There was almost no change in the intensity of the D and G$^+$ bands, with the I_D/I_{G+} ratio decreasing by 0.014 after sfGFP^{132AzF} functionalisation and increasing by 0.06 with sfGFP^{204AzF} (Figure 5.6 (E)). While one would anticipate an increase in I_D/I_{G+} ratio from the breaking of sp^2 bonds, our results more or less match Setaro et al.'s observations (2017) of an identical I_D/I_{G+} ratio before and after azide-induced [2+1] cycloaddition onto SWCNTs. Similarly, photochemical attachment of cytochrome b_{562} onto graphene via AzF produced no observable D band (Zaki et al. 2018). This could be due to low-frequency protein photochemical attachment (estimated at ~0.01 % C=C bond disruption), but it also supports the Setaro et al. (2017) hypothesis of aziridine rings forming an extension to the π-network following C=C bond disruption. Meanwhile, we observed minor changes in the G' band after protein attachment (Figure 5.6 (B) and (D)), and a slight downshift in the G$^+$ band. This indicated a weak n-type doping of the SWCNT upon protein attachment, which we attribute to the additional electron density brought within the conduction band by sfGFP (Wise et al. 2004; López-Andarias et al. 2018). The overall absence of major changes in Raman spectra normally associated with large-scale oxidation (Pal et al. 2015; Emelianov et al. 2021) is not unexpected, and is the evidence of the low protein coverage on the SWCNT we aimed to achieve.
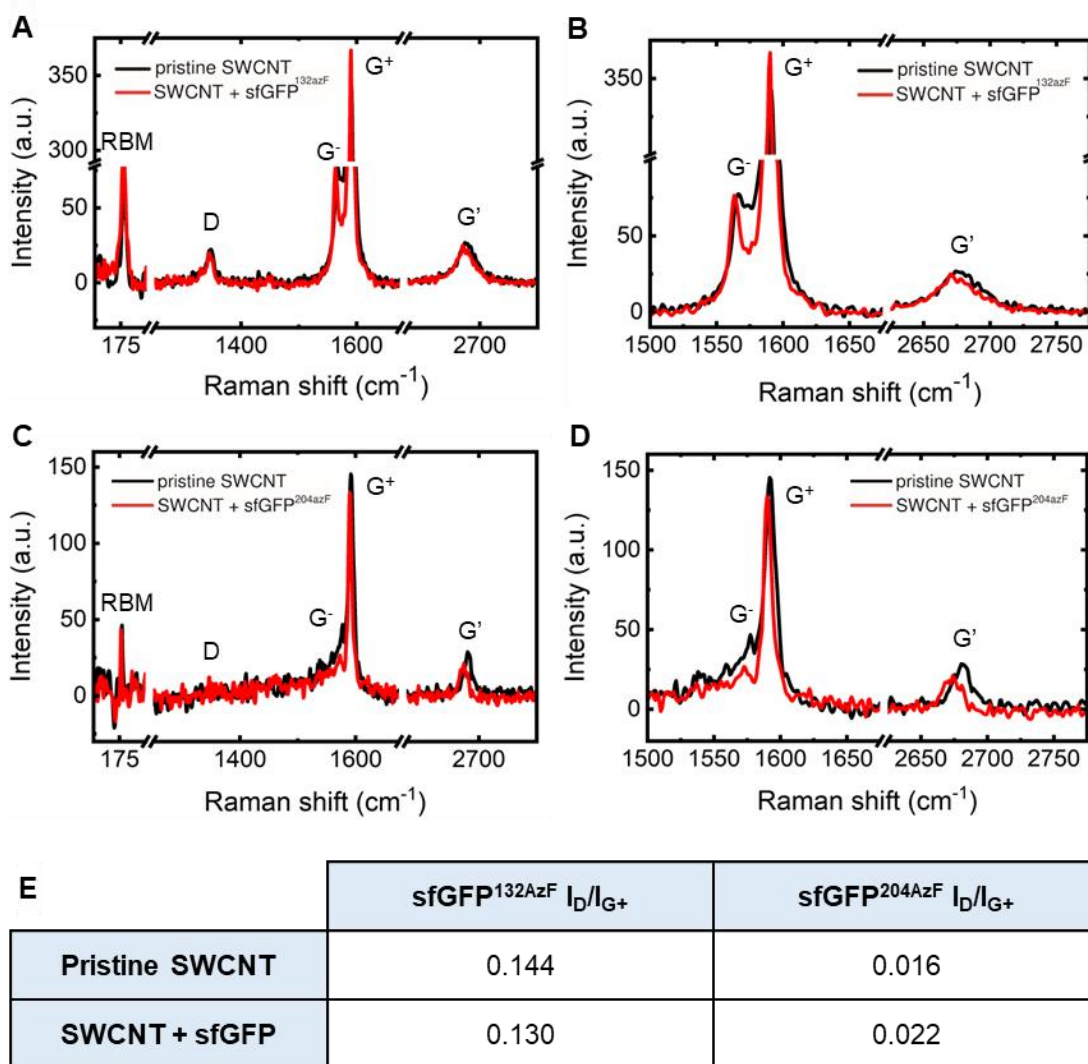
Figure 5.6 – Raman spectral analysis of sfGFP^{132AzF} and sfGFP^{204AzF} functionalised SWCNTs. Spectra of SWCNTs were recorded with an excitation wavelength of 532 nm and spot size of 1 μm, before (black) and after (red) sfGFP^{AzF} functionalisation. Spectrum for sfGFP^{132AzF} (100 nM) shown in (A), with G and G' regions magnified in (B). Spectrum for sfGFP^{204AzF} (1 μM) shown in (C), with G and G' regions magnified in (D). Intensity ratio for D/G$^+$ bands shown in (E). An average (n=5) ratio is derived for the SWCNTs + sfGFP. Figure adapted with permission from Gwyther et al. (2022).

5.2.5 Topographical characterisation of sfGFP^{132AzF}—NT-FET and sfGFP^{204AzF}—NT-FET

Atomic force microscopy (AFM) was used to assess attachment of protein molecules to the SWCNT (Figure 5.7 (A) and (B); Figure 5.8 (A) and (B)). Lateral cross sections taken from the pristine SWCNT and sfGFP^{AzF} modified SWCNT revealed consistent increases in height (~1.5 nm) after protein attachment, providing strong evidence for protein presence on the nanotube (Figure 5.7 (C) and (D); Figure 5.8 (C) and (D); Thomas et al. 2020). While the height changes are lower than expected based on the protein crystal structure dimensions, this is in line with previous observations for sfGFP and proteins in general whereby AFM can underestimate heights of soft molecules like proteins, together with protein attachment occurring around the nanotube diameter rather than solely at the apex (Santos et al. 2011; Fuentes-Perez et al. 2013; Thomas et al. 2020). Moreover, the pristine SWCNT average diameter is estimated to be 1.6 ± 0.2 nm providing a larger surface area for GFP attachment compared to previously published thinner nanotubes (Freeley et al. 2017; Thomas et al. 2020). We can also estimate protein coverage from the longitudinal cross-sectional analysis. After functionalisation with 100 nM sfGFP^{132AzF}, there is *circa* one sfGFP molecule per 60 – 80 nm, which is approximately 120 – 170 proteins across the entire channel (Figure 5.7 (E)). Increasing protein concentration to 1 µM was then shown to increase density, with sfGFP^{204AzF} coverage estimated at *circa* one sfGFP molecule per 40 – 50 nm (Figure 5.8 (E)).
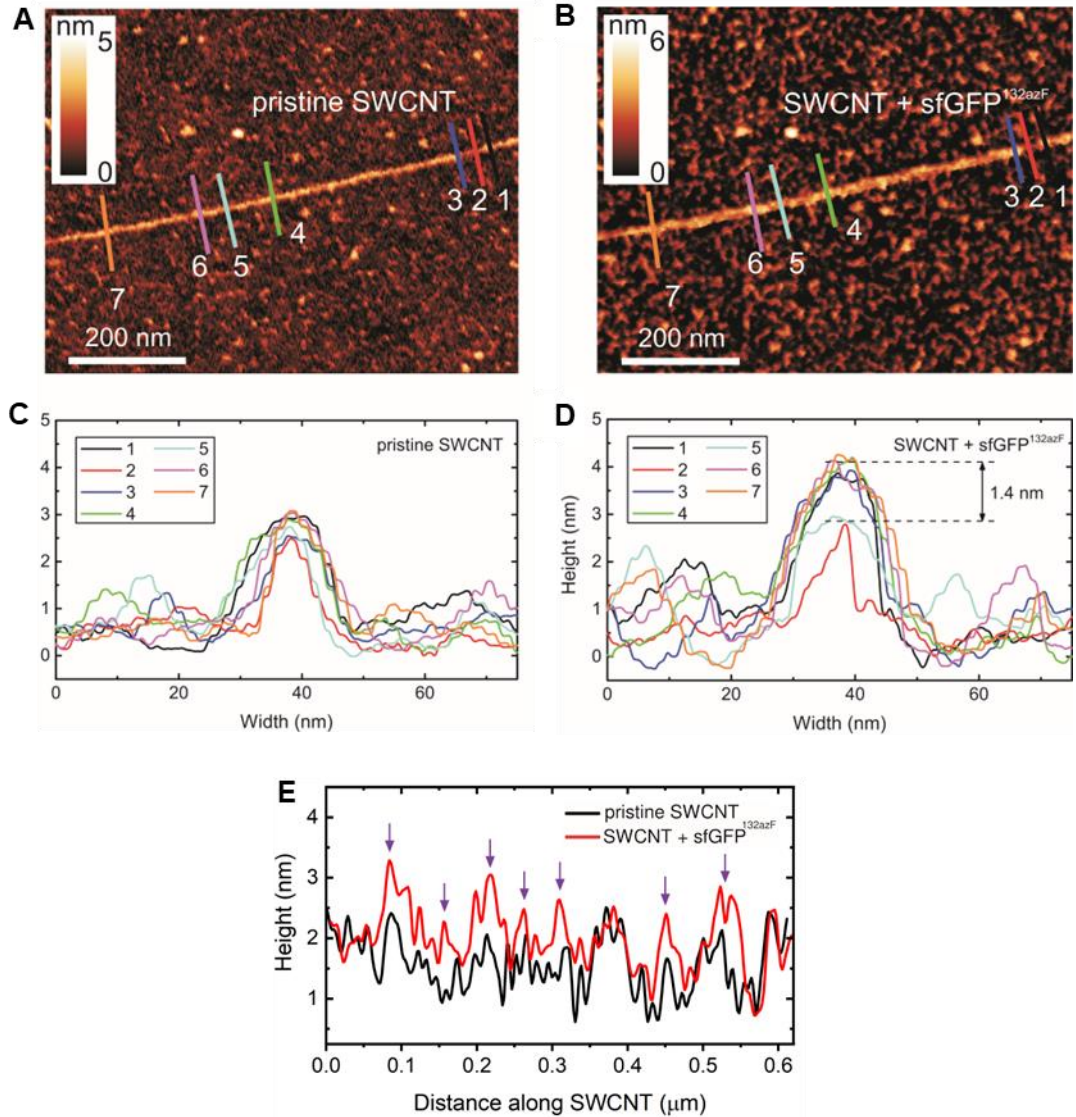
Figure 5.7 – Topographical characterisation of sfGFP[132AzF]—NT-FET device. (A) AFM image of the SWCNT before and after (B) 100 nM sfGFP[132AzF] attachment, with perpendicular cross sections coloured and numbered. Sections are plotted in (C) and (D) for pristine SWCNT and SWCNT + sfGFP[132AzF], with sections 2 and 5 corresponding to bare SWCNT in the latter. Figures (A – D) were produced by Dr. Aleksei Emilianov. (E) Longitudinal topography along nanotube axis before (black) and after (red) sfGFP[132AzF] attachment, with purple arrows indicating likely sites of protein attachment. Figure adapted with permission from Gwyther et al. (2022).
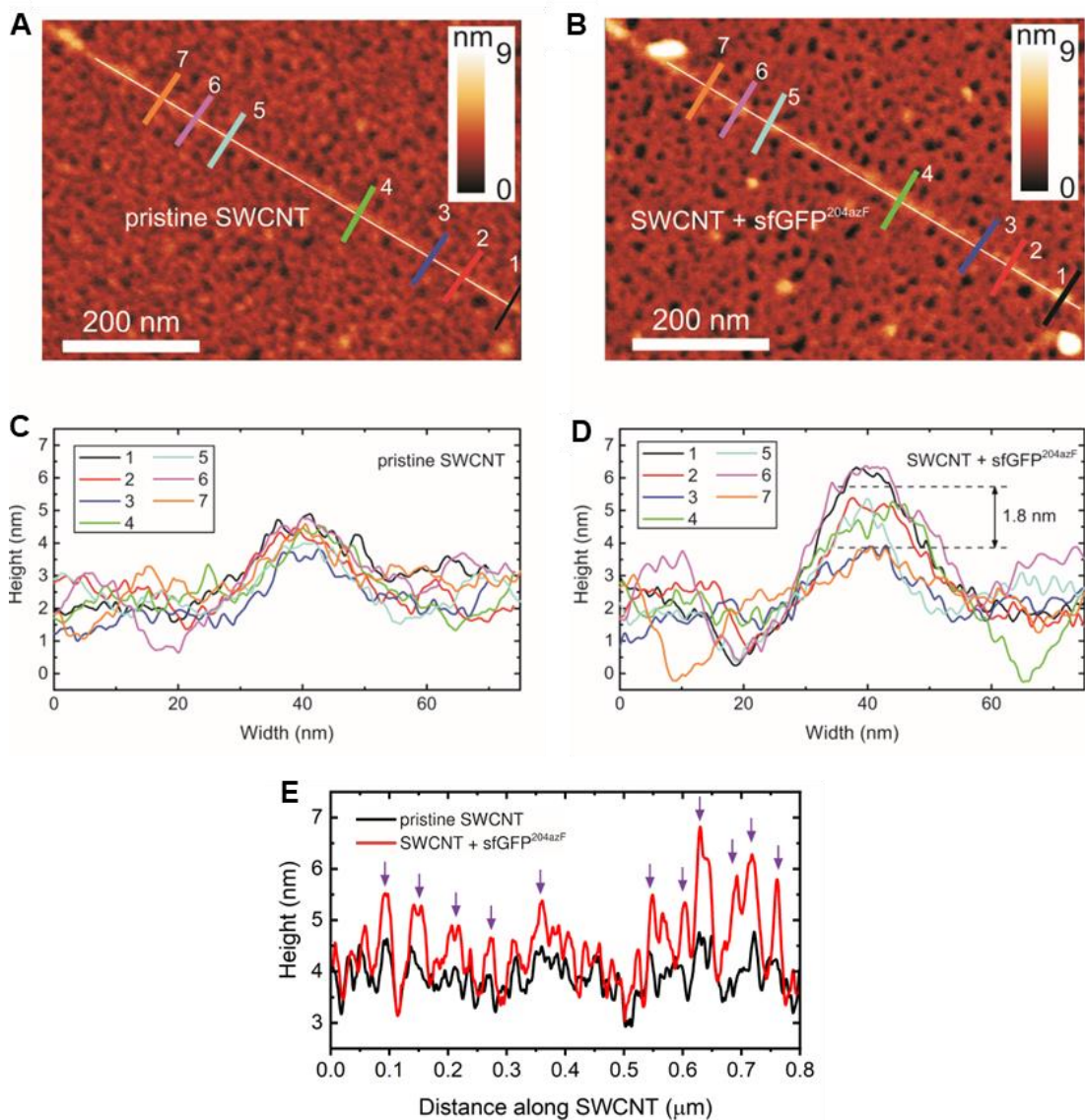
Figure 5.8 – Topographical characterisation of sfGFP^{204AzF}—NT-FET device. (A) AFM image of the SWCNT before and after (B) 1 μM sfGFP^{204AzF} attachment, with perpendicular cross sections coloured and numbered. Sections are plotted in (C) and (D) for pristine SWCNT and SWCNT + sfGFP^{204AzF}, with sections 3 and 7 corresponding to bare SWCNT in the latter. Figures (A – D) were produced by Dr. Aleksei Emilianov. (E) Longitudinal topography along nanotube axis before (black) and after (red) sfGFP^{204AzF} attachment, with purple arrows indicating likely sites of protein attachment. Figure adapted with permission from Gwyther et al. (2022).

5.2.6 Electrical characterisation of sfGFP^{132AzF}—NT-FET and sfGFP^{204AzF}—NT-FET

Current-voltage characteristics (IVs) were first recorded for the NT-FETs prior to protein attachment. The devices showed typical p-doped semiconducting behaviour, with a Schottky barrier formed between the metal electrodes and semiconducting SWCNTs (Figure 5.9 (A) and (B)). Follow up electrical characterisation then revealed the extent of modulation to output IVs from sfGFP^{132AzF} and sfGFP^{204AzF} attachment. Both proteins caused a drop in conductivity, but this was particularly pronounced for sfGFP^{132AzF} (Figure 5.9 (A) and (B)). Electrostatic gating was unlikely to be the mechanism behind this because a loss of charge carriers is associated with a positive gating voltage, and the area surrounding 132 AzF is dominated by neutral and acidic groups (Figure 5.9 (C)). sfGFP^{204AzF}, meanwhile, experienced a negligible loss in conductance despite a higher-density coverage of basic residues around 204 AzF (Figure 5.9 (D)). Other mechanisms for conductance loss could therefore include non-specific adsorption of unbound protein, as observed in our WT sfGFP treated quasi-metallic SWCNT (qmSWCNT) device (Figure 5.10 (A)), trapped states from structural defects, or n-doping via direct charge transfer. The latter mechanism was also speculated from the Raman analysis (Figure 5.6) and would explain the loss of charge carrier population, as electrons quench the free holes. Overall, the small loss of conductance in these devices is testament to the minimal number of defects introduced by AzF cross-linking, and is far less abrasive than other SWCNT functionalisation methodologies, e.g., diazonium salt coupling or oxidation (Lerner et al. 2012; Stando et al. 2022). Transfer IVs collected from semiconducting NT-FETs then allowed us to establish the operational gate voltage (V_{GS}; Figure 5.10 (B)). Our semiconducting NT-FETs had a negative threshold voltage (V_T) and drain current (I_D) close to zero, when a source-drain bias (V_{DS}) was applied at 1 V and V_{GS} = 0 V. The highest possible conductance was observed at $V_{GS} \leq$ -10 V across all six devices (Figure 5.10 (B)), so this was applied in the optoelectronic experiments hereafter. This ensured the NT-FETs were operating in the p-type region, and had conductance limited only by variations in channel length and contact resistance properties.
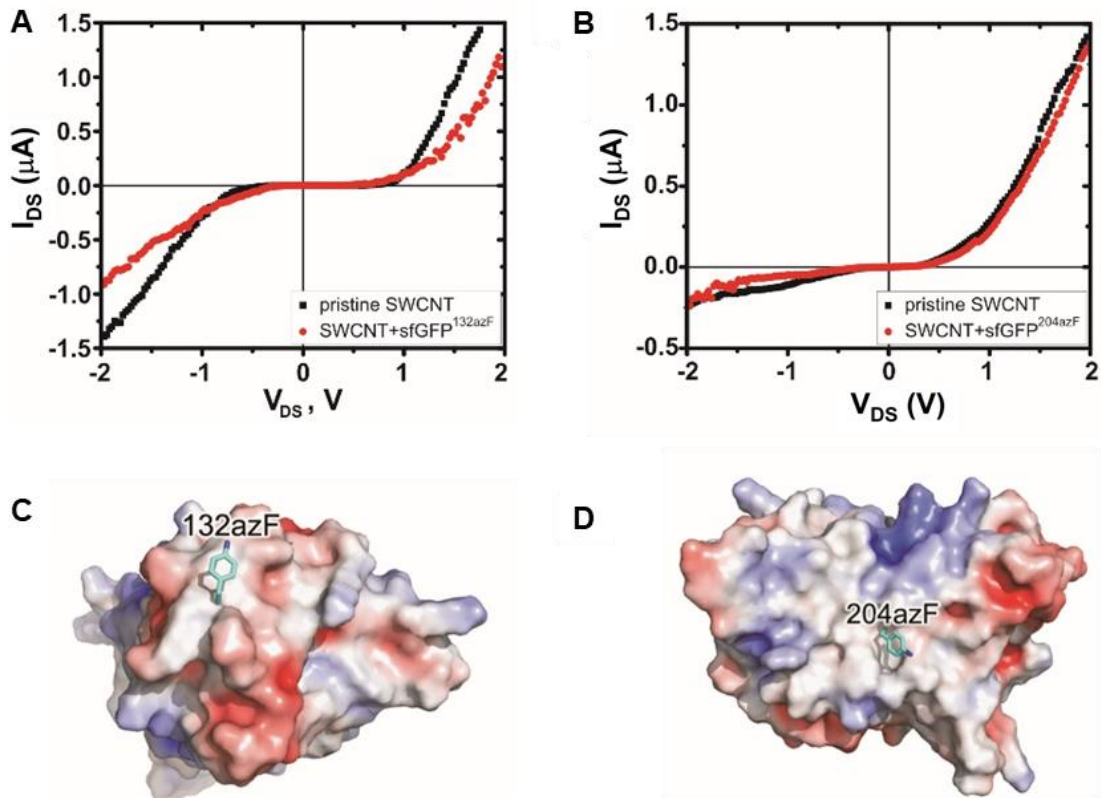
Figure 5.9 – Electrical characterisation of sfGFP^{132AzF}—NT-FET and sfGFP^{204AzF}—NT-FET. Output current-voltage characteristics of SWCNT-FETs before and after AzF containing GFP attachment to SWCNTs for sfGFP^{132AzF} (A) and sfGFP^{204AzF} (B). In each case, protein attachment was performed with 100 nM of the sfGFP variant. Electrostatic surface profile of sfGFP from the perspective of 132 AzF (C) and 204 AzF (D) residue sites (coloured cyan). The colour change from blue to red at (C, D) corresponds to a shift from positive to negative charges while white is neutral. Figure adapted with permission from Gwyther et al. (2022).
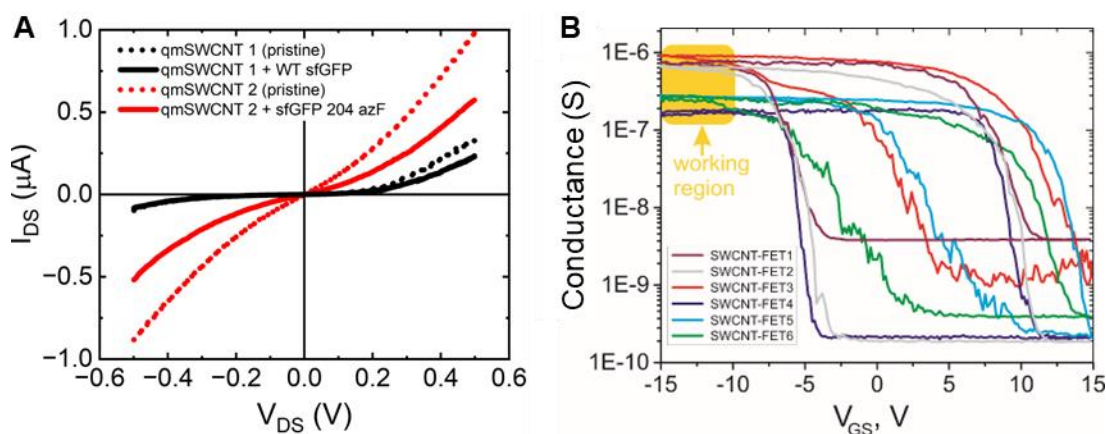
Figure 5.10 – Electrical characterisation of control devices. (A) Output IV curves of control qmSWCNT before (black, dotted) and after (black, solid) UV irradiation of qmSWCNT in the presence of WT sfGFP. (B) Transfer IV curves for six semiconducting NT-FETs before modification with protein. Operational range of V_{GS} used in this work is depicted by a yellow square. Figure (B) was produced by Dr. Aleksei Emlianov. Figure adapted with permission from Gwyther et al. (2022).

5.2.7 Photoresponse of sfGFP^{132AzF}—NT-FET and sfGFP^{204AzF}—NT-FET

Fluorescent proteins like sfGFP are considered to have inherent light-dependent charge transfer and redox properties (Stoner-Ma et al. 2008; van Thor 2009; Oltrogge et al. 2014; Lv et al. 2015; Acharya et al. 2017; Tang et al. 2018; Sen et al. 2021) in addition to their surface protein electrostatics (*vide supra*). These properties can, in turn, change carrier density in SWCNTs, with a loss of holes associated with conductance decrease and gain of holes associated with a conductance increase. Charge carriers can be modulated through local field effects, such as electrostatic gating by the proximal protein surface (Brejc et al. 1997) or by direct charge transfer (Bradley et al. 2004; Du et al. 2020). We hypothesise the latter method will be the mechanism for conductance modulation when testing the optoelectronic control of our sfGFP^{AzF} functionalised NT-FETs. Inherent sfGFP function permits electronic excitation through light absorption, and so covalent bonding to a SWCNT may provide a viable n-doping transduction pathway (Thomas et al. 2020; Yoo et al. 2021). By this hypothesis, the attachment site of sfGFP to SWCNT will significantly affect the nature and extent of conductance modulation.

We studied the photoresponse of the sfGFP^{AzF} modified NT-FETs by irradiation at different wavelengths (445, 470, and 590 nm). As shown in Figure 5.3, the original WT sfGFP and the two AzF containing variants free in solution excite and emit to

different degrees at the chosen wavelengths (445 and 470 nm). Electronic excitation is most efficient at 470 nm (closest to the λ_{max} at 490 nm), and there is no electronic excitation or fluorescence emission at 590 nm. Based on the solution spectral properties, we measured the optical response of our NT-FETs on irradiation at 470 nm first. Both sfGFP[132AzF]—NT-FET and sfGFP[204AzF]—NT-FET showed a significant light-dependent conductance decrease on illumination at 470 nm (Figure 5.11 and Figure 5.12). By comparison, a small increase in conductance is observed on illumination at 470 nm of pristine and WT sfGFP (no AzF) treated NT-FETs (Figure 5.13 (A – C)). For the sfGFP[132AzF]—NT-FET, a 15-fold reduction of conductance occurred within 15.0 ± 1.7 seconds of illumination (Figure 5.11 (A)), with no recovery to the initial state on removal of the light source even after 10 minutes in the dark. To regenerate the sfGFP[132AzF]—NT-FET we applied a gate voltage sweep from -15 to 15 V. After the sweep, illumination of the FET at 470 nm again resulted in a current drop until the next V_{GS} sweep, demonstrating the system can be switched multiple times. For the sfGFP[204AzF] —NT-FET, we also observed a ~80 % drop in current upon 470 nm illumination with a response time of 38.0±1.5 seconds. Unlike sfGFP[132AzF], total recovery of conductance occurred in the dark within 200 s without applying any V_{GS} sweep. This recovery behaviour showed good reproducibility over multiple irradiation/dark steps (Figure 5.11 (B)). The two different protein attachment sites and, hence, molecular configurations result in a different response to light. Thus, we have demonstrated two different and novel bio-optoelectronic effects in NT-FETs: optical gated transistor (for sfGFP[204AzF]) and optoelectronic memory (for sfGFP[132AzF]). It is worth noting that sfGFP[132AzF]—NT-FET behaves similarly to the optoelectronic memory device ORAM (Zhou et al. 2019a), optical switching that is restored under gate voltage sweeping.
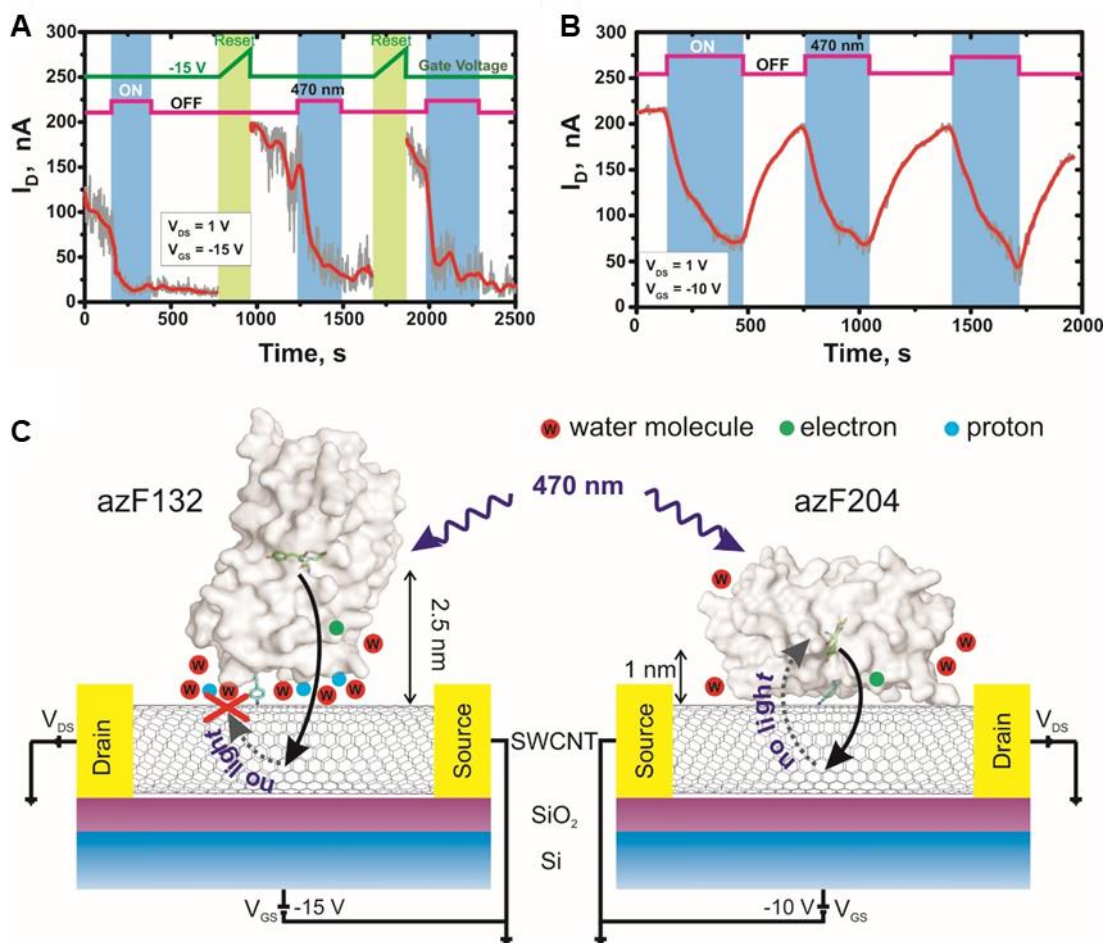
Figure 5.11 – Photoresponse of sfGFP^{132AzF}—NT-FET and sfGFP^{204AzF}—NT-FET transistors: time course and mechanism. (A) Light-induced signal recording with gate voltage-induced dark state recovery in sfGFP^{132AzF}—NT-FET upon on 470 nm (50 mW cm^{-2}) illumination cycling. (B) Time course current evolution of the sfGFP^{204AzF}—NT-FET on 470 nm (50 mW cm^{-2}) illumination cycling. Data was collected after NT-FET was stored for six months and rehydrated for reproducibility testing (*vide infra*). (C) Two proposed mechanisms of photoinduced electron transfer from the chromophore in sfGFP^{132AzF} (left) and sfGFP^{204AzF} (right) variants to the SWCNT. Black solid and dotted arrows indicate the pathway of electron transport from the chromophore into SWCNT upon illumination and back under dark, respectively. Figure copied with permission from Gwyther et al. (2022).
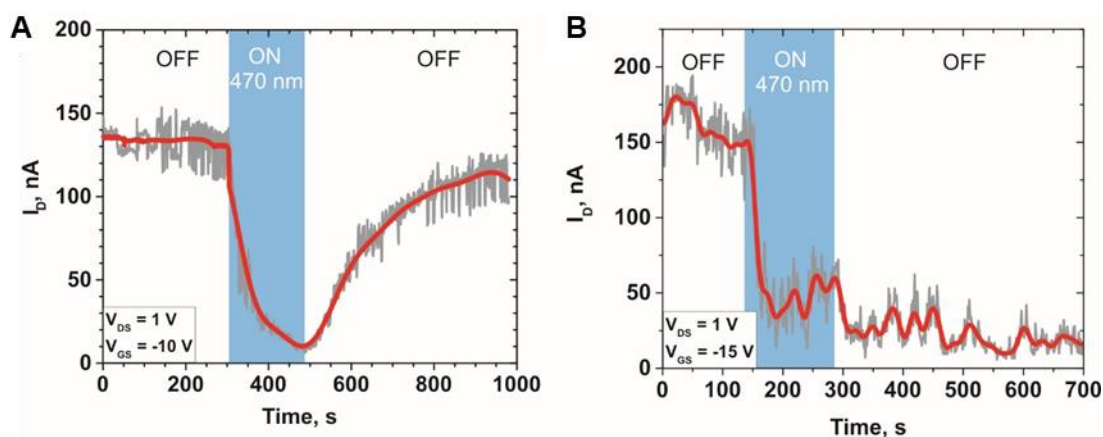
Figure 5.12 – Photoresponse cycle. A detailed time course evolution of sfGFP^{132AzF}—NT-FET (A) and sfGFP^{204AzF}—NT-FET (B) upon one pulse of 470 nm LED (50 mW cm^{-2}) illumination. Data was collected shortly after NT-FET arrival in Russia, with the figures produced by Dr. Aleksei Emilianov. Figure adapted with permission from Gwyther et al. (2022).

We attribute the optical response of the sfGFP-modified NT-FETs to electronic excitation, together with the associated charge transfer process, energy emission and the subsequent return to the ground state. For both sfGFP^{132AzF} and sfGFP^{204AzF}, illumination causes a decrease in conductance in p-type semiconducting SWCNTs (Figure 5.12). The likely mechanism for the observed current drop is the electron transfer to the SWCNTs from the photoexcited sfGFP, similar to that previously suggested for GFP bound to graphene, but fabricated via a different chemical attachment process (Lu et al. 2012). Attachment position with respect to the protein thus plays a major role in the optoelectronic characteristics of the fabricated devices.

The chromophore, central to sfGFP function, is buried within the β-barrel of the protein (Figure 5.1) and contributes to an extended polar interaction network of neighbouring residues and buried water molecules (Brejc et al. 1997; Stepanenko et al. 2008). These networks comprise the charge transfer pathways of sfGFP (Shinobu et al. 2010; Acharya et al. 2017). Differences between the relative chromophore distance of sfGFP^{132AzF} (~2.5 nm) and sfGFP^{204AzF} (~1 nm) were thought to explain the less-conductive state observed for sfGFP^{132AzF}, as electrons had to tunnel over a greater distance (Stuchebrukhov 2010; Winkler and Gray 2014). Indeed, it was suggested as a possible explanation for the previously observed difference in fluorescence characteristics on attachment to SWCNTs

(Thomas et al. 2020). The CAVER analysis (Chovancova et al. 2012) performed by Thomas et al. (2020) proposed a long (4 – 5 nm) and an indirect charge transfer pathway between the chromophore and residue 132. For electrons to tunnel effectively over that distance, significant potential energy is required (Winkler et al. 1999). The reduced photo-cycling rate (Thomas et al. 2020) and the less conductive state of the SWCNT demonstrated here (Figure 5.11 (A) and Figure 5.12), suggests the photoexcited electron fails to cross this tunnelling barrier – possibly getting trapped on the water molecules at the protein and nanotube interface (Figure 5.11 (C)). Switching the gate voltage could explain restoration of the photoresponse by relaxing the dipole moment on the water molecule and driving an electron back to the protein. Meanwhile, sfGFP[204AzF] exhibits a closer coupling between the sfGFP chromophore and SWCNT (Figure 5.11 (C)). An established water tunnel is already known to connect the chromophore to the bulk solvent adjacent to residue 204 (Shinobu and Agmon 2015). This potential charge transfer pathway is much shorter (~ 1 nm) and more direct than in sfGFP[132AzF], so electron tunnelling is anticipated to be more successful. Indeed, increased photo-cycling rates were observed by Thomas et al. (2020), and conductance was demonstrated to recover here (Figure 5.11 (B) and Figure 5.12).
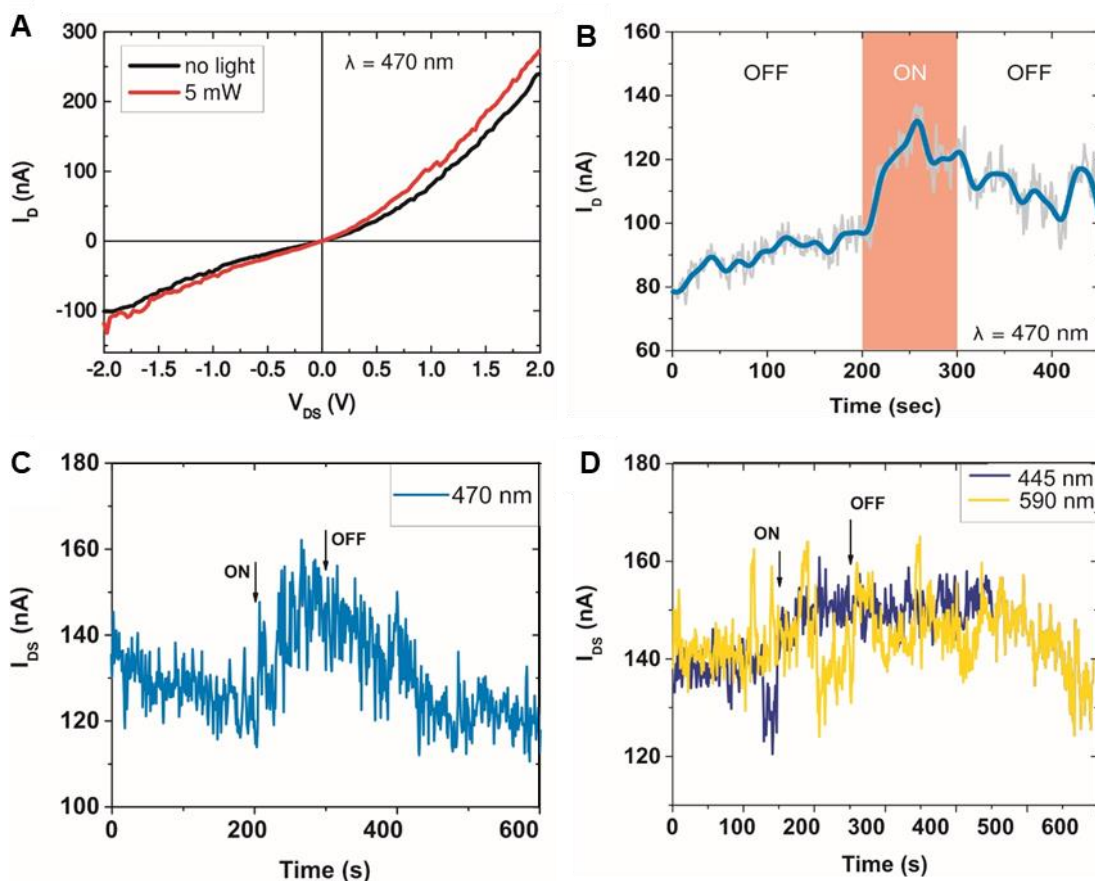
Figure 5.13 – Photoresponse of control semiconducting SWCNT transistors.
(A) The output curves of pristine semiconducting NT-FET in the dark and upon LED
illumination with 5 mW cm^{-2} at 470 nm. (B) Time course of pristine semiconducting
NT-FET upon 5 mW cm^{-2} at 470 nm light irradiation, V_{DS}= 1 V and V_{GS}= -10 V. (C)
Photoresponse of NT-FET after UV treatment in the presence of WT sfGFP upon
(C) 470 nm, and (D) 445 and 590 nm wavelength irradiation at V_{DS} = 1 V, V_{GS} = -10
V and LED power = 30 mW cm^{-2} for all wavelengths. Figures (A – D) produced by
Dr. Aleksei Emilianov, and adapted with permission from Gwyther et al. (2022).

5.2.8 Effect of wavelength and power on sfGFP^{204AzF}—NT-FET photoresponse

To further investigate the link between chromophore electronic excitation and
nanotube conductance, we exposed the sfGFP^{204AzF}—NT-FETs to monochromatic
light of different wavelengths and different powers, measuring I_{ph}: the difference in
current with and without illumination ($I_{ph} = |I_{light} − I_{dark}|$). We observed a wavelength
dependent response between I_{ph} and power (Figure 5.14 (A)) which correlated well
with the absorbance spectra of sfGFP^{204AzF} (Figure 5.3 (A)). The largest I_{ph} was
measured when sfGFP^{204AzF} was illuminated close to its λ_{max} at 470 nm, which has

an estimated molar absorption coefficient (ε) of ~43,000 M^{-1} cm^{-1}. I_{ph} then decreased for 445 nm (ε = ~23,000 M^{-1} cm^{-1}) and was negligible under 590 nm, due to the lack of electronic excitation at this wavelength. This established that the higher the molar absorption coefficient of a wavelength, the greater the change in I_{ph}. Control experiments with pristine NT-FETs, undergoing the same photochemical attachment procedure with WT sfGFP, showed a small current rise on illumination with 470 nm light (Figure 5.13 (C)), and negligible change with 445 and 590 nm light (Figure 5.13 (D)). Pristine NT-FETs not exposed to any protein also resulted in a slight rise in the conductance on illumination with 470 nm light (Figure 5.13 (A) and (B)), highlighting the thermoelectric effect in the SWCNT/electrode interface that accompanies significant illumination (Emelianov et al. 2021).

A power dependent response of sfGFP^{204AzF}—NT-FET was observed across Figure 5.14 (A) and (B). Above a power of 20 mW cm^{-2}, a saturation effect was observed across 445 nm, 470 nm, and to some extent, 590 nm (Figure 5.14 (A)), as no further change in I_{ph} was recorded. The 470 nm illumination time course (Figure 5.14 (B)) then showed this effect in real time, with increasing power leading to a faster and larger loss of current until the 20 mW cm^{-2} saturation threshold was met and I_{ph} decreased no further.

To consider how effective the sfGFP^{204AzF}—NT-FET device is at converting an optical input to an electrical output when responding to light at different wavelengths, we calculated a maximum value for photoresponsivity (R), whereby: $R = I_{ph} / P$. The value for P was derived from: $P = P_{LED} \times (A_{active} / A_{spot})$, where P_{LED} was the power of the incident light, A_{active} was the area of a device, and A_{spot} was the spot size of the diode (Nguyen et al. 2018). We choose A_{active} as the device area, which was defined as the distance between source and drain electrodes multiplied by an effective area of nanotube and SiO_2 trapping area (~30 nm) (Emelianov et al. 2021). We found that photoresponsivity for sfGFP^{204AzF}—NT-FET reached 0.45 x 10^3 A W^{-1} for 470 nm with 20 mW cm^{-2} illumination and up to 7 x 10^3 A W^{-1} at 470 nm with 1 mW cm^{-2}. This suggested the NT-FET worked most effectively at low-power optical input. Furthermore, the photoresponsivity across 445 nm and 590 nm correlated to the absorbance spectrum of sfGFP (Figure 5.14 (C)), opening up the possibility of low-intensity wavelength-specific detection, via the attachment of several different fluorescent proteins with a different λ_{max} to form an array of SWCNT transistors.
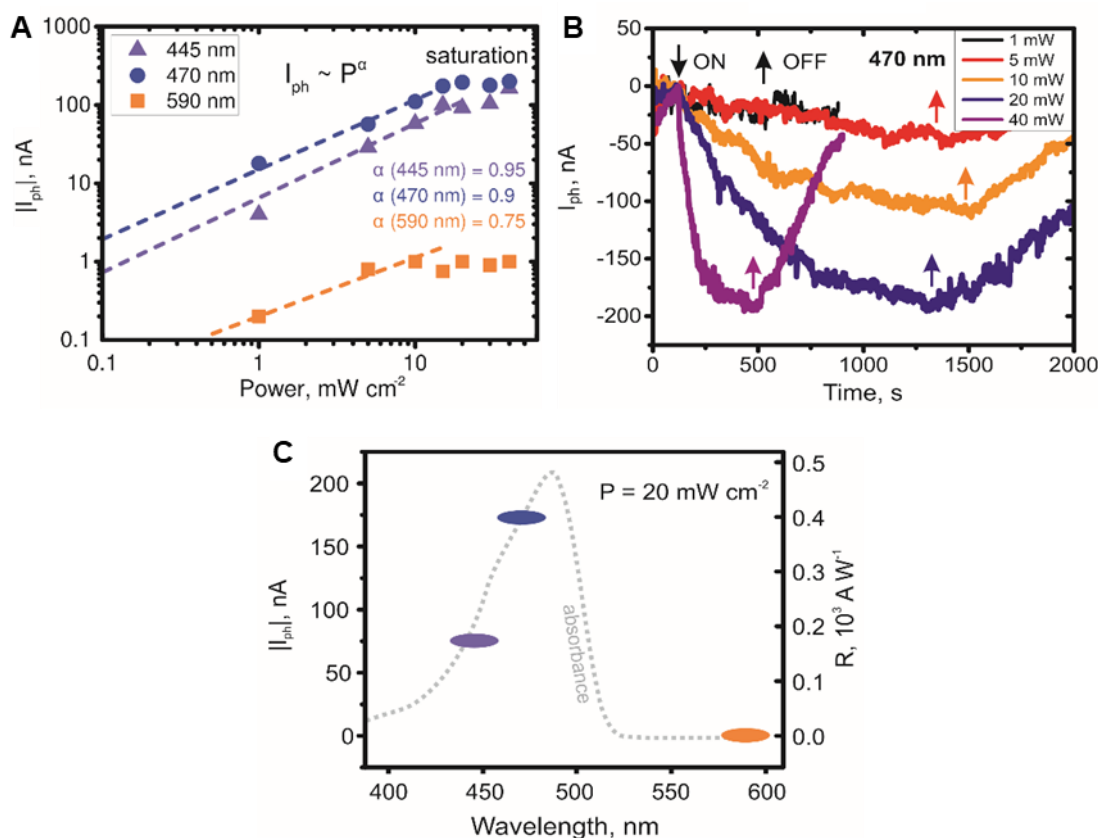
Figure 5.14 – Wavelength-specific response of sfGFP^{204AzF}—NT-FET. (A) Non-linear dependence of I_{ph} on irradiation power for different wavelengths. (B) Transient photoresponse behavior of sfGFP^{204AzF}—NT-FET under different power input from the 470 nm LED. (C) I_{ph} and R of phototransistor at different wavelengths. The UV-vis absorbance spectra curve of sfGFP^{204AzF} is shown as grey dotted lines for comparison. V_{GS} and V_{DS} were set as −10 and 1 V, respectively, during the measurements. Figures (A – C) produced by Dr. Aleksei Emilianov, and adapted with permission from Gwyther et al. (2022).

To hypothesise a mechanism behind the observed photoresponses, energy band diagrams are a useful visual reference (Figure 5.15). In p-type SWCNTs, the majority charge carrier (holes) are found in abundance in the lower energy (valence) band, while free electrons are found in negligible concentrations in the upper energy (conduction) band. When sfGFP is electronically excited through light absorption, the photogenerated electrons in sfGFP are thought to move into the SWCNT conduction band. Some of these electrons can become trapped at the SWCNT/protein interface, while others directly transfer into the valence band via electron tunnelling to form an electron-hole pair. The direct covalent phenylazide linkage helps to facilitate this, as electron tunnelling via bonded contacts (e.g.,

alkanes) has proven considerably more efficient than non-bonded contacts such as water molecules (Winkler and Gray 2014). However, the destination of these electrons will ultimately depend on their potential energy, as energetic barriers are put in place by (i) moving to the SWCNT/protein interface, and (ii) crossing from the conduction band into the valence. It is the formation of electron-hole pairs that then cause a loss of conductance, as the concentration of holes decreases.
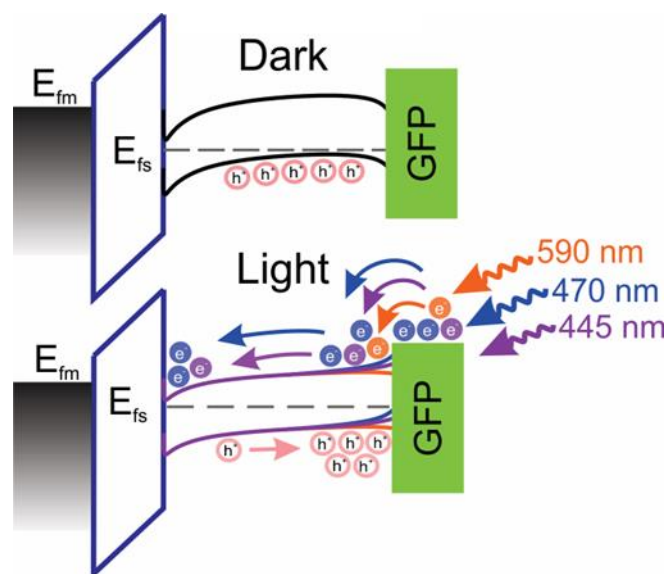
Figure 5.15 – Proposed mechanism for direct electron transfer between sfGFP and SWCNT. Illustrated as an energy band diagram in the dark (top), and upon light illumination (bottom), at three different wavelengths. Photoexcited electrons move into the SWCNT conduction band becoming trapped or crossing into the valence band to pair with holes. E_{fm} = metal Fermi level, E_{fs} = source contact Fermi level, h^+ = hole, e^- = electron. Figure adapted with permission from Gwyther et al. (2022).

The exact nature of electron transfer will depend on the quantity of light absorbed. Light wavelength and irradiation power are identified as two key parameters, with the fastest optical response being detected with 470 nm illumination (Figure 5.16 (A)), and irradiation power being shown to have a linear relationship with response time (Figure 5.16 (B)). By absorbing a higher quantity of light (either via wavelengths close to λ_{max}, or at an increased irradiation power) the probability of electrons transferring into the valence band via tunnelling or hopping mechanisms significantly increases, leading to a rapid and higher amplitude change in I_{ph}. Absorbing a lower quantity light (via wavelengths distant from λ_{max}, or at a reduced irradiation power), the probability of charge transfer is lower. Electrons may be

trapped at the interfacial states or have returned to the chromophore, resulting in a slower and smaller change in I_{ph}. To increase the speed of the photogenerated charge carrier separation, one can change the FET channel size either by decreasing the length or by increasing the number of nanotubes in a channel by using a nanotube network (He et al. 2015). We have demonstrated that decreasing the channel length of a single SWCNT by about an order of magnitude results in a quicker response time of more than two orders of magnitude (Figure 5.16 (C)). Furthermore, the use of a proper substrate material and operation at lower temperatures could act as a way to boost the response time in NT-FET devices (Fedorov et al. 2013).
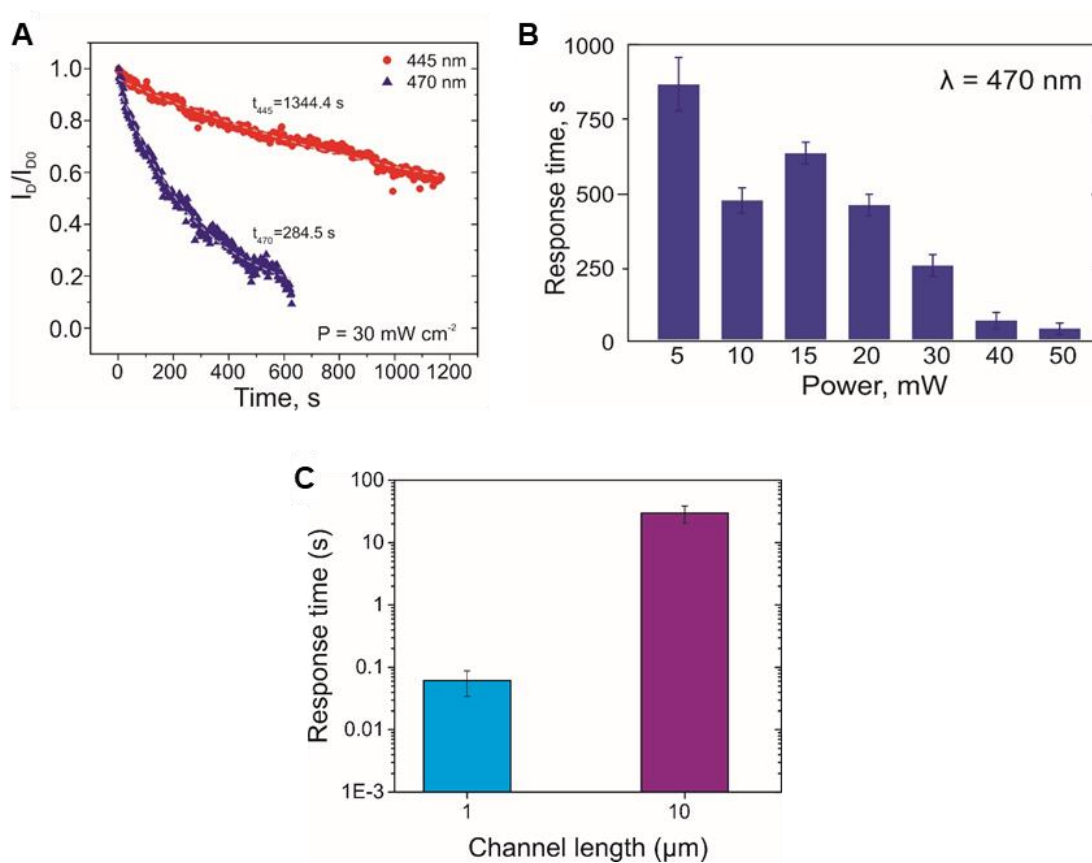
Figure 5.16 – Analysis of photoresponse time. (A) Photoresponse on irradiation at 445 and 470 nm wavelengths at 30 mW cm^{-2}, with response time calculated by exponential fitting. (B) Effect of irradiation power at 470 nm on photoresponse time. (C) Effect of channel length (1 and 10 μm) on pristine NT-FET response time after

illumination at 470 nm. Figures (A – C) produced by Dr. Aleksei Emilianov, and adapted with permission from Gwyther et al. (2022).

5.2.9 Water regeneration of sfGFP[204AzF]—NT-FET device

A novel property arising from the sfGFP[AzF] functionalised NT-FETs is their ability to be regenerated with water after a considerable period of time. Protein structure and function is inherently supported by a network of water molecules (Bellissent-Funel et al. 2016), and long-term storage in a non-aqueous environment was anticipated to cause irreversible structural damage from water evaporation (Prestrelski et al. 1993). To our surprise, the sfGFP[204AzF]—NT-FET (stored at room temperature for 6 months) still showed signs of life after exposure to 470 nm light (Figure 5.17 (A)). Current was seen to drop by ~15 nA across the NT-FET when the LED was switched on, and recovered when it was switched off, albeit with considerable noise. The amplitude of current loss and gain in response to 470 nm on/off cycles was approximately a tenth of the original experiment (Figure 5.12). In attempt to regenerate the sfGFP[204AzF]—NT-FET, the device was soaked in water for 10 minutes and the experiment repeated (Figure 5.17 (B)). Exposure to 470 nm light then caused a ~130 nA drop in current and recovered fully in the absence of light. The amplitude of current change in the on/off cycles and photoresponse time matched the original experiment (Figure 5.12), proving water regeneration could recover full-functionality after 6 months of storage at room temperature. Not only is this testament to the robustness of sfGFP in structure, but it also highlights the role water molecules play in the observed photoresponse. Two water molecules are found in the sfGFP chromophore, with one of those structurally conserved and proven to play a crucial role in the proton transfer network and fluorescence (Hanson et al. 2002; Agmon 2005; Arpino et al. 2012; Hartley et al. 2016). The water molecules are connected to the external environment via a 'water wire' (Shinobu and Agmon 2015), and evaporation along it could jeopardise the charge transfer mechanism, along with the photoresponse (Hanson et al. 2002; Hartley et al. 2016). Indirect roles for water molecules are also found in the hydration shell that cloaks sfGFP (Perticaroli et al. 2017). Evaporation here will likely be a contributing factor towards the weakened photoresponse, due to the structural and functional damage that accompanies water loss.
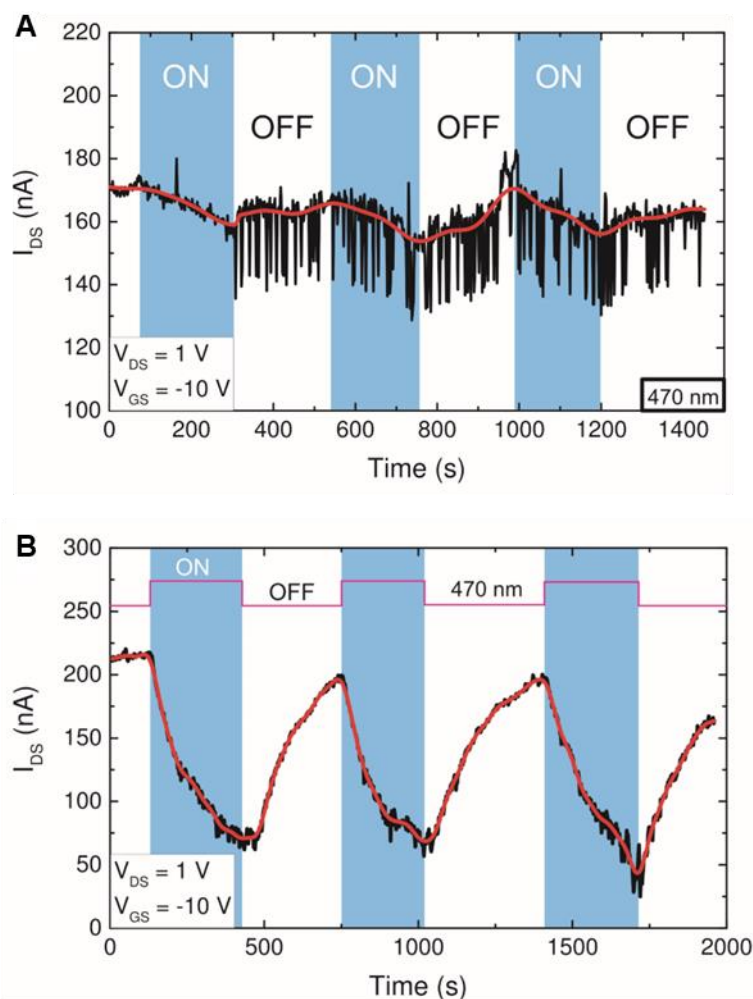
Figure 5.17 – Regeneration of sfGFP^{204AzF}—NT-FET after 6 months storage. (A) Effect of 50 mW cm^{-2} 470 nm light cycling on sfGFP^{204AzF}—NT-FET after storage at room temperature for 6 months. The device was then soaked in water for 10 minutes, and the experiment repeated (B). A source-drain bias of 1V was applied, with a gate voltage of -10 V. Figures produced by Dr. Aleksei Emilianov.

As an important note of disclosure, Figure 5.17 (B) is the same electrical trace used in Figure 5.11 (B). The idea to investigate the reproducibility of the sfGFP^{204AzF}—NT-FET photoresponse arose during the writing process of our Advanced Functional Materials paper (Gwyther et al. 2022). The original experiment only measured one pulse of 470 nm illumination (Figure 5.12), and so six months after this experiment, we looked to test the sfGFP^{204AzF}—NT-FET again for reproducibility. This led to the results depicted in Figure 5.17 (A), where the photoresponse was shown to be damaged from six months' worth of dehydration. After soaking the sfGFP^{204AzF}—NT-FET for 10 minutes, the experiment was repeated and the reproducibility of the photoresponse was proven (Figure 5.17 (B)). This was highlighted in Figure 5.11 (B)

as it was a key feature of the sfGFP[204AzF]—NT-FET. The water regeneration aspect described here was therefore a serendipitous discovery made alongside the sfGFP[204AzF]—NT-FET reproducibility experiment.

5.3 Conclusions and Future Perspectives

To summarise the key results from this chapter, we have produced optoelectronic biohybrid NT-FET devices, developed using a simple photochemical attachment process via residue-specific covalent attachment of engineered sfGFP to sidewalls of individual carbon nanotubes. The covalent functionalisation of SWCNTs resulted in a weak decrease in transconductance, yet highly effective optical performance as field-effect transistors. By varying the attachment residue position of sfGFP, we changed the characteristics of the fabricated device: a phototransistor with the sensitivity of about·7 x 10^3 A W^{-1} or optoelectronic memory, with rapid photoresponse, low power consumption and 15-fold current modulation. Light-induced direct charge transfer at the sfGFP/SWCNT interface was the likely driver for the optical response, with the different protein attachment sites dictating device characteristics.

In terms of research significance, we have taken a novel approach to improve the sustainability of optoelectronic platforms. These devices typically depend on inorganic and finite materials, such as silicon and gallium arsenide, to detect and respond to light (Xu et al. 2018a). By substituting these materials for highly evolved and renewable alternatives: light-responsive proteins, we take an innovative and holistic approach to optoelectronic design. This approach joins the ranks of other green-led technology for sustainable optoelectronics, for example using paper or keratin as substrate materials (Posati et al. 2019; Pan et al. 2022), the development of organic solar cells (Zhao et al. 2016), and fully biodegradable electronic platforms (Han and Shin 2020; Jiang et al. 2021). The incorporation of sfGFP not only highlights the potential biomolecules have to transduce optical energy into electrical, but it also provides a case for their sustainable longevity in the absence of an aqueous environment. To the best of our knowledge, this was the first-time protein-functionalised optoelectronic devices were (i) observed to have such a significant lifespan and (ii) used water soaking to recover full functionality of the protein after 6 months of dehydration.

The potential applications of our sfGFP[AzF] functionalised NT-FETs can be considered in terms of the distinct characteristics they possess: optoelectronic

194

memory and optoelectronic gating. Optoelectronic memory in the context of sfGFP[132AzF]—NT-FET describes the ability of light irradiation to 'switch off' current flowing to the drain electrode. Current is only restored upon a voltage gate sweep, so the device will effectively 'remember' absorbing light at that particular wavelength until manually reset. While this on/off behaviour is fundamental in practise, it mirrors the logic data processing used in next generation photonic semiconductor microchips (Xu et al. 2005; Sun et al. 2015); a global market where demand is continuing to grow. Applications in image capturing circuitry are also easily envisaged, with photodetection at specific wavelengths stored immediately as memory (Fossum 1997; Zhou et al. 2019a). Our NT-FETs have the potential to expand into this, by substituting sfGFP with the plethora of fluorescent proteins that absorb across the electromagnetic spectrum with different λ_{max} (Rodriguez et al. 2017).

Optoelectronic transistors, in the context of our sfGFP[204AzF]—NT-FET, use light irradiation as a gating mechanism to reduce drain current. The key difference to optoelectronic memory is that in the absence of the gating mechanism (light), current recovers without any voltage input, reducing overall power consumption. The drain current in our sfGFP[204AzF]—NT-FET device responded proportionately to changes in wavelength and light power, with the highest photoresponse linked to low light levels. Integration of these transistors into circuits could therefore contribute to low light sensing applications, e.g. night vision technology (Kufer and Konstantatos 2016; Shao et al. 2019), or be used directly as a measurement device for fluorescence detection (Liao et al. 2013).

Overall, we present a methodology that successfully integrates light-responsive proteins into NT-FETs, with novel gating mechanisms that are dictated by the protein—SWCNT interface. Further mechanisms may be discovered, or optical memory and gating characteristics may be improved by testing different interfacing residues. Likewise, NT-FET photoresponsivity can be broadened by integrating light-responsive proteins with a different λ_{max}. Research into this field will help to increase the sustainability of optoelectronic devices, with applications that span from LEDs and lasers to the next generation of photonic semiconductors.

6. Discussion

Work in this chapter contributed to a published, peer-reviewed review paper where I am joint 1st author. With permission from the publisher, text and figures have been taken and adapted for my thesis.

Lee, C.S., **Gwyther, R.**, Freeley, M., Jones, D., Palma, M., 2022. Fabrication and Functionalisation of Nanocarbon-based Field-Effect Transistor Biosensors. *ChemBioChem*, 23, e202200282.

6.1 Overview

Research and development in the 21st century favours an interdisciplinary approach, with knowledge transfer leading to high-impact discoveries (Van Noorden 2015; Szell et al. 2018; Sun et al. 2021). This thesis applies synthetic biology, biochemistry, nanotechnology and physics to great effect, as I integrate nature's own nanomachines (proteins) into a fundamental electronic platform (NT-FETs). The proximal, covalent link between the two species allow for highly evolved protein function to be transduced and communicated through an electrical signal. Applications for this are limited only by the biological molecule in question, with this thesis considering biosensing by protein-protein interaction, and optoelectronic transduction.

To summarise the methodology in brief, I genetically reprogram *E. coli* to recognise the amber stop codon (UAG) as the site of non-natural amino acid AzF incorporation. The AzF-containing protein is expressed recombinantly, purified and characterised by a variety of biochemical techniques, before drop-casting onto a fabricated NT-FET device. UV irradiation activates the protein, generating a nitrene radical to attack the side walls of the SWCNT channel in a [2+1] cycloaddition reaction. This covalently bonds the two species, integrating the protein in a defined-residue specific manner to ensure it remains functionally active. Connecting the NT-FET to a voltage source and applying the independent variable, e.g., the target analyte or light, then allows electrical signals to be monitored as conductance varies across the channel.

Across the three research chapters of this thesis, key themes and novel findings have been established. To be considered further in this discussion are (i) diagnostic biosensing for antibiotic resistance and beyond, (ii) a computational pipeline to predict electrostatic gating, and (iii) optoelectronic transduction: towards green

electronics. The limitations of NT-FETs will then be discussed, along with a future research direction.

6.2 Diagnostic biosensing for antibiotic resistance and beyond

NT-FETs have been earmarked for biosensing since their inception (Schasfoort et al. 1990). The ability to integrate biomolecules with carbon nanotubes opened the doorway for bionanohybrid systems, as a wide-range of functionalisation routes were available to link the two species (Lee et al. 2022). In particular, the pioneering use of AzF chemistry to integrate proteins through direct covalent attachment, or non-covalent attachment via a DBCO-pyrene linker, allowed protein orientation to be defined and controlled (Zaki et al. 2018; Thomas et al. 2020; Xu et al. 2021; Gwyther et al. 2022). The Jones and Palma labs have been collaborating on this approach for the past few years to integrate BLIP-II, a potent inhibitor to class A β-lactamases, to selectively transduce the presence of ABR biomarkers.

In a bid to continue the research directive and build on the non-covalent prototype developed in 2021 (Xu et al. 2021), Chapter 3 focused on the covalent integration of BLIP-II to an NT-FET. Two notable research outcomes can be considered. Firstly, the attachment of the BLIP-II[41AzF] and BLIP-II[213AzF] increased conductance across the NT-FET channel. This has significant impact on the field of NT-FETs, and more generally on SWCNT functionalisation, as it defies the notion that covalent functionalisation will always damage SWCNT conductivity (Zeng et al. 2008). Instead, the [2+1] cycloaddition reaction preserves the π-conjugation of the SWCNT, while forming a strong and intimate covalent linkage with a biomolecule (Setaro et al. 2017). This benefits the biosensor design by increasing the likelihood of analytes passing within the Debye length. The second key outcome was the successful sensing experiments against two prevalent β-lactamases: TEM-1 and KPC-2. The BLIP-II[41AzF] and BLIP-II[213AzF] functionalised devices could successfully discriminate between the two proteins, with BLIP-II[213AzF] eliciting a stronger signal in response to the β-lactamases than BLIP-II[41AzF]. These conductance changes were seen to correlate to the electrostatic surface potential (ESP) of the incoming β-lactamases, supporting the gating hypothesis (Heller et al. 2008). The devices also achieved a minimum sensitivity of 50 nM (or 0.5 pmol) in a physiological strength ionic buffer (DPBS). This was similar to our non-covalent prototype (Xu et al. 2021) and approaches the sensitivity range of common biochemical assays used for

protein detection, such as western blotting or enzyme-linked immunosorbent assays (ELISAs) (Zhang et al. 2014; Goldman et al. 2016).

To briefly discuss the commercial potential of my biosensing NT-FET platform, there are two perspectives to consider: (i) the performance of my NT-FET against other SWCNT-based FETs, and (ii) the potential for my NT-FET in the ABR diagnostics market. In the first instance, my BLIP-II[AzF] functionalised NT-FETs would be considered less sensitive than the top performing NT-FET biosensors, as Tung et al. (2017) achieved a 2.3 pM limit of detection to their Cathepsin E analyte, and Li et al. (2021) achieved a 0.87 aM limit of detection to their exosomal miRNA analyte. Distinct differences in functionalisation strategy and detection method contribute to their success, with both approaches measuring analyte concentration through transfer characteristics. In my experimental approach, transfer characteristics were not collected as we were specifically investigating the protein electrostatic gating effect, and thus chose not to employ a back gate voltage. It is possible that greater sensitivity could be achieved by changing the detection method. Further experiments to derive transfer characteristics and real-time sensing would allow a more balanced comparison between the sensitivity of my BLIP-II[AzF] functionalised NT-FETs, and others recorded in the literature.

With that in mind, I still believe there is huge potential for my BLIP-II[AzF] functionalised NT-FETs in the ABR diagnostics market. The current approach to antimicrobial susceptibility testing is dominated by time-consuming methodologies (e.g., disc diffusion and broth dilution; Vasala et al. 2020), while faster, non-phenotypic routes to diagnosis (e.g., DNA/RNA sequencing) are being overlooked by the FDA due to the less reliable link between genotype and pathogenicity (Laing 2021). Lateral flow tests to specific resistant proteins (with a 23.7 pM limit of detection) have also been developed, but the vast variety in antibiotic resistance mechanisms prevents a realistic adoption of this approach (Boutal et al. 2017). The need for a rapid, point-of-care diagnostic that can identify any type of resistance proteins is thus still needed. For my BLIP-II[AzF] functionalised NT-FETs to fill this gap, however, further research and development needs to be carried out. The future perspectives in Chapter 3 (section 3.3) cover these suggestions in great detail, but to summarise the three most important, there are: (i) improved device uniformity, (ii) device multiplexing and ESP database generation, and (iii) 1000-fold increase in device sensitivity, to match equivalent testing standards (Boutal et al. 2017).

Overall, I believe my BLIP-II[AzF] functionalised NT-FETs are successful biosensors which can effectively detect and discriminate between different types of class A β-

lactamase. Its commercial potential depends upon several developmental measures, but its ease of integration into portable platforms would allow this to become a next generation, rapid diagnostic tool for antibiotic resistance. Further to this, the modular design complements future application, with a simple substitution of the receptor protein adapting the device to a whole new range of analytes and label-free sensing. This is an exciting platform for diagnostic technology.

6.3 Computational pipeline to predict electrostatic gating

As a fundamental mechanism behind NT-FET biosensing, electrostatic gating needs to be modelled effectively to inform important aspects of design. The defined assembly of proteins via AzF chemistry offers better chances of ESP prediction than the most, as the anchor is limited to one residue site only. However, the ability of AzF to adopt a gauche$^+$ or trans conformation about the χ_1 angle means the perpendicular hetero-bridged structure formed by UV irradiation can result in the protein's orientation differing by up to 120° when binding the SWCNT. Compounding factors including changes to the local backbone angle (φ and ψ), secondary structure and intramolecular bonding, instil further rotameric states that can only be acknowledged through molecular dynamic studies (Dunbrack 2002; Chamberlain and Bowie 2004).

The research undertaken in Chapter 4 built a computational pipeline to elucidate and model the rotameric states of AzF using BLIP-II[41AzF] and BLIP-II[213AzF]. Two notable research outcomes can be considered. Firstly, non-natural amino acid AzF was parameterised into the CHARMM36 simulation forcefield (Best et al. 2012). Despite recent publication of an additive forcefield for non-standard amino acids, AzF wasn't part of the 333-strong set (Croitoru et al. 2021). Manual parameterisation was therefore carried out, with partial charges generated by ACPYPE using the bond charge corrections method (Sousa Da Silva and Vranken 2012), and the relevant terms updated in the CHARMM36 parameter files. As a time-consuming and complex process, the completed parameterisation is a beneficial research outcome as the files can be distributed for use in modelling any AzF-containing protein, and not selectively BLIP-II. The second outcome considers the computational pipeline as a whole, with a strong link to the experimental data suggesting this is an effective way to model electrostatic gating. The rotameric analysis formed the scientific basis of the *in silico* modelling approach, with considerable time spent refining the RMSD calculation to accurately reflect the

rotamer clusters observed from the superimposed frame stack. After identifying rotamer propensity and extracting representative structures, the proximity and ESP of β-lactamases could be measured with respect to the SWCNT. Using the electrostatic gating hypothesis of p-type semiconductors, negative ESP was predicted to increase conductance by increasing the number of holes, while positive ESP was predicted to reduce conductance through depletion of holes; with the magnitude of change depending on the strength of the gating voltage. The results corroborated in part with the BLIP-II[41AzF]—NT-FETs, as 92.5 % of the AzF rotamers were deemed unsuitable for mediating β-lactamase binding within the Debye length, and experimentally the electrical signal observed was very weak. The results corroborated more confidently with the BLIP-II[213AzF]—NT-FETs, as 46.6 % of the AzF rotamers aligned the β-lactamases within 2 Å of the SWCNT and thus the Debye length. TEM-1 presented a strongly negative ESP (~ -5 $k_BTe_c^{-1}$), while KPC-2 presented a weakly positive ESP (1.5 $k_BTe_c^{-1}$), matching the experimental observations of current increasing by 0.64 µA with TEM-1 and decreasing by -0.25 µA with KPC-2.

Overall, the computational pipeline has a significant future, for NT-FET development and beyond. Operating through an easier and simpler setup than Côte et al. (2021), this approach to measure electrostatic gating is user-friendly and transferable. This is of particular importance in the growing field of molecular dynamics, as many users are novices from different disciplines, and this methodology bypasses more complex protocols around SWCNT parameterisation or analysing multiple χ angles (Altis et al. 2007; Watanabe et al. 2013; Hollingsworth and Dror 2018; Côte et al. 2021). The potential for electrostatic gating to be predicted in biosensing NT-FETs also yields significant potential. In cases of receptor proteins binding a wide variety of analytes, e.g., BLIP-II could potentially bind > 550 class A β-lactamases (Philippon et al. 2016), computational prediction to build a library of protein electrostatic signatures makes for a far more efficient and cost-effective approach than manual collection. Finally, a notable individual aspect of the computational pipeline is the rotamer analysis methodology. Conformations of individual amino acids are often overlooked for global protein conformation, but on a smaller scale, residue analysis can answer a wealth of biological questions. Applying the RMSD analysis to any residue (not just AzF), could provide invaluable insight to the flexibility and behaviour of residues involved in protein-protein interactions or enzyme active sites (Riziotis et al. 2022).

6.4 Optoelectronic transduction: towards green electronics

In an evolving world where sustainability is at the heart of new technological developments, the opportunity to integrate proteins into NT-FETs offers a renewable twist on traditional electronic devices. The protein must be of useful application to incorporate into NT-FET design, as the possible reduction in device performance and substitution of cheap, abundant, and well-functioning materials will be a difficult sell regardless of the environmental benefit. An optoelectronic device therefore became the focus, with light-responsive proteins such as GFP and photosystem I and II being well-adapted for light absorption and energy transfer (Bogdanov et al. 2009; Nelson and Junge 2015).

In collaboration with the Bobrinetskiy lab in Moscow, Chapter 5 focuses on the integration of sfGFP with an NT-FET, attaching the protein through two different AzF anchor sites: sfGFP[132AzF] and sfGFP[204AzF]. Three notable research outcomes can be considered. Firstly, the attachment of sfGFP[132AzF] generated a device with optoelectronic memory as characterised by its on/off behaviour. Illumination with 470 nm switched the device 'off' as it reduced the current 15-fold, and a gate voltage sweep from -15 to 15 V switched it back 'on'. This has real world application as all digital circuits require the storage and transmission of data in a binary format, and photonic semiconductors have already been tipped as the next generation of microprocessors (Sun et al. 2015). The second outcome was achieved with the sfGFP[204AzF] functionalised NT-FET, which optically gated the source-drain current by ~80 % under 470 nm illumination. This differs from the optoelectronic memory observed with sfGFP[132AzF], as the current autonomously restores itself under dark conditions. Phototransistors such as this can have useful application in low-light detection, e.g., night vision and fluorescence, and offers novel device architecture similar to organic phototransistors (Liao et al. 2013; Kufer and Konstantatos 2016; Shao et al. 2019; Huang et al. 2020). The final research outcome considers the novel water regeneration properties of the sfGFP[204AzF] functionalised NT-FET. Water has an underlying role in maintaining protein structure, function and dynamics, so integration into a non-aqueous environment like an NT-FET will introduce a shelf life (Bellissent-Funel et al. 2016). Soaking the sfGFP[204AzF]—NT-FET in water after six months of storage, however, allowed a complete restoration of functionality. To the best of my knowledge, this was the first-time protein-functionalised optoelectronic devices were (i) observed to have such a significant lifespan and (ii) shown to recover full functionality after 6 months of dehydration.

Overall, the integration of sfGFP into NT-FETs showcased novel properties which hold great promise for future research and development. Water regeneration, in particular, is an interesting concept as we shift towards more sustainable electronics. A comparative study of other protein—NT-FET setups and their ability to recover functionality after long-term storage and dehydration would give good insight into which devices may be suitable for commercialisation and scaling. To expand further on the potential applications of sfGFP functionalised NT-FETs, one could also consider switching the conductive mechanism. At present, our NT-FETs are inherent p-type semiconductors due to the adsorption of oxygen and water from air, and the high work function of the metal contacts (Avouris 2007; Aguirre et al. 2009; Obite et al. 2018). By converting the SWCNTs to n-type semiconductors (Shim et al. 2001; Kim et al. 2021), sfGFP would be able to increase current upon 470 nm illumination, instead of decrease. This could reverse the on/off polarity in sfGFP[132AzF]—NT-FETs, so the light instead switches the device 'on' from its 'off' state. Alternatively, there is scope to develop novel bionanohybrid solar cells for sustainable energy conversion. Photosystem I has been the focus of similar electrochemical setups (Nguyen and Bruce 2014) and this form of green electronics holds huge promise.

6.5 Limitations of NT-FETs

As with most emerging technologies, limitations arise as a product is scaled up for commercialisation. NT-FETs are no exception, and several areas require further research to accomplish product viability. Firstly, the heterogeneity of NT-FET devices (Liu and Guo 2012; Lee et al. 2022). Stemming primarily from a lack of uniformity in SWCNT deposition, the semiconductor channel displays variable baseline topographical and electronic properties, as demonstrated in Chapter 3. Uniformity can be improved on the smaller scale by optimising the deposition parameters, including concentration of SWCNTs, time, temperature, and solvent (Liu et al. 2011; Prasek et al. 2011; Eatemadi et al. 2014; Yomogida et al. 2016). However, an encouraging breakthrough by Bishop et al. (2020) demonstrated how silicon semiconductor manufacturing plants could be adapted to achieve SWCNT uniformity on a commercial scale. Advances like this will be crucial for the mass production of NT-FETs, as we switch from silicon to SWCNTs (Avouris 2007; Service 2009). Another challenge lies in the system integration of NT-FETs. Biosensing NT-FETs, in particular, need to factor in practical considerations around sample delivery and the salt concentration of physiological buffers, while

technological advances in multiplexed NT-FETs and machine learning algorithms will help to evolve the technology further (Liu and Guo 2012; Hwang et al. 2019; Musala and Vasavi 2022). On a similar note, non-specific binding events can also disrupt the label-free biosensing setup of NT-FETs. Passivation can be used to tackle this, with polymers such as polyethylene glycol, or bovine serum albumin (Cid et al. 2008; Ishikawa et al. 2009). However, these surface modifications can also reduce sensitivity by providing a barrier that masks the incoming analyte. Designed interfacing of high affinity receptors is therefore seen as an alternative approach to counteract this (Lee et al. 2022). A final limitation regards the protein functionalisation strategy utilised in this thesis. AzF is a photoreactive reagent, and as such, the expression, purification and functionality testing of these proteins must be performed in the dark to minimise light exposure. On a commercial scale, bacterial expression can take place in UV-blocking growth chambers, but downstream processing may require awkward alterations for testing to take place in dark rooms (Ericson et al. 2015). Availability of AzF has also been hampered by discovery of previously undocumented explosive characteristics (Richardson et al. 2018). The risk is concentrated around AzF synthesis, and protocols involving heating near its exothermic decomposition point (124 °C), but this has led to difficulty in sourcing AzF, and consequently a higher cost. Commercial contracting would likely fare better at sourcing stable supply of AzF at a reduced cost than small academic labs. Overall, the prospect of commercial NT-FETs is now closer than ever, with strategies to overcome limitations persistently being researched (Li et al. 2023).

6.6 Future work

The research showcased in this thesis has created new avenues to explore and further areas to develop. Within the scope of the Jones and collaborator labs, the future work available to each chapter will be considered.

Chapter 3 focused on the development of a biosensing NT-FET, with receptor protein BLIP-II covalently integrated into the SWCNT channel. A future optimisation of the fabrication setup would be limiting SWCNT deposition to a channel height range of 10 – 15 nm. The range observed in Chapter 3 (10 – 40 nm) was not uniform enough and weakens the reproducibility of the experiments. Further electrical characterisation would also be a priority for future research, as there is a wealth of output characteristics available to NT-FETs. Repeating the real-time sensing experiments could offer a more accurate estimate of NT-FET sensitivity, as

the effect of analytes can be observed instantly through a spike or drop in current. Meanwhile, a back gate voltage could be employed, and transfer characteristics collected, to allow alternative sensitivity data to be derived and the contribution of Schottky barrier modifications to NT-FET conductance to be revealed. Further β-lactamase sensing experiments should then follow suit of Xu et al. (2021) and test the analytes in the presence of serum to consider how NT-FET sensitivity may change with a reduced Debye length. Testing the NT-FET against more β-lactamases, e.g., SHV, CTX-M, PME, BlaC and BCL-1, would also help build a picture on how easily the NT-FET can discriminate between different class A β-lactamases (Philippon et al. 2016). Finally, in the broader picture, the adaptability of the biosensing platform ought to be showcased. This would comprise of integrating different receptor proteins to prove the biosensing potential. For example, a diagnostic biosensor for the ongoing SARS-CoV-2 outbreak could be easily built by integrating the human ACE2 receptor protein into the NT-FET, as it offers nanomolar affinity towards the spike protein antigen (Lu and Sun 2020).

Chapter 4 focused on a computational pipeline that assessed the potential for electrostatic gating, based on the rotamer analysis of anchor residue, AzF. A favourable upgrade to this workflow would see full automation of the computational pipeline, with only the *in silico* modelling needing to be performed manually. This would be an efficiency saving and would generate higher throughput in mutation site assessment. An improvement for the rotamer analysis would be to take a closer look at the steric clash incidents. Currently all incidents of steric clash rule the rotamer as non-viable for SWCNT interfacing, but individual cases of amino acid—SWCNT clash could be susceptible to molecular dynamic flux, e.g., clashes only occur 50 % of the time. Therefore, it could be valuable to set a limit for steric clash incidents, where rotamers are ruled non-viable above the limit, and below the limit, they may be partially-viable. Population sampling of the partially-viable rotamers would then allow an estimate of steric clash probability, improving the accuracy of rotamer characterisation. A final area of future work would be to improve the quantification of electrostatic gating. Since the release of the Côte et al. (2021) paper on the molecular origin of electrostatic gating on SWCNTs, I set up a collaboration with the first author, Dr. Sébastien Côté. His modelling and quantification of ESP was an advanced form of molecular dynamics simulation, and we have since applied his methodology to our BLIP-II[AzF]—SWCNT setup with analytes TEM-1 and KPC-2. His results corroborated the electrostatic gating we predicted from the AzF rotamer analysis, and we have since written a paper

together (pending publication) that combines the modelling with the β-lactamase sensing experiments.

Chapter 5 focused on the integration of light-responsive protein, sfGFP, into an NT-FET platform to investigate optoelectronic transduction. The novel discovery of optoelectronic memory and optoelectronic gating from two different AzF anchor sites leads me to question what further behaviours could arise, so developing new sfGFP[AzF] variants would allow me to explore this. The light-induced charge transfer in sfGFP[132AzF] and sfGFP[204AzF] functionalised NT-FETs would also benefit from further study. Applying the rotamer analysis used in Chapter 3 to the sfGFP[AzF] variants would give a better understanding of rotamer propensity and allow more accurate *in silico* models to be generated. From these, a structural assessment of the possible charge transfer pathways between the sfGFP chromophore and SWCNT could be elucidated. In the broader picture, substituting sfGFP for different fluorescent proteins (e.g., varying the λ_{max}) could facilitate optoelectronic transduction across the electromagnetic spectrum (Rodriguez et al. 2017). The Jones lab have numerous fluorescent proteins in stock (e.g., mCherry, mRhubarb and mNeptune) and incorporating AzF is a routine methodology, so this could quickly extend the field of application.

7. Bibliography

Abraham, E.P. and Chain, E. 1940. An enzyme from bacteria able to destroy penicillin. *Nature* 146(3713), p. 837. Available at: http://www.nature.com/articles/146837a0 [Accessed: 11 March 2019].

Abràmoff, M.D., Magalhães, P. and Ram, S. 2004. Image Processing with ImageJ. *Biophotonics International* 11(7), pp. 36–42.

Acharya, A., Bogdanov, A.M., Grigorenko, B.L., Bravaya, K.B., Nemukhin, A. V., Lukyanov, K.A. and Krylov, A.I. 2017. Photoinduced chemistry in fluorescent proteins: Curse or blessing? *Chemical Reviews* 117(2), pp. 758–795. Available at: https://pubs.acs.org/doi/abs/10.1021/acs.chemrev.6b00238 [Accessed: 13 February 2023].

Agard, N.J., Prescher, J.A. and Bertozzi, C.R. 2004. A strain-promoted [3 + 2] azide-alkyne cycloaddition for covalent modification of biomolecules in living systems. *Journal of the American Chemical Society* 126(46), pp. 15046–15047. Available at: https://pubs.acs.org/doi/abs/10.1021/ja044996f [Accessed: 20 March 2023].

Agmon, N. 2005. Proton Pathways in Green Fluorescence Protein. *Biophysical Journal* 88(4), p. 2452. Available at: /pmc/articles/PMC1305344/ [Accessed: 1 March 2023].

Aguirre, C.M., Levesque, P.L., Paillet, M., Lapointe, F., St-Antoine, B.C., Desjardins, P. and Martel, R. 2009. The Role of the Oxygen/Water Redox Couple in Suppressing Electron Conduction in Field-Effect Transistors. *Advanced Materials* 21(30), pp. 3087–3091. Available at: https://onlinelibrary.wiley.com/doi/full/10.1002/adma.200900550 [Accessed: 24 March 2023].

Alder, B.J., Wainwright, T.E., Alder, B.J. and Wainwright, T.E. 1957. Phase Transition for a Hard Sphere System. *JChPh* 27(5), pp. 1208–1209. Available at: https://ui.adsabs.harvard.edu/abs/1957JChPh..27.1208A/abstract [Accessed: 19 July 2023].

Alderson, R.G., Barker, D. and Mitchell, J.B.O. 2014. One origin for metallo-β-lactamase activity, or two? An investigation assessing a diverse set of reconstructed ancestral sequences based on a sample of phylogenetic trees. *Journal of Molecular Evolution* 79(3), pp. 117–129. Available at: https://doi.org/10.1007/s00239-014-9639-7.

Alim, S., Vejayan, J., Yusoff, M.M. and Kafi, A.K.M. 2018. Recent uses of carbon nanotubes & gold nanoparticles in electrochemistry with application in biosensing: A review. *Biosensors and Bioelectronics* 121, pp. 125–136. doi: 10.1016/J.BIOS.2018.08.051.

Allen, B.L., Kichambare, P.D. and Star, A. 2007. Carbon Nanotube Field-Effect-Transistor-Based Biosensors. *Advanced Materials* 19(11), pp. 1439–1451. Available at: https://onlinelibrary.wiley.com/doi/full/10.1002/adma.200602043 [Accessed: 18 January 2023].

Almagro Armenteros, J.J. et al. 2019. SignalP 5.0 improves signal peptide predictions using deep neural networks. *Nature Biotechnology 2019 37:4* 37(4), pp. 420–423. Available at: https://www.nature.com/articles/s41587-019-0036-z [Accessed: 20 June 2022].

Altis, A., Nguyen, P.H., Hegger, R. and Stock, G. 2007. Dihedral angle principal

component analysis of molecular dynamics simulations. *The Journal of Chemical Physics* 126(24), p. 244111. Available at: https://aip.scitation.org/doi/abs/10.1063/1.2746330 [Accessed: 1 February 2023].

Ambler, R.P. 1980. The structure of beta-lactamases. *Philosophical transactions of the Royal Society of London. Series B, Biological sciences* 289(1036), pp. 321–331. doi: 10.1098/rstb.1980.0049.

Amusengeri, A., Khan, A. and Tastan Bishop, Ö. 2022. The Structural Basis of Mycobacterium tuberculosis RpoB Drug-Resistant Clinical Mutations on Rifampicin Drug Binding. *Molecules* 27(3). doi: 10.3390/molecules27030885.

Amusengeri, A., Tata, R.B. and Tastan Bishop, Ö. 2020. Understanding the Pyrimethamine Drug Resistance Mechanism via Combined Molecular Dynamics and Dynamic Residue Network Analysis. *Molecules* 25(4). doi: 10.3390/molecules25040904.

Arnesano, F., Banci, L., Bertini, I., Faraone-Mennella, J., Rosato, A., Barker, P.D. and Fersht, A.R. 1999. The solution structure of oxidized Escherichia coli cytochrome b562. *Biochemistry* 38(27), pp. 8657–8670. Available at: https://pubmed.ncbi.nlm.nih.gov/10393541/ [Accessed: 13 February 2023].

Arnittali, M., Rissanou, A.N., Amprazi, M., Kokkinidis, M. and Harmandaris, V. 2021. Structure and thermal stability of wtrop and rm6 proteins through all-atom molecular dynamics simulations and experiments. *International Journal of Molecular Sciences* 22(11), p. 22. Available at: /pmc/articles/PMC8199364/ [Accessed: 18 April 2023].

Arnittali, M., Rissanou, A.N. and Harmandaris, V. 2019. ScienceDirect Structure Of Biomolecules Through Molecular Dynamics Simulations. *Procedia Computer Science* 156, pp. 69–78. Available at: www.sciencedirect.comwww.sciencedirect.com [Accessed: 18 April 2023].

Arpino, J.A.J., Rizkallah, P.J. and Jones, D.D. 2012. Crystal Structure of Enhanced Green Fluorescent Protein to 1.35 A ˚ Resolution Reveals Alternative Conformations for Glu222. *PLoS ONE* 7(10), p. 47132. Available at: www.plosone.org [Accessed: 31 March 2023].

Artyukhin, A.B., Stadermann, M., Friddle, R.W., Stroeve, P., Bakajin, O. and Noy, A. 2006. Controlled electrostatic gating of carbon nanotube FET devices. *Nano Letters* 6(9), pp. 2080–2085. Available at: https://pubs.acs.org/doi/full/10.1021/nl061343j [Accessed: 24 March 2023].

Avouris, P. 2007. Electronics with carbon nanotubes. *Physics World* 20(3), p. 40. Available at: https://iopscience.iop.org/article/10.1088/2058-7058/20/3/32 [Accessed: 9 March 2023].

Awasthi, K., Singh, D.P. and Singh, S. 2009. Attachment of biomolecules (protein and DNA) to amino-functionalized carbon nanotubes. *New Carbon Materials* 24(4), pp. 301–306. doi: 10.1016/S1872-5805(08)60053-0.

Bakaraju, V., Prasad, E.S., Meena, B. and Chaturvedi, H. 2020. An Electronic and Optically Controlled Bifunctional Transistor Based on a Bio-Nano Hybrid Complex. *ACS Omega* 5(17), pp. 9702–9706. Available at: https://pubs.acs.org/doi/full/10.1021/acsomega.9b03904 [Accessed: 13 February 2023].

Baker, N.A., Sept, D., Joseph, S., Holst, M.J. and McCammon, J.A. 2001. Electrostatics of nanosystems: Application to microtubules and the ribosome. *Proceedings of the National Academy of Sciences of the United States of America*

98(18), pp. 10037–10041. Available at:
https://www.pnas.org/doi/abs/10.1073/pnas.181342398 [Accessed: 6 December 2022].

Baquero, F. 2021. Threats of antibiotic resistance: an obliged reappraisal. *International Microbiology* 24(4), pp. 499–506. Available at: https://link.springer.com/article/10.1007/s10123-021-00184-y [Accessed: 28 March 2023].

Baskin, J.M. et al. 2007. Copper-free click chemistry for dynamic in vivo imaging. *Proceedings of the National Academy of Sciences of the United States of America* 104(43), pp. 16793–16797. Available at: https://www.pnas.org/doi/abs/10.1073/pnas.0707090104 [Accessed: 20 March 2023].

Bekker, H. et al. 1993. GROMACS - A Parallel Computer For Molecular-Dynamics Simulations. G. Balint, Antala, B., Carty, C., Mabieme, J.-M. A., Amar, I. B., and Kaplanova, A. eds. *Physics Computing* 7(1), pp. 252–256. Available at: https://research.rug.nl/en/publications/gromacs-a-parallel-computer-for-molecular-dynamics-simulations [Accessed: 24 October 2022].

Bell, G. and MacLean, C. 2018. The Search for "Evolution-Proof" Antibiotics. *Trends in microbiology* 26(6), pp. 471–483. Available at: https://pubmed.ncbi.nlm.nih.gov/29191398/ [Accessed: 18 January 2023].

Bellissent-Funel, M.C. et al. 2016. Water Determines the Structure and Dynamics of Proteins. *Chemical reviews* 116(13), p. 7673. Available at: /pmc/articles/PMC7116073/ [Accessed: 28 February 2023].

Berman, H.M. et al. 2000. The Protein Data Bank. *Nucleic Acids Research* 28(1), pp. 235–242. Available at: https://dx.doi.org/10.1093/nar/28.1.235 [Accessed: 24 July 2023].

Best, R.B., Zhu, X., Shim, J., Lopes, P.E.M., Mittal, J., Feig, M. and MacKerell, A.D. 2012. Optimization of the additive CHARMM all-atom protein force field targeting improved sampling of the backbone φ, ψ and side-chain χ1 and χ2 Dihedral Angles. *Journal of Chemical Theory and Computation* 8(9), pp. 3257–3273. Available at: https://pubs.acs.org/doi/abs/10.1021/ct300400x [Accessed: 26 October 2022].

Bishop, M.D. et al. 2020. Fabrication of carbon nanotube field-effect transistors in commercial silicon manufacturing facilities. *Nature Electronics 2020 3:8* 3(8), pp. 492–501. Available at: https://www.nature.com/articles/s41928-020-0419-7 [Accessed: 10 March 2023].

Blattner, F.R. et al. 1997. The complete genome sequence of Escherichia coli K-12. *Science (New York, N.Y.)* 277(5331), pp. 1453–1462. Available at: https://pubmed.ncbi.nlm.nih.gov/9278503/ [Accessed: 13 April 2023].

Blight, S.K. et al. 2004. Direct charging of tRNA(CUA) with pyrrolysine in vitro and in vivo. *Nature* 431(7006), pp. 333–335. Available at: https://pubmed.ncbi.nlm.nih.gov/15329732/ [Accessed: 12 May 2022].

Bogan, A.A. and Thorn, K.S. 1998. Anatomy of hot spots in protein interfaces. *Journal of Molecular Biology* 280(1), pp. 1–9. doi: 10.1006/jmbi.1998.1843.

Bogdanov, A.M. et al. 2009. Green fluorescent proteins are light-induced electron donors. *Nature chemical biology* 5(7), pp. 459–461. Available at: https://pubmed.ncbi.nlm.nih.gov/19396176/ [Accessed: 13 February 2023].

Bolhuis, P.G. 2006. Sampling Kinetic Protein Folding Pathways using All-Atom Models BT - Computer Simulations in Condensed Matter Systems: From Materials to Chemical Biology Volume 1. In: Ferrario, M., Ciccotti, G., and Binder, K. eds. Berlin, Heidelberg: Springer Berlin Heidelberg, pp. 393–433. Available at: https://doi.org/10.1007/3-540-35273-2_11.

Bornhorst, J.A. and Falke, J.J. 2000. [16] Purification of Proteins Using Polyhistidine Affinity Tags. *Methods in enzymology* 326, p. 245. Available at: /pmc/articles/PMC2909483/ [Accessed: 16 June 2022].

Boutal, H. et al. 2017. Development and validation of a lateral flow immunoassay for rapid detection of NDM-producing enterobacteriaceae. *Journal of Clinical Microbiology* 55(7), pp. 2018–2029. Available at: https://journals.asm.org/doi/10.1128/jcm.00248-17 [Accessed: 2 August 2023].

Bowen, B.J. 2020. *From carbon nanotubes to zinc porphyrins: engineering proteins to interface with non_biological molecular systems*. Cardiff University.

Bradley, K., Briman, M., Star, A. and Gruner, G. 2004. Charge Transfer from Adsorbed Proteins. *Nano Letters* 4(2), pp. 253–256. Available at: https://pubs.acs.org/doi/full/10.1021/nl0349855 [Accessed: 24 March 2023].

Bräse, S., Gil, C., Knepper, K. and Zimmermann, V. 2005. Organic Azides: An Exploding Diversity of a Unique Class of Compounds. *Angewandte Chemie International Edition* 44(33), pp. 5188–5240. Available at: http://doi.wiley.com/10.1002/anie.200400657 [Accessed: 8 March 2019].

Brejc, K., Sixma, T.K., Kitts, P.A., Kain, S.R., Tsien, R.Y., Ormö, M. and Remington, S.J. 1997. Structural basis for dual excitation and photoisomerization of the Aequorea victoria green fluorescent protein. *Proceedings of the National Academy of Sciences of the United States of America* 94(6), pp. 2306–11. Available at: http://www.ncbi.nlm.nih.gov/pubmed/9122190 [Accessed: 28 July 2019].

Brooks, B.R. et al. 2009. CHARMM: The Biomolecular Simulation Program. *Journal of computational chemistry* 30(10), p. 1545. Available at: /pmc/articles/PMC2810661/ [Accessed: 31 October 2022].

Brooks, B.R., Bruccoleri, R.E., Olafson, B.D., States, D.J., Swaminathan, S. and Karplus, M. 1983. CHARMM: A program for macromolecular energy, minimization, and dynamics calculations. *Journal of Computational Chemistry* 4(2), pp. 187–217. doi: 10.1002/JCC.540040211.

Brown, N.G., Chow, D.C. and Palzkill, T. 2013a. BLIP-II is a highly potent inhibitor of Klebsiella pneumoniae carbapenemase (KPC-2). *Antimicrobial agents and chemotherapy* 57(7), pp. 3398–3401. Available at: https://pubmed.ncbi.nlm.nih.gov/23587951/ [Accessed: 25 January 2023].

Brown, N.G., Chow, D.C., Ruprecht, K.E. and Palzkill, T. 2013b. Identification of the β-Lactamase Inhibitor Protein-II (BLIP-II) interface residues essential for binding affinity and specificity for class A β-lactamases. *Journal of Biological Chemistry* 288(24), pp. 17156–17166. Available at: /pmc/articles/PMC3682521/ [Accessed: 10 May 2021].

Brown, N.G., Chow, D.C., Sankaran, B., Zwart, P., Venkataram Prasad, B. V. and Palzkill, T. 2011. Analysis of the binding forces driving the tight interactions between β-lactamase inhibitory protein-II (BLIP-II) and class A β-lactamases. *Journal of Biological Chemistry* 286(37), pp. 32723–32735. Available at: /pmc/articles/PMC3173220/ [Accessed: 10 May 2021].

Brown, N.G.G. and Palzkill, T. 2010. Identification and characterization of β-lactamase inhibitor protein-II (BLIP-II) interactions with β-lactamases using phage display. *Protein Engineering, Design and Selection* 23(6), pp. 469–478. Available at: https://academic.oup.com/peds/article/23/6/469/1540198 [Accessed: 10 March 2019].

Bruker Corporation 2015. NanoScope Analysis.

Burnham, C.A.D., Leeds, J., Nordmann, P., O'Grady, J. and Patel, J. 2017. Diagnosing antimicrobial resistance. *Nature Reviews Microbiology 2017 15:11* 15(11), pp. 697–703. Available at: https://www.nature.com/articles/nrmicro.2017.103 [Accessed: 18 January 2023].

Bush, K. 2002. The impact of beta-lactamases on the development of novel antimicrobial agents. *Current opinion in investigational drugs (London, England : 2000)* 3(9), pp. 1284–1290.

Bush, K. and Fisher, J.F. 2011. Epidemiological Expansion, Structural Studies, and Clinical Challenges of New β-Lactamases from Gram-Negative Bacteria. *Annual Review of Microbiology* 65(1), pp. 455–478. Available at: https://doi.org/10.1146/annurev-micro-090110-102911.

Calvaresi, M. and Zerbetto, F. 2013. The devil and holy water: Protein and carbon nanotube hybrids. *Accounts of Chemical Research* 46(11), pp. 2454–2463. Available at: https://pubs.acs.org/doi/abs/10.1021/ar300347d [Accessed: 13 February 2023].

Carfi, A., Pares, S., Duée, E., Galleni, M., Duez, C., Frère, J.M. and Dideberg, O. 1995. The 3-D structure of a zinc metallo-beta-lactamase from Bacillus cereus reveals a new type of protein fold. *The EMBO journal* 14(20), pp. 4914–4921. doi: 10.1002/j.1460-2075.1995.tb00174.x.

Carpenter, A., Paulsen, I. and Williams, T. 2018. Blueprints for Biosensors: Design, Limitations, and Applications. *Genes* 9(8), p. 375. Available at: http://www.ncbi.nlm.nih.gov/pubmed/30050028 [Accessed: 28 July 2019].

Chae, S.H. and Lee, Y.H. 2014. Carbon nanotubes and graphene towards soft electronics. *Nano Convergence* 1(1). Available at: /pmc/articles/PMC5591626/ [Accessed: 23 March 2023].

Chalfie, M., Tu, Y., Euskirchen, G., Ward, W.W. and Prasher, D.C. 1994. Green fluorescent protein as a marker for gene expression. *Science (New York, N.Y.)* 263(5148), pp. 802–805. doi: 10.1126/science.8303295.

Chamberlain, A.K. and Bowie, J.U. 2004. Analysis of Side-Chain Rotamers in Transmembrane Proteins. *Biophysical Journal* 87(5), pp. 3460–3469. doi: 10.1529/BIOPHYSJ.104.044024.

Chattoraj, M., King, B.A., Bublitz, G.U. and Boxer, S.G. 1996. Ultra-fast excited state dynamics in green fluorescent protein: multiple states and proton transfer. *Proceedings of the National Academy of Sciences* 93(16), pp. 8362–8367. Available at: https://www.pnas.org/doi/abs/10.1073/pnas.93.16.8362 [Accessed: 31 March 2023].

Chen, R.J. et al. 2004. An Investigation of the Mechanisms of Electronic Sensing of Protein Adsorption on Carbon Nanotube Devices. *Journal of the American Chemical Society* 126(5), pp. 1563–1568. Available at: https://pubs.acs.org/doi/full/10.1021/ja038702m [Accessed: 24 March 2023].

Chen, R.J., Zhang, Y., Wang, D. and Dai, H. 2001. Noncovalent sidewall functionalization of single-walled carbon nanotubes for protein immobilization [11]. *Journal of the American Chemical Society* 123(16), pp. 3838–3839. Available at: https://pubs.acs.org/doi/full/10.1021/ja010172b [Accessed: 25 January 2022].

Chin, J.W. 2017. Expanding and reprogramming the genetic code. *Nature 2017 550:7674* 550(7674), pp. 53–60. Available at: https://www.nature.com/articles/nature24031 [Accessed: 13 April 2023].

Chin, J.W., Santoro, S.W., Martin, A.B., King, D.S., Wang, L. and Schultz, P.G. 2002. Addition of p-azido-L-phenylalanine to the genetic code of Escherichia coli. *Journal of the American Chemical Society* 124(31), pp. 9026–9027. doi: 10.1021/ja027007w.

Chovancova, E. et al. 2012. CAVER 3.0: a tool for the analysis of transport pathways in dynamic protein structures. *PLoS computational biology* 8(10). Available at: https://pubmed.ncbi.nlm.nih.gov/23093919/ [Accessed: 21 April 2023].

Ciccotti, G., Dellago, C., Ferrario, M., Hernández, E.R. and Tuckerman, M.E. 2022. Molecular simulations: past, present, and future (a Topical Issue in EPJB). *The European Physical Journal B 2021 95:1* 95(1), pp. 1–12. Available at: https://link.springer.com/article/10.1140/epjb/s10051-021-00249-x [Accessed: 19 July 2023].

Cid, C.C., Riu, J., Maroto, A. and Rius, F.X. 2008. Carbon nanotube field effect transistors for the fast and selective detection of human immunoglobulin G. *Analyst* 133(8), pp. 1005–1008. Available at: https://pubs.rsc.org/en/content/articlehtml/2008/an/b805301b [Accessed: 11 April 2023].

Cormack, B.P., Valdivia, R.H. and Falkow, S. 1996. FACS-optimized mutants of the green fluorescent protein (GFP). *Gene* 173(1), pp. 33–38. Available at: https://www.sciencedirect.com/science/article/pii/0378111995006850.

Côte, S., Bouilly, D. and Mousseau, N. 2021. The molecular origin of the electrostatic gating of single-molecule field-effect biosensors investigated by molecular dynamics simulations. *Physical Chemistry Chemical Physics* . Available at: https://pubs.rsc.org/en/content/articlehtml/2021/cp/d1cp04626h [Accessed: 28 January 2022].

Coyle, B.L., Rolandi, M. and Baneyx, F. 2013. Carbon-binding designer proteins that discriminate between sp2- and sp3-hybridized carbon surfaces. *Langmuir* 29(15), pp. 4839–4846. Available at: https://pubs.acs.org/doi/full/10.1021/la4000846 [Accessed: 27 January 2022].

Croitoru, A., Park, S.-J., Kumar, A., Lee, J., Im, W., MacKerell Jr, A.D. and Aleksandrov, A. 2021. Additive CHARMM36 Force Field for Nonstandard Amino Acids. *Journal of chemical theory and computation* 17(6), pp. 3554–3570. Available at: https://pubmed.ncbi.nlm.nih.gov/34009984.

Danielson, E. et al. 2020. Graphene based field-effect transistor biosensors functionalized using gas-phase synthesized gold nanoparticles. *Sensors and Actuators B: Chemical* 320, p. 128432. doi: 10.1016/J.SNB.2020.128432.

Das, S., Das, S., Roy, A., Pal, U. and Maiti, N.C. 2016. Orientation of tyrosine side chain in neurotoxic Aβ differs in two different secondary structures of the peptide. *Royal Society Open Science* 3(10). Available at: /pmc/articles/PMC5098961/ [Accessed: 1 February 2023].

Debye, P. 1913. Interferenz von Röntgenstrahlen und Wärmebewegung. *Annalen der Physik* 348(1), pp. 49–92. Available at: https://onlinelibrary.wiley.com/doi/full/10.1002/andp.19133480105 [Accessed: 19 April 2023].

Deng, Y., Liu, L., Li, J. and Gao, L. 2022. Sensors Based on the Carbon Nanotube Field-Effect Transistors for Chemical and Biological Analyses. *Biosensors* 12(10). Available at: https://pubmed.ncbi.nlm.nih.gov/36290914/ [Accessed: 18 January 2023].

Dolk, F.C.K., Pouwels, K.B., Smith, D.R.M., Robotham, J. V and Smieszek, T. 2018. Antibiotics in primary care in England: which antibiotics are prescribed and for which conditions? *Journal of Antimicrobial Chemotherapy* 73(suppl_2), pp. ii2–ii10. Available at: https://doi.org/10.1093/jac/dkx504.

Dresselhaus, M.S., Dresselhaus, G. and Jorio, A. 2004. Unusual properties and structure of carbon nanotubes. *Annual Review of Materials Research* 34, pp. 247–278. doi: 10.1146/ANNUREV.MATSCI.34.040203.114607.

Dresselhaus, M.S., Dresselhaus, G. and Saito, R. 1995. Physics of carbon nanotubes. *Carbon* 33(7), pp. 883–891. doi: 10.1016/0008-6223(95)00017-8.

Du, L., Xiong, W., Chan, W.K. and Phillips, D.L. 2020. Photoinduced electron transfer processes of single-wall carbon nanotube (SWCNT)-based hybrids. *Nanophotonics* 9(16), pp. 4689–4701. Available at: https://www.degruyter.com/document/doi/10.1515/nanoph-2020-0389/html?lang=en [Accessed: 13 February 2023].

Dubey, R., Dutta, D., Sarkar, A. and Chattopadhyay, P. 2021. Functionalized carbon nanotubes: synthesis, properties and applications in water purification, drug delivery, and material and biomedical sciences. *Nanoscale Advances* 3(20), pp. 5722–5744. Available at: https://pubs.rsc.org/en/content/articlehtml/2021/na/d1na00293g [Accessed: 8 December 2021].

Dunakey, S.J.G., Coyle, B.L., Thomas, A., Xu, M., Swift, B.J.F. and Baneyx, F. 2019. Selective Labeling and Decoration of the Ends and Sidewalls of Single-Walled Carbon Nanotubes Using Mono- and Bispecific Solid-Binding Fluorescent Proteins. *Bioconjugate Chemistry* . Available at: https://pubs.acs.org/doi/full/10.1021/acs.bioconjchem.9b00097 [Accessed: 27 January 2022].

Dunbrack, R.L. 2002. Rotamer Libraries in the 21st Century. *Current Opinion in Structural Biology* 12(4), pp. 431–440. doi: 10.1016/S0959-440X(02)00344-5.

Dunbrack, R.L. and Cohen, F.E. 1997. Bayesian statistical analysis of protein side-chain rotamer preferences. *Protein Science* 6(8), pp. 1661–1681. doi: 10.1002/PRO.5560060807.

Dunbrack, R.L. and Karplus, M. 1993. Backbone-dependent rotamer library for proteins. Application to side-chain prediction. *Journal of molecular biology* 230(2), pp. 543–574. Available at: https://pubmed.ncbi.nlm.nih.gov/8464064/ [Accessed: 31 January 2023].

Dürkop, T., Getty, S.A., Cobas, E. and Fuhrer, M.S. 2004. Extraordinary Mobility in Semiconducting Carbon Nanotubes. *Nano Letters* 4(1), pp. 35–39. Available at: https://pubs.acs.org/doi/full/10.1021/nl034841q [Accessed: 22 March 2023].

Dyke, C.A. and Tour, J.M. 2004. Covalent Functionalization of Single-Walled

Carbon Nanotubes for Materials Applications. *Journal of Physical Chemistry A* 108(51), pp. 11151–11159. Available at: https://pubs.acs.org/doi/full/10.1021/jp046274g [Accessed: 22 November 2021].

Eatemadi, A. et al. 2014. Carbon nanotubes: properties, synthesis, purification, and medical applications. *Nanoscale research letters* 9(1), p. 393. Available at: https://pubmed.ncbi.nlm.nih.gov/25170330.

Ee, L.G. et al. 2007. DNA sensing by field-effect transistors based on networks of carbon nanotubes. *Journal of the American Chemical Society* 129(46), pp. 14427–14432. Available at: https://pubs.acs.org/doi/full/10.1021/ja075176g [Accessed: 24 March 2023].

Eiamphungporn, W., Schaduangrat, N., Malik, A.A. and Nantasenamat, C. 2018. Tackling the Antibiotic Resistance Caused by Class A β-Lactamases through the Use of β-Lactamase Inhibitory Protein. *International Journal of Molecular Sciences* 19(8). doi: 10.3390/ijms19082222.

Ekins, S., Mestres, J. and Testa, B. 2007. In silico pharmacology for drug discovery: methods for virtual ligand screening and profiling. *British Journal of Pharmacology* 152(1), p. 9. Available at: /pmc/articles/PMC1978274/ [Accessed: 10 July 2023].

Emelianov, A. V. et al. 2021. Individual SWCNT Transistor with Photosensitive Planar Junction Induced by Two-Photon Oxidation. *Advanced Electronic Materials* 7(3), p. 2000872. Available at: https://onlinelibrary.wiley.com/doi/full/10.1002/aelm.202000872 [Accessed: 24 June 2022].

Engh, R.A., Chen, L.X.Q. and Fleming, G.R. 1986. Conformational dynamics of tryptophan: a proposal for the origin of the non-exponential fluorescence decay. *Chemical Physics Letters* 126(3–4), pp. 365–372. doi: 10.1016/S0009-2614(86)80100-2.

Ericson, S., Ericson, S. and Ericson, M. 2015. *UV Light-Blocking Fermenting Container System and Related Methods* 20150272147 [Patent]. Available at: https://patents.justia.com/patent/20150272147 [Accessed: 11 April 2023].

Fedorov, G. et al. 2013. Photothermoelectric response in asymmetric carbon nanotube devices exposed to sub-terahertz radiation. *Applied Physics Letters* 103(18), p. 181121. doi: 10.1063/1.4828555.

Fernández-Luna, V., Coto, P.B. and Costa, R.D. 2018. When Fluorescent Proteins Meet White Light-Emitting Diodes. *Angewandte Chemie (International ed. in English)* 57(29), pp. 8826–8836. Available at: https://pubmed.ncbi.nlm.nih.gov/29288605/ [Accessed: 13 February 2023].

Fernando, K.A.S. et al. 2004. Diminished band-gap transitions of single-walled carbon nanotubes in complexation with aromatic molecules - PubMed. *ACS* 126(33), pp. 10234–10235. Available at: https://pubmed.ncbi.nlm.nih.gov/15315422/ [Accessed: 25 January 2022].

Fossum, E.R. 1997. CMOS image sensors: electronic camera-on-a-chip. *IEEE Transactions on Electron Devices* 44(10), pp. 1689–1698. doi: 10.1109/16.628824.

Freeley, M. et al. 2017. Site-Specific One-to-One Click Coupling of Single Proteins to Individual Carbon Nanotubes: A Single-Molecule Approach. *Journal of the American Chemical Society* 139(49), pp. 17834–17840. Available at: http://pubs.acs.org/doi/10.1021/jacs.7b07362 [Accessed: 8 March 2019].

Freeley, M., Gwyther, R.E.A., Jones, D.D. and Palma, M. 2021. DNA-Directed Assembly of Carbon Nanotube-Protein Hybrids. *Biomolecules* 11(7). Available at: https://pubmed.ncbi.nlm.nih.gov/34209628/ [Accessed: 24 January 2022].

Frey, J.T. and Doren, D.J. 2011. TubeGen. Available at: http://turin.nss.udel.edu/research/tubegenonline.html.

Friedland, G.D., Linares, A.J., Smith, C.A. and Kortemme, T. 2008. A simple model of backbone flexibility improves modeling of side-chain conformational variability. *Journal of molecular biology* 380(4), pp. 757–774. doi: 10.1016/j.jmb.2008.05.006.

Fuentes-Perez, M.E., Dillingham, M.S. and Moreno-Herrero, F. 2013. AFM volumetric methods for the characterization of proteins and nucleic acids. *Methods* 60(2), pp. 113–121. doi: 10.1016/j.ymeth.2013.02.005.

Furniss, R.C.D. et al. 2022. Breaking antimicrobial resistance by disrupting extracytoplasmic protein folding. *eLife* 11. doi: 10.7554/ELIFE.57974.

Gaetke, L.M., Chow-Johnson, H.S. and Chow, C.K. 2014. Copper: toxicological relevance and mechanisms. *Archives of toxicology* 88(11), pp. 1929–1938. Available at: https://pubmed.ncbi.nlm.nih.gov/25199685/ [Accessed: 21 March 2023].

Gao, Y. and Kyratzis, I. 2008. Covalent immobilization of proteins on carbon nanotubes using the cross-linker 1-ethyl-3-(3-dimethylaminopropyl)carbodiimide--a critical assessment. *Bioconjugate chemistry* 19(10), pp. 1945–1950. Available at: https://pubmed.ncbi.nlm.nih.gov/18759407/ [Accessed: 14 January 2022].

García, R. and Pérez, R. 2002. Dynamic atomic force microscopy methods. *Surface Science Reports* 47(6–8), pp. 197–301. Available at: https://www.sciencedirect.com/science/article/pii/S0167572902000778 [Accessed: 14 March 2019].

Gather, M.C. and Yun, S.H. 2014. Bio-optimized energy transfer in densely packed fluorescent protein enables near-maximal luminescence and solid-state lasers. *Nature Communications 2014 5:1* 5(1), pp. 1–8. Available at: https://www.nature.com/articles/ncomms6722 [Accessed: 13 February 2023].

Georgakilas, V. et al. 2012. Functionalization of graphene: Covalent and non-covalent approaches, derivatives and applications. *Chemical Reviews* 112(11), pp. 6156–6214. Available at: https://pubs.acs.org/doi/full/10.1021/cr3000412 [Accessed: 13 February 2023].

Gfeller, D., Michielin, O. and Zoete, V. 2013. SwissSidechain: a molecular and structural database of non-natural sidechains. *Nucleic acids research* 41(Database issue). Available at: https://pubmed.ncbi.nlm.nih.gov/23104376/ [Accessed: 25 October 2022].

Ghasemi, F. and Salimi, A. 2023. Advances in 2d based field effect transistors as biosensing platforms: From principle to biomedical applications. *Microchemical Journal* 187, p. 108432. doi: 10.1016/J.MICROC.2023.108432.

Ghasemi, S. and Moth-Poulsen, K. 2021. Single molecule electronic devices with carbon-based materials: status and opportunity. *Nanoscale* 13(2), pp. 659–671. Available at: https://pubs.rsc.org/en/content/articlehtml/2021/nr/d0nr07844a [Accessed: 13 February 2023].

Goldman, A., Harper, S. and Speicher, D.W. 2016. Detection of Proteins on Blot Membranes. *Current Protocols in Protein Science* 86(1), pp. 10.8.1-10.8.11.

Available at: https://doi.org/10.1002/cpps.15.

González, M.A. 2011. Force fields and molecular dynamics simulations. *Collection SFN* 12, pp. 169–200. doi: 10.1051/sfn/201112009.

Gritsan, N. and Platz, M. 2010. Photochemistry of Azides: The Azide/Nitrene Interface. *Organic Azides: Syntheses and Applications* , pp. 311–372. Available at: https://onlinelibrary.wiley.com/doi/full/10.1002/9780470682517.ch11 [Accessed: 20 March 2023].

Gu, Z., Yang, Z., Chong, Y., Ge, C., Weber, J.K., Bell, D.R. and Zhou, R. 2015. Surface Curvature Relation to Protein Adsorption for Carbon-based Nanomaterials. *Scientific Reports 2015 5:1* 5(1), pp. 1–9. Available at: https://www.nature.com/articles/srep10886 [Accessed: 26 January 2022].

Guiseppi-Elie, A., Lei, C. and Baughman, R.H. 2002. Direct electron transfer of glucose oxidase on carbon nanotubes. *Nanotechnology* 13, pp. 559–564.

Guy, O.J. and Walker, K.A.D. 2016. Graphene Functionalization for Biosensor Applications. *Silicon Carbide Biotechnology: A Biocompatible Semiconductor for Advanced Biomedical Devices and Applications: Second Edition* , pp. 85–141. doi: 10.1016/B978-0-12-802993-0.00004-6.

Gwyther, R.E.A. et al. 2022. Differential Bio-Optoelectronic Gating of Semiconducting Carbon Nanotubes by Varying the Covalent Attachment Residue of a Green Fluorescent Protein. *Advanced Functional Materials* 32(22), p. 2112374. Available at: https://onlinelibrary.wiley.com/doi/full/10.1002/adfm.202112374 [Accessed: 15 March 2023].

Haddad, Y., Adam, V. and Heger, Z. 2019. Rotamer Dynamics: Analysis of Rotamers in Molecular Dynamics Simulations of Proteins. *Biophysical journal* 116(11), pp. 2062–2072. Available at: https://pubmed.ncbi.nlm.nih.gov/31084902/ [Accessed: 1 February 2023].

Han, S. and Shin, G. 2020. Biodegradable Optical Fiber in a Soft Optoelectronic Device for Wireless Optogenetic Applications. *Coatings 2020, Vol. 10, Page 1153* 10(12), p. 1153. Available at: https://www.mdpi.com/2079-6412/10/12/1153/htm [Accessed: 2 March 2023].

Han, X., Li, Y. and Deng, Z. 2007. DNA-wrapped single-walled carbon nanotubes as rigid templates for assembling linear gold nanoparticle arrays. *Advanced Materials* 19(11), pp. 1518–1522. doi: 10.1002/ADMA.200602861.

Hanson, G.T. et al. 2002. Green fluorescent protein variants as ratiometric dual emission ph sensors. 1. Structural characterization and preliminary application. *Biochemistry* 41(52), pp. 15477–15488. Available at: https://pubs.acs.org/doi/full/10.1021/bi026609p [Accessed: 1 March 2023].

Hartley, A.M., Worthy, H.L., Reddington, S.C., Rizkallah, P.J. and Dafydd Jones, D. 2016. Molecular basis for functional switching of GFP by two disparate non-native post-translational modifications of a phenyl azide reaction handle †. *Chemical Science* 7(10), pp. 6484–6491. Available at: http://web.expasy.org/ [Accessed: 28 July 2019].

Havranek, J.J. and Baker, D. 2009. Motif-directed flexible backbone design of functional interactions. *Protein science : a publication of the Protein Society* 18(6), pp. 1293–1305. doi: 10.1002/pro.142.

He, X., Léonard, F. and Kono, J. 2015. Uncooled Carbon Nanotube Photodetectors.

Advanced Optical Materials 3(8), pp. 989–1011. doi: 10.1002/adom.201500237.

Heim, R., Cubitt, A.B. and Tsien, R.Y. 1995. Improved green fluorescence. *Nature* 373(6516), pp. 663–664. Available at: https://doi.org/10.1038/373663b0.

Heller, I., Janssens, A.M., Männik, J., Minot, E.D., Lemay, S.G. and Dekker, C. 2008. Identifying the mechanism of biosensing with carbon nanotube transistors. *Nano Letters* 8(2), pp. 591–595. Available at: https://pubmed.ncbi.nlm.nih.gov/18162002/ [Accessed: 11 May 2021].

Hollingsworth, S.A. and Dror, R.O. 2018. Molecular dynamics simulation for all. *Neuron* 99(6), p. 1129. Available at: /pmc/articles/PMC6209097/ [Accessed: 5 April 2023].

Holzinger, M. et al. 2004. [2+1] cycloaddition for cross-linking SWCNTs. *Carbon* 42(5), pp. 941–947. Available at: https://www.sciencedirect.com/science/article/pii/S0008622303005803.

Hölzl, J. and Schulte, F.K. 1979. Work function of metals. In: *Solid Surface Physics*. Springer, Berlin, Heidelberg, pp. 1–150. Available at: https://link.springer.com/chapter/10.1007/BFb0048919 [Accessed: 9 March 2023].

Horowitz, G. 1998. Organic Field-Effect Transistors. *Advanced Materials* 10(5), pp. 365–377. Available at: https://doi.org/10.1002/(SICI)1521-4095(199803)10:5%3C365::AID-ADMA365%3E3.0.CO.

Huang, W. et al. 2002. Attaching Proteins to Carbon Nanotubes via Diimide-Activated Amidation. *Nano Letters* 2(4), pp. 311–314. Available at: https://pubs.acs.org/doi/abs/10.1021/nl010095i [Accessed: 14 January 2022].

Huang, X., Ji, D., Fuchs, H., Hu, W. and Li, T. 2020. Recent Progress in Organic Phototransistors: Semiconductor Materials, Device Structures and Optoelectronic Applications. *ChemPhotoChem* 4(1), pp. 9–38. Available at: https://onlinelibrary.wiley.com/doi/full/10.1002/cptc.201900198 [Accessed: 6 April 2023].

Hwang, S.I. et al. 2019. Tetrahydrocannabinol Detection Using Semiconductor-Enriched Single-Walled Carbon Nanotube Chemiresistors. *ACS Sensors* 4(8), pp. 2084–2093. Available at: https://pubs.acs.org/doi/abs/10.1021/acssensors.9b00762 [Accessed: 11 April 2023].

Insightful Science 2022. SnapGene. Available at: https://www.snapgene.com/.

Ishikawa, F.N., Stauffer, B., Caron, D.A. and Zhou, C. 2009. Rapid and label-free cell detection by metal-cluster-decorated carbon nanotube biosensors. *Biosensors and Bioelectronics* 24(10), pp. 2967–2972. doi: 10.1016/J.BIOS.2009.03.001.

Islam, S. et al. 2019. A smart nanosensor for the detection of human immunodeficiency virus and associated cardiovascular and arthritis diseases using functionalized graphene-based transistors. *Biosensors and Bioelectronics* 126, pp. 792–799. doi: 10.1016/J.BIOS.2018.11.041.

Israelachvili, J. 1991. *Intermolecular & Surface Forces*. 2nd ed. London: Academic Press.

Jariwala, D., Sangwan, V.K., Lauhon, L.J., Marks, T.J. and Hersam, M.C. 2013. Carbon nanomaterials for electronics, optoelectronics, photovoltaics, and sensing. *Chemical Society Reviews* 42(7), pp. 2824–2860. Available at: https://pubs.rsc.org/en/content/articlehtml/2013/cs/c2cs35335k [Accessed: 18 January 2023].

Jazayeri, M.H., Amani, H., Pourfatollah, A.A., Pazoki-Toroudi, H. and Sedighimoghaddam, B. 2016. Various methods of gold nanoparticles (GNPs) conjugation to antibodies. *Sensing and Bio-Sensing Research* 9, pp. 17–22. doi: 10.1016/J.SBSR.2016.04.002.

Jeon, I.-Y. et al. 2011. Functionalization of Carbon Nanotubes. In: *Carbon Nanotubes - Polymer Nanocomposites*. IntechOpen, pp. 91–110. Available at: https://www.intechopen.com/state.item.id [Accessed: 13 January 2023].

Jiang, K., Schadler, L.S., Siegel, R.W., Zhang, X., Zhang, H. and Terrones, M. 2004. Protein immobilization on carbon nanotubes via a two-step process of diimide-activated amidation. *Journal of Materials Chemistry* 14(1), pp. 37–39. Available at: https://pubs.rsc.org/en/content/articlehtml/2004/jm/b310359e [Accessed: 14 January 2022].

Jiang, T. et al. 2021. Highly flexible and degradable memory electronics comprised of all-biocompatible materials. *Nanoscale* 13(2), pp. 724–729. Available at: https://pubs.rsc.org/en/content/articlehtml/2021/nr/d0nr05858k [Accessed: 13 February 2023].

Jordan, P., Fromme, P., Witt, H.T., Klukas, O., Saenger, W. and Krauß, N. 2001. Three-dimensional structure of cyanobacterial photosystem I at 2.5 A resolution. *Nature* 411(6840), pp. 909–917. Available at: https://pubmed.ncbi.nlm.nih.gov/11418848/ [Accessed: 13 February 2023].

Jullien, N. 2021. AmplifX. Available at: https://inp.univ-amu.fr/en/amplifx-manage-test-and-design-your-primers-for-pcr.

Jumper, J. et al. 2021. Highly accurate protein structure prediction with AlphaFold. *Nature 2021 596:7873* 596(7873), pp. 583–589. Available at: https://www.nature.com/articles/s41586-021-03819-2 [Accessed: 21 October 2022].

Kabsch, W. 1976. A solution for the best rotation to relate two sets of vectors. *Acta Crystallographica Section A* 32(5), pp. 922–923. Available at: https://onlinelibrary.wiley.com/doi/full/10.1107/S0567739476001873 [Accessed: 18 April 2023].

Kaderabkova, N., Bharathwaj, M., Furniss, R.C.D., Gonzalez, D., Palmer, T. and Mavridou, D.A.I. 2022. The biogenesis of β-lactamase enzymes. *Microbiology (Reading, England)* 168(8). Available at: https://pubmed.ncbi.nlm.nih.gov/35943884/ [Accessed: 4 January 2023].

Kahng, D. 1960. Silicon-silicon dioxide field induced surface devices. In: *IRE Solid State Device Res. Conf.*

Kaisti, M. 2017. Detection principles of biological and chemical FET sensors. *Biosensors and Bioelectronics* 98, pp. 437–448. doi: 10.1016/J.BIOS.2017.07.010.

Karajanagi, S.S., Vertegel, A.A., Kane, R.S. and Dordick, J.S. 2004. Structure and function of enzymes adsorbed onto single-walled carbon nanotubes. *Langmuir* 20(26), pp. 11594–11599. Available at: https://pubs.acs.org/doi/full/10.1021/la047994h [Accessed: 24 January 2022].

Karousis, N., Tagmatarchis, N. and Tasis, D. 2010. Current progress on the chemical modification of carbon nanotubes. *Chemical Reviews* 110(9), pp. 5366–5397. Available at: https://pubs.acs.org/doi/abs/10.1021/cr100018g [Accessed: 13 February 2023].

Katz, E. and Willner, I. 2004. Integrated nanoparticle-biomolecule hybrid systems:

Synthesis, properties, and applications. *Angewandte Chemie - International Edition* 43(45), pp. 6042–6108. doi: 10.1002/ANIE.200400651.

Ke, W., Bethel, C.R., Thomson, J.M., Bonomo, R.A. and Van Den Akker, F. 2007. Crystal structure of KPC-2: Insights into carbapenemase activity in class A β-lactamases. *Biochemistry* 46(19), pp. 5732–5740. Available at: https://pubs.acs.org/doi/abs/10.1021/bi700300u [Accessed: 7 December 2022].

Kim, S., Baek, G.W., Jeong, J., Seo, S.G. and Jin, S.H. 2021. Scalable and selective N-type conversion for carbon nanotube transistors via patternable polyvinyl alcohol stacked with hydrophobic layers and their application to complementary logic circuits. *Journal of Materials Research and Technology* 12, pp. 243–256. doi: 10.1016/J.JMRT.2021.02.074.

Kodali, V.K. et al. 2011. Nonperturbative chemical modification of graphene for protein micropatterning. *Langmuir : the ACS journal of surfaces and colloids* 27(3), pp. 863–865. Available at: https://pubmed.ncbi.nlm.nih.gov/21182241/ [Accessed: 25 January 2022].

Korpany, K. V., Langat, P., Kim, D.M., Edelman, N., Cooper, D.R., Nadeau, J. and Blum, A.S. 2012. Conductance switching in the photoswitchable protein Dronpa. *Journal of the American Chemical Society* 134(39), pp. 16119–16122. Available at: https://pubmed.ncbi.nlm.nih.gov/22967233/ [Accessed: 13 February 2023].

Kuang, Z., Kim, S.N., Crookes-Goodson, W.J., Farmer, B.L. and Naik, R.R. 2010. Biomimetic chemosensor: Designing peptide recognition elements for surface functionalization of carbon nanotube field effect transistors. *ACS Nano* 4(1), pp. 452–458. Available at: www.acsnano.org [Accessed: 27 January 2022].

Kufer, D. and Konstantatos, G. 2016. Photo-FETs: Phototransistors Enabled by 2D and 0D Nanomaterials. *ACS Photonics* 3(12), pp. 2197–2210. Available at: https://pubs.acs.org/doi/full/10.1021/acsphotonics.6b00391 [Accessed: 3 March 2023].

Laemmli, U.K. 1970. Cleavage of Structural Proteins during the Assembly of the Head of Bacteriophage T4. *Nature 1970 227:5259* 227(5259), pp. 680–685. Available at: https://www.nature.com/articles/227680a0 [Accessed: 21 June 2022].

Lai, C.-Y., Santos, S. and Chiesa, M. 2015. General interpretation and theory of apparent height in dynamic atomic force microscopy. *RSC Advances* 5(97), pp. 80069–80075. Available at: http://xlink.rsc.org/?DOI=C5RA16695K [Accessed: 14 March 2019].

Laing, L. 2021. The Antimicrobial Susceptibility Testing Conundrum. *European Biopharmaceutical Review* (January), pp. 64–67. Available at: https://www.calameo.com/read/0061133855113beda8ddd [Accessed: 1 August 2023].

Lee, C.-S., Kim, S.K. and Kim, M. 2009. Ion-Sensitive Field-Effect Transistor for Biological Sensing. *Sensors* 9, pp. 7111–7131. Available at: www.mdpi.com/journal/sensors [Accessed: 19 January 2023].

Lee, C.S., Gwyther, R.E.A., Freeley, M., Jones, D. and Palma, M. 2022. Fabrication and Functionalisation of Nanocarbon-Based Field-Effect Transistor Biosensors. *ChemBioChem* 23(23), p. e202200282. Available at: https://onlinelibrary.wiley.com/doi/full/10.1002/cbic.202200282 [Accessed: 19 January 2023].

De Leo, F., Magistrato, A. and Bonifazi, D. 2015. Interfacing proteins with graphitic

nanomaterials: from spontaneous attraction to tailored assemblies. *Chemical Society Reviews* 44(19), pp. 6916–6953. Available at: https://pubs.rsc.org/en/content/articlehtml/2015/cs/c5cs00190k [Accessed: 13 February 2023].

Lerner, M.B., D'Souza, J., Pazina, T., Dailey, J., Goldsmith, B.R., Robinson, M.K. and Johnson, A.T.C. 2012. Hybrids of a Genetically Engineered Antibody and a Carbon Nanotube Transistor for Detection of Prostate Cancer Biomarkers. *ACS Nano* 6(6), p. 5143. Available at: /pmc/articles/PMC3383883/ [Accessed: 26 February 2023].

Levitt, M. and Warshel, A. 1975. Computer simulation of protein folding. *Nature 1975 253:5494* 253(5494), pp. 694–698. Available at: https://www.nature.com/articles/253694a0 [Accessed: 19 July 2023].

Levitt, P.S. et al. 2012. Exploring the Role of a Conserved Class A Residue in the Ω-Loop of KPC-2 β-Lactamase: A Mechanism for Ceftazidime Hydrolysis. *The Journal of Biological Chemistry* 287(38), p. 31783. Available at: /pmc/articles/PMC3442512/ [Accessed: 29 March 2023].

Li, T. et al. 2021. Carbon Nanotube Field-Effect Transistor Biosensor for Ultrasensitive and Label-Free Detection of Breast Cancer Exosomal miRNA21. *Analytical Chemistry* 93(46), pp. 15501–15507. Available at: https://pubs.acs.org/doi/abs/10.1021/acs.analchem.1c03573 [Accessed: 1 August 2023].

Li, Z., Xiao, M., Jin, C. and Zhang, Z. 2023. Toward the Commercialization of Carbon Nanotube Field Effect Transistor Biosensors. *Biosensors 2023, Vol. 13, Page 326* 13(3), p. 326. Available at: https://www.mdpi.com/2079-6374/13/3/326/htm [Accessed: 11 April 2023].

Liao, C.-Y., Hsueh, K.-P., Tsai, J.-Z., Lee, Y.-S., Hsin, W.-M. and Hsin, Y.-M. 2013. An AlGaAs/GaAs Photo-Transistor-Based Fluorescence Detection System for Human Serum Albumin. *Journal of The Electrochemical Society* 160(9), pp. B156–B159. Available at: https://iopscience.iop.org/article/10.1149/2.077309jes [Accessed: 3 March 2023].

Lilienfeld, J.E. 1926. *Method and apparatus for controlling electric currents* 1745175 [Patent].

Lim, D. et al. 2001a. Crystal structure and kinetic analysis of β-lactamase inhibitor protein-II in complex with TEM-1 β-lactamase. *Nature Structural Biology* 8(10), pp. 848–852. Available at: http://structbio.nature.com [Accessed: 10 May 2021].

Lim, D. et al. 2001b. Crystal structure and kinetic analysis of β-lactamase inhibitor protein-II in complex with TEM-1 β-lactamase. *Nature Structural Biology 2001 8:10* 8(10), pp. 848–852. Available at: https://www.nature.com/articles/nsb1001-848 [Accessed: 7 December 2022].

Liu, C.C. and Schultz, P.G. 2010. Adding New Chemistries to the Genetic Code. *Annual review of biochemistry* 79, pp. 413–444. Available at: www.annualreviews.org [Accessed: 17 March 2023].

Liu, H., Nishide, D., Tanaka, T. and Kataura, H. 2011. Large-scale single-chirality separation of single-wall carbon nanotubes by simple gel chromatography. *Nature communications* 2, p. 309. Available at: https://pubmed.ncbi.nlm.nih.gov/21556063.

Liu, S. and Guo, X. 2012. Carbon nanomaterials field-effect-transistor-based biosensors. *NPG Asia Materials 2012 4:8* 4(8), pp. e23–e23. Available at:

https://www.nature.com/articles/am201242 [Accessed: 23 March 2023].

Ljungblad, J. 2009. *Antibody-conjugated Gold Nanoparticles integrated in a Fluorescence based Biochip*. Linköping University. Available at: https://www.diva-portal.org/smash/get/diva2:271859/FULLTEXT01.pdf [Accessed: 26 January 2022].

López-Andarias, J. et al. 2018. Toward Bioelectronic Nanomaterials: Photoconductivity in Protein–Porphyrin Hybrids Wrapped around SWCNT. *Advanced Functional Materials* 28(24), p. 1704031. Available at: https://onlinelibrary.wiley.com/doi/full/10.1002/adfm.201704031 [Accessed: 21 February 2023].

Lovell, S.C., Word, J.M., Richardson, J.S. and Richardson, D.C. 2000. The penultimate rotamer library. *Proteins: Structure, Function, and Bioinformatics* 40(3), pp. 389–408. Available at: https://doi.org/10.1002/1097-0134(20000815)40:3%3C389::AID-PROT50%3E3.0.CO.

Lu, J. and Sun, P.D. 2020. High affinity binding of SARS-CoV-2 spike protein enhances ACE2 carboxypeptidase activity. *The Journal of Biological Chemistry* 295(52), p. 18579. Available at: /pmc/articles/PMC7833600/ [Accessed: 11 April 2023].

Lu, Y., Lerner, M.B., John Qi, Z., Mitala, J.J., Hsien Lim, J., Discher, B.M. and Charlie Johnson, A.T. 2012. Graphene-protein bioelectronic devices with wavelength-dependent photoresponse. *Applied Physics Letters* 100(3), p. 033110. Available at: https://aip.scitation.org/doi/abs/10.1063/1.3678024 [Accessed: 13 February 2023].

Luo, X. and Davis, J.J. 2013. Electrical biosensors and the label free detection of protein disease biomarkers. *Chemical Society Reviews* 42(13), pp. 5944–5962. Available at: https://pubs.rsc.org/en/content/articlehtml/2013/cs/c3cs60077g [Accessed: 18 January 2023].

Lv, X. et al. 2015. Ultrafast Photoinduced Electron Transfer in Green Fluorescent Protein Bearing a Genetically Encoded Electron Acceptor. *Journal of the American Chemical Society* 137(23), pp. 7270–7273. doi: 10.1021/jacs.5b03652.

Mackerell, A.D., Feig, M. and Brooks, C.L. 2004. Extending the treatment of backbone energetics in protein force fields: limitations of gas-phase quantum mechanics in reproducing protein conformational distributions in molecular dynamics simulations. *Journal of computational chemistry* 25(11), pp. 1400–1415. Available at: https://pubmed.ncbi.nlm.nih.gov/15185334/ [Accessed: 31 October 2022].

Maehashi, K., Katsura, T., Kerman, K., Takamura, Y., Matsumoto, K. and Tamiya, E. 2007. Label-free protein biosensor based on aptamer-modified carbon nanotube field-effect transistors. *Analytical Chemistry* 79(2), pp. 782–787. Available at: https://pubs-acs-org.abc.cardiff.ac.uk/doi/full/10.1021/ac060830g [Accessed: 28 January 2022].

Mallakpour, S. and Soltanian, S. 2016. Surface functionalization of carbon nanotubes: Fabrication and applications. *RSC Advances* 6(111), pp. 109916–109935. doi: 10.1039/C6RA24522F.

Mao, J., Wang, Y., Zhu, J., Yu, J. and Hu, Z. 2018. Thiol functionalized carbon nanotubes: Synthesis by sulfur chemistry and their multi-purpose applications. *Applied Surface Science* 447, pp. 235–243. doi: 10.1016/J.APSUSC.2018.03.188.

Marchesan, S. and Prato, M. 2015. Under the lens: carbon nanotube and protein

interaction at the nanoscale. *Chemical Communications* 51(21), pp. 4347–4359. Available at: https://pubs.rsc.org/en/content/articlehtml/2015/cc/c4cc09173f [Accessed: 13 February 2023].

Martel, R., Schmidt, T., Shea, H.R., Hertel, T. and Avouris, P. 1998. Single- and multi-wall carbon nanotube field-effect transistors. *Applied Physics Letters* 73(17), p. 2447. Available at: https://aip.scitation.org/doi/abs/10.1063/1.122477 [Accessed: 22 March 2023].

Martín, O., Gutierrez, H.R., Maroto-Valiente, A., Terrones, M., Blanco, T. and Baselga, J. 2013. An efficient method for the carboxylation of few-wall carbon nanotubes with little damage to their sidewalls. *Materials Chemistry and Physics* 140(2–3), pp. 499–507. doi: 10.1016/J.MATCHEMPHYS.2013.03.060.

Massova, I. and Mobashery, S. 1998. Kinship and diversification of bacterial penicillin-binding proteins and beta-lactamases. *Antimicrobial agents and chemotherapy* 42(1), pp. 1–17. doi: 10.1128/AAC.42.1.1.

Mayrhofer, S., Domig, K.J., Mair, C., Zitz, U., Huys, G. and Kneifel, W. 2008. Comparison of Broth Microdilution, Etest, and Agar Disk Diffusion Methods for Antimicrobial Susceptibility Testing of Lactobacillus acidophilus Group Members. *Applied and Environmental Microbiology* 74(12), p. 3745. Available at: /pmc/articles/PMC2446536/ [Accessed: 18 January 2023].

McCammon, J.A., Gelin, B.R., Karplus, M., McCammon, J.A., Gelin, B.R. and Karplus, M. 1977. Dynamics of folded proteins. *Nature* 267(5612), pp. 585–590. Available at: https://ui.adsabs.harvard.edu/abs/1977Natur.267..585M/abstract [Accessed: 19 July 2023].

Mehta, S.C., Rice, K. and Palzkill, T. 2015. Natural Variants of the KPC-2 Carbapenemase have Evolved Increased Catalytic Efficiency for Ceftazidime Hydrolysis at the Cost of Enzyme Stability. *PLoS Pathogens* 11(6). Available at: /pmc/articles/PMC4452179/ [Accessed: 14 June 2022].

Miller, D.A.B. 1995. Silicon sees the light. *Nature 1995 378:6554* 378(6554), pp. 238–238. Available at: https://www.nature.com/articles/378238a0 [Accessed: 15 February 2023].

Miseta, A. and Csutora, P. 2000. Relationship Between the Occurrence of Cysteine in Proteins and the Complexity of Organisms. *Mol. Biol. Evol* 17(8), pp. 1232–1239. Available at: https://academic.oup.com/mbe/article/17/8/1232/992796 [Accessed: 26 January 2022].

Miyake-Stoner, S., Refakis, C., Hammill, J., Lusic, H., Hzen, J., Deiters, A. and Mehl, R. 2010. Generating Permissive Site-Specific Unnatural Aminoacyl-tRNA Synthetases. *Biochemistry* 49(8), pp. 1667–1677.

Mojica, M.F., Bonomo, R.A. and Fast, W. 2016. B1-Metallo-β-Lactamases: Where Do We Stand? *Current drug targets* 17(9), pp. 1029–1050. doi: 10.2174/1389450116666151001105622.

Moon, H.K., Chang, C. Il, Lee, D.-K. and Choi, H.C. 2008. Effect of Nucleases on the Cellular Internalization of Fluorescent Labeled DNA-Functionalized Single-Walled Carbon Nanotubes. *Nano Res* 1, p. 360. doi: 10.1007/s12274-008-8038-z.

Moore, G.E. 1965. Cramming more components onto integrated circuits. *Electronics* 38(8), p. 114. doi: 10.1109/N-SSC.2006.4785860.

Muckley, E.S., Nelson, A.J., Jacobs, C.B. and Ivanov, I.N. 2016. Effect of UV

irradiation on adsorption/desorption of oxygen and water on carbon nanotubes. *https://doi.org/10.1117/12.2214462* 9745, pp. 107–115. Available at: https://www.spiedigitallibrary.org/conference-proceedings-of-spie/9745/97451K/Effect-of-UV-irradiation-on-adsorption-desorption-of-oxygen-and/10.1117/12.2214462.full [Accessed: 22 June 2022].

Mukai, T. et al. 2015. Highly reproductive Escherichia coli cells with no specific assignment to the UAG codon. *Scientific Reports 2015 5:1* 5(1), pp. 1–9. Available at: https://www.nature.com/articles/srep09699 [Accessed: 14 April 2023].

Musala, S. and Vasavi, P.D. 2022. A Novel Quaternary Multiplexer using CNTFET. *ICDCS 2022 - 2022 6th International Conference on Devices, Circuits and Systems* , pp. 196–199. doi: 10.1109/ICDCS54290.2022.9780772.

Nelson, N. and Junge, W. 2015. Structure and energy transfer in photosystems of oxygenic photosynthesis. *Annual review of biochemistry* 84, pp. 659–683. Available at: https://pubmed.ncbi.nlm.nih.gov/25747397/ [Accessed: 5 April 2023].

New England Biolabs 2022. Tm Calculator. Available at: https://tmcalculator.neb.com/#!/main.

Nguyen, K. and Bruce, B.D. 2014. Growing green electricity: Progress and strategies for use of Photosystem I for sustainable photovoltaic energy conversion. *Biochimica et Biophysica Acta (BBA) - Bioenergetics* 1837(9), pp. 1553–1566. doi: 10.1016/J.BBABIO.2013.12.013.

Nguyen, V.T. et al. 2018. Phototransistors with Negative or Ambipolar Photoresponse Based on As-Grown Heterostructures of Single-Walled Carbon Nanotube and MoS 2. *Advanced Functional Materials* 28(40), p. 1802572. doi: 10.1002/adfm.201802572.

Nishiori, D. et al. 2019. Photosensing System Using Photosystem i and Gold Nanoparticle on Graphene Field-Effect Transistor. *ACS Applied Materials and Interfaces* 11(45), pp. 42773–42779. Available at: https://pubs.acs.org/doi/full/10.1021/acsami.9b14771 [Accessed: 25 January 2022].

Van Noorden, R. 2015. Interdisciplinary research by the numbers. *Nature* 525(7569), pp. 306–307. doi: 10.1038/525306A.

Norizan, M.N. et al. 2020. Carbon nanotubes: functionalisation and their application in chemical sensors. *RSC Advances* 10(71), pp. 43704–43732. Available at: https://pubs.rsc.org/en/content/articlehtml/2020/ra/d0ra09438b [Accessed: 13 February 2023].

O'Connor, D.A. 1975. Thermal Vibrations in Crystallography. *Physics Bulletin* 26(11), p. 498. Available at: https://iopscience.iop.org/article/10.1088/0031-9112/26/11/033 [Accessed: 19 April 2023].

Obite, F., Ijeomah, G. and Bassi, J.S. 2018. Carbon nanotube field effect transistors: toward future nanoscale electronics. *https://doi.org/10.1080/1206212X.2017.1415111* 41(2), pp. 147–162. Available at: https://www.tandfonline.com/doi/abs/10.1080/1206212X.2017.1415111 [Accessed: 7 March 2023].

Oltrogge, L.M., Wang, Q. and Boxer, S.G. 2014. Ground-State Proton Transfer Kinetics in Green Fluorescent Protein. *Biochemistry* 53(37), pp. 5947–5957. doi: 10.1021/bi500147n.

OriginLab Corporation 2022. OriginPro (Learning Edition).

Ou, Q. et al. 2021. Degradable Photonic Synaptic Transistors Based on Natural Biomaterials and Carbon Nanotubes. *Small* 17(10), p. 2007241. Available at: https://onlinelibrary.wiley.com/doi/full/10.1002/smll.202007241 [Accessed: 13 February 2023].

Pachauri, V. and Ingebrandt, S. 2016. Biologically sensitive field-effect transistors: from ISFETs to NanoFETs. *Essays in Biochemistry* 60(1), p. 81. Available at: /pmc/articles/PMC4986460/ [Accessed: 6 March 2023].

Pal, P.P. et al. 2015. Dry Functionalization and Doping of Single-Walled Carbon Nanotubes by Ozone. *The Journal of Physical Chemistry C* 119(49), pp. 27821–27828. doi: 10.1021/acs.jpcc.5b08832.

Palczewski, K. et al. 2000. Crystal structure of rhodopsin: A G protein-coupled receptor. *Science (New York, N.Y.)* 289(5480), pp. 739–745. Available at: https://pubmed.ncbi.nlm.nih.gov/10926528/ [Accessed: 13 February 2023].

Palzkill, T. 2018. Structural and Mechanistic Basis for Extended-Spectrum Drug-Resistance Mutations in Altering the Specificity of TEM, CTX-M, and KPC β-lactamases. *Frontiers in Molecular Biosciences* 5. Available at: https://www.frontiersin.org/articles/10.3389/fmolb.2018.00016.

Pan, T., Liu, S., Zhang, L. and Xie, W. 2022. Flexible organic optoelectronic devices on paper. *iScience* 25(2), p. 103782. doi: 10.1016/J.ISCI.2022.103782.

Papp-Wallace, K.M., Bethel, C.R., Distler, A.M., Kasuboski, C., Taracila, M. and Bonomo, R.A. 2010. Inhibitor resistance in the KPC-2 β-lactamase, a preeminent property of this class a β-lactamase. *Antimicrobial Agents and Chemotherapy* 54(2), pp. 890–897. Available at: https://journals.asm.org/doi/10.1128/AAC.00693-09 [Accessed: 29 March 2023].

Parmley, S.F. and Smith, G.P. 1988. Antibody-selectable filamentous fd phage vectors: affinity purification of target genes. *Gene* 73(2), pp. 305–318. doi: 10.1016/0378-1119(88)90495-7.

Pédelacq, J.-D., Cabantous, S., Tran, T., Terwilliger, T.C. and Waldo, G.S. 2006. Engineering and characterization of a superfolder green fluorescent protein. *Nature Biotechnology* 24(1), pp. 79–88. Available at: http://www.nature.com/articles/nbt1172 [Accessed: 13 March 2019].

Perez, F. 2013. Serial Cloner. Available at: http://serialbasics.free.fr/Serial_Cloner.html.

Perticaroli, S. et al. 2017. Description of hydration water in protein (green fluorescent protein) solution. *Journal of the American Chemical Society* 139(3), pp. 1098–1105. Available at: https://pubs.acs.org/doi/full/10.1021/jacs.6b08845 [Accessed: 1 March 2023].

Petrosino, J., Rudgers, G., Gilbert, H. and Palzkill, T. 1999. Contributions of aspartate 49 and phenylalanine 142 residues of a tight binding inhibitory protein β-lactamases. *Journal of Biological Chemistry* 274(4), pp. 2394–2400. doi: 10.1074/jbc.274.4.2394.

Philippon, A., Slama, P., Dény, P. and Labia, R. 2016. A Structure-Based Classification of Class A β-Lactamases, a Broadly Diverse Family of Enzymes. *Clinical Microbiology Reviews* 29(1), p. 29. Available at: /pmc/articles/PMC4771212/ [Accessed: 19 January 2023].

Posati, T. et al. 2019. Keratin Film as Natural and Eco-Friendly Support for Organic

Optoelectronic Devices. *Advanced Sustainable Systems* 3(11), p. 1900080. Available at: https://onlinelibrary.wiley.com/doi/full/10.1002/adsu.201900080 [Accessed: 2 March 2023].

Prasek, J., Drbohlavova, J., Chomoucka, J., Hubalek, J., Jasek, O., Adam, V. and Kizek, R. 2011. Methods for carbon nanotubes synthesis—review. *Journal of Materials Chemistry* 21(40), p. 15872. Available at: http://dx.doi.org/10.1039/c1jm12254a.

Prestrelski, S.J., Tedeschi, N., Arakawa, T. and Carpenter, J.F. 1993. Dehydration-induced conformational transitions in proteins and their inhibition by stabilizers. *Biophysical journal* 65(2), pp. 661–671. doi: 10.1016/S0006-3495(93)81120-2.

Rahman, A., Stillinger, F.H., Rahman, A. and Stillinger, F.H. 1971. Molecular Dynamics Study of Liquid Water. *JChPh* 55(7), pp. 3336–3359. Available at: https://ui.adsabs.harvard.edu/abs/1971JChPh..55.3336R/abstract [Accessed: 19 July 2023].

Ramanathan, T., Fisher, F.T., Ruoff, R.S. and Brinson, L.C. 2005. Amino-Functionalized Carbon Nanotubes for Binding to Polymers and Biological Systems. *Chemistry of Materials* 17(6), pp. 1290–1295. Available at: https://pubs.acs.org/doi/full/10.1021/cm048357f [Accessed: 19 January 2022].

Ramnani, P., Saucedo, N.M. and Mulchandani, A. 2016. Carbon nanomaterial-based electrochemical biosensors for label-free sensing of environmental pollutants. *Chemosphere* 143, pp. 85–98. doi: 10.1016/J.CHEMOSPHERE.2015.04.063.

Reddington, S., Watson, P., Rizkallah, P., Tippmann, E. and Jones, D.D. 2013a. Genetically encoding phenyl azide chemistry: new uses and ideas for classical biochemistry. *Biochemical Society transactions* 41(5), pp. 1177–82. Available at: http://www.ncbi.nlm.nih.gov/pubmed/24059505 [Accessed: 29 July 2019].

Reddington, S.C., Rizkallah, P.J., Watson, P.D., Pearson, R., Tippmann, E.M. and Jones, D.D. 2013b. Different Photochemical Events of a Genetically Encoded Phenyl Azide Define and Modulate GFP Fluorescence. *Angewandte Chemie International Edition* 52(23), pp. 5974–5977. Available at: http://www.ncbi.nlm.nih.gov/pubmed/23620472 [Accessed: 8 March 2019].

Reddington, S.C., Tippmann, E.M. and Jones, D.D. 2012. Residue choice defines efficiency and influence of bioorthogonal protein modification via genetically encoded strain promoted Click chemistry. *Chemical Communications* 48(67), pp. 8419–8421. Available at: https://pubs.rsc.org/en/content/articlehtml/2012/cc/c2cc31887c [Accessed: 11 May 2022].

Remington, S.J. 2011. Green fluorescent protein: a perspective. *Protein science : a publication of the Protein Society* 20(9), pp. 1509–1519. Available at: https://pubmed.ncbi.nlm.nih.gov/21714025/ [Accessed: 30 March 2023].

Richard, C., Balavoine, F., Schultz, P., Ebbesen, T.W. and Mioskowski, C. 2003. Supramolecular self-assembly of lipid derivatives on carbon nanotubes. *Science (New York, N.Y.)* 300(5620), pp. 775–778. Available at: https://pubmed.ncbi.nlm.nih.gov/12730595/ [Accessed: 25 January 2022].

Richardson, M.B., Brown, D.B., Vasquez, C.A., Ziller, J.W., Johnston, K.M. and Weiss, G.A. 2018. Synthesis and Explosion Hazards of 4-Azido- l -phenylalanine. *Journal of Organic Chemistry* 83(8), pp. 4525–4536. Available at: https://pubs.acs.org/doi/abs/10.1021/acs.joc.8b00270 [Accessed: 11 April 2023].

Riziotis, I.G., Ribeiro, A.J.M., Borkakoti, N. and Thornton, J.M. 2022. Conformational Variation in Enzyme Catalysis: A Structural Study on Catalytic Residues. *Journal of Molecular Biology* 434(7). Available at: /pmc/articles/PMC9005782/ [Accessed: 2 February 2023].

Rodriguez, E.A. et al. 2017. The Growing and Glowing Toolbox of Fluorescent and Photoactive Proteins. *Trends in biochemical sciences* 42(2), pp. 111–129. Available at: https://pubmed.ncbi.nlm.nih.gov/27814948/ [Accessed: 13 February 2023].

Rostovtsev, V. V, Green, L.G., Fokin, V. V and Sharpless, K.B. 2002. A stepwise huisgen cycloaddition process: copper(I)-catalyzed regioselective "ligation" of azides and terminal alkynes. *Angewandte Chemie (International ed. in English)* 41(14), pp. 2596–2599. doi: 10.1002/1521-3773(20020715)41:14<2596::AID-ANIE2596>3.0.CO;2-4.

Rudikoff, S. and Potter, M. 1976. Size differences among immunoglobulin heavy chains from phosphorylcholine-binding proteins. *Proceedings of the National Academy of Sciences of the United States of America* 73(6), p. 2109. Available at: /pmc/articles/PMC430459/?report=abstract [Accessed: 25 January 2022].

Ruscito, A. and DeRosa, M.C. 2016. Small-molecule binding aptamers: Selection strategies, characterization, and applications. *Frontiers in Chemistry* 4(MAY), p. 14. doi: 10.3389/FCHEM.2016.00014/BIBTEX.

Ruvinsky, A.M., Kirys, T., Tuzikov, A. V. and Vakser, I.A. 2011. Side-chain conformational changes upon Protein-Protein Association. *Journal of molecular biology* 408(2), pp. 356–365. Available at: https://pubmed.ncbi.nlm.nih.gov/21354429/ [Accessed: 31 January 2023].

Sadighbayan, D., Hasanzadeh, M. and Ghafar-Zadeh, E. 2020. Biosensing based on field-effect transistors (FET): Recent progress and challenges. *TrAC Trends in Analytical Chemistry* 133, p. 116067. doi: 10.1016/J.TRAC.2020.116067.

Salice, P., Gambarin, A., Daldosso, N., Mancin, F. and Menna, E. 2014. Noncovalent Interaction between Single-Walled Carbon Nanotubes and Pyrene-Functionalized Gold Nanoparticles in Water-Soluble Nanohybrids. *Journal of Physical Chemistry C* 118(46), pp. 27028–27038. Available at: https://pubs.acs.org/doi/abs/10.1021/jp505005e [Accessed: 25 January 2022].

Salverda, M.L.M., de Visser, J.A.G.M. and Barlow, M. 2010. Natural evolution of TEM-1 β-lactamase: experimental reconstruction and clinical relevance. *FEMS Microbiology Reviews* 34(6), pp. 1015–1036. Available at: https://academic.oup.com/femsre/article/34/6/1015/592234 [Accessed: 28 March 2023].

Samuel, V.R. and Rao, K.J. 2022. A review on label free biosensors. *Biosensors and Bioelectronics: X* 11, p. 100216. doi: 10.1016/J.BIOSX.2022.100216.

Santos, S., Barcons, V., Christenson, H.K., Font, J. and Thomson, N.H. 2011. The intrinsic resolution limit in the atomic force microscope: implications for heights of nano-scale features. *PloS one* 6(8), p. e23821. Available at: http://www.ncbi.nlm.nih.gov/pubmed/21912608 [Accessed: 14 March 2019].

Sanyanga, T.A. and Tastan Bishop, Ö. 2020. Structural Characterization of Carbonic Anhydrase VIII and Effects of Missense Single Nucleotide Variations to Protein Structure and Function. *International Journal of Molecular Sciences* 21(8). doi: 10.3390/ijms21082764.

Satco, D., Nugraha, A.R.T., Ukhtary, M.S., Kopylova, D., Nasibulin, A.G. and Saito,

R. 2019. Intersubband plasmon excitations in doped carbon nanotubes. *Physical Review B* 99(7), p. 075403. Available at: https://journals.aps.org/prb/abstract/10.1103/PhysRevB.99.075403 [Accessed: 21 February 2023].

Scaffaro, R., Maio, A., Agnello, S. and Glisenti, A. 2012. Plasma Functionalization of Multiwalled Carbon Nanotubes and Their Use in the Preparation of Nylon 6-Based Nanohybrids. *undefined* 9(5), pp. 503–512. doi: 10.1002/PPAP.201100140.

Schasfoort, R.B.M., Bergveld, P., Kooyman, R.P.H. and Greve, J. 1990. Possibilities and limitations of direct detection of protein charges by means of an immunological field-effect transistor. *Analytica Chimica Acta* 238(C), pp. 323–329. doi: 10.1016/S0003-2670(00)80554-1.

Schrödinger, L. and Delano, W. 2015. The PyMOL Molecular Graphics System. Available at: http://www.pymol.org/pymol.

Schroeder, V., Savagatrup, S., He, M., Lin, S. and Swager, T.M. 2019. Carbon Nanotube Chemical Sensors. *Chemical reviews* 119(1), p. 599. Available at: /pmc/articles/PMC6399066/ [Accessed: 22 November 2021].

Scouras, A.D. and Daggett, V. 2011. The Dynameomics rotamer library: amino acid side chain conformations and dynamics from comprehensive molecular dynamics simulations in water. *Protein Science* 20(2), pp. 341–352. Available at: https://pubmed.ncbi.nlm.nih.gov/21280126/ [Accessed: 31 January 2023].

Sen, T., Ma, Y., Polyakov, I. V., Grigorenko, B.L., Nemukhin, A. V. and Krylov, A.I. 2021. Interplay between Locally Excited and Charge Transfer States Governs the Photoswitching Mechanism in the Fluorescent Protein Dreiklang. *The Journal of Physical Chemistry B* 125(3), pp. 757–770. doi: 10.1021/acs.jpcb.0c09221.

Seo, G. et al. 2020. Rapid Detection of COVID-19 Causative Virus (SARS-CoV-2) in Human Nasopharyngeal Swab Specimens Using Field-Effect Transistor-Based Biosensor. *ACS nano* 14(4), pp. 5135–5142. Available at: /pmc/articles/PMC7172500/ [Accessed: 25 January 2022].

Service, R.F. 2009. Is silicon's reign nearing its end? *Science* 323(5917), pp. 1000–1002. Available at: https://www.science.org/doi/10.1126/science.323.5917.1000 [Accessed: 7 March 2023].

Setaro, A. et al. 2017. Preserving π-conjugation in covalently functionalized carbon nanotubes for optoelectronic applications. *Nature Communications* 8(1), p. 14281. Available at: https://doi.org/10.1038/ncomms14281.

Shah, A.A., Hasan, F., Ahmed, S. and Hameed, A. 2004. Characteristics, epidemiology and clinical importance of emerging strains of Gram-negative bacilli producing extended-spectrum beta-lactamases. *Research in microbiology* 155(6), pp. 409–421. Available at: https://pubmed.ncbi.nlm.nih.gov/15249058/ [Accessed: 28 March 2023].

Shao, J., Tanner, S.W., Thompson, N. and Cheatham, T.E. 2007. Clustering molecular dynamics trajectories: 1. Characterizing the performance of different clustering algorithms. *Journal of Chemical Theory and Computation* 3(6), pp. 2312–2334. Available at: https://pubs.acs.org/doi/full/10.1021/ct700119m [Accessed: 1 February 2023].

Shao, W., Shurin, M.R., Wheeler, S.E., He, X. and Star, A. 2021. Rapid Detection of SARS-CoV-2 Antigens Using High-Purity Semiconducting Single-Walled Carbon Nanotube-Based Field-Effect Transistors. *ACS Applied Materials and Interfaces*

13(8), pp. 10321–10327. Available at: https://pubs.acs.org/doi/full/10.1021/acsami.0c22589 [Accessed: 12 November 2021].

Shao, Z. et al. 2019. Memory phototransistors based on exponential-association photoelectric conversion law. *Nature Communications 2019 10:1* 10(1), pp. 1–10. Available at: https://www.nature.com/articles/s41467-019-09206-w [Accessed: 3 March 2023].

Shim, M., Javey, A., Kam, N.W.S. and Dai, H. 2001. Polymer functionalization for air-stable n-type carbon nanotube field-effect transistors [9]. *Journal of the American Chemical Society* 123(46), pp. 11512–11513. Available at: https://pubs.acs.org/doi/abs/10.1021/ja0169670 [Accessed: 6 April 2023].

Shimomura, O., Johnson, F.H. and Saiga, Y. 1962. Extraction, purification and properties of aequorin, a bioluminescent protein from the luminous hydromedusan, Aequorea. *Journal of cellular and comparative physiology* 59, pp. 223–239. doi: 10.1002/jcp.1030590302.

Shinobu, A. and Agmon, N. 2015. The hole in the barrel: Water exchange at the GFP chromophore. *Journal of Physical Chemistry B* 119(8), pp. 3464–3478. Available at: https://pubs.acs.org/doi/full/10.1021/jp5127255 [Accessed: 1 March 2023].

Shinobu, A., Palm, G.J., Schierbeek, A.J. and Agmon, N. 2010. Visualizing Proton Antenna in a High-Resolution Green Fluorescent Protein Structure. *Journal of the American Chemical Society* 132(32), pp. 11093–11102. doi: 10.1021/ja1010652.

Simanouti, T. 1949. The Normal Vibrations of Polyatomic Molecules as Calculated by Urey-Bradley Field. III. A Table of Force Constants. *The Journal of Chemical Physics* 17(10), p. 848. Available at: https://aip.scitation.org/doi/abs/10.1063/1.1747075 [Accessed: 27 October 2022].

Smolskaya, S. and Andreev, Y.A. 2019. Site-Specific Incorporation of Unnatural Amino Acids into Escherichia coli Recombinant Protein: Methodology Development and Recent Achievement. *Biomolecules* 9(7). Available at: /pmc/articles/PMC6681230/ [Accessed: 13 April 2023].

So, H.M. et al. 2005. Single-walled carbon nanotube biosensors using aptamers as molecular recognition elements. *Journal of the American Chemical Society* 127(34), pp. 11906–11907. Available at: https://pubs.acs.org/doi/full/10.1021/ja053094r [Accessed: 28 January 2022].

Sosa-Peinado, A., Mustafi, D. and Makinen, M.W. 2000. Overexpression and biosynthetic deuterium enrichment of TEM-1 beta-lactamase for structural characterization by magnetic resonance methods. *Protein expression and purification* 19(2), pp. 235–245. Available at: https://pubmed.ncbi.nlm.nih.gov/10873536/ [Accessed: 9 May 2022].

Sousa Da Silva, A.W. and Vranken, W.F. 2012. ACPYPE - AnteChamber PYthon Parser interfacE. *BMC Research Notes* 5(1), pp. 1–8. Available at: https://bmcresnotes.biomedcentral.com/articles/10.1186/1756-0500-5-367 [Accessed: 14 December 2022].

Spampinato, V., Parracino, M.A., La Spina, R., Rossi, F. and Ceccone, G. 2016. Surface analysis of gold nanoparticles functionalized with thiol-modified glucose SAMs for biosensor applications. *Frontiers in Chemistry* 4(FEB), p. 8. doi: 10.3389/FCHEM.2016.00008/BIBTEX.

Spellberg, B. and Bonomo, R.A. 2016. Editorial Commentary: Ceftazidime-Avibactam and Carbapenem-Resistant Enterobacteriaceae: "We're Gonna Need a Bigger Boat." *Clinical Infectious Diseases* 63(12), pp. 1619–1621. Available at: https://academic.oup.com/cid/article/63/12/1619/2645594 [Accessed: 29 March 2023].

Stando, G., Han, S., Kumanek, B., Łukowiec, D. and Janas, D. 2022. Tuning wettability and electrical conductivity of single-walled carbon nanotubes by the modified Hummers method. *Scientific Reports 2022 12:1* 12(1), pp. 1–13. Available at: https://www.nature.com/articles/s41598-022-08343-5 [Accessed: 27 February 2023].

Star, A., Gabriel, J.C.P., Bradley, K. and Grüner, G. 2003. Electronic detection of specific protein binding using nanotube FET devices. *Nano Letters* 3(4), pp. 459–463. Available at: https://pubs.acs.org/doi/full/10.1021/nl0340172 [Accessed: 24 March 2023].

Star, A., Tu, E., Niemann, J., Gabriel, J.C.P., Joiner, C.S. and Valcke, C. 2006. Label-free detection of DNA hybridization using carbon nanotube network field-effect transistors. *Proceedings of the National Academy of Sciences* 103(4), pp. 921–926. Available at: https://www.pnas.org/content/103/4/921 [Accessed: 24 January 2022].

Stepanenko, O. V., Verkhusha, V. V., Shavlovsky, M.M., Kuznetsova, I.M., Uversky, V.N. and Turoverov, K.K. 2008. Understanding the role of Arg96 in structure and stability of green fluorescent protein. *Proteins: Structure, Function, and Bioinformatics* 73(3), pp. 539–551. doi: 10.1002/prot.22089.

Stern, E., Wagner, R., Sigworth, F.J., Breaker, R., Fahmy, T.M. and Reed, M.A. 2007. Importance of the debye screening length on nanowire field effect transistor sensors. *Nano Letters* 7(11), pp. 3405–3409. Available at: https://pubs.acs.org/doi/full/10.1021/nl071792z [Accessed: 19 January 2023].

Stoner-Ma, D., Jaye, A.A., Ronayne, K.L., Nappa, J., Meech, S.R. and Tonge, P.J. 2008. An Alternate Proton Acceptor for Excited-State Proton Transfer in Green Fluorescent Protein: Rewiring GFP. *Journal of the American Chemical Society* 130(4), pp. 1227–1235. doi: 10.1021/ja0754507.

Stuchebrukhov, A.A. 2010. Long-distance electron tunneling in proteins: A new challenge for time-resolved spectroscopy. *Laser Physics* 20(1), pp. 125–138. doi: 10.1134/S1054660X09170186.

Studier, F. 2005. Protein production by auto-induction in high-density shaking cultures. *Protein Expression and Purification* 41(1), pp. 207–234.

Su, Z., Leung, T. and Honek, J.F. 2006. Conformational selectivity of peptides for single-walled carbon nanotubes. *Journal of Physical Chemistry B* 110(47), pp. 23623–23627. Available at: https://pubs.acs.org/doi/full/10.1021/jp065837g [Accessed: 27 January 2022].

Sun, C. et al. 2015. Single-chip microprocessor that communicates directly using light. *Nature* 528(7583), pp. 534–538. Available at: https://pubmed.ncbi.nlm.nih.gov/26701054/ [Accessed: 3 March 2023].

Sun, Y., Livan, G., Ma, A. and Latora, V. 2021. Interdisciplinary researchers attain better long-term funding performance. *Communications Physics 2021 4:1* 4(1), pp. 1–7. Available at: https://www.nature.com/articles/s42005-021-00769-z [Accessed: 3 April 2023].

Szell, M., Ma, Y. and Sinatra, R. 2018. A Nobel opportunity for interdisciplinarity. *Nature Physics 2018 14:11* 14(11), pp. 1075–1078. Available at: https://www.nature.com/articles/s41567-018-0314-6 [Accessed: 3 April 2023].

Tang, L., Wang, Y., Zhu, L., Kallio, K., Remington, S.J. and Fang, C. 2018. Photoinduced proton transfer inside an engineered green fluorescent protein: a stepwise–concerted-hybrid reaction. *Physical Chemistry Chemical Physics* 20(18), pp. 12517–12526. doi: 10.1039/C8CP01907J.

Tans, S.J., Verschueren, A.R.M. and Dekker, C. 1998. Room-temperature transistor based on a single carbon nanotube. *Nature 1998* 393(6680), pp. 49–52. Available at: https://www.nature.com/articles/29954 [Accessed: 22 March 2023].

Teillaud, J.L. et al. 1983. Monoclonal Antibodies Reveal the Structural Basis of Antibody Diversity. *Science* 222(4625), pp. 721–726. Available at: https://www.science.org/doi/abs/10.1126/science.6356353 [Accessed: 25 January 2022].

Thomas, S.K. et al. 2020. Site-Specific Protein Photochemical Covalent Attachment to Carbon Nanotube Side Walls and Its Electronic Impact on Single Molecule Function. *Bioconjugate Chemistry* 31(3), pp. 584–594. Available at: https://pubs.acs.org/doi/abs/10.1021/acs.bioconjchem.9b00719 [Accessed: 11 May 2021].

van Thor, J.J. 2009. Photoreactions and dynamics of the green fluorescent protein. *Chemical Society Reviews* 38(10), p. 2935. doi: 10.1039/b820275n.

Tian, X.J., Wang, Y.C., Yu, H.B., Dong, Z.L., Xi, N. and Tung, S. 2009. Di-electrophoresis assembly and fabrication of SWCNT field-effect transistor. *Chinese Science Bulletin 2009 54:23* 54(23), pp. 4451–4457. Available at: https://link.springer.com/article/10.1007/s11434-009-0206-3 [Accessed: 13 May 2022].

Tlili, C., Myung, N. V., Shetty, V. and Mulchandani, A. 2011. Label-free, chemiresistor immunosensor for stress biomarker cortisol in saliva. *Biosensors and Bioelectronics* 26(11), pp. 4382–4386. doi: 10.1016/J.BIOS.2011.04.045.

Tong, J., Zhang, L., Wang, Y. and Li, T. 2020. High Response Photodetection by Applying the Optimized Photoreceptor Protein Modification on Graphene Based Field Effect Transistors. *Frontiers in Materials* 7, p. 222. doi: 10.3389/fmats.2020.00222.

Tooke, C.L., Hinchliffe, P., Bragginton, E.C., Colenso, C.K., Hirvonen, V.H.A., Takebayashi, Y. and Spencer, J. 2019. β-Lactamases and β-Lactamase Inhibitors in the 21st Century. *Journal of molecular biology* 431(18), pp. 3472–3500. doi: 10.1016/j.jmb.2019.04.002.

Tornøe, C.W., Christensen, C. and Meldal, M. 2002. Peptidotriazoles on solid phase: [1,2,3]-triazoles by regiospecific copper(i)-catalyzed 1,3-dipolar cycloadditions of terminal alkynes to azides. *The Journal of organic chemistry* 67(9), pp. 3057–3064. Available at: https://pubmed.ncbi.nlm.nih.gov/11975567/ [Accessed: 20 March 2023].

Tran, T.T. and Mulchandani, A. 2016. Carbon nanotubes and graphene nano field-effect transistor-based biosensors. *TrAC Trends in Analytical Chemistry* 79, pp. 222–232. doi: 10.1016/J.TRAC.2015.12.002.

Tsien, R.Y. 1998. The green fluorescent protein. *Annual review of biochemistry* 67, pp. 509–544. Available at: https://pubmed.ncbi.nlm.nih.gov/9759496/ [Accessed: 13

February 2023].

Tuerk, C. and Gold, L. 1990. Systematic Evolution of Ligands by Exponential Enrichment: RNA Ligands to Bacteriophage T4 DNA Polymerase. *Science* 249(4968), pp. 505–510. Available at: https://www.science.org/doi/abs/10.1126/science.2200121 [Accessed: 28 January 2022].

Tung, N.T. et al. 2017. Peptide aptamer-modified single-walled carbon nanotube-based transistors for high-performance biosensors. *Scientific Reports 2017 7:1* 7(1), pp. 1–9. Available at: https://www.nature.com/articles/s41598-017-18169-1 [Accessed: 1 August 2023].

Uvdal, K., Bodö, P. and Liedberg, B. 1992. l-cysteine adsorbed on gold and copper: An X-ray photoelectron spectroscopy study. *Journal of Colloid and Interface Science* 149(1), pp. 162–173. doi: 10.1016/0021-9797(92)90401-7.

Vasala, A., Hytönen, V.P. and Laitinen, O.H. 2020. Modern Tools for Rapid Diagnostics of Antimicrobial Resistance. *Frontiers in Cellular and Infection Microbiology* 10, p. 526944. doi: 10.3389/FCIMB.2020.00308/BIBTEX.

Walker, J.M. et al. 2005. Protein Identification and Analysis Tools on the ExPASy Server. *The Proteomics Protocols Handbook* , pp. 571–607. Available at: https://link.springer.com/protocol/10.1385/1-59259-890-0:571 [Accessed: 20 June 2022].

Wang, Q.H. et al. 2012. Understanding and controlling the substrate effect on graphene electron-transfer chemistry via reactivity imprint lithography. *Nature Chemistry* 4(9), pp. 724–732. Available at: https://asu.pure.elsevier.com/en/publications/understanding-and-controlling-the-substrate-effect-on-graphene-el [Accessed: 13 February 2023].

Wang, S. et al. 2003. Peptides with selective affinity for carbon nanotubes. *Nature Materials 2003 2:3* 2(3), pp. 196–200. Available at: https://www.nature.com/articles/nmat833 [Accessed: 27 January 2022].

Wang, X. et al. 2009. Fabrication of Ultralong and Electrically Uniform Single-Walled Carbon Nanotubes on Clean Substrates. *Nano Letters* 9(9), pp. 3137–3141. Available at: http://www.ncbi.nlm.nih.gov/pubmed/19650638 [Accessed: 7 March 2019].

Warshel, A. and Levitt, M. 1976. Theoretical studies of enzymic reactions: Dielectric, electrostatic and steric stabilization of the carbonium ion in the reaction of lysozyme. *Journal of Molecular Biology* 103(2), pp. 227–249. doi: 10.1016/0022-2836(76)90311-9.

Watanabe, H., Elstner, M. and Steinbrecher, T. 2013. Rotamer decomposition and protein dynamics: efficiently analyzing dihedral populations from molecular dynamics. *Journal of computational chemistry* 34(3), pp. 198–205. Available at: https://pubmed.ncbi.nlm.nih.gov/23007849/ [Accessed: 1 February 2023].

Waterhouse, A. et al. 2018. SWISS-MODEL: homology modelling of protein structures and complexes. *Nucleic Acids Research* 46(W1), pp. W296–W303. Available at: https://academic.oup.com/nar/article/46/W1/W296/5000024 [Accessed: 21 October 2022].

Winkler, J.R., Di Bilio, A.J., Farrow, N.A., Richards, J.H. and Gray, H.B. 1999. Electron tunneling in biological molecules. *Pure and Applied Chemistry* 71(9), pp. 1753–1764. Available at:

https://www.degruyter.com/document/doi/10.1351/pac199971091753/html?lang=en [Accessed: 21 April 2023].

Winkler, J.R. and Gray, H.B. 2014. Long-Range Electron Tunneling. *Journal of the American Chemical Society* 136(8), pp. 2930–2939. doi: 10.1021/ja500215j.

Wise, K.E., Park, C., Siochi, E.J. and Harrison, J.S. 2004. Stable dispersion of single wall carbon nanotubes in polyimide: the role of noncovalent interactions. *Chemical Physics Letters* 391(4–6), pp. 207–211. doi: 10.1016/J.CPLETT.2004.04.096.

Wu, X., Wu, D., Lu, Z., Chen, W., Hu, X. and Ding, Y. 2009. A novel method for high-level production of TEV protease by superfolder GFP tag. *Journal of biomedicine & biotechnology* 2009, p. 591923. doi: 10.1155/2009/591923.

Xu, H., Yin, L., Liu, C., Sheng, X. and Zhao, N. 2018a. Recent Advances in Biointegrated Optoelectronic Devices. *Advanced Materials* 30(33). doi: 10.1002/ADMA.201800156.

Xu, Q., Schmidt, B., Pradhan, S. and Lipson, M. 2005. Micrometre-scale silicon electro-optic modulator. *Nature* 435(7040), pp. 325–327. Available at: https://pubmed.ncbi.nlm.nih.gov/15902253/ [Accessed: 3 March 2023].

Xu, X. et al. 2021. Tuning Electrostatic Gating of Semiconducting Carbon Nanotubes by Controlling Protein Orientation in Biosensing Devices. *Angewandte Chemie* 133(37), pp. 20346–20351. Available at: https://onlinelibrary.wiley.com/doi/full/10.1002/ange.202104044 [Accessed: 22 November 2021].

Xu, X., Clément, P., Eklöf-Österberg, J., Kelley-Loughnane, N., Moth-Poulsen, K., Chávez, J.L. and Palma, M. 2018b. Reconfigurable Carbon Nanotube Multiplexed Sensing Devices. *Nano Letters* 18(7), pp. 4130–4135. Available at: https://pubs.acs.org/doi/full/10.1021/acs.nanolett.8b00856 [Accessed: 24 January 2022].

Yang, C.-W., Hwang, I.-S., Chen, Y.F., Chang, C.S. and Tsai, D.P. 2007. Imaging of soft matter with tapping-mode atomic force microscopy and non-contact-mode atomic force microscopy. *Nanotechnology* 18(8), p. 084009. Available at: http://stacks.iop.org/0957-4484/18/i=8/a=084009?key=crossref.31792e1867341c628bb97cc24d25e914 [Accessed: 14 March 2019].

Yang, T.-T., Cheng, L. and Kain, S.R. 1996. Optimized Codon Usage and Chromophore Mutations Provide Enhanced Sensitivity with the Green Fluorescent Protein. *Nucleic Acids Research* 24(22), pp. 4592–4593. Available at: https://doi.org/10.1093/nar/24.22.4592.

Yao, X., Zhang, Y., Jin, W., Hu, Y. and Cui, Y. 2021. Carbon Nanotube Field-Effect Transistor-Based Chemical and Biological Sensors. *Sensors* 21(3). doi: 10.3390/s21030995.

Yomogida, Y., Tanaka, T., Zhang, M., Yudasaka, M., Wei, X. and Kataura, H. 2016. Industrial-scale separation of high-purity single-chirality single-wall carbon nanotubes for biological imaging. *Nature communications* 7, p. 12056. Available at: https://pubmed.ncbi.nlm.nih.gov/27350127.

Yoo, S. et al. 2021. Enhanced Ultraviolet Photoresponse Characteristics of Indium Gallium Zinc Oxide Photo-Thin-Film Transistors Enabled by Surface Functionalization of Biomaterials for Real-Time Ultraviolet Monitoring. *ACS Applied*

Materials & Interfaces , p. acsami.1c15565. doi: 10.1021/acsami.1c15565.

Zajac, J.M., Schubert, M., Roland, T., Keum, C., Samuel, I.D.W. and Gather, M.C. 2018. Time-Resolved Studies of Energy Transfer in Thin Films of Green and Red Fluorescent Proteins. *Advanced Functional Materials* 28(24), p. 1706300. Available at: https://onlinelibrary.wiley.com/doi/full/10.1002/adfm.201706300 [Accessed: 13 February 2023].

Zaki, A.J. et al. 2018. Defined covalent assembly of protein molecules on graphene using a genetically encoded photochemical reaction handle. *RSC Advances* 8(11), pp. 5768–5775. Available at: http://xlink.rsc.org/?DOI=C7RA11166E [Accessed: 13 March 2019].

Zeng, L., Alemany, L.B., Edwards, C.L., Barron, A.R. and Smalley, R.E. 2008. Demonstration of Covalent Sidewall Functionalization of Single Wall Carbon Nanotubes by NMR Spectroscopy: Side Chain Length Dependence on the Observation of the Sidewall sp 3 Carbons. *Nano Res* . doi: 10.1007/s12274-008-8004-9.

Zhang, S., Garcia-D'Angeli, A., Brennan, J.P. and Huo, Q. 2014. Predicting detection limits of enzyme-linked immunosorbent assay (ELISA) and bioanalytical techniques in general. *Analyst* 139(2), pp. 439–445. Available at: http://dx.doi.org/10.1039/C3AN01835K.

Zhao, J. et al. 2016. Efficient organic solar cells processed from hydrocarbon solvents. *Nature Energy 2016 1:2* 1(2), pp. 1–7. Available at: https://www.nature.com/articles/nenergy201527 [Accessed: 2 March 2023].

Zheng, H.Y., Alsager, O.A., Zhu, B., Travas-Sejdic, J., Hodgkiss, J.M. and Plank, N.O.V. 2016a. Electrostatic gating in carbon nanotube aptasensors. *Nanoscale* 8(28), pp. 13659–13668. Available at: https://pubs.rsc.org/en/content/articlehtml/2016/nr/c5nr08117c [Accessed: 13 January 2023].

Zheng, H.Y., Alsager, O.A., Zhu, B., Travas-Sejdic, J., Hodgkiss, J.M. and Plank, N.O.V. 2016b. Electrostatic gating in carbon nanotube aptasensors. *Nanoscale* 8(28), pp. 13659–13668. Available at: https://pubs.rsc.org/en/content/articlehtml/2016/nr/c5nr08117c [Accessed: 11 May 2021].

Zheng, L., Jain, D. and Burke, P. 2009. Nanotube-peptide interactions on a silicon chip. *Journal of Physical Chemistry C* 113(10), pp. 3978–3985. Available at: https://pubs.acs.org/doi/full/10.1021/jp809370z [Accessed: 27 January 2022].

Zheng, M. et al. 2003. DNA-assisted dispersion and separation of carbon nanotubes. *Nature Materials 2003 2:5* 2(5), pp. 338–342. Available at: https://www.nature.com/articles/nmat877 [Accessed: 13 December 2021].

Zheng, Z., Zhang, H., Zhai, T. and Xia, F. 2021. Overcome Debye Length Limitations for Biomolecule Sensing Based on Field Effective Transistors†. *Chinese Journal of Chemistry* 39(4), pp. 999–1008. Available at: https://doi.org/10.1002/cjoc.202000584.

Zhou, F., Chen, J., Tao, X., Wang, X. and Chai, Y. 2019a. 2D Materials Based Optoelectronic Memory: Convergence of Electronic Memory and Optical Sensor. *Research* 2019, pp. 1–17. doi: 10.34133/2019/9490413.

Zhou, Y., Fang, Y. and Ramasamy, R.P. 2019b. Non-Covalent Functionalization of Carbon Nanotubes for Electrochemical Biosensor Development. *Sensors (Basel,*

Switzerland) 19(2). Available at: /pmc/articles/PMC6358788/ [Accessed: 24 January 2022].

Zimmer, M. 2009. GFP: from jellyfish to the Nobel prize and beyond. *Chemical Society Reviews* 38(10), pp. 2823–2832. Available at: https://pubs.rsc.org/en/content/articlehtml/2009/cs/b904023d [Accessed: 13 February 2023].

Zitti, A. and Jones, D. 2023. Expanding the genetic code: a non-natural amino acid story. *The Biochemist* 45(1), pp. 2–6. Available at: /biochemist/article/45/1/2/232654/Expanding-the-genetic-code-a-non-natural-amino [Accessed: 17 March 2023].

Zorn, N.F. and Zaumseil, J. 2021. Charge transport in semiconducting carbon nanotube networks. *Applied Physics Reviews* 8(4), p. 041318. Available at: https://aip.scitation.org/doi/abs/10.1063/5.0065730 [Accessed: 24 March 2023].

8. Appendix

Table 8.1 – Gene sequence copied into AlphaFold.

Protein	Sequence (one letter code)
BLIP-II WT	ATSVVAWGGNNDWGEATVPAEAQSGVDAIAGGYFHGLALKGGKVL GWGANLNGQLTMPAATQSGVDAIAAGNYHSLALKDGEVIAWGGNE DGQTTVPAEARSGVDAIAAGAWASYALKDGKVIAWGDDSDGQTTV PAEAQSGVTALDGGVYTALAVKNGGVIAWGDNYFGQTTVPAEAQS GVDDVAGGIFHSLALKDGKVIAWGDNRYKQTTVPTEALSGVSAIAS GEWYSLALKNGKVIAWGSSRTAPSSVQSGVSSIEAGPNAAYALKGG SGSGHHHHHH

Table 8.2 – Atom types.

Atom type	Mass	Definition
C	12.01100	Carbonyl C, peptide backbone
CA	12.01100	Aromatic C
CT1	12.01100	Aliphatic sp3 C for CH
CT2	12.01100	Aliphatic sp3 C for CH2
H	1.00800	Polar H
HA2	1.00800	Alkane, CH2, new LJ params
HB1	1.00800	Backbone H
HP	1.00800	Aliphatic backbone H, to CT2
ND	14.00700	N=N=N for azide
NE	14.00700	N=N for azide
NH1	14.00700	Peptide nitrogen

NX	14.00700	C=N=N for azide	
O	15.99900	Carbonyl oxygen	

Table 8.3 – Residue type (*atoms*).

Atom name	Atom type	Charge	Atom count
N	NH1	-0.415700	0
HN	H	0.271900	1
CA	CT1	0.012019	2
HA	HB1	0.051465	3
CB	CT2	-0.037897	4
HB1	HA2	0.057901	5
HB2	HA2	0.057901	6
CG	CA	0.014483	7
CD1	CA	-0.203794	8
HD1	HP	0.170701	9
CE1	CA	-0.165912	10
HE1	HP	0.160099	11
CZ	CA	0.317371	12
N01	NX	-0.613208	13
N02	ND	0.725516	14

N03	NE	-0.317488	15
CD2	CA	-0.182445	16
HD2	HP	0.178643	17
CE2	CA	-0.264857	18
HE2	HP	0.153902	19
C	C	0.597300	20
O	O	-0.567900	21

Table 8.4 – Residue type (*bonds*).

Atom i	Atom j
CB	CA
CG	CB
CD2	CG
CE1	CD1
CZ	CE2
N01	CZ
N02	N01
N03	N02
N	HN
N	CA

C	CA
C	+N
CA	HA
CB	HB1
CB	HB2
CD1	HD1
CD2	HD2
CE1	HE1
CE2	HE2
O	C
CD1	CG
CE1	CZ
CE2	CD2

Table 8.5 – Residue type (*impropers*).

Atom i	Atom j	Atom k	Atom l
N	-C	CA	HN
C	CA	+N	O

Table 8.6 – Residue type (*cmap*).

Atom i	Atom j	Atom k	Atom l	Atom m
-C	N	CA	C	+N

Table 8.7 – Bonded interactions (*bonds*). Only showing new additions to the forcefield.

Atom i	Atom j	Func	Bθ	Kb
CA	NX	1	0.14079000	325770.00
NX	ND	1	0.12714000	587180.00
ND	NE	1	0.13524000	444680.00

Table 8.8 – Bonded interactions (angle types). Only showing new additions to the forcefield.

Atom i	Atom j	Atom k	Func	Thetaθ	Ktheta
CA	CA	NX	5	120.61	567.35
CA	NX	ND	5	114.35	589.94
NX	ND	NE	5	113.34	621.74

Table 8.9 – Bonded interactions (*dihedral types*). Only showing new additions to the forcefield.

Atom i	Atom j	Atom k	Atom l	Func	Phiθ	Kphi	Mult
CA	CA	CA	NX	9	180	15.1670	2

CA	CA	NX	ND	9	180	0.0000	3
CA	NX	ND	NE	9	0	11.7152	1
CA	NX	ND	NE	9	180	12.5520	2
NX	CA	CA	HP	9	180	15.1670	2

Table 8.10 – Bonded interactions (*impropers*). Only showing new additions to the forcefield.

Atom i	Atom j	Atom k	Atom l	Func	Phiθ	Kphi	Pn
CA	CA	CA	NX	4	180	4.6024	2

Table 8.11 – Non-bonded interactions (*atom types*). Only showing new additions to the forcefield.

Atom type	Atom number	Mass	Charge	P type	Sigma	Epsilon
NX	7	14.0070	0.000	A	0.3250	0.71128
ND	7	14.0070	0.000	A	0.3250	0.71128
NE	7	14.0070	0.000	A	0.3250	0.71128

Table 8.12 – Termini database (*replace*). Only showing new additions to the forcefield for BLIP-II[41AzF].

Old atom name	New atom name	New atom type	Mass	Charge
N	N	NH3	14.0070	-0.417000

CA	CA	CT1	12.0110	0.013219
HA	HA	HB1	1.0080	0.053465

Table 8.13 – Termini database (*add* line 1). Only showing new additions to the forcefield.

Hydrogen type	Hydrogen type	Atom i	Atom j	Atom k	Atom l
3	4	H	N	CA	C

Table 8.14 – Termini database (*add* line 2).

Atom type	Mass	Charge	Charge group
HC	1.008	0.009	-1

Table 8.15 - Termini database (*delete*).

Atom type
HN